ON THE EFFECTS OF TEXTURE AND STRAIN-PATH CHANGES ON THE DUCTILE FRACTURE OF MG ALLOYS

A Dissertation

by

SHAMIK BASU

Submitted to the Office of Graduate and Professional Studies of
Texas A&M University
in partial fulfillment of the requirements for the degree of

DOCTOR OF PHILOSOPHY

Chair of Committee,	Amine A. Benzerga
Committee Members,	Ibrahim Karaman
	Ramesh Talreja
	Jyhwen Wang
Head of Department,	Ibrahim Karaman

August 2016

Major Subject: Materials Science & Engineering

ABSTRACT

Increasing need for weight reduction to improve fuel efficiency and reduce emissions makes Magnesium alloys ideal candidates for structural applications, notably in transportation. However, limited formability at room temperature along with catastrophic failure after limited necking are among the drawbacks that limit their application. Plastic anisotropy is often invoked to rationalize low formability of strongly anisotropic materials. However, analysis based on homogenization theory suggests that certain forms of plastic anisotropy may hinder void growth under any triaxial stress state or loading orientation. Here, two textures produced through Equi-Channel Angular Extrusion (ECAE), a severe plastic deformation technique were investigated and compared with the well-known rolling texture. Deformation anisotropy and damage accumulation were investigated at room temperature. A suite of analytical measurements and observations were carried out to characterize the microstructure in the as-rolled, post-processing and post-deformation states under multiaxial stress states. Their connection to macroscopic fracture strains and frac-ture mode (normal versus shear) was elucidated using postmortem fractography and microscopic analysis. A simple model was proposed to rationalize the trends. The major findings suggest that anisotropy can be altered to aid ductility. The trends were well captured by the model and can help guide new processing routes. Any progress in fundamental understanding of limiting factors affecting ductility of Mg alloys must translate into tangible metrics in Mg sheets. For this reason, part of this work was aimed at addressing aspects of anisotropy and failure in Mg sheets through some punch stretching tests. In sheet metal forming, it is customary to use forming limit diagrams (FLDs) to determine formability limits. An important limitation of FLDs

is that they are strictly valid under proportional loading conditions. However, metal forming operations involve various non-proportional loading paths. In addition, it is not clear whether the formability of Mg sheets is determined by plastic instabilities such as necking or by fracture. For these reasons, understanding the effect of strain path changes on the ductility, flow and ductile fracture of these alloys is important. In particular, a thorough experimental study of Mg sheet fracture under combined tension and shear was conducted during a five-month visit to Texas A& M Qatar in Doha. Digital image correlation was extensively used to obtain whole field strain maps. An extensive set of finite element analyses were subsequently carried out to extract key information from the experiments regarding stress distributions and stress state indicators. Using this combined experimental/computational methodology, the fracture loci of the sheet were obtained according to various definitions. The designed program enables a comparison to be made between the fracture loci with and without load path change.

DEDICATION

This work is dedicated to my parents Mr. Subir Basu and Mrs. Mausumi Basu for having unbounded faith in my ability and for showing immense patience throughout the course of my PhD.

ACKNOWLEDGEMENTS

First and foremost I would like to thank my adviser, Prof. Amine Benzerga for providing me a environment where I enjoyed freedom to pursue my ideas. He always had confidence in my engineering and scientific abilities. I had some great discussions and brain storming sessions that provided more clarity into the subject. The knowledge and enthusiasm he has for his research was contagious and motivational for me, even during tough times in the Ph.D. His advice on both career as well as on my research have been invaluable which taught me enjoy my work in graduate school.

I want to thank my committee members Dr. Ibrahim Karaman, Dr. Ramesh Talreja and Dr. Jyhwen Wang for giving me guidance, brilliant comments and suggestions through the course of the research as and when I needed and letting my defense be an enjoyable moment, thanks to you.

Thanks also go to NSF and QNRF for providing the funding for this research. These enabled me to work with great colleagues like Dr. Ebubekir Dogan, Dr. Stefan Soare, Dr. Georges Ayoub, Dr. Bilal Mansoor. Special thanks to Dr. Yazid Madi for his help during short visit at Texas A& M.

Thanks to my research group mates especially Babak and Nithin who have helped me on numerous accounts both scientifically and for providing immense support in data acquisition, data interpretation and theoretical conceptualization. It was often a result of long discussions with them that new ideas emerged and major challenges were overcome.

A special thanks to my family. Words can not express how grateful I am to my mother, father, mother-in-law, father-in-law and my sister Sayoni Basu and everyone

else for all of the sacrifices that youve made to support my research. Most of all I would like to thank my dear wife, Madhavi Sinha, for all the sacrifices without which it would not have been possible to complete this work.

My daughter, Shanaya Basu, was my biggest motivation and inspiration to accomplish my work. Thanks to all my friend for supporting me in the most difficult times and writing this thesis, they always gave me the moral support and strength I needed to keep going.

Last but not the least, I extend my thanks to department to the Materials Science and Engineering and Aerospace Engineering department for facilities and equipment. Yolanda Veals and Newton Michelle, Miriam Brown, Jules Henry, Ashley for extending full cooperation. Thanks to Rodney Inmon the lab manager Aerospace Engineering for never stopping to help me during my experimental work.

TABLE OF CONTENTS

Page

LIST OF FIGURES

FIGURE Page

LIST OF TABLES

TABLE Page

1. INTRODUCTION

1.1 Motivation

The growing need for lightweight structures is important to address both energy and environmental concerns. Magnesium alloys have been very attractive materials for applications that require energy efficiency. Due to their light weight and high strength to weight ratio they have been projected as prime candidates for applications such as transport industry[1]. There are many applications in which cast magnesium alloys are currently used e.g., racing cars and helicopters. However their application has been restricted to only small scale due to the high cost of production and low formability of these alloys for complex shapes and geometries. The limited ductility and poor formability at room temperature is mainly attributed to the absence of sufficiently active deformation systems[2]. This is a result of the large differences in critical resolved shear stress of basal and non-basal slip systems.

The design of these lightweight alloys has to meet certain specifications of stiffness, strength, formability, durability and impact and damage tolerance based on its applications. In the current approach the stiffness and strength issues are met through some ad hoc methodology during alloy development stages. However, formability or impact tolerance are met later though some costly post processing. These inefficient approaches to material design is due to lack of understanding of the material system and lack of robust models that can connect macroscale and microscale features such as grain size, texture and inclusions.

A lot of studies in the recent few years have been dedicated more towards understanding the plastic flow behavior and strengthening of Mg alloys[3, 4, 5, 6, 7, 8, 9]. However, little is known about the damage and fracture behavior of these

alloys inspite of the pressing issues of limited formability and poor ductility[10, 11, 12]. Mg alloys are inherently anisotropic due to the HCP crystal structure (c/a ratio) and processing by conventional thermo-mechanical processes such as rolling and extrusion induced strong textures. The strong basal texture in wrought magnesium alloys leads to strong anisotropy. It is a general belief that this strong anisotropy in plastic flow is responsible for poor ductility in Mg alloys. Research in the last two decades have been dedicated to alleviate these shortcomings by developing knowledge about the complex deformation mechanisms and structural manipulations to reduce or suppress the anisotropy. WE43, which exhibits isotropic behavior by addition of rare earth (RE) metals, was considered better than AZ31 in terms of ductility[13]. However, these ductilities are only characterized under uniaxial loading conditions. When studied under triaxial loadings by some researchers recently, the results were surprisingly low as shown in Fig. 1. Hence it is important to characterize ductility under a wide range of stress triaxialities.

Mukai et. al.[15] were the first to process AZ31 by ECAE processing to improve the ductility more than twofold. This improvement in ductility was attributed to the randomness in texture. Agnew et. al.[16] challenged the claims of Mukai[15] and repeated the experiments and showed that the texture was not random by performing experiments in different principal and off-axis directions. Most directions showed similar or poorer response than the conventionally extruded alloy. The latter[16] concluded that ECAE produces stronger texture than the conventional processes. However, the authors in [16] did not provide a rationale for the increase in ductility observed in most directions as compared to as-rolled AZ31. Meanwhile, most other efforts on texture engineering have focused on generating random textures or atleast weak textures, that is on eliminating the anisotropy.

The main hypothesis of this research is that the plastic anisotropy of Mg alloys

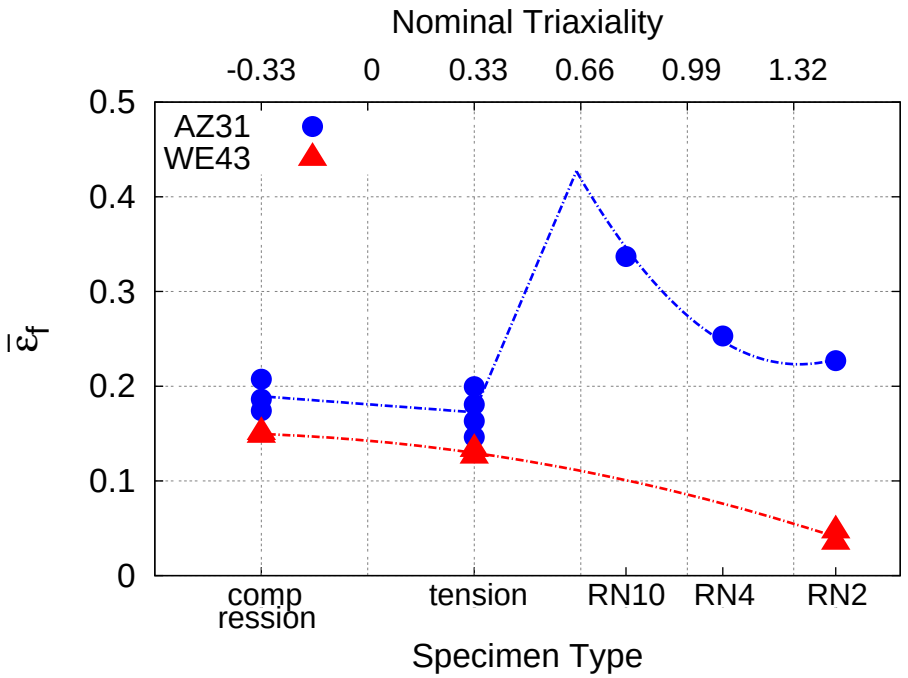

Figure 1: Fracture locus for WE43 and AZ31 Mg alloys under different stress states.[14]

can be engineered to yield materials with good strength and ductility combinations. This is guided through an indicator for characterizing the effect of anisotropy on ductility in a material. This anisotropy effect on ductility (AED) factor also known as the h-factor emerges in the nonlinear homogenization problem of Benzerga and Besson[17] who obtained the effective behavior of a porous material made up of a plastically anisotropic matrix along with a damage growth law in the form of the void volume fraction. They modeled the matrix as a Hill type orthotropic material. The AED or h-factor emerged as a scalar invariant of Hill's anisotropy tensor. Later Keralavarma and Benzerga[18] extended the early model[17] to couple void shape/orientation effects with matrix anisotropy effects. In their model too the AED directly affects void growth, hence ductility. This micromechanical model predicts the influence of plastic anisotropy on cavity growth in a material. A value greater than 2 for

this factor would mean beneficial effects on ductility.

This motivated the study to aim at altering/tailoring the anisotropy to obtain suitable textures that would aid ductility. ECAE has been proved to be an effective method to improve mechanical properties in a material by reduction in grain size [5]. Through this method texture can also be modified. It should be mentioned that some investigators [19, 20, 21, 22] have also tried to use ECAP to modify the texture, but often with the intent to reduce the texture intensity based on the common belief that a strong texture causes a reduction in ductility. Processing routes chosen were carefully guided by VPSC(Visco-Plastic Self-Consistent) models to choose paths that would aid processability. The experiments performed would help corroborate/falsify the hypothesis based on microscopic evidence.

To sum up, there is need for understanding the role of texture on damage accumulation processes that ultimately affect the ductility in Mg alloys. This would help us guide crystal plasticity to design new manufacturing processes that would not only mitigate the adverse effects of anisotropy but also tailor it for improved processablity and performance.

Any progress in fundamental understanding of limiting factors affecting ductility of Mg alloys must translate into tangible metrics in Mg sheets, as the final product e.g. in the transportation industry. For this reason, part of this work will address aspects of anisotropy and failure in Mg sheets. In sheet metal forming, it is customary to use forming limit diagrams (FLDs) to determine formability limits. An important limitation of FLDs is that they are strictly valid under proportional loading conditions. However, metal forming operations involve various nonproportional loading paths. In addition, it is not clear whether the formability of Mg sheets is determined by plastic instabilities such as necking or by fracture. For these reasons, another topic this thesis addresses is the effect of strain path changes on the duc-

tility of Mg alloys. Plasticity is path dependent and hence ductile fracture which involves large plastic deformation before failure is also path dependent. Hence it is important to understand the effect of these strain path changes on flow and ductile fracture. The initial part of this study aimed at understanding the effect of this non-proportionality under relatively simple conditions by choosing a material which is (i) mostly isotropic; and (ii) fails due to progressive cavitation. Cavitation here refers to the usual processes of void nucleation, growth and coalescence[23]. Guided by previous theoretical analyses[24], an experimental program was designed to probe the path-dependence of the fracture locus in ductile materials. The designed program enables to make a comparison between the fracture loci with and without load path change. It also allows qualitative comparisons to be made with previously published theoretical results.

Industrial metal forming processes involve complex deformation histories which consist of numerous strain path alterations. A reasonable understanding of the fracture mechanisms and the effect of anisotropy on the formability of complex material systems like Mg alloys is of prime importance. A good way of representing formability data is by use of forming limit diagrams (FLDs)[25, 26]. However, FLDs are strictly applied to proportional loading conditions. Formability operations strongly depends of the deformation history and in real applications have complex loading histories[27, 28]. Also, Mg alloys have a tendency to shear localize and hence deformation under these conditions are highly non-proportional.

1.2 Objectives

The following are the research objectives of this dissertation.

1. Investigate the effect of plastic anisotropy on the ductility of polycrystalline Mg alloys at fixed chemical composition and grain size. This involves textural modifications by means of severe plastic deformation in collaboration with the group of Prof. Karaman at TAMU. This is a purely hypothesis-driven research based on prior theoretical work in the field. As we demonstrated the success of this approach, we hopefully will open the door to engineering rather than suppressing the anisotropy of this class of advanced metallic materials.

2. Good ductility does not always translate into good formability, especially in materials prone to shear rupture, such as Mg alloys. This objective also involved a collaborative work with Prof. Karamans group for the processing part but also with Prof. Kridli and Dr. Ayoub at Texas A& M Qatar for conducting large-scale sheet metal forming experiments for demonstration purposes.

3. Investigate the ductile fracture of Mg sheets under combined tension and shear. Shear failure is major concern in various sheet metals, especially Mg. Also, this part will focus on the regime of low stress triaxialities, which has been a subject of active research over the past decade. The experimental setup for this part of the research was designed from the ground up and realized during a visit to Texas A& M Qatar in collaboration with the team of Prof. Mansoor.

4. Investigate the effect of non proportional loading on the fracture locus of a Mg alloy.

    - Demonstrate on a model material the sensitivity of fracture locus to load-path changes. What is required of the model material is that (i) it is

isotropic; (ii) it has established failure mechanisms. This research has appeared in a journal publication.

- Carry out a similar investigation in Mg sheets, which are strongly anisotopic and their fracture mechanisms are still debated.

2. ANISOTROPY EFFECTS ON DUCTILITY

2.1 Introduction

Plastic anisotropy is often invoked to rationalize the low formability of magnesium alloys at low homologous temperatures [29, 30]. Mg alloys are inherently anisotropic as a result of their hexagonal-close-packed crystalline structure. Furthermore, conventional thermo-mechanical processing, such as rolling, leads to sharp textures and associated anisotropy at the polycrystalline level [31, 32]. This anisotropy is due to large differences in critical resolved shear stress (CRSS) of basal and non-basal slip systems with the non-basal slip activated only at elevated temperatures [33]. The activated systems are often too few to satisfy the basic strain compatibility criteria [34] and the two independent slip systems have both their Burgers vector parallel to the basal plane. Thus, the anisotropy-induced incompatibility in plastic deformation is believed to trigger stress concentrations, hence failures [5]. Twinning is an additional mode of deformation that helps satisfy the Taylor criterion [35, 36]. However, twinning is a polar mechanism that can only accommodate limited amount of strain. In addition, the twinned volume undergoes sudden reorientation and this may lead to strain localization, hence failure [37].

Research in the last two decades has been dedicated to alleviating the negative effects of anisotropy. An important aspect of this is uncovering the complex deformation mechanisms [31, 4, 5, 6, 7, 8, 9]. In addition, two major approaches have been followed which aim at suppressing or reducing the anisotropy *via* structural manipulations. The first consists of alloying so as to narrow down the wide gap between CRSS values, for example through the type, shape and habit planes of precipitates. For instance, alloying by addition of RE and Y has been shown to generate weak tex-

tures, as opposed to conventionally processed Mg alloys [38, 39, 40, 30]. As a result, improvement in strength was achieved without compromising uniaxial ductility [41, 42, 43]. In addition, RE based alloys such as WE43 are plastically quasi-isotropic with no noteworthy tension-compression asymmetry. What is less emphasized in the literature, however, is that the removal of plastic flow anisotropy in RE alloys is not accompanied by an enhancement in ductility, which makes the connection between strong anisotropy and poor ductility questionable. In fact, Kondori and Benzerga [44] have shown quite recently that the notch ductility of WE43 is much reduced compared with that of AZ31. It appears therefore that mere texture weakening may not be the engineering solution of choice to enhance the ductility of Mg alloys.

Another approach to mitigating plastic anisotropy has consisted of thermomechanical processes, such as severe plastic deformation. Thus, Mukai et al. [15] showed that equal-channel angular extrusion (ECAE) followed by annealing at 300°C improved the ductility of initially textured AZ31 alloy along the extrusion direction by more than twofold. They attributed the improvement in ductility to a presumably random texture, induced by the specifically chosen ECAE route ($4B_c$). Agnew et al. [16] repeated the same experiments and confirmed the ductility enhancement along the extrusion direction. However, these authors performed, in addition, uniaxial tests along various principal and off-axes directions. The data in [16] showed clear evidence of directionality in plastic flow, consistent with a distinct texture, albeit different from the starting rolling (basal) texture. The data in [16] also revealed that while the ductility was lower in one particular orientation, all other orientations were either comparable or better than the as-received alloy. Agnew et al. concluded that ECAE produces stronger texture than conventional processing methods. However, they did not provide a rationale for the increase in ductility observed in most directions when compared to as-rolled AZ31.

The above two findings, namely (i) the lack of success in improving room temperature ductility by suppressing texture; and (ii) the (unexplained) increase in ductility concurrent with strong anisotropy, indicate that anisotropy-ductility relationships are more complex than previously believed. The early findings in [15] and [16] showed promise but clearly have not been capitalized upon. The aim of this work is to develop a mechanistic framework within which possibly contradicting effects of plastic anisotropy on ductility can be rationalized, irrespective of the inherent directionality in properties. The basis of this rationale is as follows. Contingent upon the activation of ductile failure by void growth to coalescence [45, 46], a mean-field analysis based on homogenization theory suggests that certain forms of plastic anisotropy may hinder void growth under any triaxial stress state or loading orientation [17]. For relatively simple forms of anisotropy that ignore tension-compression asymmetry altogether, the resistance to void growth depends to first order upon a scalar invariant of the anisotropy tensor [17]. This scalar is here referred to as the Anisotropy Effect on Ductility (AED) index. The fundamental hypothesis of this work is that this AED index can be tuned through processing to enhance ductility at comparable strength levels.

To test the hypothesis, three materials with potentially different degrees of plastic anisotropy were used. The first is as-received hot-rolled AZ31B. The other two were processed using ECAE, a method of severe plastic deformation [47, 48] which has proven effective in altering textures in addition to the usual grain refinement [16, 49]. To isolate the effect of texture, all processed materials were heat treated to restore the hardening capacity and grow the grain size back to the regime of the as-rolled material. Plastic flow anisotropy is characterized in full 3D, both in compression and tension. The AED index was thus calculated for each material/texture. Next, the ductility of each material was characterized using (i) the same uniaxial tension

specimens aimed at characterizing the anisotropy; and (ii) round notched bars, as in [50]. The first set of data enables probing directionality of ductility for each material. In the second set, the notched specimens were tested along the extrusion direction only due to specimen dimensions and limited material. Finally, correlations between the various measures of fracture strain and the AED index were sought and rationalized on the basis of the micromechanistic model.

2.2 Theory

The hypothesis underlying this work is that the plastic anisotropy of Mg alloys can be modified to deliver materials with enhanced ductility at comparable strength. The basis for this is the theory of void growth in anisotropic materials, as articulated in [51, 17] and further developed in [52, 18]. Consider for simplicity a Hill-type material with no tension/compression asymmetry. The yield condition reads:

$$\sigma_{\text{eq}}^2 \equiv \frac{3}{2}\,\mathbf{s} : h : \mathbf{s} = \bar{\sigma}^2 \tag{1}$$

where σ_{eq} is the Hill equivalent stress, $\mathbf{s}$ is the stress deviator, h the fourth order anisotropy tensor, and $\bar{\sigma}$ the flow stress in an arbitrarily chosen reference direction. In axes pointing onto the principal directions of orthotropy, the above equation can be expanded into the following explicit form:

$$\sigma_{\text{eq}}^2 = \frac{3}{2}\left(h_1 s_{11}^2 + h_2 s_{22}^2 + h_3 s_{33}^2 + 2h_4 s_{23}^2 + 2h_5 s_{31}^2 + 2h_6 s_{12}^2\right) = \bar{\sigma}^2 \tag{2}$$

where the anisotropy coefficients h_i are related to those used by Hill [53]; see [17] and [54] for further details.

The micromechanics of void growth in anisotropic materials of the type (2) is

captured in the following equation [17, 46]:

$$\frac{\dot{f}}{\dot{\epsilon}_{\text{eq}} f} \approx \frac{3}{h} \sinh\left(\frac{3}{h} T\right) \tag{3}$$

where f is the void volume fraction, $\dot{\epsilon}_{\text{eq}}$ is the effective plastic strain rate, T is the stress triaxiality ratio, and h is a scalar invariant of tensor h used in (1). In terms of the h_i coefficients entering the yield condition (2), this scalar invariant is given by

$$h = 2\left[\frac{2}{5}\frac{h_1 + h_2 + h_3}{h_1 h_2 + h_2 h_3 + h_3 h_1} + \frac{1}{5}\left(\frac{1}{h_4} + \frac{1}{h_5} + \frac{1}{h_6}\right)\right]^{\frac{1}{2}} \tag{4}$$

Equation (3) shows that the rate of growth of porosity, $\dot{f}$, in a plastically deforming material is dependent on the 'degree of anisotropy' of the material, as lumped in the h factor. This factor is a potent one since it appears inside the exponential term. Thus, small changes in h could lead to large variations in void growth rate. Examination of equation (4) reveals that $h = 2$ for an isotropic von Mises material (since all h_i's are then equal to 1). According to this theory, values of h greater than 2 would decrease the porosity rate, on average, while values less than 2 would lead to an increase in porosity rate. This would hold for any triaxiality T and most, if not all loading directions. Hence, the h factor may be used as an index for the anisotropy effect on ductility. In what follows, we shall refer to it as the AED index.

In practice the h_i coefficients are determined either based on yield stresses or anisotropy strain ratios. The two methods deliver the same set of values insofar as Schmid's law holds. For example, Benzerga [54] developed the equations relating the h_i coefficients to the strain ratios. These relations are recalled in Appendix A. The dual relations in terms of yield stresses may be found, for example, in [55].

A quadratic yield criterion such as (2) has obvious limitations when it comes to

modeling the anisotropy in Mg alloys. It is assumed therefore that the AED index (or h factor) is robust enough to apply to more complex materials. Note that in some Mg alloys, the tension–compression asymmetry gradually decreases upon straining, although it is large initially. It is emphasized that the objective here is to estimate the AED index on the basis of the Hill anisotropy coefficients that provide the closest fit to experimental data, not advocate using a quadratic yield criterion to model the plasticity of Mg. Better constitutive models are now available, e.g., see [56, 57] and references therein. However, for such constitutive models the relationships between model parameters and anisotropy strain ratios are not readily available in closed form.

2.3 Experimental Procedure

2.3.1 Materials

The as-received material is commercial alloy AZ31B (H24 temper) with nominal composition (3.33 Al, 0.88 Zn, 0.21 Mn, balance Mg, all in %wt) in the form of hot rolled 1"-thick plate. The microstructure and two pole figures are shown in figure 2.

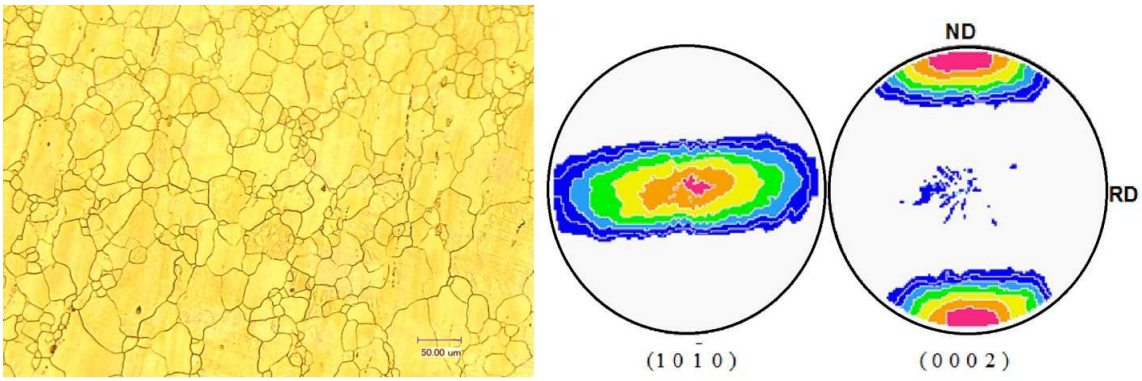

Figure 2: As-rolled microstructure and texture of a hot rolled AZ31B plate.

The material has an average grain size of 20-25μm and a distinct basal texture. The principal directions of the plate are referred to as R, T, N for rolling, transverse and normal directions, respectively (figure 3a).

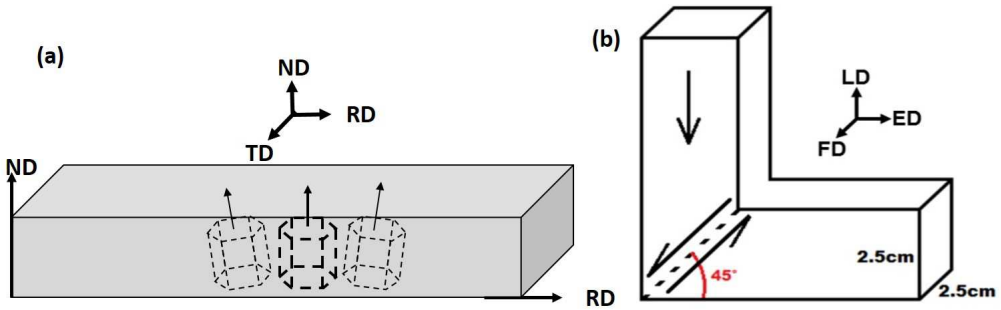

Figure 3: Schematic showing the die geometry used for performing severe plastic deformation using ECAE and the direction convention used for the directions on the billet after processing.

In order to produce materials having the same chemical composition and average grain size, severe plastic deformation was used by means of equal-channel angular extrusion (ECAE). Two 25mm×25mm×150mm billets were cut from the plate and passed through a 90° ECAE die with sharp corners (figure 3b). A backpressure of 20 MPa and an extrusion rate of 4.57mm/min at 200°C were the parameters used to process the material without surface cracks. Two routes were used with multiple (four) passes to obtain different textures. In route A, the billet orientation is not changed between two successive passes, while for route C the billet is rotated by 180° about the extrusion axis after each pass are referred to as 4A and 4C. For the ECAE processed materials, the principal directions are denoted E, F, L for the extrusion, flow and longitudinal directions, respectively (figure 3b).

The material obtained after ECAE is a material that has been hardened by

heavy shear strains causing grain size reduction. In order to compare the processed materials with the as-received one, the processed billets were heat treated for 24 hours at 350°C so as to grow the grain size back to its value in the as-received plate. With this procedure, the grain size is nominally controlled and the only independent variable is the texture, hence the degree of plastic anisotropy. A line intercept method was used to determine the average grain size. X-ray diffraction (XRD) was used at time intervals of 0, 2, 10 and 24 hours to verify that the processing induced texture of each route was not altered during annealing. This was accomplished by using small coupons of 4A and 4C material taken from the billet's mid-section in a Bruker-AXS D8 X-ray diffractometer with Cu Kα radiation using a 5° grid size and an 85° sample tilt.

2.3.2 Microstructure Characterization

Optical microscopy was used to characterize the initial and processed microstructures. Metallographic sections from different planes were prepared by cutting samples using a diamond saw, ground with SiC paper and fine polished using 1μm diamond solution and 0.3μm colloidal silica suspensions. Water was used during grinding only. In particular, the solutions used for fine polishing were alchohol based; this includes the diamond solution and the lubricant. Ethanol was used for rinsing and sometimes acetone as ultrasonic cleanser. For etching, acetic picral solution (4.2 g picric acid, 10 ml acetic acid, 70 ml ethanol and 10 ml water) was used for time periods up to 5s. The materials that were processed without annealing had a quicker response to the etching process due to the higher stored energy from processing.

2.3.3 Mechanical Tests

2.3.3.1 Uniaxial Tests

In each billet, round compression and flat tension specimens were cut out along the three principal directions E, F and L in addition to three off-axes directions, at 45° from a principal direction in a principal plane. Each off-axis direction is referred to using the two letters defining the principal plane. For example, EF is the direction at 45° from E in the E–F plane. Cylindrical specimens are generally preferred in characterizing anisotropy [50]. However, due to limited availability of material, flat specimens had to be used in tension. Two specimens were used per test condition. The geometry of the specimens used is shown in figure 4a & (b) for compression and tension, respectively. Since ECAE leads to undeformed ends in the billets, these ends were truncated and all specimens were carved out of regions of (nominally) uniform deformation.

All tests were performed at room temperature on a MTS servo-hydraulic frame at a nominal strain rate of 5×10^{-4} s^{-1}. The axial strain was measured in tension using a MTS axial extensometer. For compression a nickel based lubricant was used to prevent early barreling. All compression pins failed in shear and broke in two pieces. Fracture strain ϵ_f is defined as the sum of the lateral strains in the two principal directions at load drop as seen in equation 5.

$$\epsilon_f{}^L = \ln\left(\frac{\Phi_{\mathrm{E}}}{\Phi_0}\right) + \ln\left(\frac{\Phi_{\mathrm{F}}}{\Phi_0}\right) \tag{5}$$

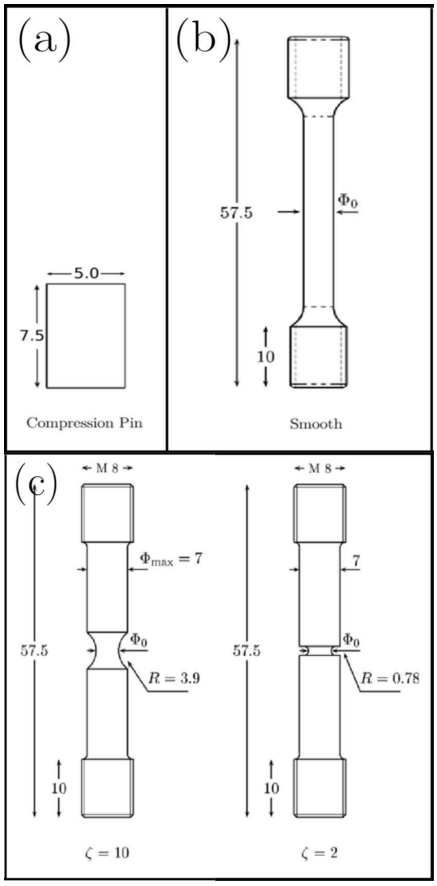

Figure 4: Geometry of samples used for mechanical property and for fracture characterization. From left to right, the samples used are cylindrical compression pins for compression tests, axis-symmetric smooth bar for obtaining tensile properties and axis-symmetric notched bars of RN10 and RN2 geometries for fracture under triaxial stress state.

2.3.3.2 Measurement of Anisotropy Ratios

Given a loading orientation, say L, and a loading mode (tension or compression) define the true axial and transverse strains as follows:

$$\varepsilon_{\mathrm{L}} = \ln\left(\frac{H}{H_0}\right); \quad \varepsilon_{\mathrm{X}} = \ln\left(\frac{\Phi_{\mathrm{X}}}{\Phi_0}\right) \tag{6}$$

where H and H_0 denote current and initial gage heights, respectively, X refers to a transverse direction (either E or F when loading along L), and Φ_{X} and Φ_0 are the current and initial diameters, respectively. In pin compression, initially circular cross-sections become oval so that Φ_{X} refers specifically to the "oval's diameter" along X. In flat tensile specimens, Φ_{X} refers to either the width or thickness of the current cross-section.

With that as basis, the anisotropy strain ratio for loading along L is then defined as

$$R^{\mathrm{L}} = \frac{\varepsilon_{\mathrm{E}}}{\varepsilon_{\mathrm{F}}} \tag{7}$$

The other two strain ratios, R^{E} and R^{F}, are defined following a cyclic permutation (L,E,F) [54, 55]. For off-axis loading, say along the EF direction, the anisotropy strain ratio is conveniently defined as:

$$R^{\mathrm{EF}} = \frac{\varepsilon_{\mathrm{FE}}}{\varepsilon_{\mathrm{L}}} \tag{8}$$

where the FE direction stands for the dual direction perpendicular to EF in the E-F plane. The other two off-axis strain ratios, R^{FL} and R^{LE}, are defined in a similar way. These strain ratios are akin the so-called Lankford coefficients, albeit the definitions differ. They also generalize the notion of r-value used in sheet metal forming.

To enable the measurement of diameters Φ_X entering the definition of transverse (or lateral) strains in equation (6) all compression tests were interrupted multiple times. Fewer interruptions were made in tension, typically two or less, including just before the macroscopic load drop. All dimensions were measured using a high-precision micrometer so that strains were measured with an accuracy of 0.1%. Once the strain ratios are determined, the anisotropy coefficients h_i are obtained using the equation 9, then used to determine the AED index in equation (4) rewritten in the billet axes as:

$$h = 2\left[\frac{2}{5}\frac{h_E + h_F + h_L}{h_E h_F + h_F h_L + h_L h_E} + \frac{1}{5}\left(\frac{1}{h_{FL}} + \frac{1}{h_{LE}} + \frac{1}{h_{EF}}\right)\right]^{\frac{1}{2}} \tag{9}$$

2.3.3.3 Round Notched Bar Test

Round cylinders were also cut using wire electro-discharge machining (EDM) along the extrusion direction. From these cylinders, axis-symmetric notched bars were machined. These notched bars are usually employed in fracture studies [58, 59]. In strongly anisotropic materials such as Mg, introduction of a notch plays a dual role since it also allows to investigate the effect of triaxial loading on the mechanical anisotropy. Since the stress state is triaxial inside the notch, there are two equal minor principal stresses σ in addition to the major axial stess Σ such that $\sigma < \Sigma$. Stress triaxiality, T, is defined as the ratio of hydrostatic stress to the von mises stress. A geometrically based notch severity parameter, ζ defines the severity of the notch where:

$$\zeta = 10 * \frac{R}{\Phi} \tag{10}$$

Taking the notch height as a gauge length, a nominal strain rate of $3 \times 10^{-4} s^{-1}$ was imposed in all cases. In the notched bars, the use of an axial extensometer would

be pointless unless the gauge is restricted to the height of the notch, which is difficult given the size of our specimens. Continuous measurement of diameter reduction was done using a custom made knives mounted on a MTS clip-on gage, which together makes the setup of the radial extensometer[60]. The strain is measured along one of the principal directions at the minimum cross-section. Due to anisotropy, the test was interrupted multiple times and the measurements along the other principal direction was recorded. Definition of strain remains the same as in the case of compression samples. Crack initiation is detected by an abrupt change in the macroscopic slope in the load vs diameter reduction curve and is defined as strain to failure.

2.3.4 Fractography

All surfaces of fractured notched specimens were observed in FEI Quanta 600 SEM. Since Mg is notorious for quickly oxidizing in air the surfaces were observed shortly after each experiment. The surfaces were sprayed with silicone immediately after fracture and placed in desiccators under vacuum prior to observations. Yet, each sample could be observed only once even with care taken to prevent oxidation.

After the fracture surfaces were observed in SEM, one half of the specimen was sectioned longitudinally using EDM and metallographically prepared and observed under both OM and SEM in the E-F and the E-L planes. The aim was to observe the extent of damage beneath fracture surfaces. Fine polishing was done as described above with particular care given so as not smear out voids smaller than a few microns in size. When voids were found to initiate at second-phase particles, dispersion spectroscopy was used to characterize their composition. Similar techniques were used in [50, 61].

2.4 Results

2.4.1 Processed Textures and Microstructures

The textures obtained by ECAE processing are shown in Figure 5 and compared with the as-rolled texture.

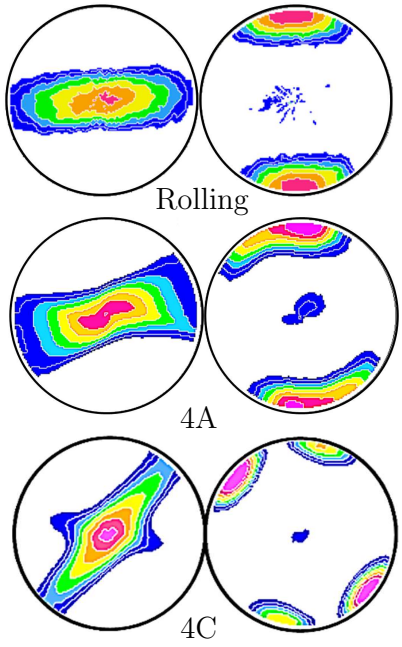

Figure 5: Figure showing the alteration of texture by the process of ECAE by following different process routes and obtaining 2 different processing routes 4A and 4C at 200C which is used as the material for this study.

The texture of material 4A has rotational symmetry about the flow plane normal. A single pass through route A leads to a rolling-like texture. Subsequent route-A passes strengthen this texture by reorientation to a very similar texture after each pass. On the other hand, route C is a redundant strain path whereby the direction of simple shear is reversed after each pass. However, the second pass does not erase

the texture developed in the first, demonstrating path dependence in deformation induced textures.

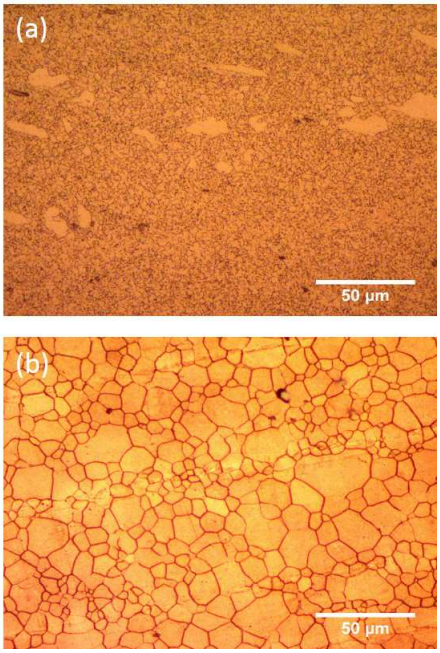

Figure 6: Figure showing evolution of the grain size due to the annealing heat treatment. The initial microstructure is shown for (a) 4A , (b) 4A after annealing for 24 hours at 350°C

The outcome of the post-processing heat treatment is shown in Figure 6 for material 4A. The as-processed material exhibits a fine grain microstructure (Fig. 6a) with few large grains elongated along the extrusion direction, as often reported for this particular route [9]. Fig. 6b shows the microstructure after annealing at 350°C for 24 hours. Similar dual grain size distribution was observed in the annealed microstructure. The average grain size was $\bar{d} \sim 3\mu$m and $\bar{d} \sim 15\mu$m before and after annealing, respectively. For reference, the as-received AZ31 material had $\bar{d} \sim 20\mu$m and the annealing was done to recover the microstructure and grow the grains back

to the regime of the as-received material so as to focus on texture effects only.

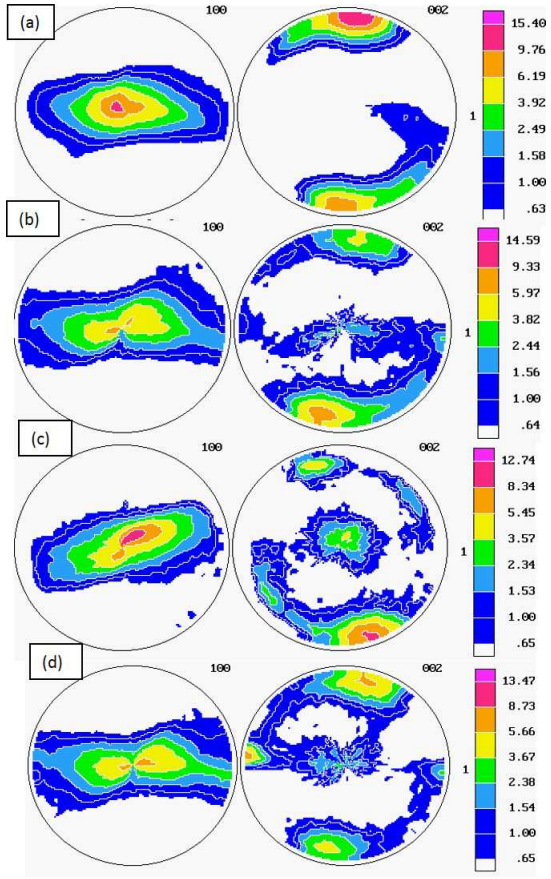

Figure 7: Figure showing the texture evolution during the process of annealing for material 4A at different time steps (a) initial (b) 2 hours (c) 10 hours (d) 24 hours.

Figure 7 shows the evolution of texture during annealing. The texture was not significantly altered during the process of annealing.

The result of annealing on the microstructure of material 4C is shown in Fig. 8. It is known that the microstructure of the as-processed material is more uniform in this route. This is indeed confirmed by Fig. 8a. The same applies to the annealed microstructure shown in Fig. 8b. For this material, the average grain sizes were

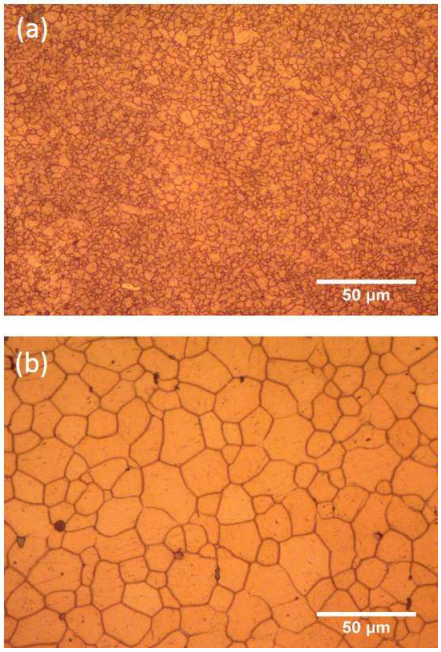

Figure 8: Figure showing evolution of the grain size due to the annealing heat treatment. The initial microstructure is shown for (a) 4C , (b) 4C after annealing for 24 hours at 350°C

$\bar{d} \sim 3\mu$m and $\bar{d} \sim 18\mu$m before and after annealing, respectively; compare with $\bar{d} \sim 20\mu$m for the as-received material.

Figure 9 shows the evolution of texture during the process of annealing for the material processed through route 4C. Here too minimal change in texture occurs subsequent to annealing.

2.4.2 Stress-strain Behavior

As mentioned in Section 2.3.3.1 each ECAE processed material was tested along six orientations, both in tension and compression. In addition, results for the as-received material tested along three principal directions were taken from [62]. Details about the tensile stress–strain curves for all orientations will be shown later in the context of discussing the directionality of ductility. Here, it suffices to recall that

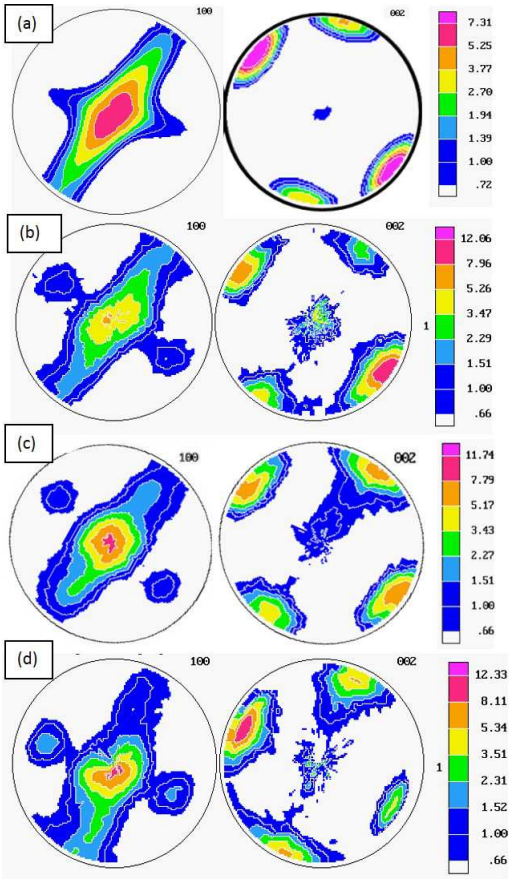

Figure 9: Figure showing the texture evolution during the process of annealing for material 4C at different time steps (a) initial (b) 2 hours (c) 10 hours (d) 24 hours.

material 4A exhibits the usual tension compression asymmetry in all orientations whereas material 4C exhibits asymmetry when tested along the flow direction F; The other two principal directions (E and L) had negligible tension-compression asymmetry in yield but some in subsequent flow, in keeping with previously published results [21]. Typical nominal stress versus logarithmic strain responses in tension along the extrusion direction are shown in Fig. 10 for both 4A and 4C materials and compared with the response of the as-received material loaded along the processing (rolling) direction.

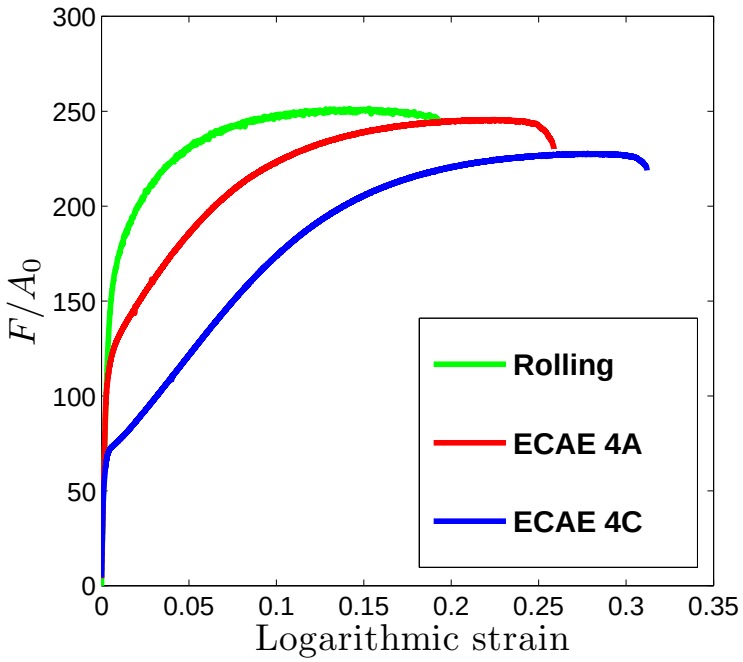

Figure 10: Force vs displacement response for smooth bars along extrusion direction processed by 4A and 4C routes compared with the as-received AZ31.

2.4.3 Anisotropy Ratios

To estimate the AED index of each material using (9) and the equations (see Appendix B) the anisotropy strain ratios must be reported. As described in Section 2.3.3.2 the evolution of the strain ratios was followed in compression through frequent test interruptions whereas up to two measurements were made in tension. Fig. 11 shows the evolution of the strain ratios with plastic strain for material 4A in compression.

The five ratios reported in the figure (R^{E} and R^{F} for principal directions, R^{EF}, R^{FL} and R^{LE} for off-axes directions) are those that appear in the equations (see Appendix B). Furthermore, to avoid data clutter the results are grouped in two sets. In the first, Fig. 11a, the strain ratio keeps evolving with plastic strain with no indication of a steady-state behavior. In the second set, Fig. 11b, the two ratios R^{LE} and R^{E} exhibit a steady state behavior after a transient, as discussed in [50] for as-received AZ31. These trends underscore the complex evolving plastic anisotropy in the material and will be further discussed in Section 2.5. In tension, the existence of a steady state could not be ascertained because of a restricted set of measurements. In all six loading orientations, the strain ratios were determined at sufficiently large strains prior to fracture.

The evolution of the anisotropy strain ratios with plastic strain is shown for material 4C in Fig. 12 using the same principle for grouping the data sets as in Fig. 11. Interestingly, here the two ratios that exhibit clear steady state are R^{E} and R^{FL}. The R^{X} values are generally greater for material 4C than for material 4A despite the more "distributed" character of the texture in 4C (see Fig. 5.)

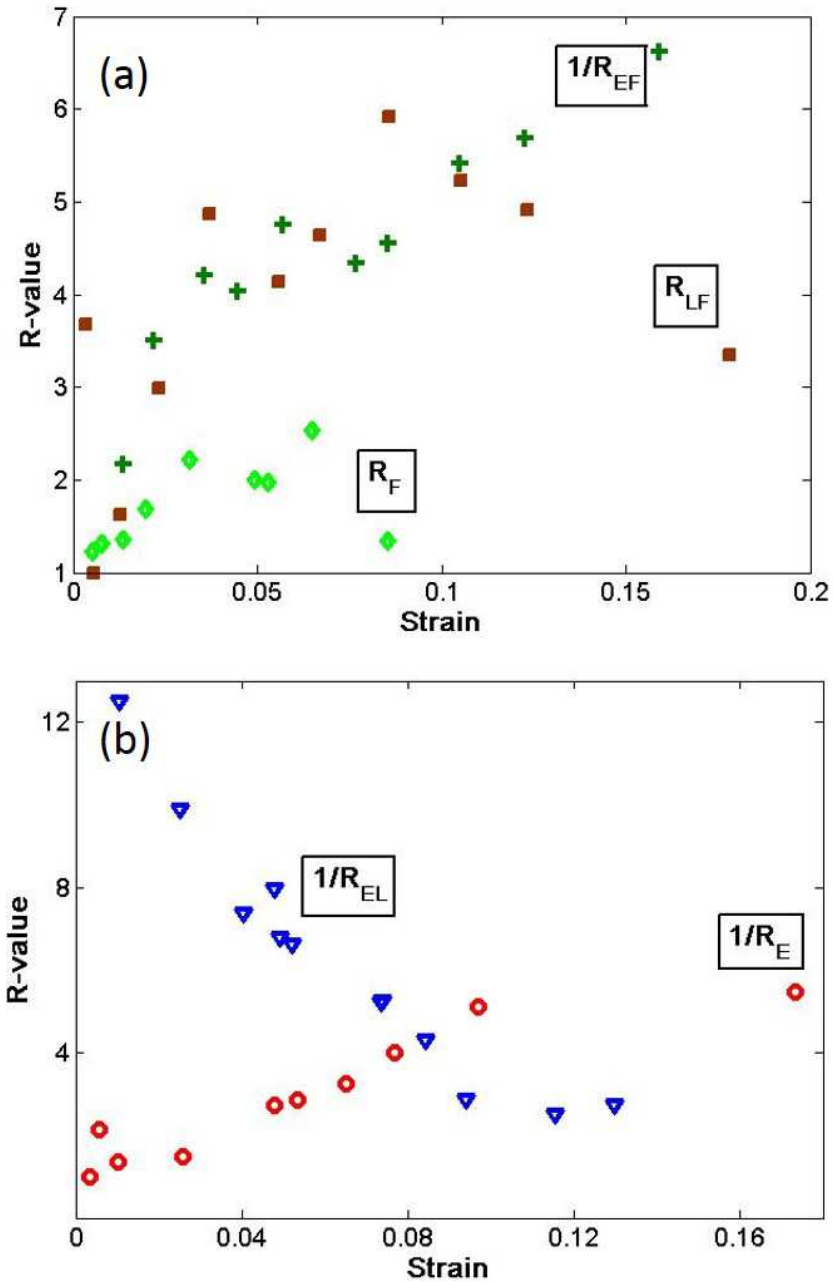

Figure 11: R-values plotted along with evolution of strain in compression along 3 off-axis and 2 principal directions for material processed through route 4A split according to (a) directions that did not reached a stable state called transient stage (b)directions where ratios reached a stable regime

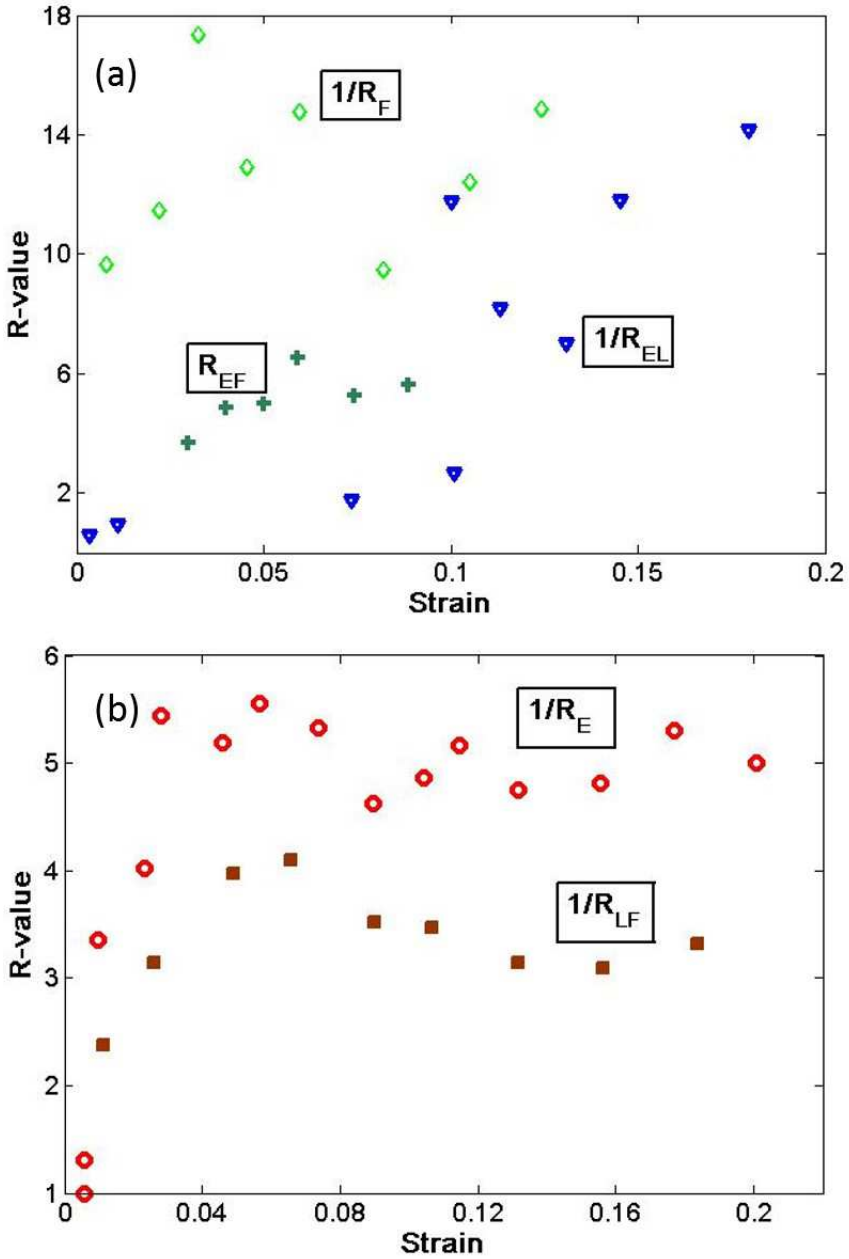

Figure 12: R-values plotted along with evolution of strain in compression along 3 off-axis and 2 principal directions for material processed through route 4C split according to (a) directions that did not reached a stable state called transient stage (b)directions where ratios reached a stable regime.

2.4.4 AED Index

Next, the AED index, or h factor in equation (9), may be calculated at any stage. Here, near terminal values of the strain ratios were used consistently, since these were always available in tension. The results are reported in Fig. 13 for all three materials in both tension and compression. For the as-received material the data is taken from [50, 55].

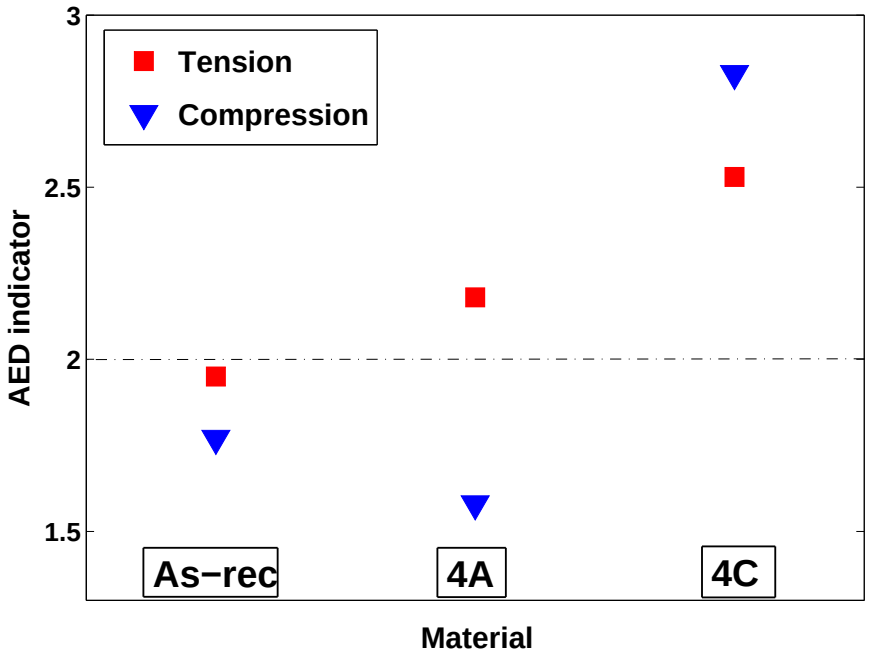

Figure 13: Anisotropy indicating factor (AED) under compression and tension for as-rolled sheet, 4A and 4C

A few remarks are in order based on the theory of Section 2.2. In the as-received material, the AED index takes values smaller than 2 either in tension or compression. This suggests that its anisotropy is of the bad kind. By way of contrast, material

4C exhibits AED values larger than 2 whereas material 4A has the AED > 2 in tension but < 2 in compression. Thus, when voids are present, it is expected that the rank ordering of tensile ductility be: as-received, 4A then 4C in increasing order. The values in compression are provided for completeness. It is not clear whether the theory can be invoked to make projections for ductility under compressive loading.

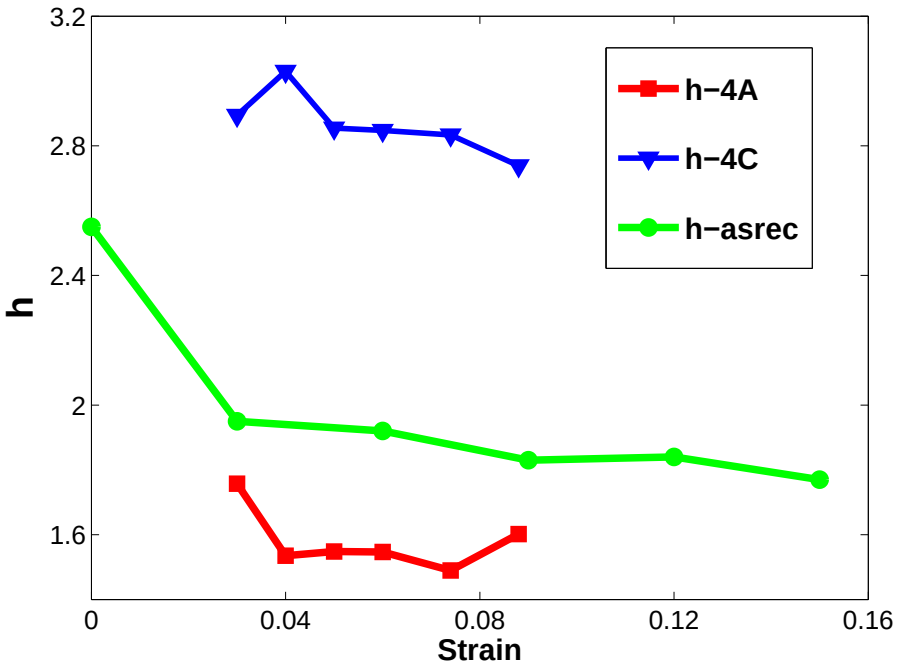

Figure 14: Evolution of AED factor with strain for as-received, 4A and 4C material

To examine the robustness of this order of the AED index, Fig. 14 shows its evolution with plastic strain based on the systematic investigation of the compression case. Remarkably, the AED values obey the same rank ordering as for terminal values at all stages. Presumably, the same holds for tension. Also, the variations with plastic strain of the AED values (Fig. 14) are not as erratic as some strain-ratio

values (Figs. 11 and 12).

2.4.5 Notch Ductility

In characterizing resistance to ductile fracture, any measure of uniaxial ductility (elongation to fracture, area reduction or the logarithmic measure adopted here) should be supplemented with at least a measure of notch ductility [46]. This is because of the widely documented stress-state dependence of ductility, as partly embodied in the fundamental equation (3) via the triaxiality term. In the case of Mg alloys, this is further required due to recent findings by Kondori and Benzerga that (i) the notch ductility of Mg alloy AZ31 is greater than its uniaxial ductility (adopting comparable measures) [50]; and (ii) the notch ductility of WE43 alloy, on the other hand, deteriorates quite drastically with notch severity [44]. Therefore, even when uniaxial ductility is enhanced, further checks are needed for the notch ductility.

Fig. 15 compares the responses of the notched bars loaded along E (or R for the as-received material. Clearly, the fracture strains follow the rank order suggested by the AED index, i.e., material 4C is more ductile than 4A, which is more ductile than the as-received alloy. The peculiar shape of the load-deflection responses is because a load cell of large capacity was used on relatively small specimens. This, however, does not alter the order of fracture strains, for example as estimated based on area reduction. While it may be argued that material 4C exhibits a softer response, the limit loads in the 4A and as-received specimens are comparable. Finally, it is worth noting that for each material the fracture strain is greater in the notched bar than it is in the smooth bar. This confirms and generalizes the trend first revealed in [50] for as-received AZ31.

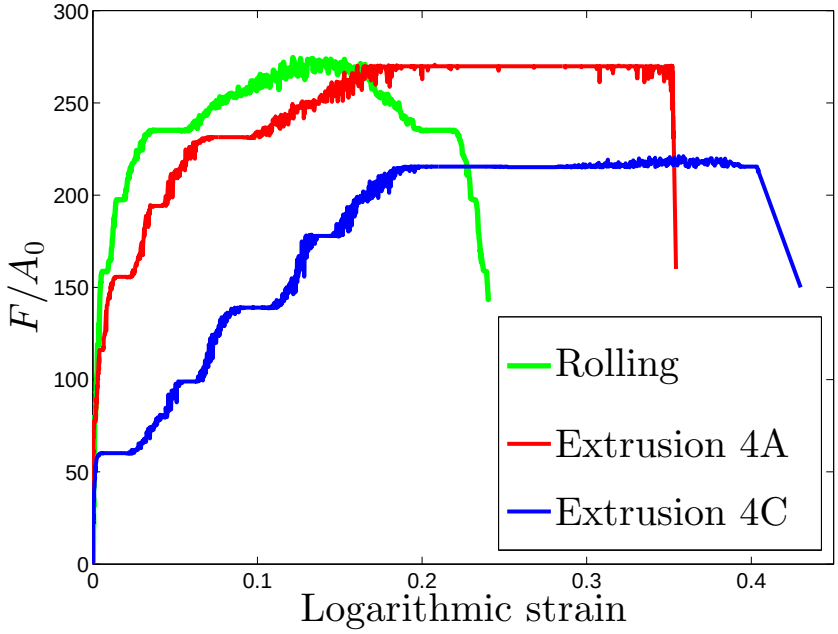

Figure 15: Force vs displacement response for shallow notched bars(RN10) processed by 4A and 4C routes compared with the as-received AZ31. These samples were used to characterize fracture under triaxial loading conditions.

2.4.6 Directionality in Ductility

While both the uniaxial and notch ductilities seem to follow the AED-based projections, it is expected that the ductility depends on loading orientation. To quantify this, Fig. 16 reports the fracture strains measured for uniaxial tension along all six orientations.

To facilitate comparison, the fracture strain for a given orientation is normalized by its value for the as-received material. With this definition, values above unity indicate an increase in ductility with respect to the as-received alloy for a given loading direction. For the three off-axis orientations, the fracture strain was normalized by that of the 4A material because the data was not available for as-received material. What is plotted in Fig. 16a is the strain to failure initiation, that is at the load drop in the global response. The latter is shown for all loading orientations in Fig. 17.

By way of variation, Fig. 16b reports the strain to complete rupture, as inferred from area reduction measurements post-mortem. The trends are insensitive to the measure used. It is clear that ductility is found to be enhanced in all directions, even if the increase is modest in some orientations. Not only this figure establishes a correlation between the AED index and ductility, irrespective of orientation, it also shows a 70% increase in ductility in certain orientations.

A good way of representing the fracture under varied stress state is by presenting a failure locus. It is a plot relating the strain-to-failure with the stress triaxiality. The locus is unique under proportional loading conditions. For non-proportional loadings the strain-to-failure is plotted against some strain-weighted average of the stress triaxiality ratio the fracture locus not only is non-monotonous, it is not one-to-one [63]. Even in lab samples it is impossible to have a situation of proportional loading. However, the samples tested here were close to proportionality. To obtain

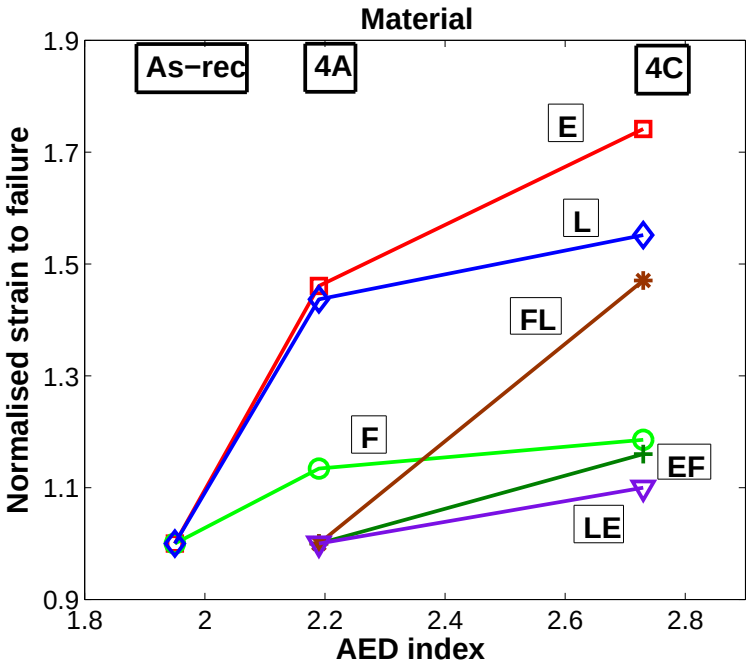

(a)

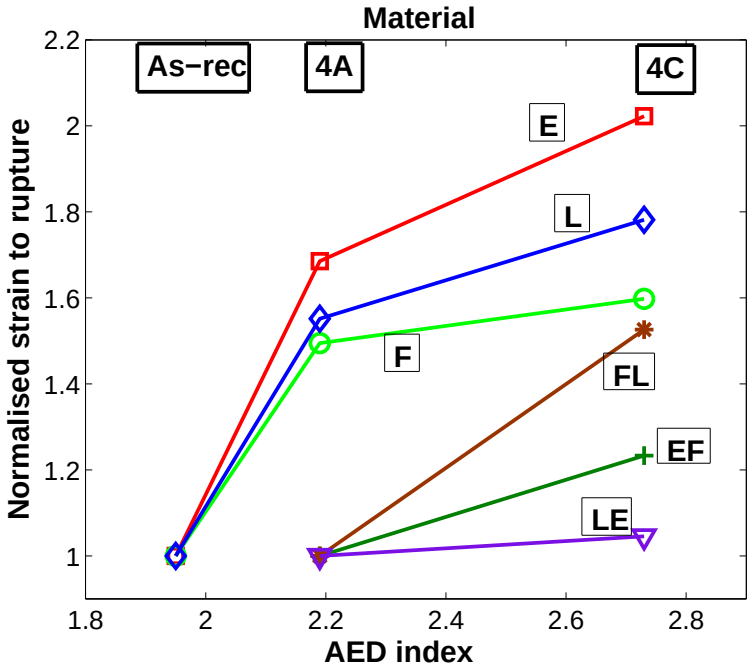

(b)

Figure 16: Correlation between the improvement in ductility with the evolution of the AED index along the 3 principal and 3 off-axis directions for the 3 materials (a) strain at failure initiation (b) strain at rupture. The plots have been normalized by the smallest value of ductility along a particular direction which is the value for the as-received material. Since the values were not available for the as-received material in the off-axis directions, the values of 4A material was used instead.

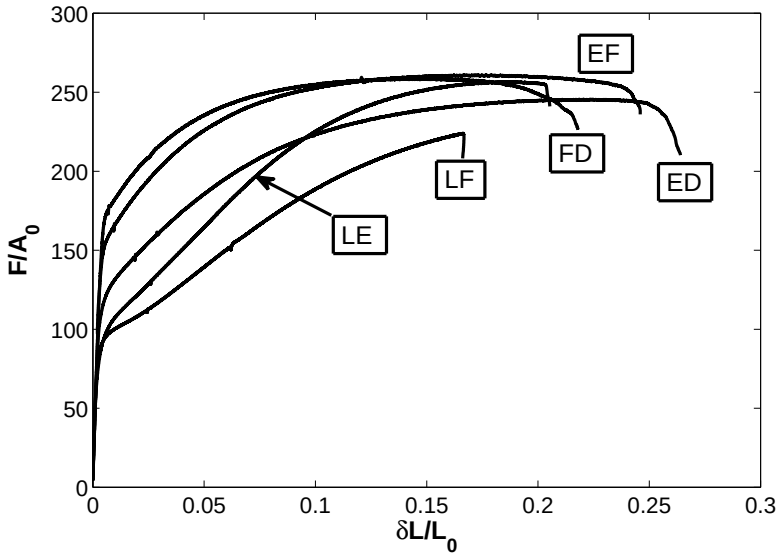

(a)

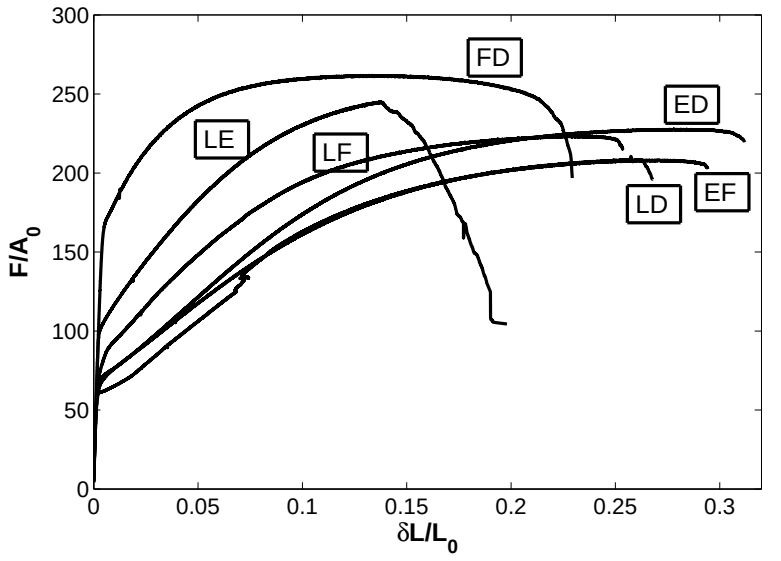

(b)

Figure 17: Stress strain curves under uniaxial loading in tension along the three principal and 3 off-axis directions for (a) 4A and (b) 4C materials

the evolution of stress triaxiality FEM calculations need to be performed as the stress-state cannot be obtained from experiments. This part is not discussed here and hence as the history of the triaxiality is unknown for the samples, the strain-to-failure is plotted with the sample type. As we move along the axis the stress triaxiality increases. Under uniaxial loading condition in compression and tension the value of stress triaxiality is -1/3 and 1/3 respectively before barelling or necking occurs.

2.4.7 Fracture Mechanisms

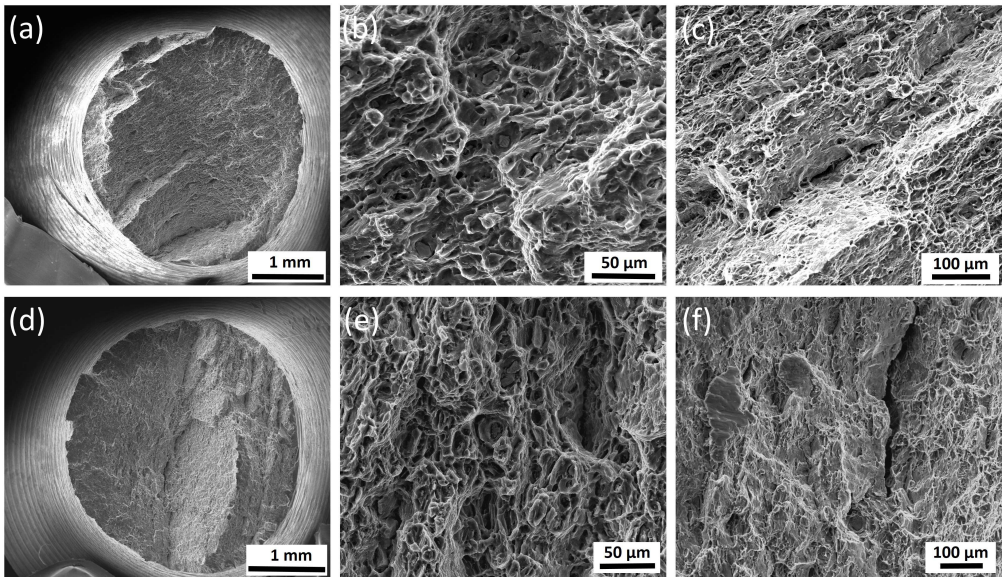

Figure 18: Fracture surface of RN10 specimen (a)-(c) 4A and (d)-(f) 4C samples showing dimpled fracture surface with particles in the dimples showing ductile fracture mechanisms are active.

The fracture surfaces of notched specimens of 4A and 4C materials both exhibit a dimpled character, Fig. 18. Initially smooth flat tensile specimens also exhibited some isolated regions with dimples for some loading orientations. However, longitudinal

cuts (not shown) invariably show shear rupture, if only partial. This is consistent with the findings in [50] for as-received AZ31. The dimpled character of fracture surfaces in notched specimens is clear indication that the well established cavitation processes are active in both materials. Zooming into the fractographs, second-phase particles may be observed in many dimples (see Fig. 18b and e) suggesting that damage occurred due to void nucleation at these particles and subsequent growth to coalescence.

In order to gain further insight into the damage mechanisms, longitudinal sections of broken bars were prepared (see Section 2.3.4). They are shown in Fig. 20. Interestingly, sections in E–L planes (Fig. 20a and b) show slightly slant fracture surfaces. Higher resolution observations (not shown) do not show extensive damage sites in such sections. On the other hand, longitudinal sections in E–F planes where the crack path is macroscopically flat (as opposed to slant) reveal extensive damage beneath the surface. An example is shown in Fig. 20c in the case of 4C material. Fig. 19 illustrates some close-ups of individual damage sites in Fig. 20c.

The various stages of void formation at second-phase particles, void enlargement and coalescence can be observed.

It appears therefore that damage develops in some rather anisotropic fashion. Although not fully investigated here, this sequence of events was studied in some detail by Kondori [55] in as-received AZ31. He showed that the above evidenced processes of cavitation lead to formation of larger blunted cracks which run parallel to one principal direction (here the flow direction F). As there are multiple such macrocracks in the specimen they link up by shear localization and shear rupture. This may explain the slanting observed in E–L sections or the macro-splits observed directly onto fracture surfaces of Fig. 18a and d.

Fig. 21 shows some high-resolution SEM images of damage nucleation sites, here

mainly second-phase particles. Analysis by EDS reveals that the particles are Al–Mn rich. The dominant nucleation mechanism is by particle cracking, although lower-resolution images may suggest decohesion at the poles.

To sum up, the fractography analyses reveal that cavitation processes are active in both processed materials. Cavitation occurs at Al–Mn second-phase particles, mostly by cracking. Also, this cavitation extends far beyond the fracture surface and may not be evident in all planes of view.

2.5 Discussion

In the Mg literature, the phrase "texture engineering" is invoked to mean, nearly systematically, reducing, weakening or randomizing the texture altogether [30]. Such engineering is predicated on the premise that the strong texture of wrought Mg alloys is deleterious to fracture resistance. The work initiated here aims at shifting the design paradigm toward engineering, not suppressing, the anisotropy of wrought metallic materials, in particular Mg alloys, for example via their texture. The rationale for this is two-fold: the lack of success in demonstrating that the more isotropic Mg alloys are considerably more ductile at ambient temperature; and a hypothesis based on mechanistic understanding of ductile damage.

Over the past decade, significant efforts have been devoted to texture weakening in Mg alloys, notably by addition of RE elements; for a review see [30]. In the most successful realizations of this concept, the following attributes have clearly been demonstrated:

1. up-to-random levels of texture with recrystallization playing a key role;

2. no tension–compression asymmetry (on strength);

3. finer grains, hence higher strength; and

4. solute segregation to grain boundaries as a key solute-related mechanism that retards recrystallization.

Many studies also claim that the ductility is improved in RE alloys. Fair examination of the results, including for WE43 alloy [44], shows however that the ductility is at best the same as in commercially available alloys such as AZ31. The mere fact that ductility levels of AZ31 have barely been retained indicates that anisotropy–ductility correlations are more complex than widely reported. The situation is in fact worse. In a recent study, two of the authors have shown that the notch ductility of WE43 alloy, with RE elements, is poor in comparison with that of AZ31 [44].

The work undertaken here is hypothesis driven. The hypothesis, which emanates from the theory of void growth in anisotropic plasticity, may be restated as follows: plastic anisotropy affects ductility to first order and this effect may be captured by the AED index. If confirmed, the hypothesis will enable to make projections regarding ductility levels on the sole basis of plastic anisotropy measurements, and by way of consequence, establish a new design paradigm whereby material attributes responsible for the anisotropy, such as textures, may be reverse engineered to obtain desired values of AED indices. Evidently, such reverse engineering would require a suite of other experimental and modeling tools to be established.

In this paper, focus has been laid on testing the validity of the said hypothesis. In order to do so, several materials sharing the same chemical composition and average grain size, but possessing different levels of plastic anisotropy had to be prepared. In addition, cavitation had to be established as the main damage mechanism (otherwise, the correlation in Fig. 16 which is in keeping with the hypothesis, would be fortuitous). Then, establishing a correlation between plastic anisotropy and ductility required that measurements of both be carried out. Several ways and definitions

of each are possible. For plastic anisotropy, what is important is that the full 3D anisotropy had to be characterized. Indeed, the AED index involves contributions from all six anisotropy coefficients (the h_i) with the shear coefficients having more weight; see equation (4). For ductility, it was important to verify not only the directionality but also the stress state dependence, i.e. notch ductility in addition to uniaxial ductility (recall that the latter is comparable between AZ31 and WE43 alloys whereas the former is much better in AZ31 [44]). In the literarture, both plastic anisotropy and ductility of Mg alloys are poorly characterized. The anisotropy is often reported in terms of r-values for sheet metals, or in terms of loadings along principal directions, whereas the ductility is often reported for initially smooth bars.

2.6 Conclusions

ECAE induces texture in Mg alloys which leads to anisotropy in flow and fracture. Engineering this could lead to improvement in ductility. The AED factor was capable of capturing the trends observed in ductility. Definition of ductility must me probed over a variety of stress states. There is a need to investigate the competing effects of plastic anisotropy on enhancing ductility & causing shear failure. The success of the AED factor will help guide new processing routes to obtain textures aiding ductility. Through this anisotropy indication factor the microstructure and texture can be controlled and help improve the formability of these alloys which is the final motive of these kind of studies.

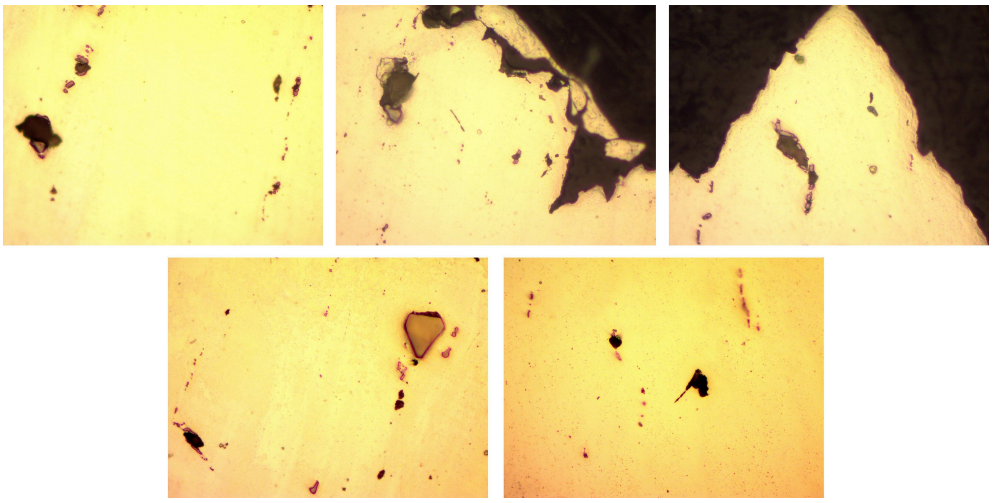

Figure 19: Magnified images capturing damage initiation sites under the fracture surface along ED-FD plane shown in 20

.

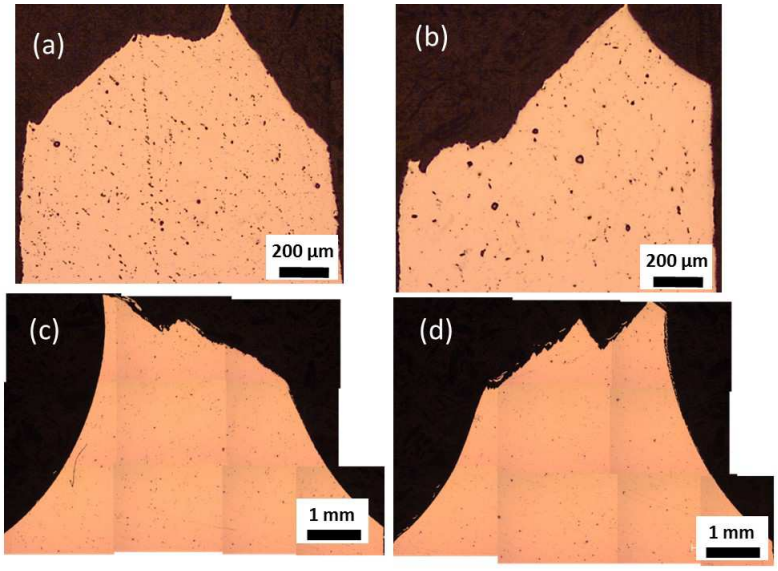

Figure 20: Profile of the fractures specimens showing macroscopic failure mode. The polished section under the fracture surface when viewed under optical microscope shows the failure profile for (a) 4A uniaxial (b) 4C uniaxial (c) 4A RN10 bar (d) 4C RN10 bar.

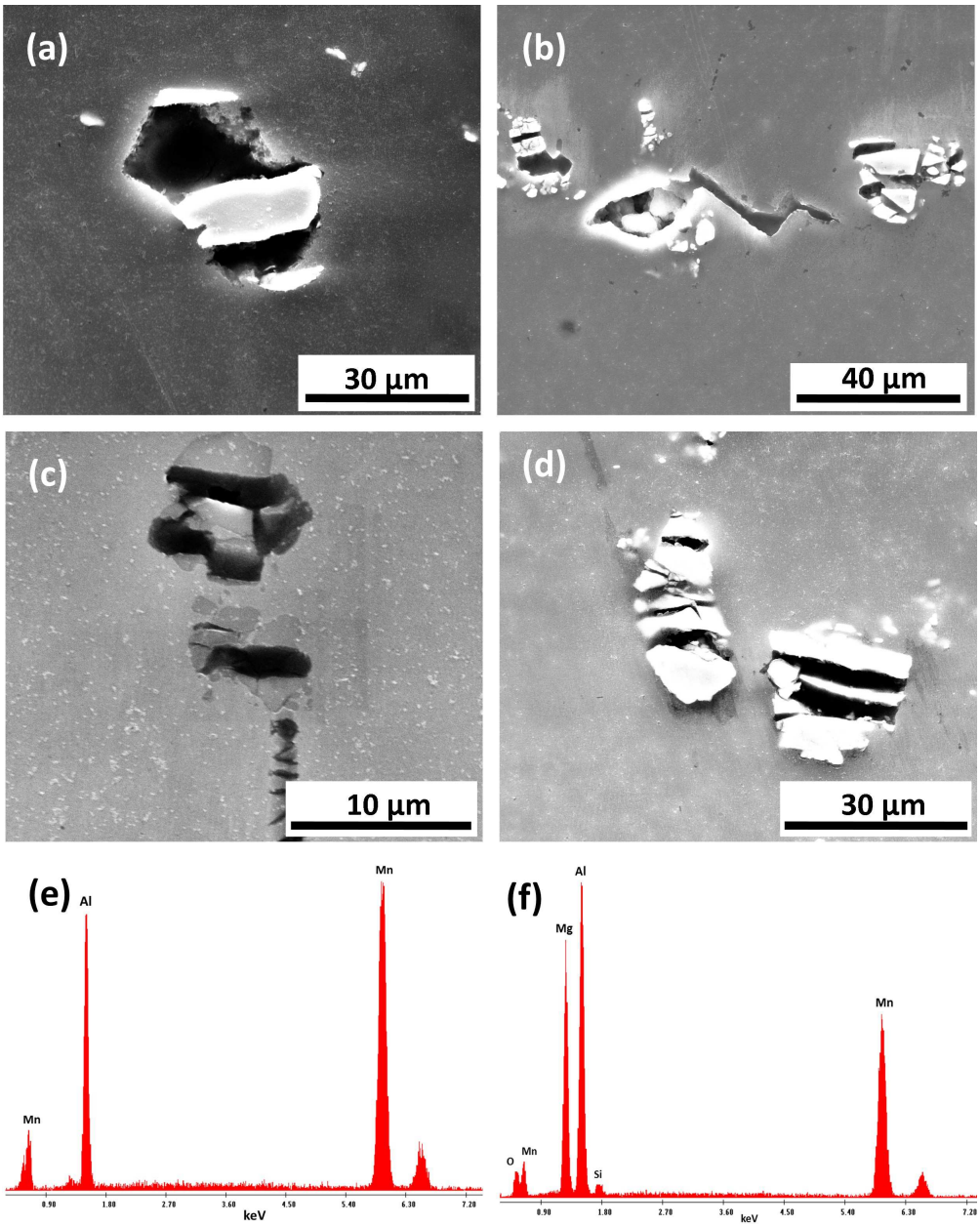

Figure 21: SEM images showing damage initialtion sites on ED-FD plane along with EDS plots of the particles participating in the damage process.

3. ANISOTROPY EFFECTS ON FORMABILITY

3.1 Introduction

Energy saving is a major concern especially in transportation industry for improved fuel economy and reduced emission levels [64, 65, 66, 67]. Light weight, high strength-to-weight ratio and their vast abundance in the earth makes magnesium alloys ideal candidates for lightweight structural applications where energy saving is a major concern [1, 68]. Most magnesium alloy components are manufactured for casting applications through processes like high-pressure die casting[69]. Wrought alloys in particular have been reported to have better mechanical properties than their casting counterparts [70]. Despite the huge advantages, the use of magnesium alloys in wrought form is rather limited compared to aluminium, steel and cast iron. Limited formability at room temperature along with catastrophic failure after limited necking are among the drawbacks that limit their application in industries with sheet metal forming applications [71].

The cold workability of wrought magnesium alloy products is limited, mainly due to the hexagonal close-packed crystal structure of magnesium and its limited number of independent slip systems [2, 72]. Due to this major limitation, a vast majority of Mg parts with small and thick geometries are fabricated by die casting processes [67, 73]. Warm forming processes at low strain rates can improve formability of Mg alloys by activation of additional slip systems [74, 75, 76, 77, 78, 79, 80, 81, 82, 83, 84]. However, at elevated temperatures ($> 300°C$) additional problems related to oxidation can complicate manufacturing [78, 79, 80, 81]. Therefore, to enable widespread use of wrought Mg, an important current objective is fabrication of Mg alloy sheets capable of being rapidly ($> 10^{-3}s^{-1}$) formed at low levels of elevated

temperatures ($< 200°C$). In general, formability not only depends on temperature and materials characteristics (chemistry, microstructure, anisotropy), but also on stress state and processing techniques, including such aspects as friction, tool geometry, shape of the deformation zone and prior deformation [85, 86]. Accordingly, warm forming by methods such as deep-drawing and isothermal superplastic blow forming processes has been extensively studied by researchers for production of Mg sheet metal components.

Several studies have focused on formability of Mg alloy sheets by deep drawing at different forming temperatures and strain rates [67, 73]. The tooling system for Mg alloys sheet forming is quite complex leading to an expensive product cost because of the elevated forming temperature between 250°C and 400°C. The deep forming of Mg sheets is a very adequate process that can be used for the manufacture of complex part geometries. It was highlighted by several studies [75, 87, 88, 89, 90] that heated tools are required for the manufacturing of component geometries from Mg sheet. Since Mg alloys are still not widely used as structural materials, formability data remain scarce. In this paper we try to probe that does engineering anisotropy (texture) guided by theory [17] lead to improved formability at low temperatures by performing biaxial stretch tests.

AZ31b has tensile elongation in the range of 20% comparable to Al alloys, yet very poor formability at room temperature. However, at temperatures higher than 175°C it shows better formability. In a recent study, Basu et al.[91], have experimentally shown that engineering the anisotropy and not suppressing it can lead to improvement in ductility. Anisotropy in this case is altered through texture modifications via Equi-Channel Angular Extrusion (ECAE) which is a method of severe plastic deformation (SPD). This method is effective in altering the texture by introducing large amounts of shear strain at the intersection of the entry and exit channel

of the die [47, 48, 21]. Two different textures produced through different processing routes via ECAE are compared to as-rolled texture. This could be rationalized based on a scalar invariant of the anisotropy matrix obtained through a homogenisation solution. The authors confirmed the predictions of the model [17] that values of this scalar invariant less than 2 are bad for ductility and values greater than 2 are good for ductility. The question arising is that, can this finding be extended to the improvement in stretch formability of these alloys.

Any progress in fundamental understanding of limiting factors affecting ductility of Mg alloys must translate into tangible metrics in Mg sheets, as the final product e.g. in the transportation industry. Hence we extend the processing used by Basu et al.[91] to sheet material and compare different textures produced by Equal Cannel Angular Plate Extrusion (ECAPE) to the rolled AZ31b to see the effect of texture engineering on formability. Hence, three starting textures (one as-received and two processed) were actually used in this part. The as-receivedeived material refers simply to EDM cutting of thin sheets out of the as-receivedeived plate. In order to keep the formability test matrix reasonable, the detailed investigation of temperature and strain rate effects on damage accumulation in as-receivedeived AZ31 sheets was carried out using uniaxial tension specimens. The formability tests were carried out at three different temperatures for all three sheet materials. Study of deformation under biaxial stress state is not enough to comment on the stretch formability. However, this paper did not aim at characterizing the formability of these alloys, instead, it was aimed at making a qualitative comparison between 3 different processed textures keeping all other effects such as grain size and others aside.

3.2 Materials

The starting material used is a commercial magnesium alloys AZ31B H24 temper with nominal composition (3.33 Al, 0.88 Zn, 0.21 Mn, balance Mg, all in %wt) in the form of hot rolled sheets. Plates of dimension 150mm x 150mm x 13mm were processed using Equal Channel Angular Plate Extrusion (ECAPE) tool. A backpressure of X MPa and an extrusion rate of 4.57mm/min through the 90 die with sharp corners were the parameters used to process the material without cracks. Two different processing routes were adopted: Route 4A (no rotation between passes) and route 4Bcp (90 CW rotation around the plate normal) both processed at 200° C. The alphabet in each case denotes the nomenclature of the route through which the material has been deformed while the number denotes the number of passes undergone. Completely crack-free processing was possible only using route 4Bcp. The plate processed through route 4A had minor cracks near the edges. It is worth mentioning that the Bcp route used in this study is completely a new route and different from the traditional Bc route used for bar specimens where the rotation is about the extrusion axis. The present Bcp route in the plate tool is not accessible in the billet ECAP tool. The plates were oriented such that the extrusion direction were initially aligned with the rolling direction. Due to geometrical restrictions of the ECAPE die, only one initial texture could be used with the basal poles parallel to the extrusion direction as shown in Fig. 22.

Sheet specimens of dimensions 60 mm x 60 mm x 1.65 mm were cut out from these ECAPE processed plates using Electro Discharge Machining (EDM). 3 sheets could be obtained through the thickness and 4 different locations on the plate. Care was taken to avoid the edges and stay away from the top and the bottom surfaces in order to stay in the uniformly deformed region. The material obtained after

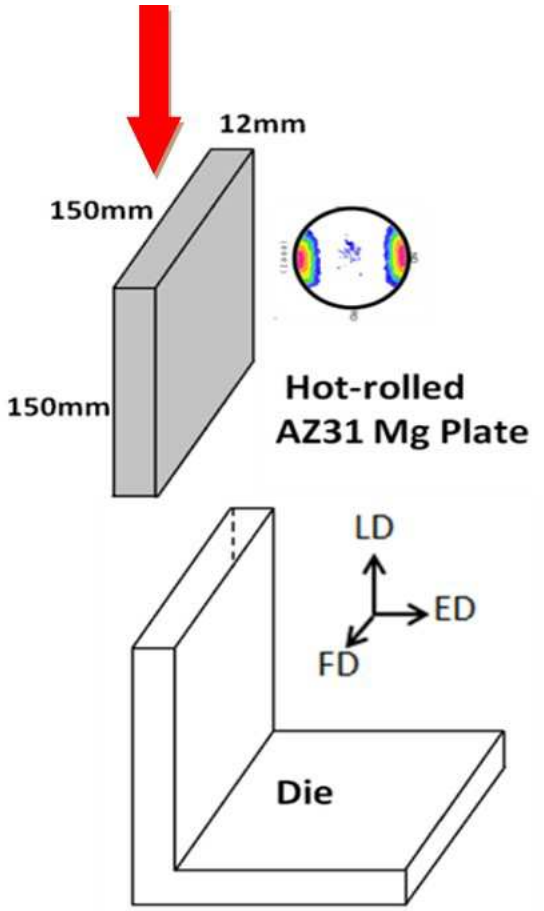

Figure 22: Schematic of ECAP die for processing of 150 mm x 150 mm x 13 mm plates. The starting texture used was basal, as the basal poles are parallel to the extrusion direction. ED: Extrusion direction, LD: Longitudinal direction, FD: Flow direction.

ECAE is a material that has been hardened by heavy shear strains causing the grain size reduction. In order to compare with the conventionally rolled alloys, the microstructure needs to be recovered off the loss in strain hardening capacity due to ECAE and grown back to the grain size regime of the reference material. Hence a heat treatment which was used in the recent study by Basu et al., was employed in this case. The processed plats were heat treated at 350°C for 24 hours. A Bruker-AXS D8 X-ray diffractometer(XRD) with Cu Kα radiation on a sample from the plate's mid-section was used to get (0002) and $(10\bar{1}0)$ pole figures using a 5° grid size and an 85° sample tilt.

In Fig.22 the notion of directions followed are RD, TD and ND refer to Rolling direction, transverse direction and normal directions respectively. The in plane directions are the rolling and transverse directions while the normal is through thickness or out of plane direction. The same directions when translated to ECAE are denoted as ED, LD and FD which refer to extrusion, longitudinal and flow directions respectively. The ED and FD being the in-plane directions. This nomenclature will be used for further reference in the course of this paper.

3.3 Microstructure Characterization

Optical microscopy was used to characterize the initial and processed microstructures. To obtain the mirostructure of the material, metallographic samples from different planes were cut using a diamond saw, ground with SiC paper and fine polished using 1μm diamond solution, 0.3μm colloidal silica suspensions. Water was used during grinding only. The solutions used for polishing were alchohol based and an alchohol based lubricant was used for polishing purposes. Ethanol was used for rinsing and sometimes acetone as ultrasonic cleanser. For etching, acetic picral solution (4.2 g picric acid, 10 ml acetic acid, 70 ml ethanol and 10 ml water) was used

for time periods upto 5s. The alloys which were processed without annealing had a quicker response to the etching process due to the higher stored energy from the processing.

3.4 Mechanical Tests

3.4.1 Uniaxial Tests

Flat tension specimens were cut out along the three principal directions E, L and F directions. These experiments were aimed at measuring the yield and flow behavior of these materials, understand the evolution of plastic anisotropy with plastic strain and obtain the strains to failure. Two samples were tested per condition to increase confidence in the scatter. These tension experiments were performed at room temperature on a MTS servo-hydraulic test frame at a constant strain rate of 5 x 10 $^{-4}$ s^{-1}. Fracture strain ϵ_f is defined as strain at which the load drop occurs. This fracture strain here is the logarithmic strain based on area reduction measure at the load drop. ‘

3.4.2 Stretch Formability Test Using Olsen Punch Setup

Biaxial stretch formability tests were performed at room temperature (RT) using the Olsen tool set. Sheet specimens were cut of dimensions mentioned in section3.2.1 from the ECAPE processed plates were used in this study. These specimens were tested both under as-processed conditions and after annealing to recover the microstructure and were compared to the as-receivedeived material (rolled AZ31b). The Olsen tool set is an instrumented double action servo hydraulic press with a maximum punch load of 60,000 lb and maximum clamping load of 75,000 lbs. A schematic of the Olsen formability test frame with dimension are given in Fig.23.

The Erichsen formability test is identical to the Olsen formability test with an exception of test dimensions. Limiting Dome Height test (LDH), it is a more com-

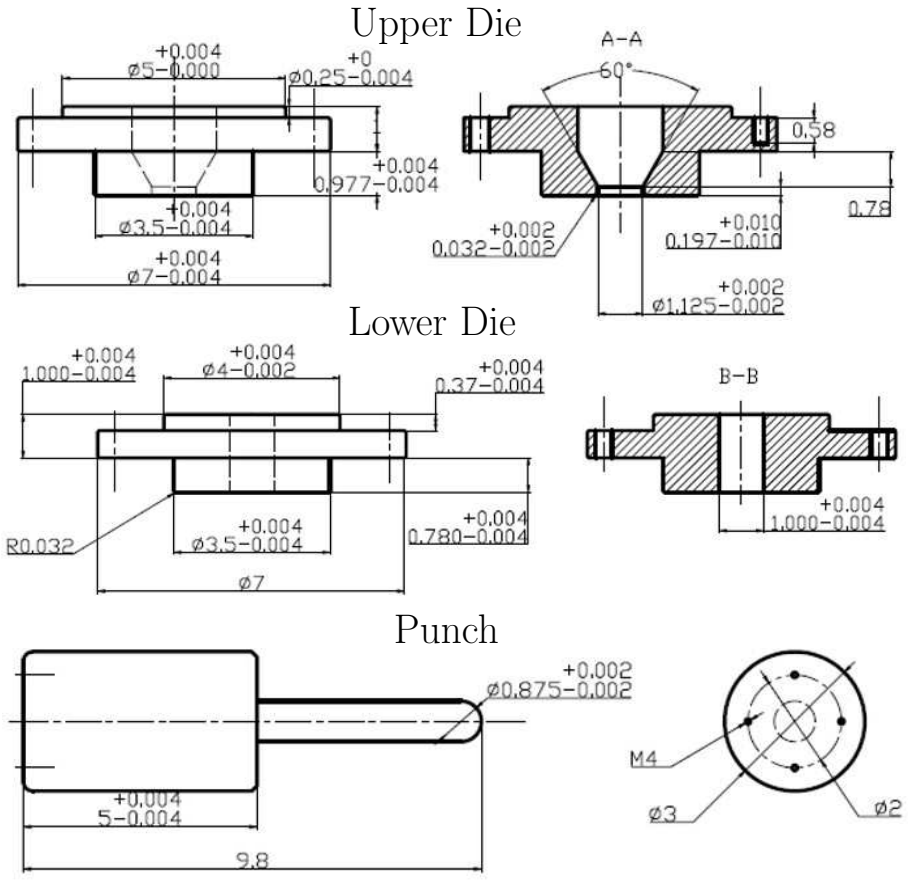

Figure 23: Schematic drawing of Olsen/Erichsen formability test setup. It comprises of 3 parts; upper die, lower die and the punch or plunger.

monly used test in evaluating the formability of sheet metals. The LDH test, which uses a 4" punch diameter, is the test used in the auto industry for sheet metal formability assessment. However, we could not use the LDH test in our study because it requires a 7" x 7" specimen size. Thus, the Erichsen test was selected due ti material restriction as the process of ECAPE led to limited material at disposal for characterization. Also, since our study was to compare specimens relative to each other based on their thermo-mechanical processing histories, rather than to establish a formability limit, the Erichsen test was adequate. The punch speed was 0.05 mm/s and the 133 kN clamp load was applied to ensure pure stretching. After the test, specimens were analyzed and it was evident that the material was not drawn into the die, but instead biaxially stretched. The picture of the punch setup is shown in Fig. 24. The specimen is clamped in between the pair of dies shown on the right of Fig. 24 and the punch of diameter 1.25" is used to deform the sheet specimen under biaxial tension.

3.5 Results

3.5.1 Processed Textures and Microstructures

The resultant microstructures and textures obtained through processing through ECAPE route 4A and 4Bcp at 200°C are shown in Fig. 25(c)-(f) are compared to the as-rolled texture in Fig.25(a)(b).

Single pass through A route, exhibits similar texture to rolling texture. Subsequent route A-passes serve to strengthen this texture by reorientation to a very similar texture after each subsequent pass. The textures possess rotational symmetry about the flow plane normal. Route Bcp is a redundant strain path where the simple shear of the 4 passes results in zero net shear. However, these steps does not erase the texture developed in the earlier pass, demonstrating the path dependence

Figure 24: Geometry of the punch setup used in this study. The figure on the left shows the punch and to the right are the geometry of the die in which the plate was tested.

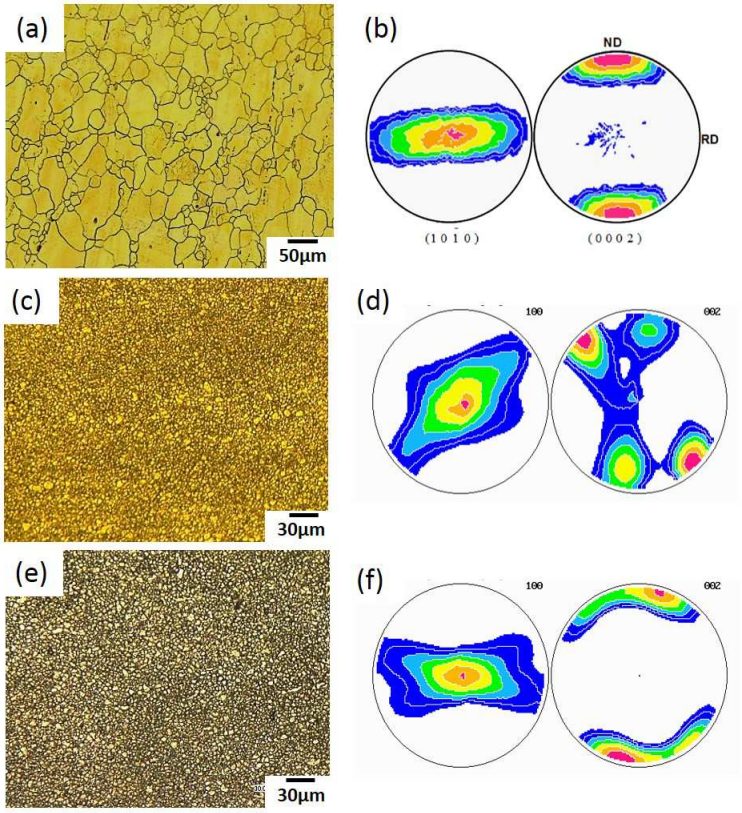

Figure 25: Optical microstructure of the (a) as-rolled AZ31 plate (c) 4A (e) 4Bcp and textures of (b) as-rolled AZ31 (d) 4A (f) 4Bcp.

in deformation induced textures. The initial rolled plate possessed a grain size of 25μm and the processed ECAPE sheets posses approx 4μm grain size. The ECAPE followed by annealing at 350°C for 24 hours led to an average grain size of approx 20μm. A line intercept method was used to determine the average grain size.

3.5.2 Stress-strain Behavior

Flat tension samples and compression samples were used to characterize the flow behavior of the processed materials in compression and tension. Typical nominal stress versus nominal strain responses in tension and compression along the principal directions of extrusion are shown in Fig. 26 exhibiting the usual tension-compression asymmetry.

3.5.3 Punch Response

Room temperature biaxial stretch formability tests were performed using an Olsen tool set on the EDM cut sheets sliced from as-rolled and ECAPE processed plates. The ECAPE processed sheets were heat treated at 350°C for 24 hours to recover the microstructure and purely compare texture effects on the formability of these magnesium sheets. Formability was evaluated by the limiting dome height (LDH) value, i.e., the value at which a macroscopic load drop occurs leading to the formation of a crack.

Fig. 27 shows the deformed samples under biaxial stretch and gives an idea about the test matrix used for these experiments. All the tests were stopped as soon as a load drop was observed in the macroscopic load displacement curve leading to formation of a macroscopic crack. The room temperature response for the 3 materials is shown in Fig. 28. From the above figure we see that the material $4B_{cp}$ shows more than 200% improvement in the value of dome height while 4A showed a poorer formability result than the as-rolled material.

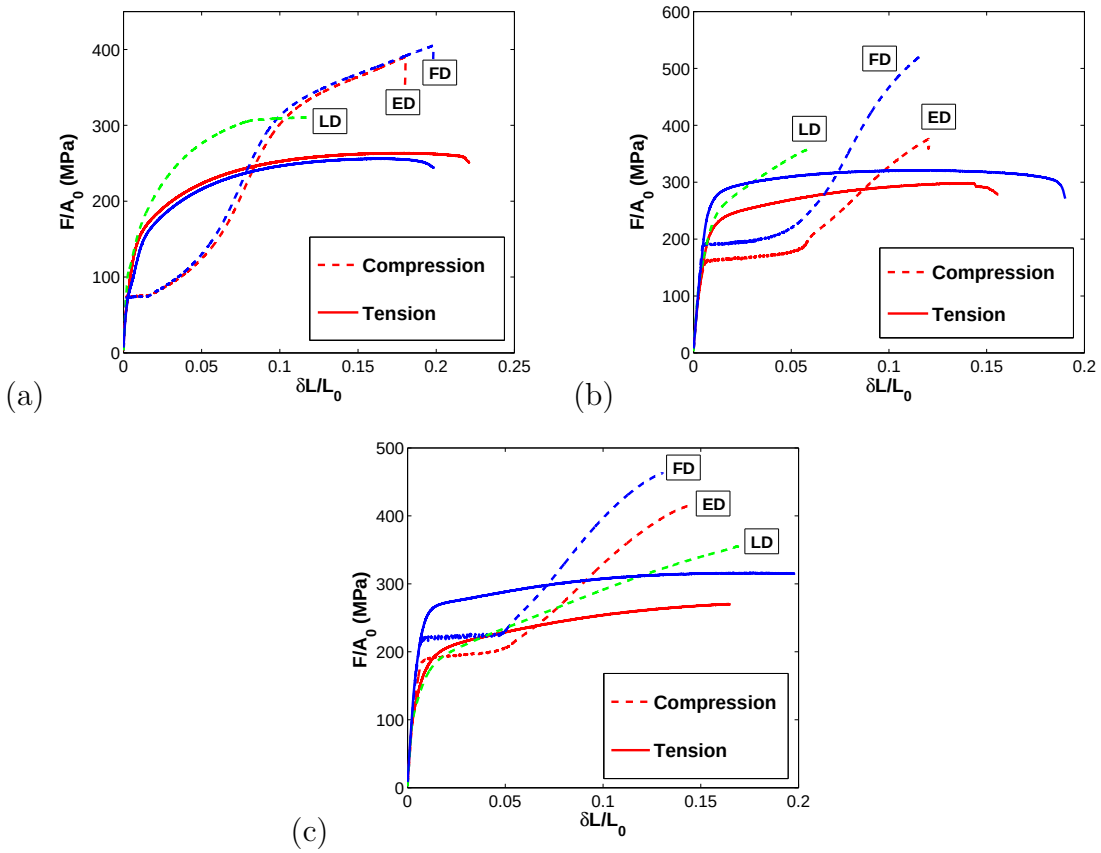

Figure 26: Room temperature stress-strain response under tension and compression for (a) as-rolled (b) 4A and (c) 4Bcp

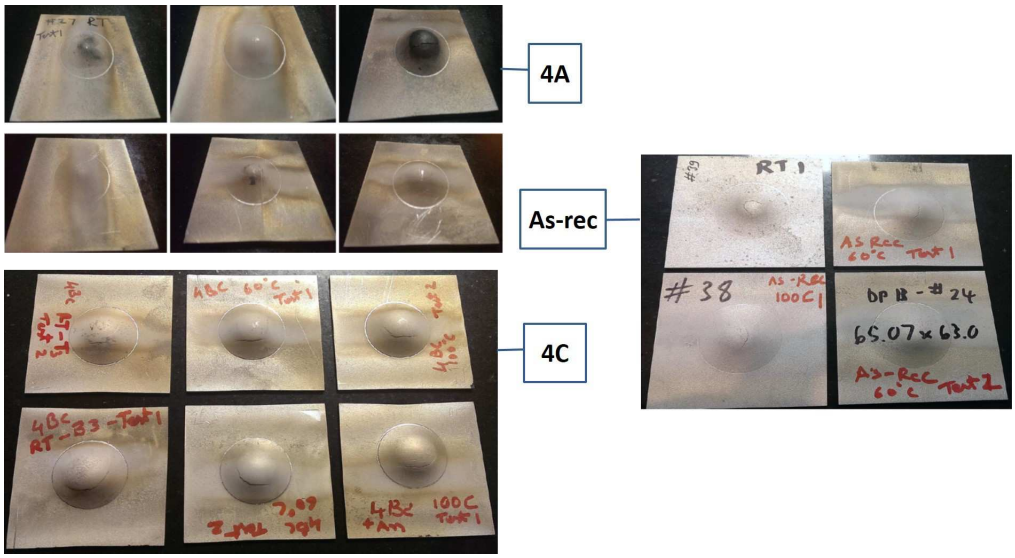

Figure 27: Deformed test matrix used to characterize biaxial stretch formability of AZ31 processed by different processing routes.

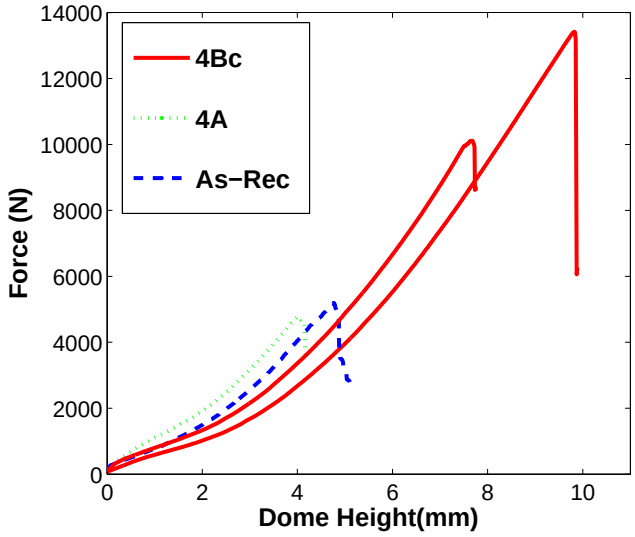

Figure 28: Load vs dome height for stretch punch tests performed using an Olsen punch setup on ECAPE + annealed processed thought 4A and 4Bcp at 200°C compared to that of rolled AZ31 plate.

Further sheets of these materials were also tested at slightly elevated temperatures than room temperature (60°C and 100°C) to compare the temperature effects on the formability results. The force vs dome height response is shown in Fig. 29 for (a) as-rolled (b) 4A (c) 4Bcp. From the figure we can see that the as-rolled material shows little temperature effect when the temperature changes from room temperature to 100°C. 4A shows huge temperature dependence in the range investigated on its formability. The cup height is seen to improve by 100% when temperature was elevated from room temperature to 100°C. Material 4Bcp shows no temperature dependence in the range investigated.

3.6 Discussion

Lack of success in techniques aimed at suppressing or reducing the anisotropy indicates that texture/anisotropy-ductility relationships are more complex than previously believed. This led to a new paradigm, "Engineer not suppress anisotropy to improve ductility". The recent studies by Basu et al.[91] showed that texture can indeed be engineered to obtain better ductility. This could be rationalized and guided by an anisotropy indicating factor "h" which emerges from the micromechanical calculation done by Benzerga et al. [17] of a hill type material. The success in improving the ductility of AZ31 by 2 fold as suggested by the invariant led the authors to check if the above findings could be extended to the formability of these materials. The findings for material processed by 4Bcp route (see Fig. 28) indicate success as such high values of dome height at room temperature were not reported earlier in the literature.

Fig. 30 shows the trends obtained in the formability data. The improvement in formability from as-received to 4A to $4B_c$ was observed for all temperatures except at room temperature as seen in Fig. 30 (a). The temperature dependence on

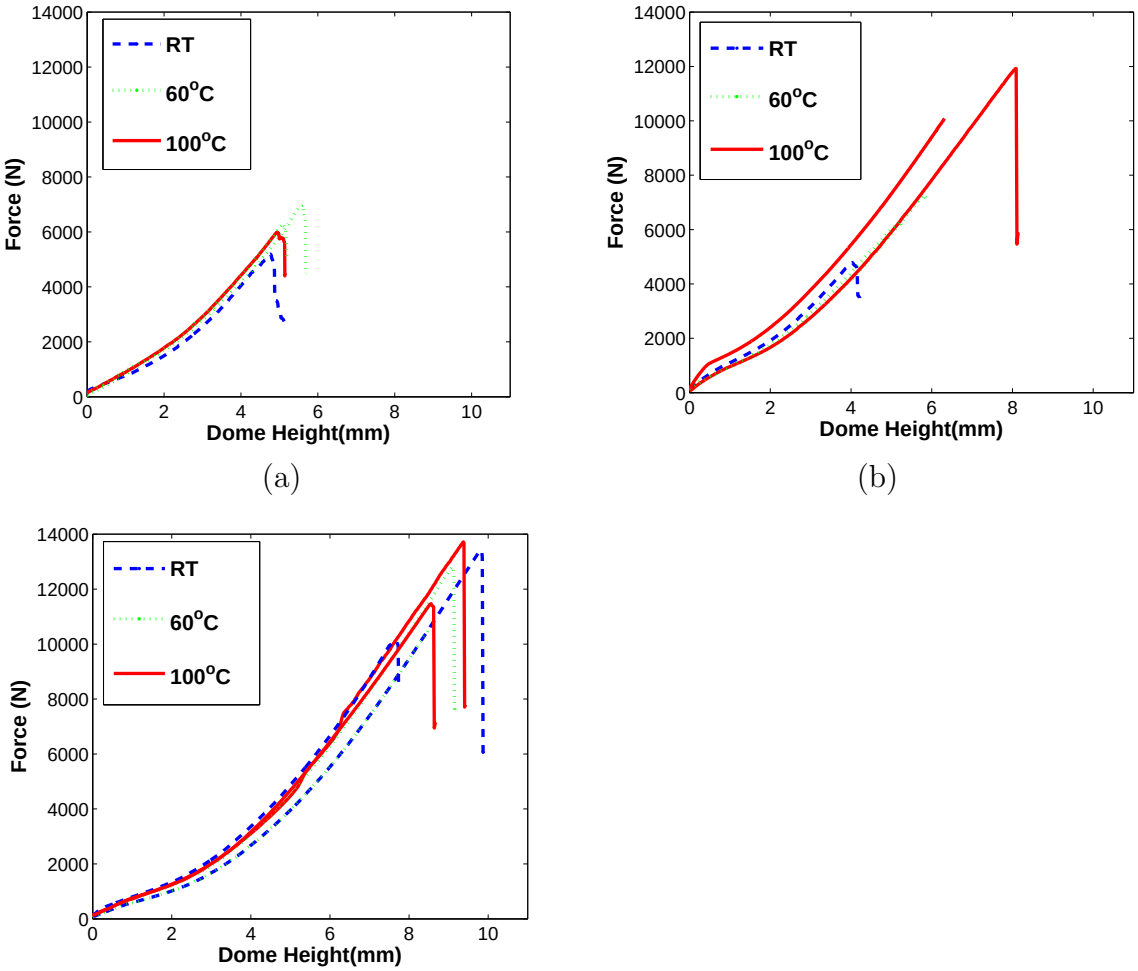

Figure 29: Load vs dome height for stretch punch tests performed using an Olsen punch setup on (a) rolled AZ31 sheet specimens compared to ECAPE + annealed processed thought (b) 4A and (c) 4Bcp at 200° C.

the formability of each material is shown in Fig. 30(b). Materials as-received and $4B_c$ show minimal effect on formability in the range of temperature studied. Material processed via 4A however, shows huge improvement in formability with the temperature range investigated.

Poorer response for 4A at room temperature was against expectations as the AED indicator and findings from uniaxial ductility indicate better results. Basu et al.[91] showed in their recent study that the AED in compression is of the bad type in 4A, although it is not clear that compressive states are relevant here. However, the anisotropy in biaxial loading has not been thoroughly characterized. Minimal variation of the limit cup height with temperature in as-received material and $4B_c$ indicate that the texture does not facilitate for activation of softer mechanisms with minor change in temperature studied here. However, improvement of formability with nominal increase in temperature for 4A suggests that the mechanisms aiding ductility were not easily activated at room temperature. Also the evolution of the stress state may play a role in generating plastic instabilities and causing early failure in 4A material.

3.7 Summary

Commercial 13mm-thick AZ31 hot rolled plates have been successfully ECAPE processed at 200°C using different routes and multiple passes to modify the initial wrought microstructure. Loss of hardening capacity if the material was recovered by heat treatment at 350°C for 24 hours which was similar to the heat treatment used by Basu et al. [91]. Sheet specimens were cut out of ECAPE processed plates. A punch experiment was carried out using an Olsen type punch. The results showed two major trends; 4Bcp showed highest dome height at room temperature and although 4Bcp and As-received AZ31 showed minimal temperature effects in the range probed, 4A

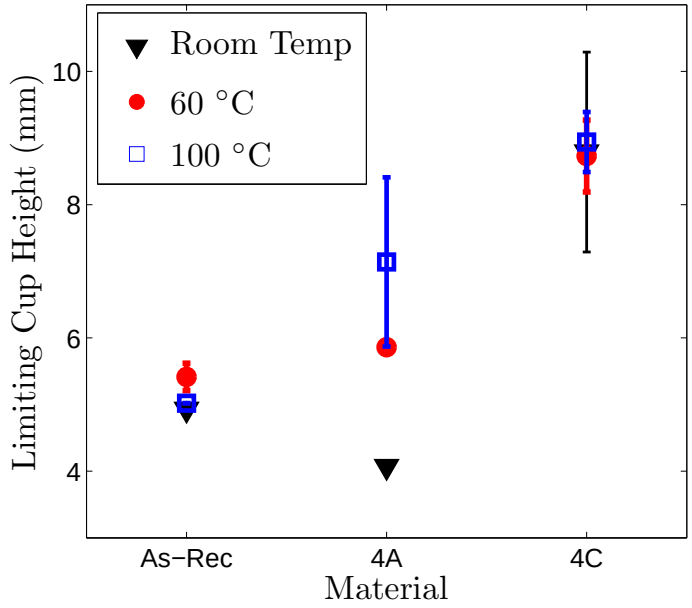

(a)

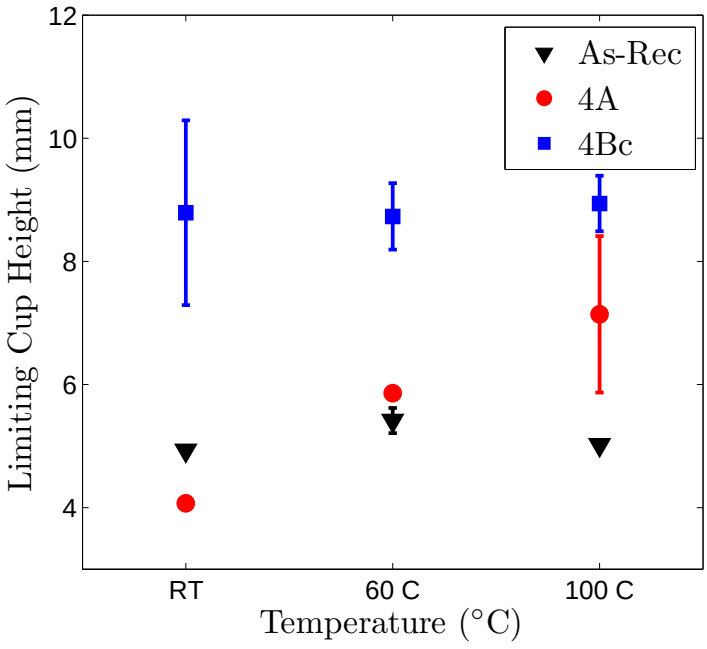

(b)

Figure 30: Limiting cup height(LCH) with respect to (a) material type as-received, 4A and $4B_{cp}$ (b) temperature. Each data set corresponds to a particular temperature and materials respectively for each figure.

which showed poor formability at room temperature, exhibits strong temperature effects causing marked improvement in the dome height within the temperature range probed. These advances in ECAP processing enabled an investigation of texture effects at fixed grain size on both the ductility and punch formability of Mg alloys. The findings introduce a paradigm shift that strong plastic anisotropy can demonstrate an enhancement of low-temperature ductility as well as formability, irrespective of loading orientation or stress state. Engineering the anisotropy by texture modifications could lead to improvement in ductility and formability at low temperatures.

4. DUCTILE FRACTURE UNDER SHEAR DOMINANT LOADINGS

4.1 Introduction

Failure mechanisms in ductile materials are broadly divided into failure due to cavitation and shear localization. In important applications such as sheet metal forming, material undergoes complex deformation paths. Often shear rupture occurs. Such failure is associated with the formation of shear bands[92] which may occur in the absence of a shear component in the remote loading. This is however, different from failure in shear where the remote loading is shear dominated. Several studies in the literature have aimed at understanding the transition from one mechanism to the other by introducing external shear loading and thus modifying the local stress state. Data for experiments involving combined tension and shear remain scarce as these experiments involving shear loadings are difficult to perform.

Hancock & Mackenzie[93] and the Beremin group (1981)[94] documented the strong dependence of the strain to failure upon stress triaxiality. Stress triaxiality ratio is related to the ratio of the first invariant of the stress tensor to the second invariant. These authors tested notched bars of different notch acuity. These studies established strain to failure as a monotonically decreasing function of stress triaxiality and rationalized it on the basis of void growth theory [95, 96]; also see [97]. One question is how this would translate to the regime of low triaxiality. Prediction of a failure measure in the low triaxiality regime still poses to be a challenging problems in the mechanics of materials community.

In a pioneering work, Johnson and co-workers from the South West Research Institute comprehensively studied failure under shear in 12 different materials systems using thin-walled torsion tubes[98, 99].

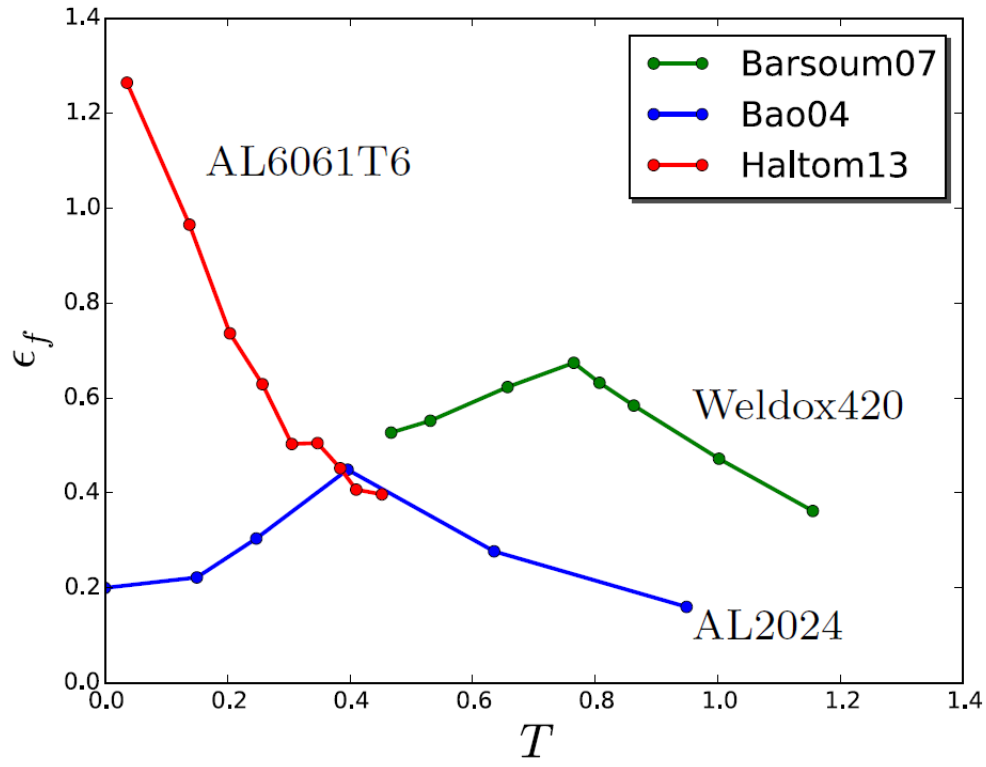

Figure 31: Equivalent strain to fracture vs average stress triaxiality (Bao and Wierzbicki, 2004)[100], Effective plastic strain to failure initiation versus stress triaxiality (Barsoum and Faleskog, 2007)[100], (Haltom et al., 2013)[101]

Fig 31 shows some of the most prominent low triaxiality experiments conducted in the past decade [100, 102], reported fracture strains which were significantly lower at low stress triaxialities. Later, experiments by Haltom et al.[101] showed that the value of the fracture strain increases with decrease in the average stress triaxiality which is similar to extrapolation of the Hancock & Mackenzie[93] curve.

Bao and Wierzbicki(2004)[100] conducted a series of tests as shown in Fig.32(a) including upsetting tests and shear tests on 2024-T351 aluminum alloy using compression specimens and butterfly specimens respectively to capture the relation between the equivalent strain to fracture versus the average stress triaxiality. Numerical simulations using ABAQUS were performed for calculating the evolution of the equivalent strain at fracture and the average stress triaxiality. They also report significant drop in ductility in the low triaxiality regime, with ϵ_f in pure shear reaching a value of 0.2. Barsoum and Faleskog(2007)[102] conducted tension and torsion experiments on double notched tube specimens as shown in fig32(b). The effective plastic strain, and the stress triaxiality were determined in the center of the notch at failure with the help of ABAQUS simulations. They too report significant drop in ductility in the low triaxiality regime. Haltom et al. (2013)[101] conducted tension and shear experiments on tubular specimens as shown in Fig.32(c). Their results show the strain to failure monotonically increases as T decreases, a result that is in contrast with previously reported results for Al alloys. In addition, the measured failure strains are significantly larger than previously reported values. Haltom et al. (2013)[101] explained the difference in results on grounds that experimental setup and diagnostic methods used can have significant influence on the results especially when resorting to indirect methods of estimating the stresses and deformations at failure.

In sheet metal forming applications, the state of stress is plane stress and hence

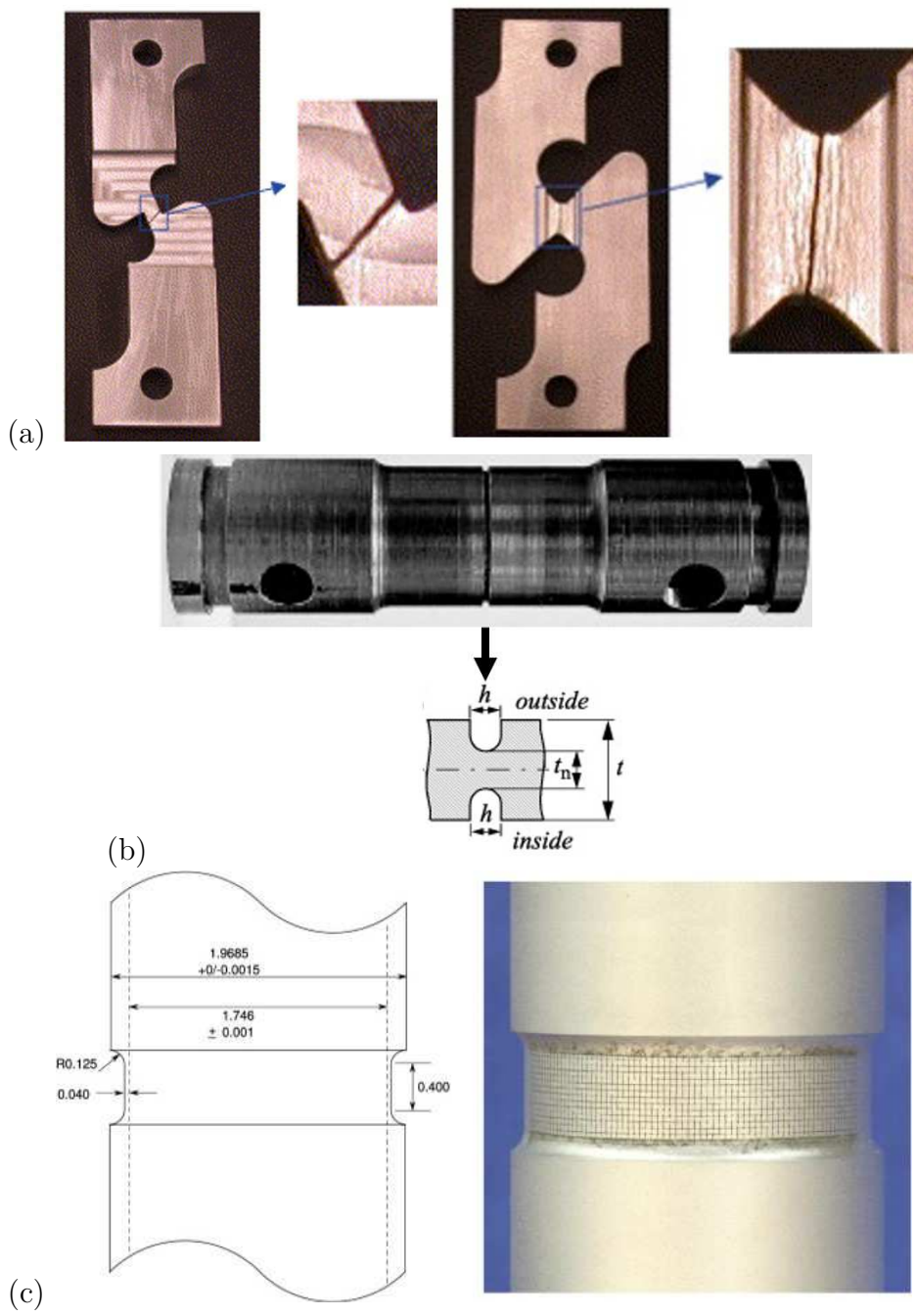

Figure 32: Samples to characterize fracture loci under shear dominant loading by (a) Bao and Wierzbicki, 2004[100] (b) Barsoum and Faleskog, 2007[100] and (c) Haltom et al., 2013[101] (Courtesy of Nithin Thomas

the stress in the third principal direction is insignificant. Therefore, it is important to determine the degree to which the metal can undergo thinning in different parts of the pressing. In addition, presence of plastic anisotropy in sheet metals also affects directional response of yielding and incompatibility in deformation.

The aim of this research is to understand how sheet materials behave and rupture under combined tension and shear i.e. in the low triaxiality regime. Magnesium alloys are prime candidates for lightweight applications and hence the primary choice of candidate for this study. High cost of production through conventional sheet forming processes and low formability at ambient temperatures further limit application of sheet metals. Combining casting and additional rolling has shown to reduce production cost of AZ31 sheets considerably commonly known as Twin-roll casting (TRC)[103]. Reducing the number of rolling passes, decreasing the temperature and producing a resultant material with finer microstructure makes TRC sheets more economic and displays better mechanical properties than its conventionally produced wrought counterpart. Understanding the behavior of this material under these shear dominated loadings (combined tension and shear) is a must in order to improve the formability and in-service performance of these alloys.

Thin-walled torsional loading leads to most uniform shear-stress state[104, 105, 106], however, tubular specimens are expensive to machine[107] and are not feasible in sheet specimens. Hence, modified arcan tests [108, 109, 110] were carried out to perform tests with combined tension and shear loadings. This was aimed at understanding the effect of low stress triaxialities on fracture, which has been a subject of active research over the past decade. These tests are similar to the Iosipescu tests[111], however, they pose greater advantages than the latter in terms of a more compact geometry that reduces bending effects and friction due to bearing friction[112, 113]. Arcan experiments can probe a variety of mixed-mode loadings

with a higher range of shear dominated failures stress-states. The initially designed Arcan experiments were disc/S shaped specimens which were later modified to have a separate holder and and interchangeable butterfly shaped specimen[108]. These were earlier used in numerous studied to understand composite failure. Recently, these tests have caught attention in metal sheet forming industry to carry out tests under mixed mode loading conditions[110, 114].

Macroscopic strains are measured at the local scale using digital image correlation (DIC) method and used to characterize the constitutive response of the material. Local displacements at the vicinity of the notches were obtained and analysis based on the effect of the effect of mix-mode loading on the ductile crack initiation was apportioned. Some preliminary numerical simulations were carried out to extract the evolution of stress triaxiality and lode parameter at failure locations using an associated flow model and a hardening curve identified experimentally using smooth specimens.

4.2 Experiments

4.2.1 Experimental Procedure

The starting material in this study is TRC AZ31 which is further rolled to a form a sheet of final thickness of 3 mm. This material was provided by POSCO. The nominal chemical composition of the material is Mg 95.4%, Al 3.32%, Zn 0.803%, Mn 0.304%, and Si 0.147% with and average grain size of 8.2 μm. All samples were CNC cut along the rolling direction from the same sheet. Basic mechanical characterization of this material has been carried out by Rodriguez et al. and Dogan et al.[115, 62] in tension and compression at various strain rates.

The material response of the material was characterized using flat tensile tests along the rolling(L), transverse(T) and the planar off-axis direction (LT) as shown

in Fig. 33.

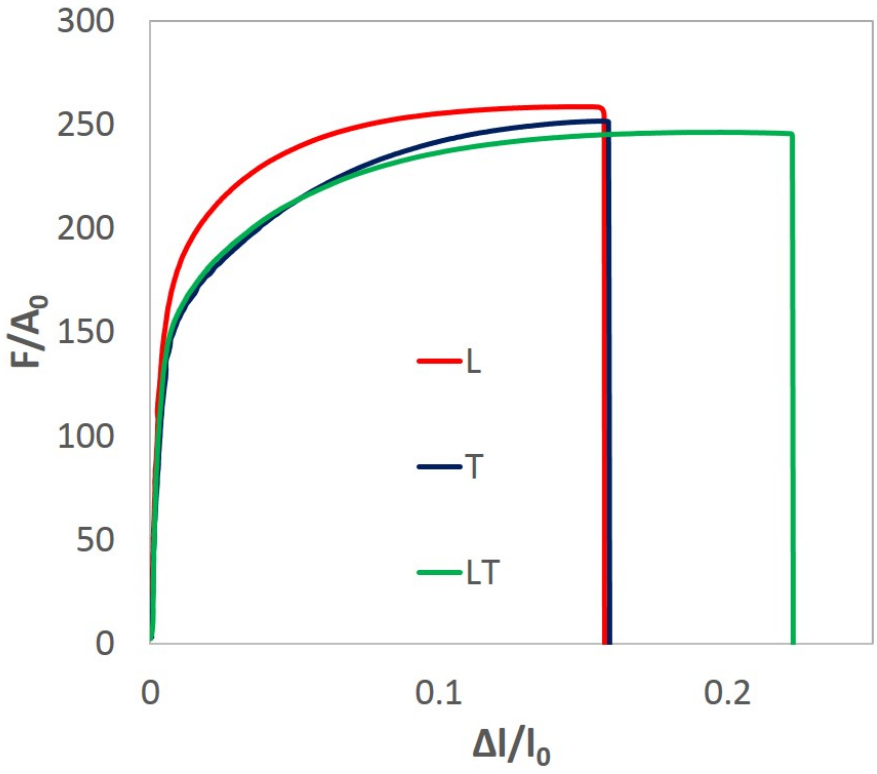

Figure 33: Tensile tests in TRC AZ31 sheet along the rolling, transverse and 45° between the principle directions.

Arcan specimens were machined out of a sheet with dimensions 150 mm x 150 mm. This specimen geometry has been used by several authors in the literature, majorly for testing composites. The geometry had to be redesigned due to greater sheet thickness and to prevent material deforming in the grip region. The size of the grip region was increased while keeping all other geometry same as used by Ghahremaninezhad et al.[110]. This was suggested through 3D FEM calculations. An additional screw/pin was added in the center to prevent twisting and provide more uniform deformation.

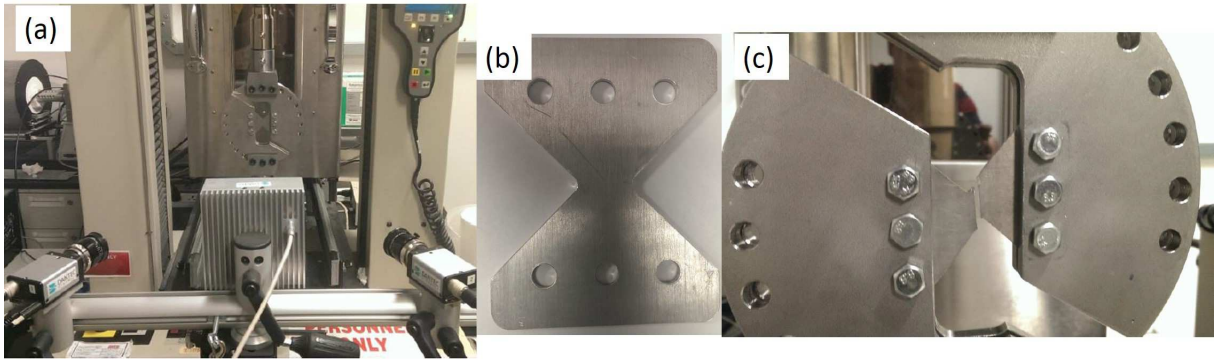

Figure 34: (a) Arcan experimental setup with the DIC cameras. (b) Sample geometry for Arcan specimen used (c) Sample holder that can orient the sample along different loading orientations. Each hole on the holder rotates the sample by 15°.

The sample was clamped in between two pairs of semi-circular discs as shown in Fig. 34(a) with the help of three screws. The holes on the outer edge of the holder are used to orient the samples along various loading directions. Each shift of a hole will lead to a 15 degree shift of the holder. Hence the range of the angles that can be probed using these experiments is between 0° and 90° with an interval of 15°, 0° denoting shear loading and 90° denoting tensile loading. Experiments were performed on a MTS insight screw driven tensile test machine as shown in Fig. 34(a) with a load cell capacity of 30 kN. A modified arcan test setup was designed and built in order to vary the stress state between close to pure shear and tensile loadings with the available uniaxial machine. The test setup comprised of a holder which acts as a mode of rotating the sample and thus varying the loading orientation. The sample as shown in Fig. 34(b) was attached in between the holders. The test setup is shown in Fig. 34(c) where the sample is oriented for shear loading conditions.

Fig. 35 shows the schematic of an arcan test in any random test orientation. The arrows indicate the direction of the loading. The angle α defines the angle between the direction of loading and the minimum cross-section (line connecting the

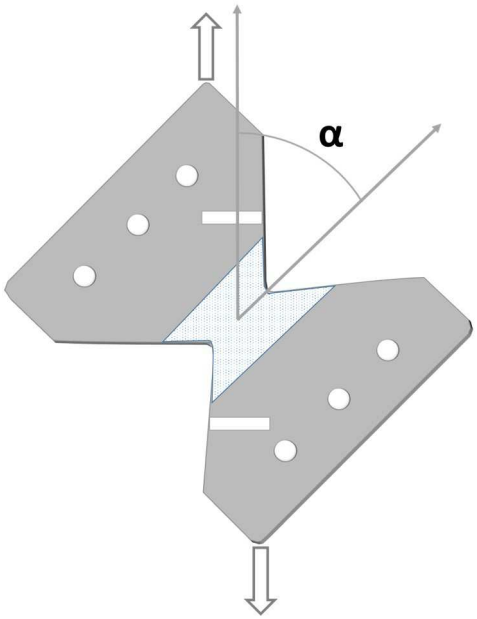

(a)

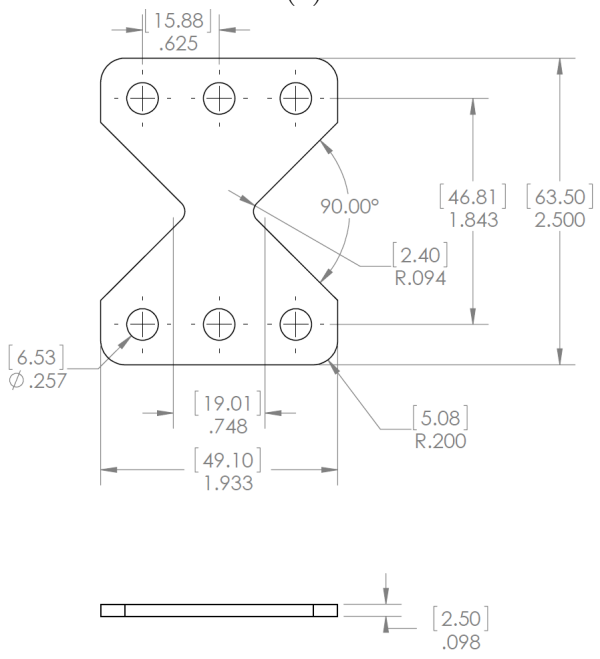

(b)

Figure 35: (a)Schematic of the arcan plate specimen showing the loading orientation and the measurements of the macroscopic strain measures at different scales. (b) Geometry of the Arcan specimen with dimension in both mm and inch. Rolling direction is along the vertical orientation of the specimen.

notch roots). The rectangles at the upper half and lower half of the specimen refer to the position of reflecting tapes used for recording laser extensometer elongation data. The laser was used as a way to extract macroscopic strains along the loading direction to get more accurate measure than the machine reported displacement.

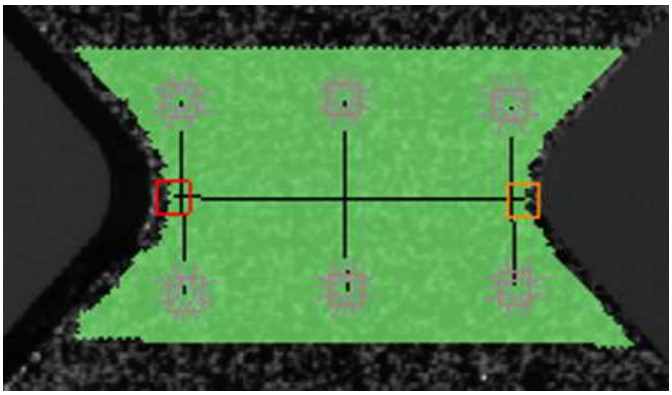

Figure 36: Locations at which local displacements and strains were reported for each specimen.

The shaded region indicates the region over which digital image correlation was used. Fig. 36 shows the area over which the whole field measurements using DIC were made. In all testing conditions the coordinate system was reoriented such that the x-axis was set to be along the minimum section. The displacements were obtained along the vertical lines as shown in Fig. 36 and displacements were obtained along the 2 principal directions of the defined coordinate system of the specimen. The points above and below the notch area were used to extract the relative displacements. In order to keep the gage length constant points were placed at $\pm 3mm$ about the minimum section. Displacement along the x-direction is termed as u and one along the y-direction is termed v. The macroscopic load was decomposed into components along these principal directions and are named T and N for the x-direction and the

y-direction components. Equation 11 denotes the definition of T and N where α is the nominal angle of loading.

$$\mathcal{T} = \mathcal{F}\cos\alpha\ , \quad \mathcal{N} = \mathcal{F}\sin\alpha \tag{11}$$

Local strains were obtained from the DIC along the line connecting the notch roots. This is the line that traverses through the minimum section of the specimen as shown in Fig. 36. The strain ϵ_{xx}, ϵ_{xy} and ϵ_{yy} were extracted at 3 different locations; center of the line, maximum location of the strain and the averaged strain over the line. ϵ_{zz} was calculated in all cases using the incompressibility criterion i.e. $\epsilon_{xx}+\epsilon_{yy}+\epsilon_{zz}=0$. This is an assumption made in many experimental reports([31]for example). However, recent findings show it is questionable[116]. An attempt has been made therefore to measure the out-of-plane strains. An equivalent measure of strain was defined as shown in equation 12. This is plotted along a stress-like measure of force normalized by the initial minimum sectional area.

$$\epsilon_{\text{eq}} = \sqrt{\frac{2}{3}[\epsilon_{xx}^2 + \epsilon_{yy}^2 + \epsilon_{zz}^2 + 2\epsilon_{xy}^2]} \tag{12}$$

The advantage of using 3D DIC is that the out of plane deformation can also be quantified. z-displacement was obtained from the full field measurement of the DIC and was plotted along the centerline running through the minimum section. The strain ϵ_{zz} was calculated using the relation given in equation 13.

$$\epsilon_{zz} = \ln\big(\frac{t}{t_0}\big) = \ln\big(1 - \frac{2w}{t_0}\big) \tag{13}$$

Where, t_0 is the initial thickness of the sheet material, t is the current thickness and w is the displacement of a material point out of plane. The reduction in the

sheet thickness along the minimum section and along vertical lines as shown in Fig. 36 was compared from among specimens of different orientations. The reason for not calculating strains using ϵ_{zz} and using incompressibility lies in issues of not being able to get rid of rigid body rotations of the specimen as enough area was not analyzed from the DIC.

4.2.2 Global Response

The load displacement curve under different loading conditions is shown in Fig. 37. These are obtained by plotting the applied load versus the elongation ΔL along the loading direction as recorded by the laser extensometer along the tapes as shown in Fig. 35(a). This is merely aimed to show macroscopic trends in the data.

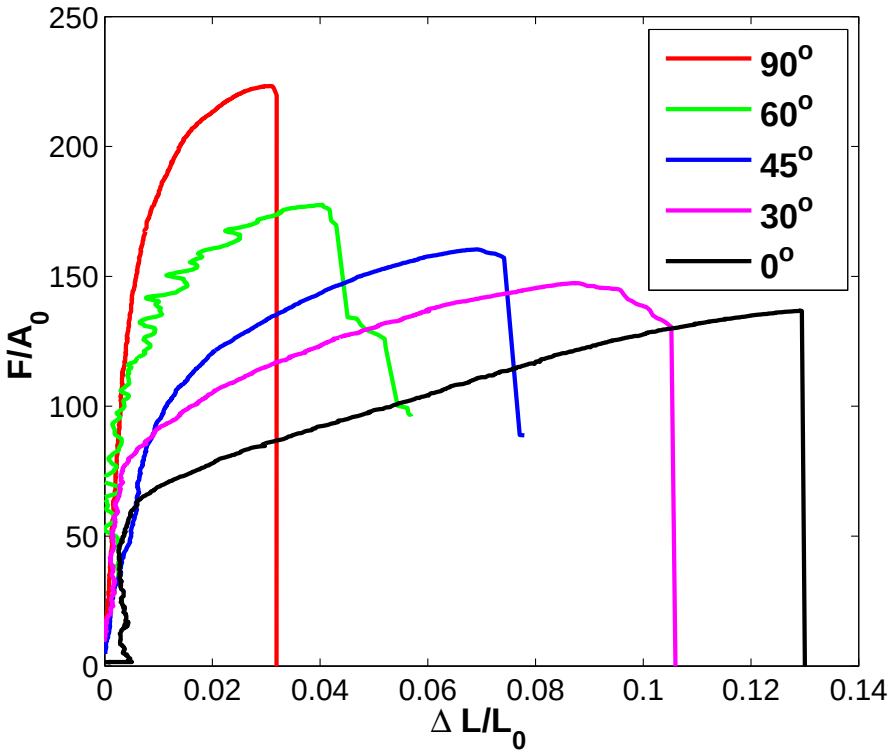

Figure 37: Force versus displacement response for experiments without path change.

It can be observed that failure is delayed as the sample orientation changes from tensile dominant loading to shear dominant loading. It is evident that the load levels reduce towards more shear dominant loading. However, displacements in Fig. 37 were obtained by recording the displacements of tapes along the loading direction and no lateral displacements could be recorded due to limitation of the laser. With the help of Digital Image Correlation we could obtain the displacements at any point in the gage area shown in Fig.36.

The force was resolved into components along the two principal directions; T denotes transverse force along the x-direction and N corresponds to normal force along the y-direction. Both vertical and horizontal displacements were extracted from the DIC. The normal component of the force shown as N in Fig. 38 was plotted against the vertical component of the displacement v. The transverse component of the force T is plotted against the horizontal displacement u. Both 0° and 90° do not have the normal and transverse component of the force respectively, which explains why the plots are blank. For all mixed mode loading conditions the shear component of the loading accounts for the majority of the deformation.

4.2.3 Whole-field Strain Maps

The evolution of each component of strain ϵ_{xx}, ϵ_{xy} and ϵ_{yy} is shown in this section. The strain maps are obtained at 20%, 50% and 90% of failure strain ($\Delta L/L_0$). Three different specimens are compared in these maps; 0°, 45° and 90° to distinguish the effects of tensile, shear and mixed mode loadings on the evolution of each component of strain.

The evolution of ϵ_{yy} as seen in Fig. 39 shows that the value of this strain measure is negligible in the 0° sample. Late into the deformation, antisymmetric localization of ϵ_{yy} is seen to develop above and below the notch root along the y-direction. This

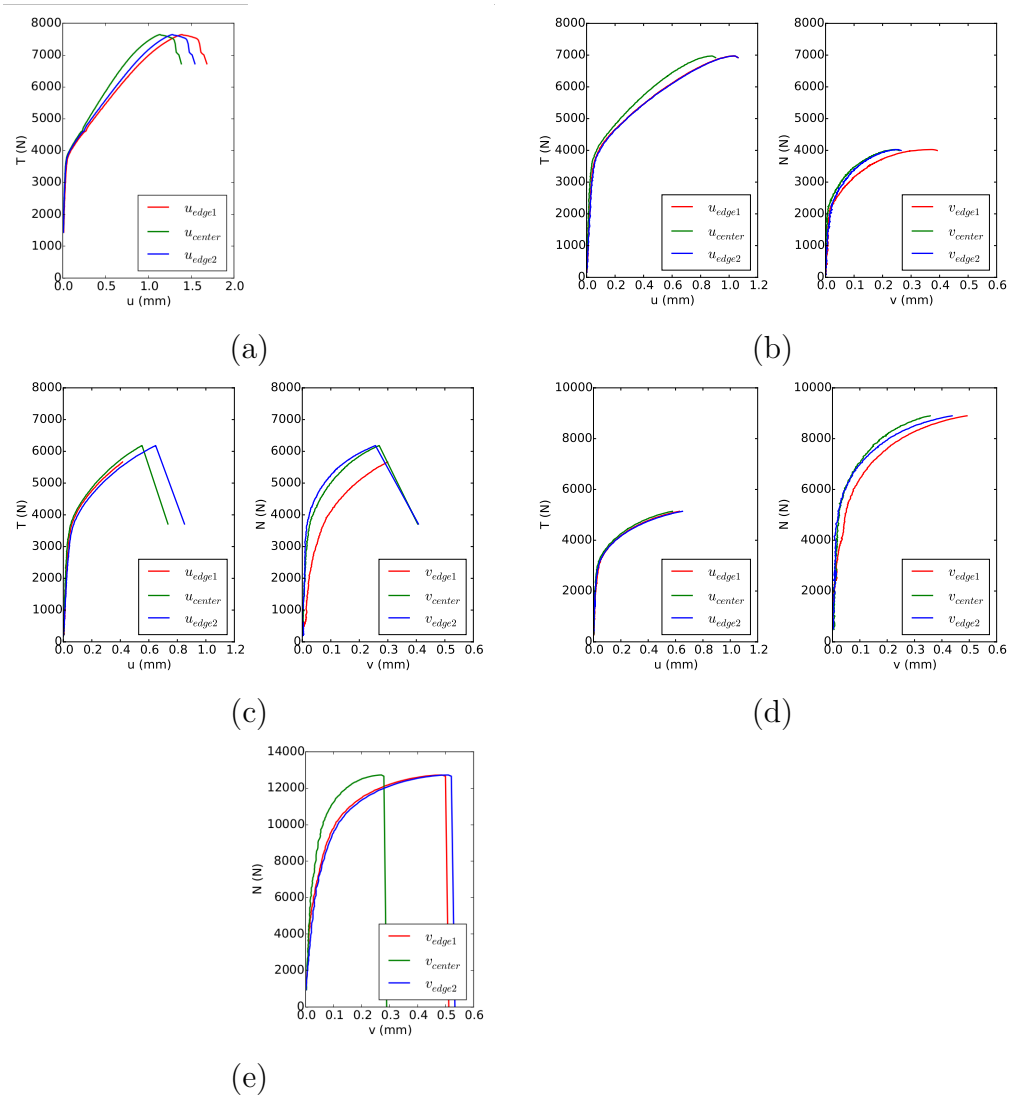

Figure 38: Force versus displacement plot resolved for experiments for different orientations (a) 0° (b) 30° (c) 45° (d) 60° (e) 90°. In each plot the normal and shear forces are N and T, resp. and their work-conjugate displacements are denoted u and v, resp.

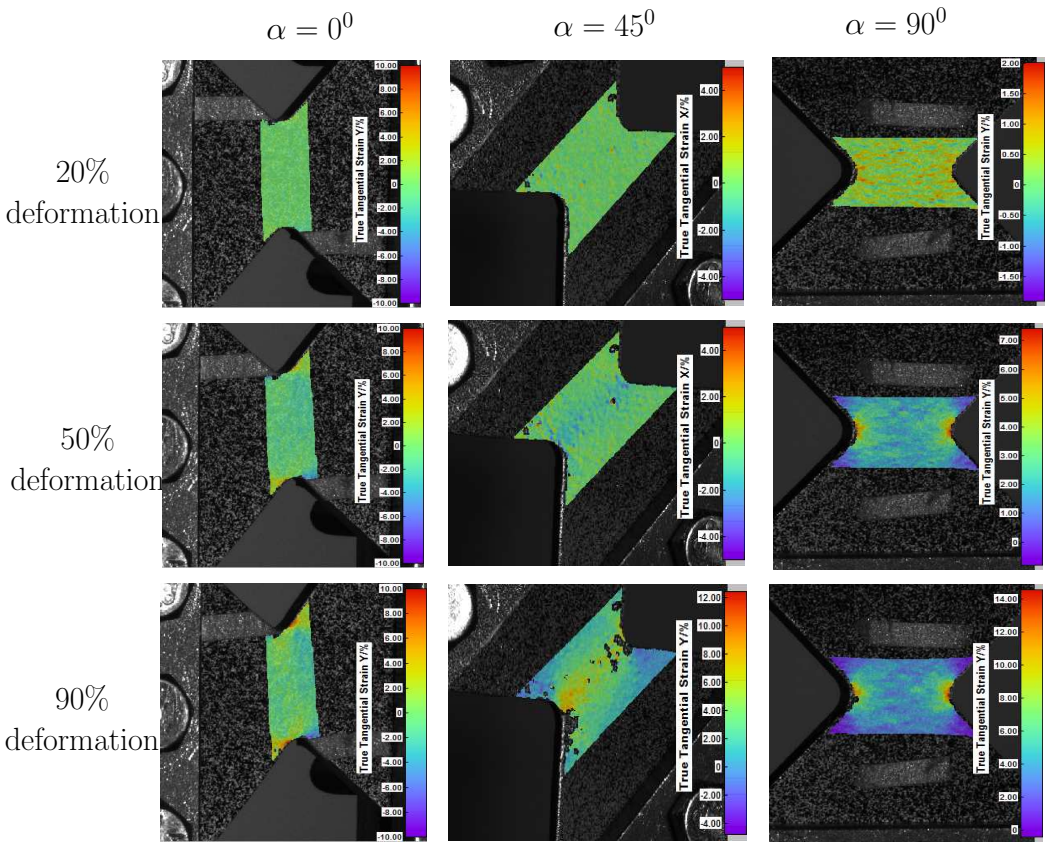

Figure 39: ϵ_{yy} strain maps in the specimens loaded under 0°, 45° and 90° at $\delta L/L_0 = 0.2, 0.5$ and 0.9.

indicates the development of these strains due to presence of large deformation. This leads to structural modifications that cannot prevent these strains from evolving.

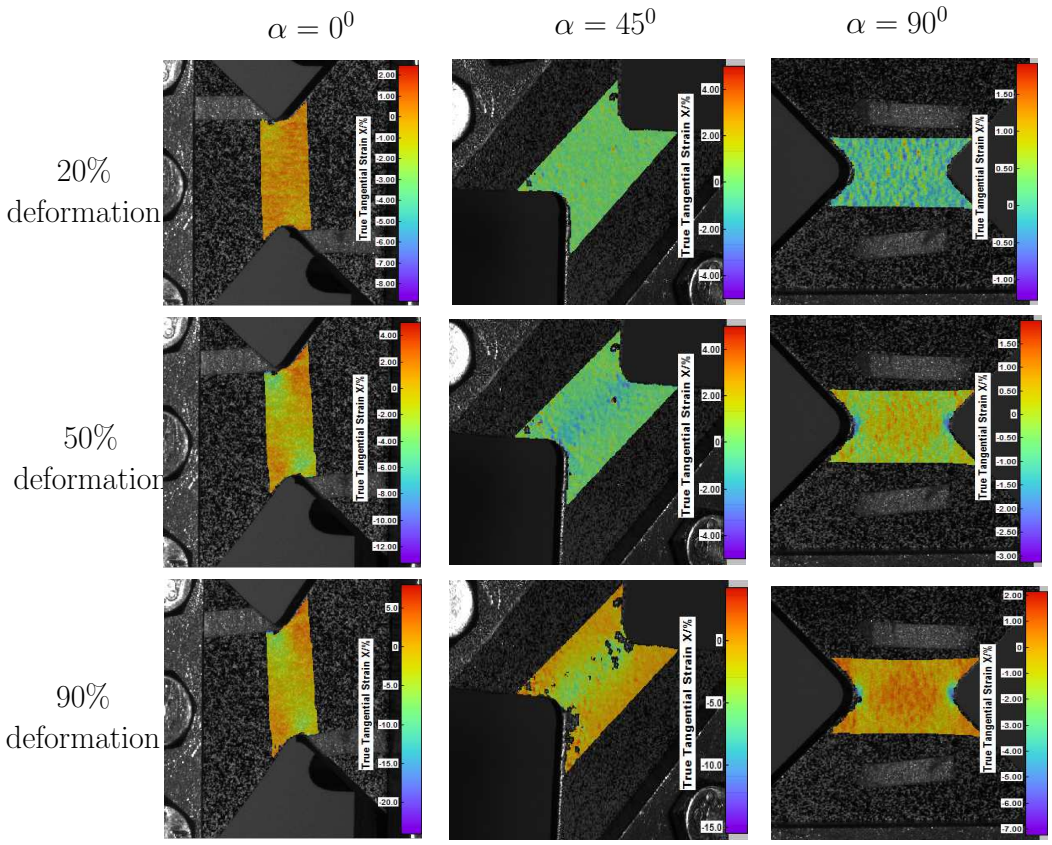

Figure 40: ϵ_{xx} strain maps in the specimens loaded under 0°, 45° and 90° at $\delta L/L_0 = 0.2, 0.5$ and 0.9.

Fig. 40 shows the evolution of ϵ_{xx} of the specimens loaded along 0°, 45° and 90° orientations. It was observed that in case of 0° loading, the deformation is quite anti-symmetric with tensile strains and compressive strains along two diagonally opposite positions above and below the notch. In case of 45° loading there is some localization of ϵ_{xx} seen in a band connecting the notch roots which intensifies with further deformation. The 90° sample shows localization in the notch root with compressive

strains early on in the deformation process.

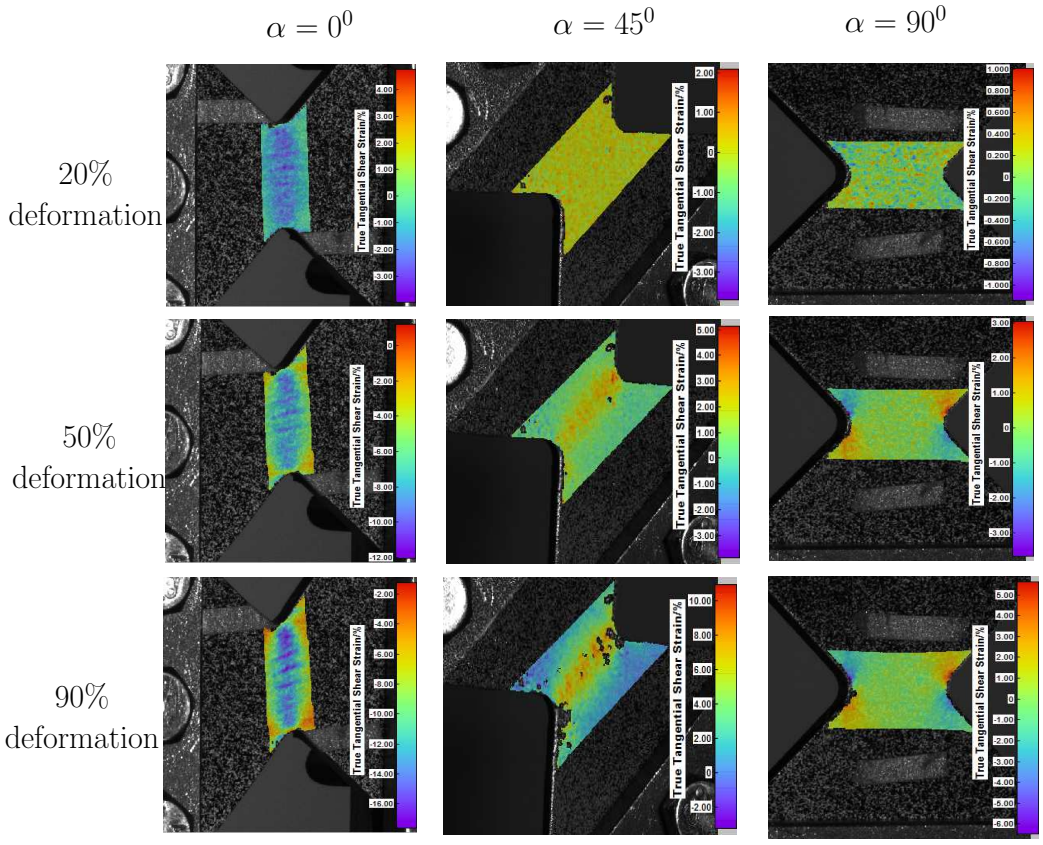

Figure 41: ϵ_{xy} strain maps in the specimens loaded under 0°, 45° and 90° at $\delta L/L_0 = 0.2, 0.5 and 0.9$.

The evolution of ϵ_{xy} is shown in Fig. 41. In the case of 0° specimen a localized band connecting the notch roots is evident at very early stages of plasticity. The band localizes further with deformation leading to much higher values of strains in the band with progressing deformation. The band has a fibrous texture with fibers running perpendicular to the major band orientation. A few perpendicular bands become more prominent with progressing deformation. The 45° samples shows a band forming in the minimum section during deformation and intensifies with further

deformation. The value of the ϵ_{xy} is considerably high in the 0° and 45° samples when compared to the other strain components. The 90° sample shows an anti-symmetric deformation pattern in this strain measure. One would expect ϵ_{xy} to be zero during the deformation under tensile dominant loadings. However, due to the presence of the notch, some shear strains are observed to develop near the notch. In fact, closer examination suggests that the shear strains are negligible away from the notch.

The 45° oriented samples show a narrow band forming along the minimum section during deformation similar to that seen in Fig. 41. However, the strain levels are lower compared to values of ϵ_{xy} indicating that the deformation in shear is an easier mode of deformation than tensile deformation, although the remote boundary conditions prescribe equal displacements in both x and y directions. Specimen oriented along 90° shows strong localization around the notch roots at moderate levels of deformation. This intensifies with deformation and leads to very high values of strains at the localized positions compared to the strain levels in the rest of the sample.

The distribution of the strain at different locations along the centerline connecting the notch roots at various stages of the deformation is shown in Fig. 42.

Fig. 42 shows the distribution of equivalent strain in samples of each orientation at different stages of the deformation. The figures indicate the distribution of strains along the minimum section remains nearly uniform except near the notch roots. This increase in the value of strain near failure indicates localization in bands leading to high values of localized strains. These plots, to some extent, confirm that failure in all samples except the 90° orientation, where the maximum location of the strain is at the notch root.

With the help of 3D DIC, strains in the thickness of the specimen could be obtained to understand qualitative trends in the z-displacements. Fig. 43 shows

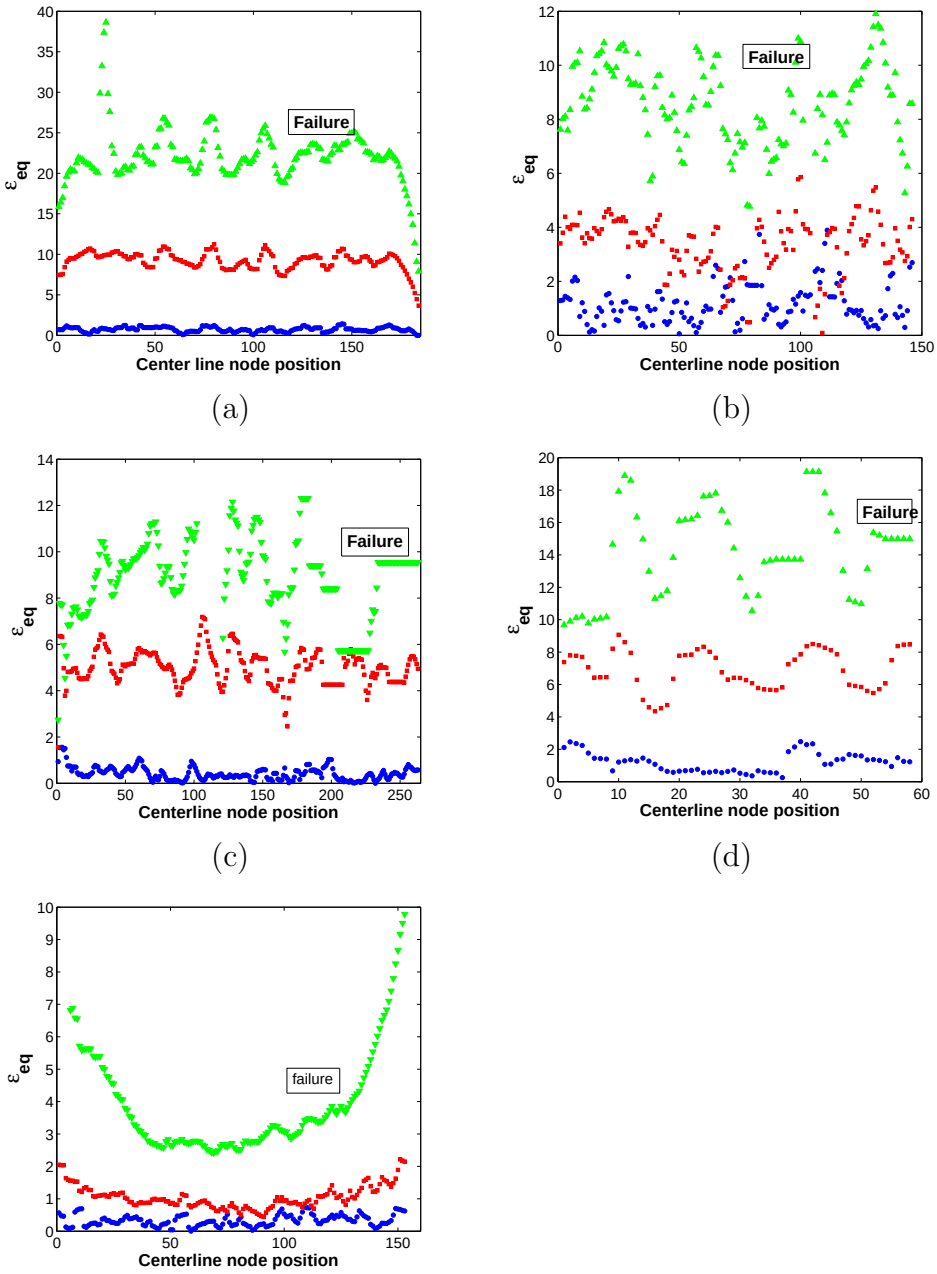

Figure 42: Equivalent strain distribution during different stages of deformation in samples with different orientations (a) 0° (b) 30° (c) 45° (d) 60° (e) 90°. The blue, red and green curve show the evolution of the strain at incipient plasticity, $\delta L/L_0 = 0.5$ and close to experimentally observed failure strain.

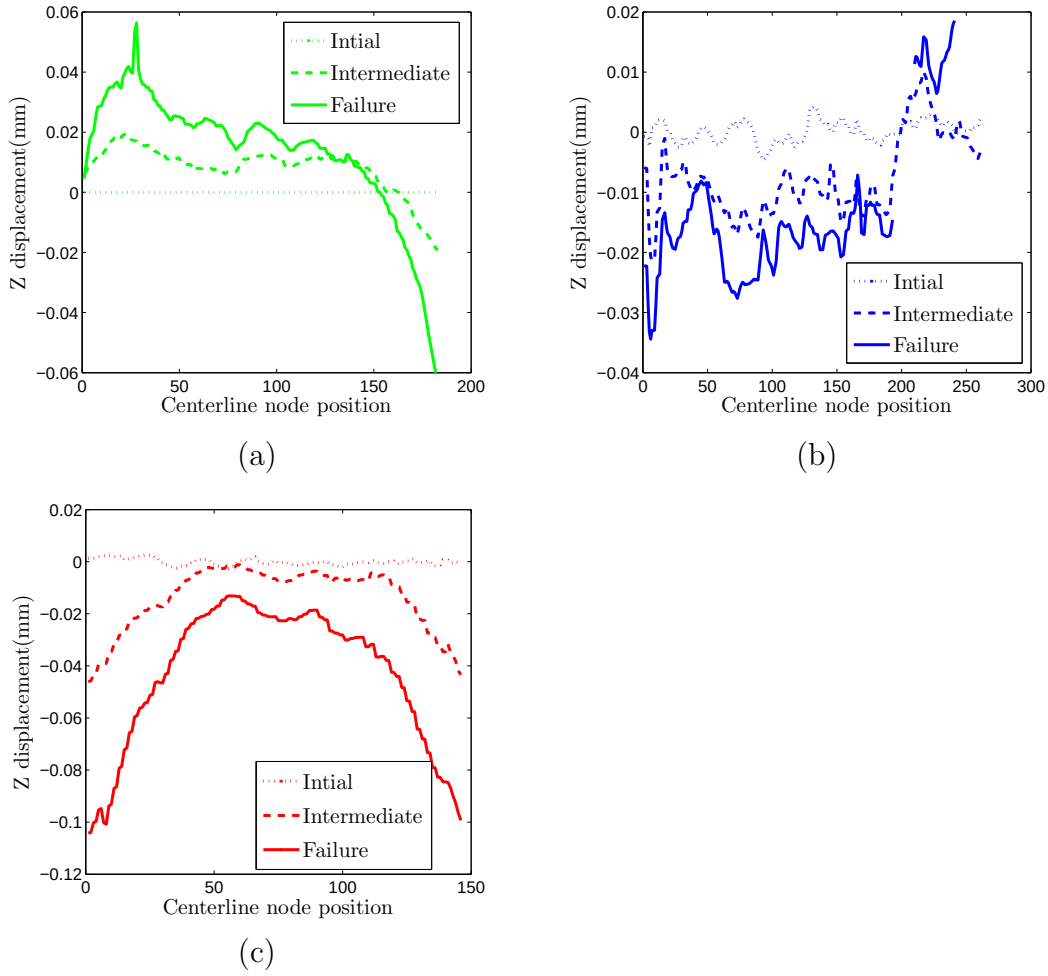

Figure 43: Z-displacement, w, in the minimum section of the sample orientation (a) 0° (b)45° (c) 90°.

the evolution of z-displacements along the line running through the notch roots for samples oriented along 0°, 45°, 90°. Similarly vertical extensometers were placed at three different locations on the sample as shown in Fig. 44.

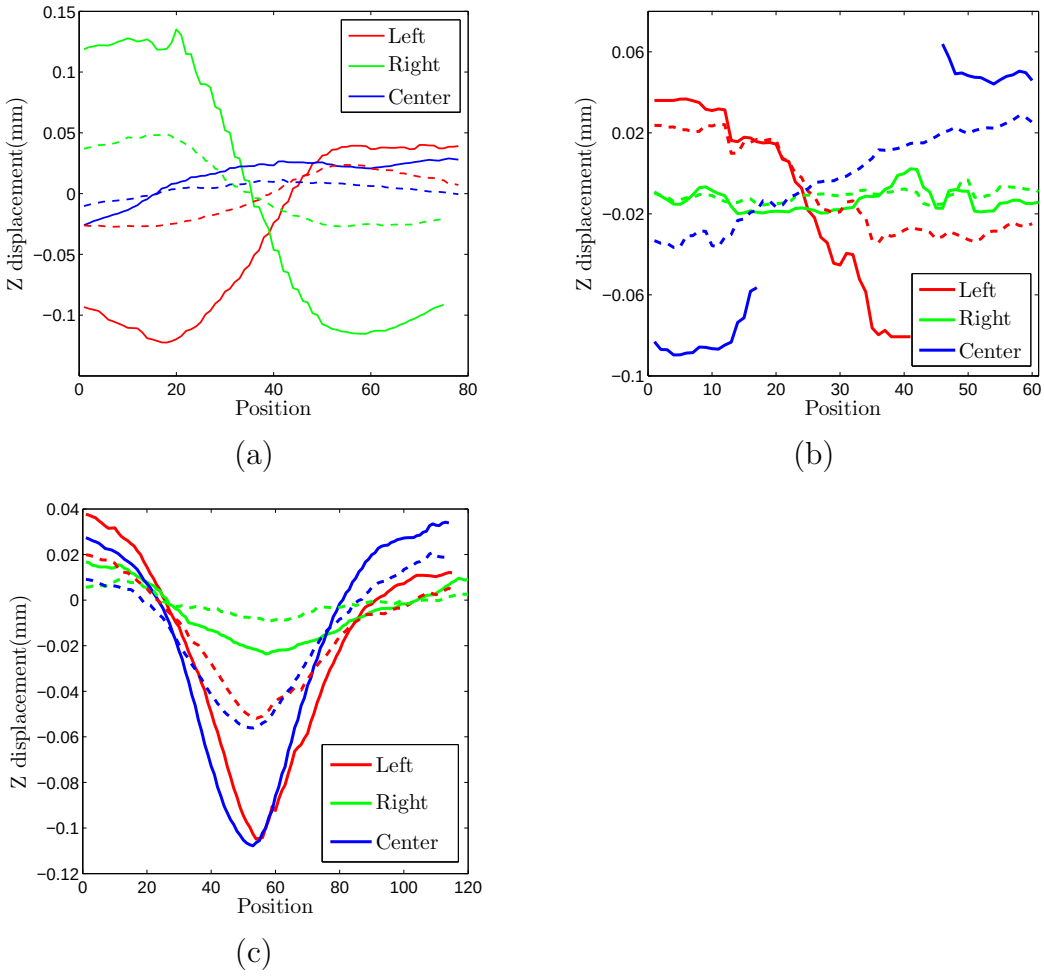

Figure 44: Z-displacement, w, along vertical lines at 3 different locations near the notch roots and at the center of the specimen(a) 0° (b)45° (c) 90°. The dashed lines indicate displacement at an intermediate level of deformation.

The presence of non symmetric values of strains at the two edges of 90° indicates twisting in the sample during deformation due to sheet material testing issues.

These twisting issues amplify further in shear dominant loading conditions. These corrections could be made to get rid of the effect of the twisting on the z-stains, by taking measure away from the plastic region. This was not accessible to us as the data was analyzed at a different location and did not have access to the test setup. However, having the DIC strain maps enabled the observation of these behaviors and the extent to which these affect sheet material testing.

Fig. 45 shows the total force normalized by the minimum section with respect to an equivalent measure of strain in the minimum section. This strain was extracted at the center, maximum location and averaged over all points along the minimum section. All the values of ϵ_{eq}^{avg}, ϵ_{eq}^{cen} & ϵ_{eq}^{max} are plotted for each loading orientation. The difference in the value of the ϵ_{eq}^{avg} and ϵ_{eq}^{cen} reduces from the tensile dominant loadings to the shear dominant loadings. This indicates that the deformation gets more uniform along the cross-section with increased shear dominant loadings. ϵ_{eq}^{max} is more or less found to exceed both the value of equivalent strain at the center and the average indicating that the maximum strain is not at center.

Fig. 46 indicates that the strain to failure increases as we change sample orientation from tensile dominant loading to shear dominant loading.

4.2.4 Fracture Initiation and Crack Path

Fig. 47 shows the mode of failure under different loading orientations. When loading a thin sheet one can get two types of shear failure: one in a plane containing the thickness as seen in case of the 90° and the other one in the plane of the sheet itself. 0° shows a step-like fracture surface which is macroscopically flat in nature. 30° and 45° as shown in Fig. 47(b)and(c) exhibit slanted cracks in-plane away from the notch root, this propagate into the sample away from the minimum section and tends to move into the grip section. The fracture surface however, shows a out-of-

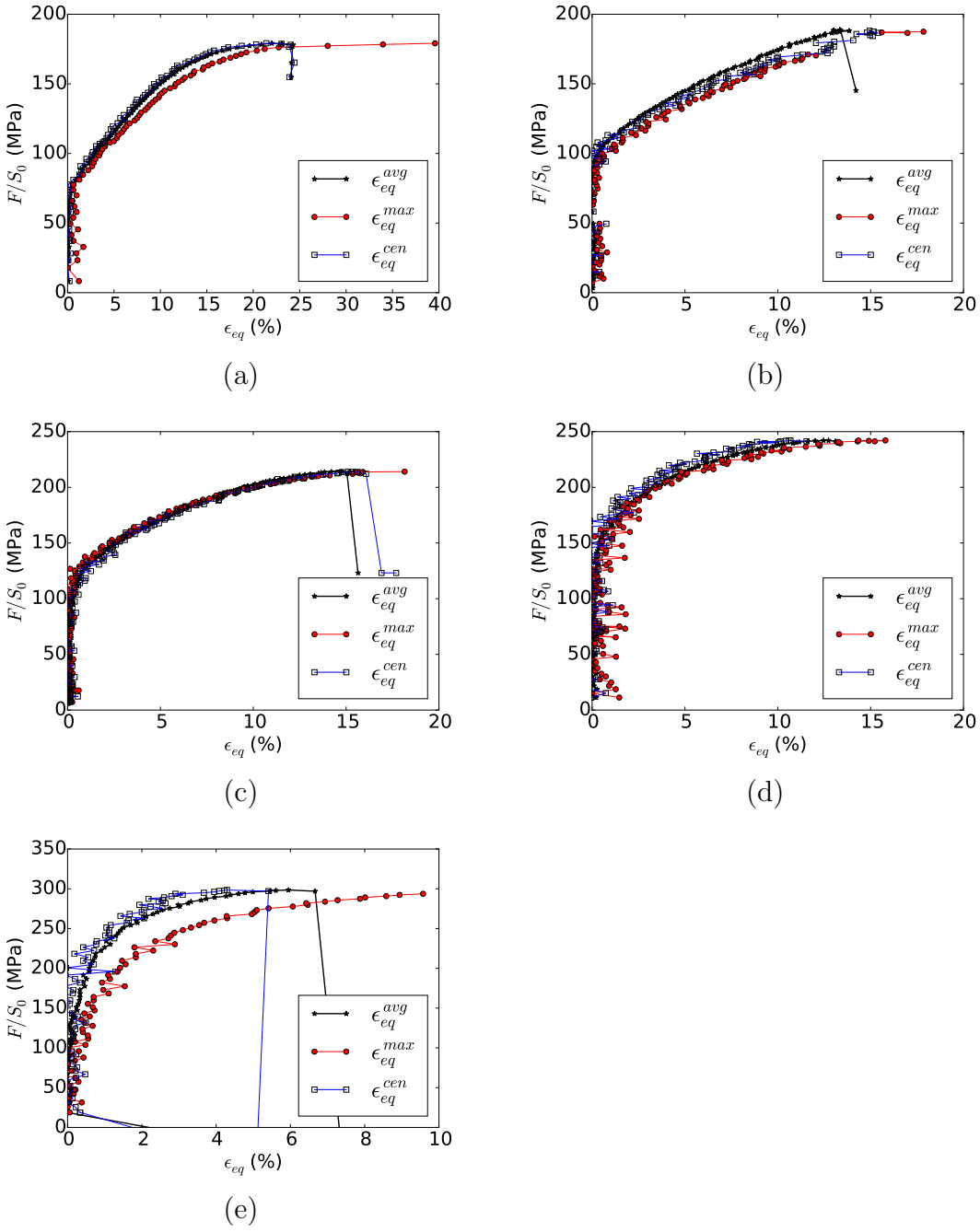

Figure 45: Force versus equivalent strain plot resolved for experiments for different orientations (a) 0° (b) 30° (c) 45° (d) 60° (e) 90°.

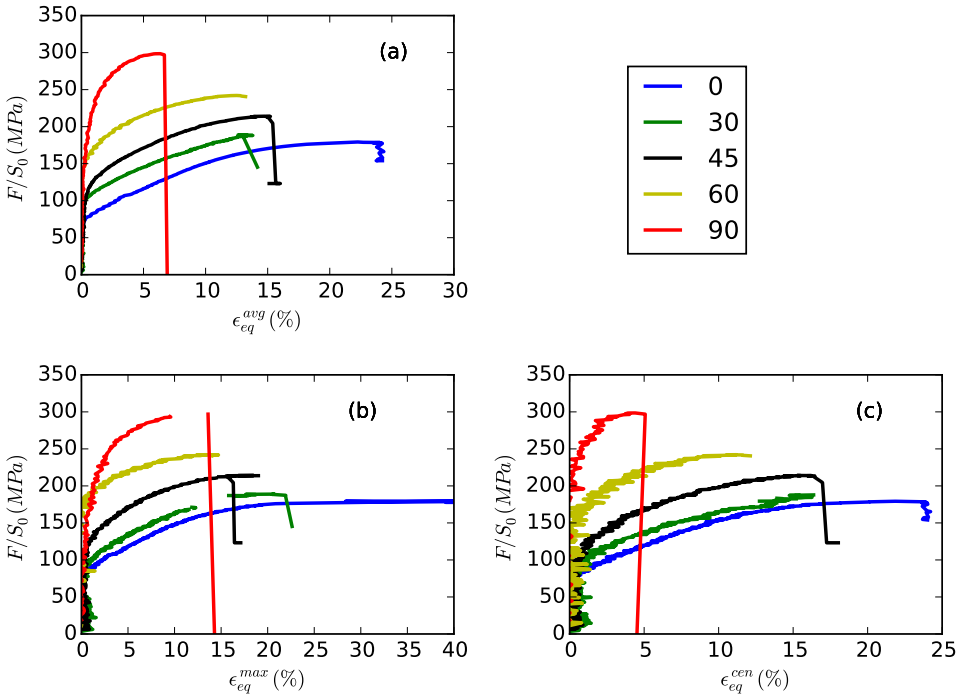

Figure 46: Force versus equivalent strain response for Arcan experiments.

plane slant which is observed in the 90° specimen. In the case of 60°, Fig. 47(d) shows the crack initiates at a location away from the notch like in the case of 30° and 45° however, soon another crack forms at symmetric position on the other notch and leads 2 slanted cracks propagating in different directions and finally joined by another in-plane slant crack making a s-shaped fracture profile. The fracture surface however, shows a out-of-plane slanted fracture in the initial 2 crack ligaments. The crack that connects these two ligaments has a flat fracture surface as exhibited by the 0° specimen. Finally, Fig. 47(e) shows a shear like fracture surface on the 90° oriented sample with a flat crack along the minimum section.

To understand crack initiation and crack path, Fig. 48 shows the strain localization in the sample when loaded along different orientations. Except for the 90°

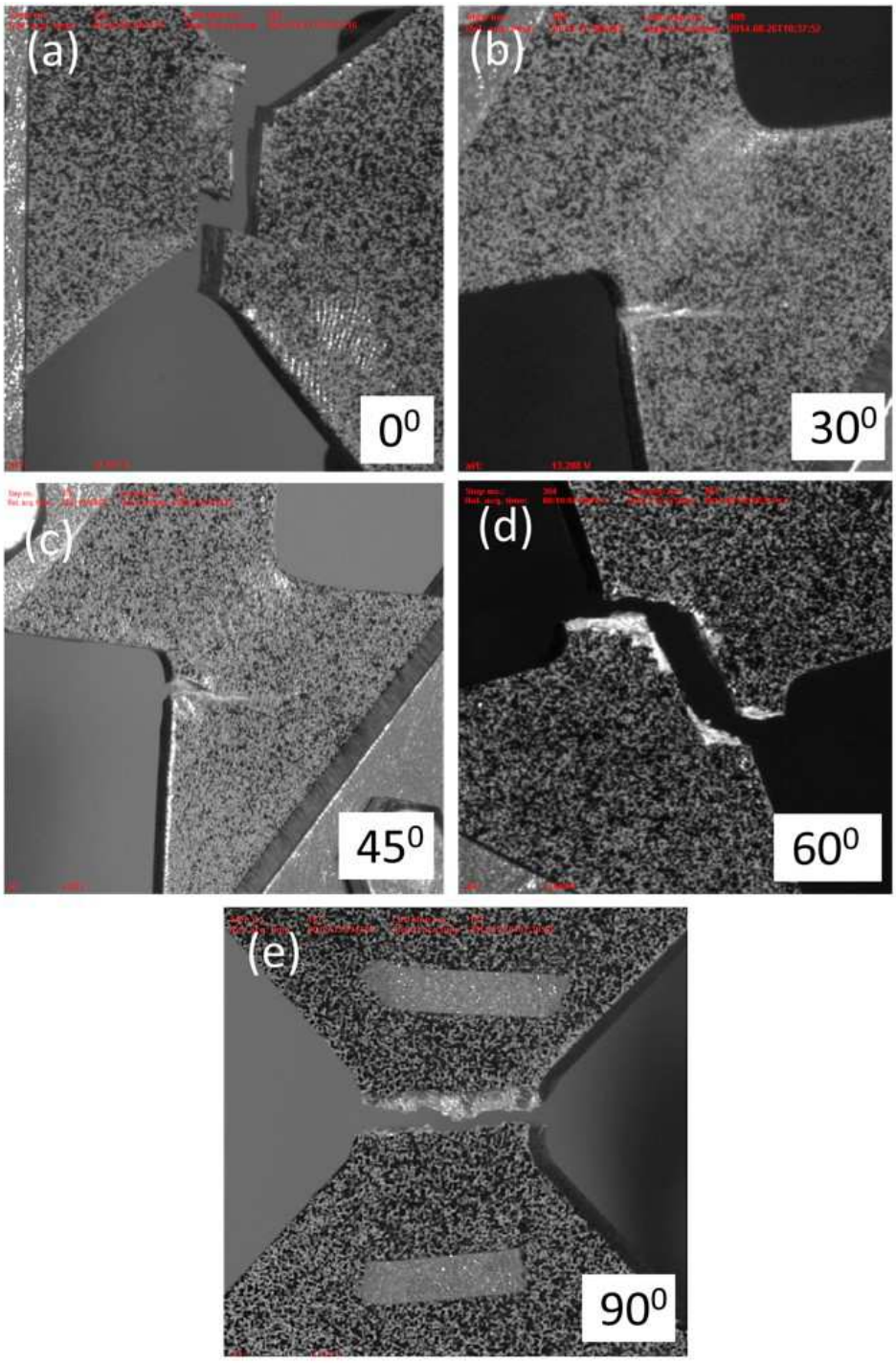

Figure 47: Failure mode in samples tested under various orientation of loading. In all cases the loading direction is vertical.

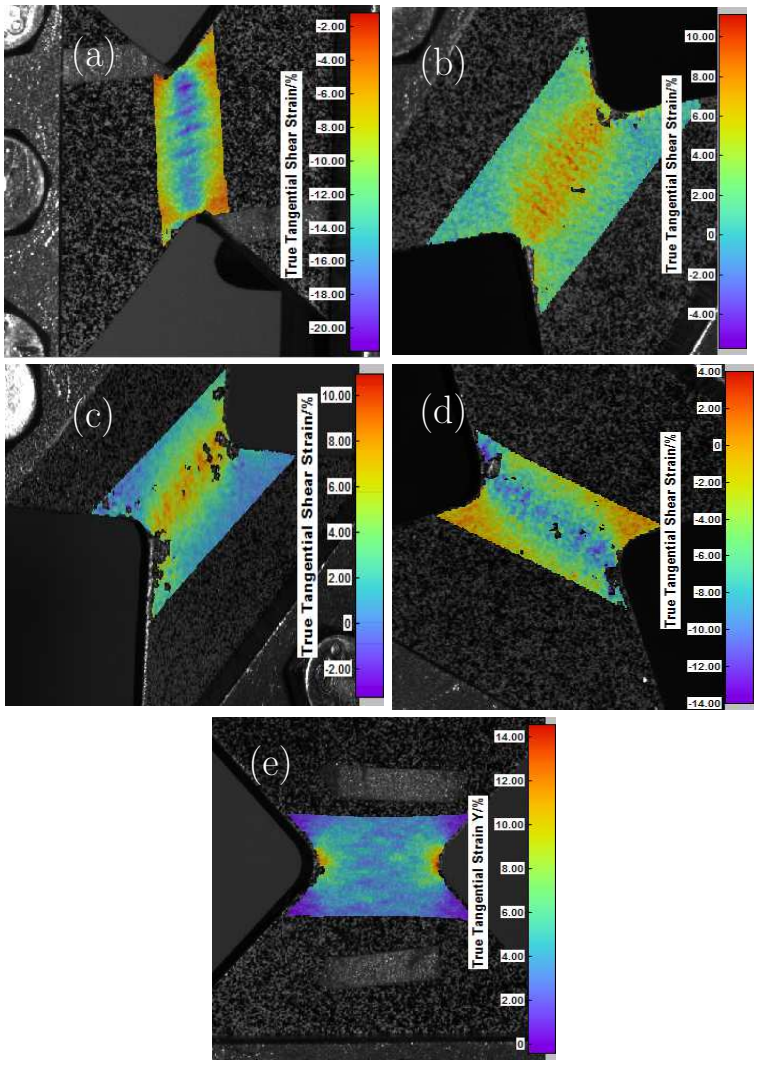

Figure 48: Strain localization in the gage section of representative specimens of (a) 0°, (b) 30° (c) 45° (d) 60° & (e) 90°

loading all other conditions exhibit a localized band during the process of loading. All the bands exhibit a characteristic fibrous nature with secondary localization bands running perpendicular to the primary localized band. Greater the amount of shear, stronger the localization. This fibrous behavior in the localization bands is even seen at early stages of plastic deformation in the material. The 90° orientation exhibits a localization at the notch region. No fibrous localization is observed indicating that presence of shear loading leads to this kind of behavior in the microstructure which indicates the role of anisotropy in activating some deformation mechanisms along these directions and get stronger with increasing values of shear. The major deformation during loading along the basal plane is attributed to easy basal glide. However, due to presence of compressive stresses in the basal plane, activation of extension twinning $\{10\bar{1}2\}$ occurs. This is considerably easy to active and is expected in the early stages of deformation. Due to the activation of these twins in the shear band region, the material possesses two texture components, corresponding to the parent and twinned volumes. This reoriented material is now susceptible to even stronger basal glide leading to formation of those strong secondary bands. Strong deformation in these bands lead to localization of deformation in these bands leading to incompatibility of deformation and thus failure. This phenomenon is only observed in the presence of shear component in the loading. Similar observations are made during the process of ECAE where the material undergoes large shear deformations leading to formations of localized bands[**dogan15**].

Fig. 49 shows the progression of damage in a shear loading condition. Fig. 49(a) shows the formation of localized strains in a narrow band in the minimum section of the sample. The fibrous bands which are smaller than the main band branch perpendicular to the rolling direction and a few of them are more prominent. One of these bands propagates to form a crack perpendicular to the loading as seen in Fig.

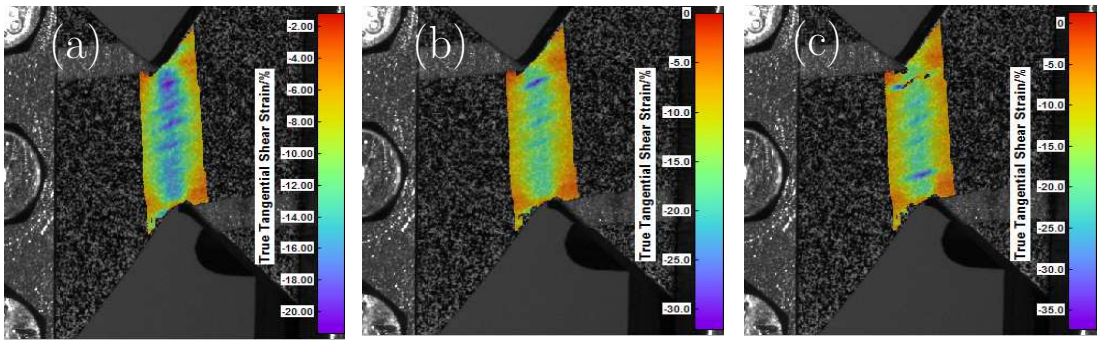

Figure 49: Strain localization in bands perpendicular to the loading direction in a zero degree test. With progression in strain one of these bands propagate to form a crack. Further a second crack is formed at another location. These cracks join up through a crack along the loading direction.

49(b) and very high strains are measured along that band. The length of the crack propagated is similar to the initial length of the fibrous band. Another band starts propagating at another location nearer to the other notch and finally these cracks are connected through a major crack developing along the localized band connecting the notch roots. This leads to a step-like fracture surface as seen in Fig. 47(a).

4.2.5 Failure Loci

Failure loci is an engineers way of representing a measure of failure strain with respect to the stress state. There could be various possible definitions of this plot. As none of these measures are intrinsic to the material, the commonly referred measures are shown here with the orientation of the sample. The value of the failure strains at maximum, average and at the center of the specimen were plotted with respect to the orientation of each specimen during loading as shown in Fig. 50. The figure indicates that all measures of strain to failure show a decreasing trend as the shear component of the deformation reduces. The case of 45 degree shows more or less uniform distribution of the strain along the cross section as the value of the maximum,

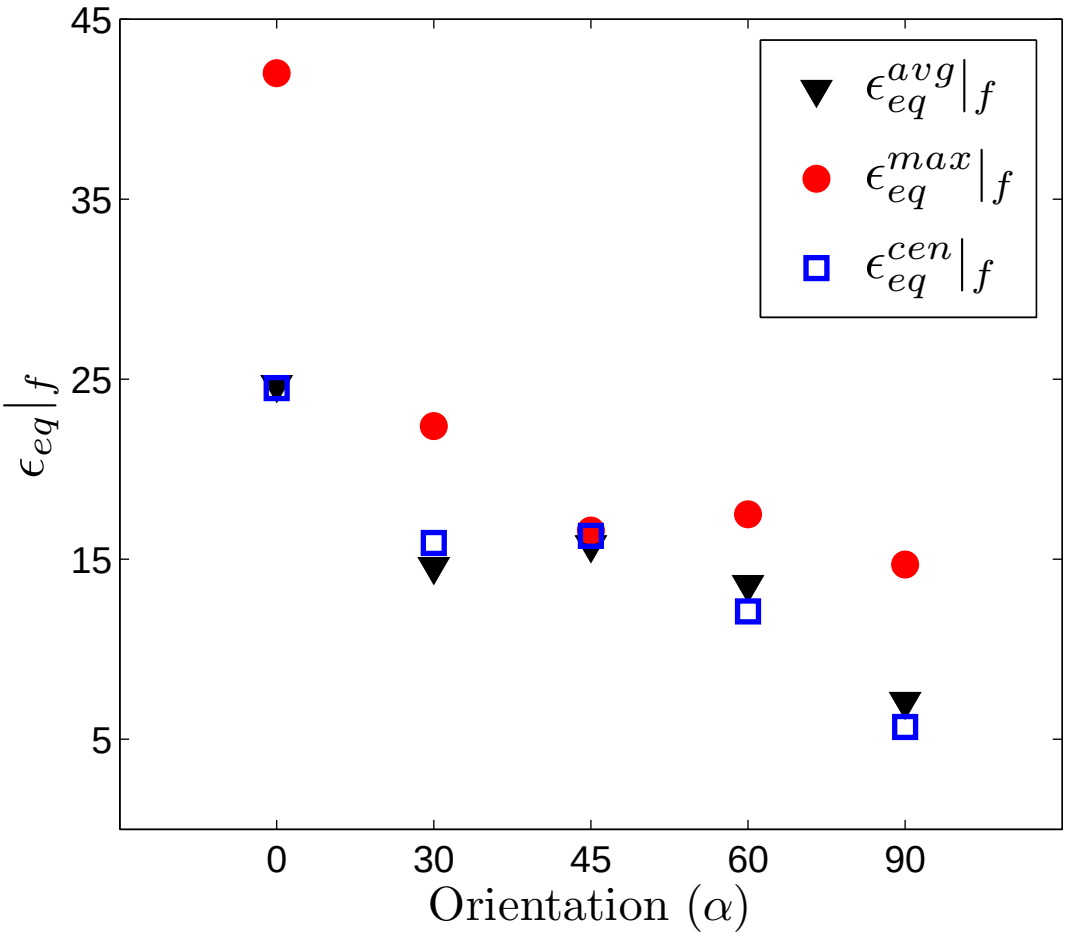

Figure 50: Failure strain with respect to orientation of the sample at maximum, center and averaged over the cross-section.

average and center strains coincide. The value of the strain at the center is in close agreement to the value of the average strain along the cross section.

4.3 Analysis

4.3.1 Identification of Material Plastic Behavior

The plastic part of the tensile curve shown in Fig.33 along rolling direction prior necking was used to obtain the hardening behavior. It is a common practice to fit the hardening curve using a power law. However, the hardening response was not captured well using a power law. Hence, a tabulated true stress true strain response upto large strains was determined.

Anisotropy was introduced using Hill anisotropic potential. The values were determined by experimental investigation through characterizing the anisotropy of the matrix. The anisotropy in plane of the sheet was calibrated using the stress ratios obtained from experiments shown in Fig. 33. The yield stress in any direction was normalised by the yield stress in the rolling direction as shown in table 1.

	Plastic Strains	σ_{11}	σ_{22}	σ_{12}	σ_{33}	σ_{23}	σ_{13}
Yield Stress	0%	67	90	82	n/a	n/a	n/a
Stress Ratio		0.74	1.00	0.91			
Yield Stress	2.5%	184	215	188	n/a	n/a	n/a
Stress Ratio		0.85	1.00	0.87			
Yield Stress	5%	214	240	216	n/a	n/a	n/a
Stress Ratio		0.86	1.00	0.88	1.32	0.92	0.97

Table 1: Yield stress and stress ratios at different values of plastic strain used for characterizing the anisotropy of the material.

These yield stress ratios were used to check how well the anisotropy was captured using a simple hill's anisotropic potential. Single element calculations were carried out in rolling, transverse and the intermediate off-axis directions using the hardening fit obtained and the yield stress ratios from the experiments. Yield stress ratios obtained at onset of plasticity, 2.5%, and 5% plastic strain were used to calibrate the material model. It was found that the yield stress ratios obtained at 5% plastic strain led to good fit with experimental plots.

It is clear that the above representation of anisotropic plasticity is approximate at best for at least two reasons. Firstly, the 3D anisotropy of Mg is quite complex, as for example examined experimentally by Kondori[117]. For sheet metal, it is difficult to conduct experiments through the thickness. Therefore, the only data used was in plane tension data. Secondly, the hardening law used will not be able to represent S-shaped hardening curves when extension twinning is active (for example when compression stresses perpendicular to the c-axis (or sheet normal) arise. This will be discussed further below.

4.3.2 Numerical Procedure

Arcan specimens were modeled using Abaqus model[1] with C3D8R (Eight-node linear brick element with reduced integration) elements as shown in Fig. 52. The specimen is only modeled till the center of the loading pins as shown in Fig. 35 (b) to be as close as possible to the applied boundary conditions. The top loading ends are not included for simplicity. The mesh was gradually refined near the minimum section of the specimen. There are a total of $\tilde{4}000$ elements in plane with 10 element along the thickness direction. Displacement boundary conditions were applied at the top and the bottom surfaces of the specimen to mimic the experiments. The

[1]Version 6.12, Simulia, Inc. and Dassault Systèmes

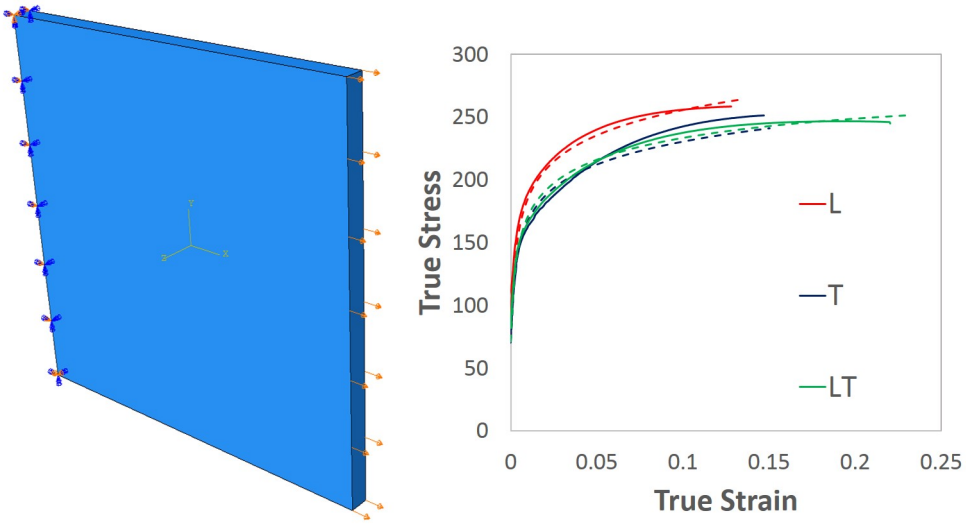

Figure 51: Near plane stress single element calculation representative of sheet specimen

bottom surface was fixed along the x and y directions and rotation about the z axis was restricted, however, contraction along z-axis was allowed. Rigid body rotation was avoided by encastring one node on the bottom surface. Displacement boundary condition was applied on the top surface depending on the loading orientation. For conditions with combined tension and shear the displacements were provided in the same ratio as that reported in the experiments.

4.3.3 Global Response

The force displacement response showing comparison between experiments and the model are shown in Fig. 53 for 0°, 30°, 45°, 60° and 90° orientations. The macroscopic force-displacement response was obtained the same way as that obtained from the experiments. The normal force, N, was obtained by obtaining the sum of resultant force along the y-direction with respect to the y-displacement, v. Similarly, resultant force along x-direction, T, was plotted with respect to the x-displacement, u. The result is compared to the data at the center and near the edge.

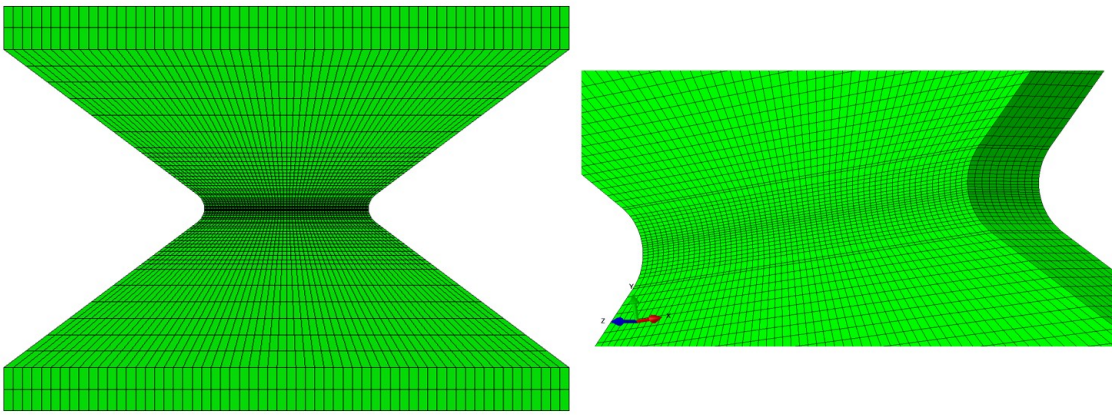

Figure 52: 3D FEM mesh of Arcan specimens modeled using Abaqus with C3D8R elements.

The model used based on planar anisotropy did not provide a good fit (not shown here) for the tension data calibrated using tensile tests on AZ31 TRC sheets. Planar anisotropy here refers to the material response being anisotrpoic only along the plane of the sheet, as this was the data available from experiments on sheet material, since, it was difficult to perform out of plane tests on sheets. On further investigation, it was found the out of plane anisotropy was the reason for this discrepancy. Fig. 54 shows the z-strain using a planar isotropy assumption. We observe that considerable necking is seen which is not observed in the experiments. AZ31 posesses a strong the basal texture with the c-axis of the crystals oriented normal to the sheet plane. Hence, it is difficult for this material to contract along the c-axis. Since the out-of-plane stress ratios of the sheet were inaccessible from the experiments performed, we obtained them from the anisotropy ratios provided in [117] which correspond to plate materials (bulk AZ31). The anisotropy ratios are reported in table 1. The anisotropy ratios have been seen to vary a lot with strain and hence the values were obtained at later stages when the values saturate. These are explained in detail in chapter 2 and [117]. Fig. 54 shows the resultant ϵ_{zz} using the 3D anisotropy and we see lesser

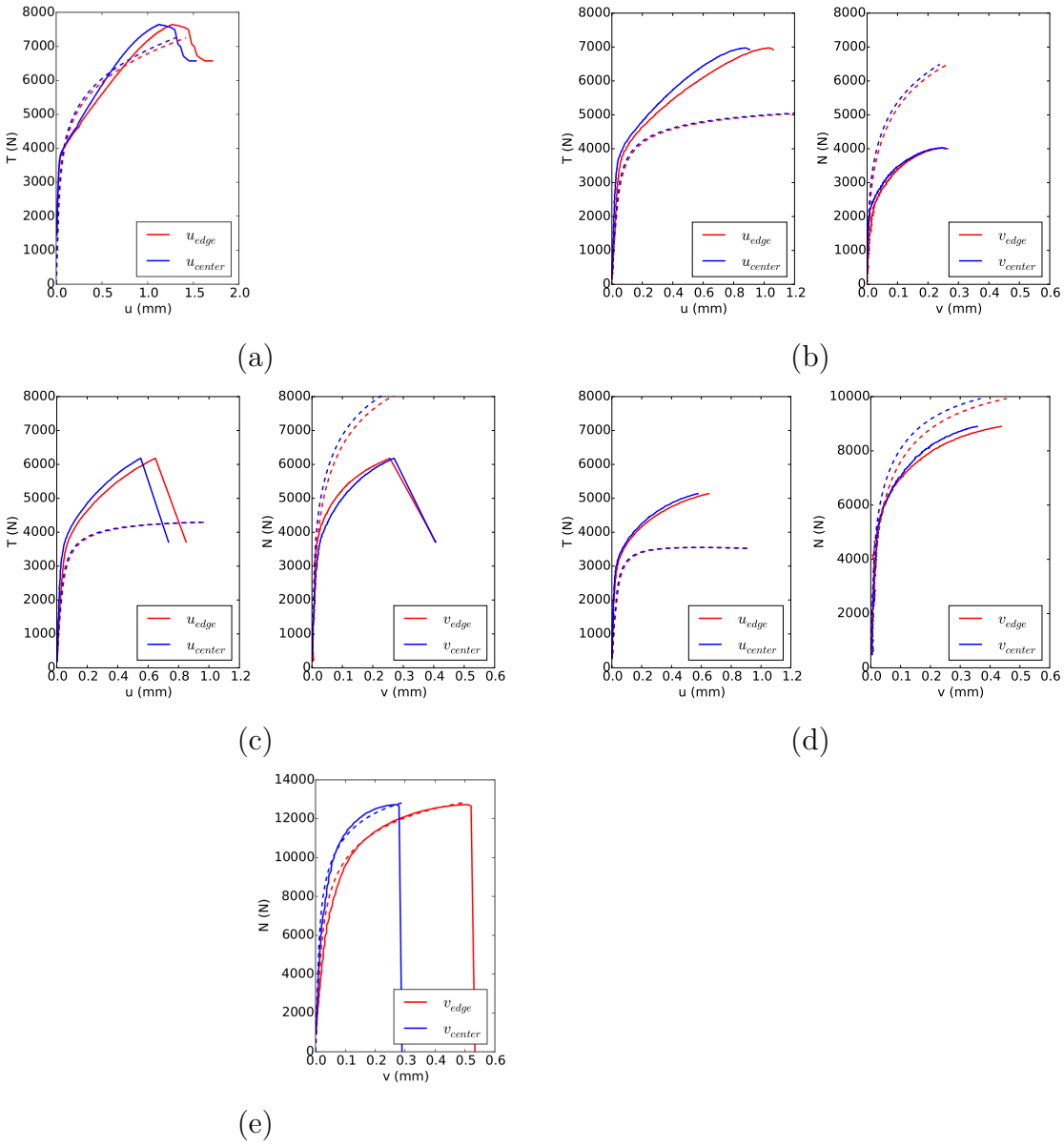

Figure 53: Force versus displacement plot from analysis superimposed on experiments for different orientations (a) 0° (b) 30° (c) 45° (d) 60° (e) 90°. The solid lines are experimental results shown above. The dashed lines shows numerical analysis results. These simulations were interrupted at load drop corresponding t0 the experiments.

necking in the material which is consistent with the experimental observations.

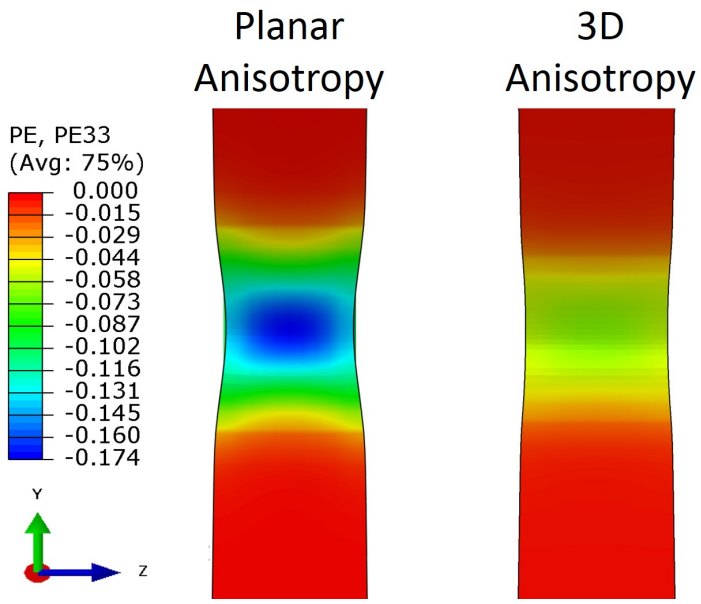

Figure 54: ϵ_{zz} strain maps in the specimens loaded under 90° comparing the planar anisotropic response to the calculation using 3D anisotropic.

It is observed that the model is capable of capturing the macro-response along 90°. Since the model did not have a damage indicator, the calculations were stopped when the displacement, v, at the center of the specimen matched the final experimental value. 0° showed close match in the load levels, however, the hardening response does not match with that observed in the experiments. This could be because of two reasons; firstly the incapability of the model to capture the anisotropy or secondly because of change in the angle α during the loading. Although an off-axis orientation was considered in identifying the plastic anisotropy, the latter exhibited similar hardening behavior to L and T directions. In the shear experiments one could imagine the activation of extension twinning (as a result of compression stresses normal to the

c-axis), either because of notch effects or because of microstructural heteroheneities. In fact the global force displacement curve in Fig.53 shows a small inflection point which is reminiscent of S-shaped curves when Mg is loaded along certain orientations. The other directions show poorer fit to the experimental data. 60° shows the closest fit while 30° shows the poorest fit, indicating that closer the model is to tension, the better the fit is. Inspite of this imperfect fit to the experimental data all at once (which is not surprising given the simplicity of the plasticity model used) we will use these calculations to extract key stress state indicators, which we believe are less sensitive to anisotropy, namely the stress triaxiality and Lode parameter. Further improvements to this approach will require a much more sophisticated plasticity model, such as crystal plasticity [118] or a multisurface model[119].

4.3.4 Strain and Stress Maps

Fig. 55 shows the contours of the component of plastic strain in the Y-direction (ϵ_{yy}) at various levels of deformation ($\delta L/L_0 = 0.2, 0.5$ and 0.9). and for different loading orientations *viz.* 0° 45° and 90°. Plastic strain ϵ_{yy} indicate similar trends in all specimen orientations, plotted at various deformation levels, as shown in Fig. 55. For shear dominated loading, anti-symmetric tensile-compressive regions with lower magnitudes are seen, gradually developing into a single band of tensile strain towards the end of deformation. For mixed-mode loading, a similar pattern in the shape and magnitude of the tensile-compressive ϵ_{yy} regions and the subsequent tensile band is observed, with a slight shift corresponding to introduction of tensile component in the applied loading at the boundary.

Fig. 56 shows the contours of the component of plastic strain in the X-direction (ϵ_{xx}) at various levels of deformation *20%, 50%, and 90%* and for different loading orientations *viz.* 0° 45° and 90°. The leftmost column shows the evolution of plastic

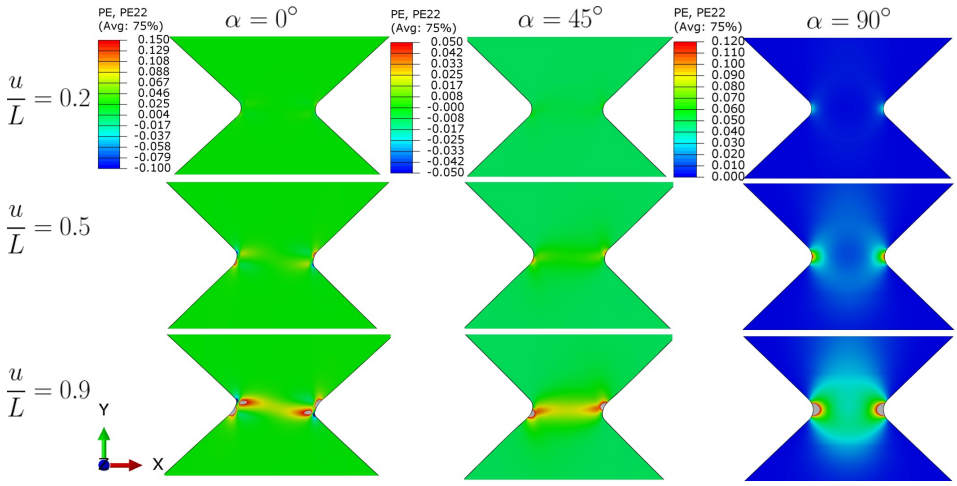

Figure 55: ϵ_{yy} strain maps in the specimens loaded under 0°, 45° and 90° at $\delta L/L_0 = 0.2, 0.5$ and 0.9.

strain ϵ_{xx} when the applied loading is shear dominated. At a lower level of deformation ($\delta L/L_0 = 0.2$), as seen in the top left figure, tensile and compressive strains start to develop in an anti-symmetric manner, above and below the notches. With increasing load, at higher deformation level ($\delta L/L_0 = 0.5$), these tensile-compressive regions grow in size and magnitude and when the deformation reaches $\delta L/L_0 = 0.9$ of its total magnitude, the tensile strains are suppressed whereas compressive strain dominate to form a localized band. This band is due to the loss of notch integrity resulting from geometry changes.

With the introduction of a tensile component in the applied loading, as seen in the 45° case, formation of the aforementioned compressive band occurs at a relatively lower level of deformation. Subsequent increase in applied loading and overall deformation leads to a further widening of this region of compressive strains and is followed by initiation another region of higher compression with higher strain magnitude but smaller size at the notches. When $\alpha = 90^\circ$, the applied loading is purely tensile and the evolution of the corresponding plastic strain ϵ_{xx} is shown in the right-

most set of figures. Here, tensile ϵ_{xx} strain is distributed throughout the specimen whereas compressive strains begin to appear at the notches. Unlike the dominant strain band seen in shear dominated and mixed loading cases, regions of compressive strain in the purely tensile case start evolving from the notches and increase in size and magnitude, indicating a localization of contraction at the notch root.

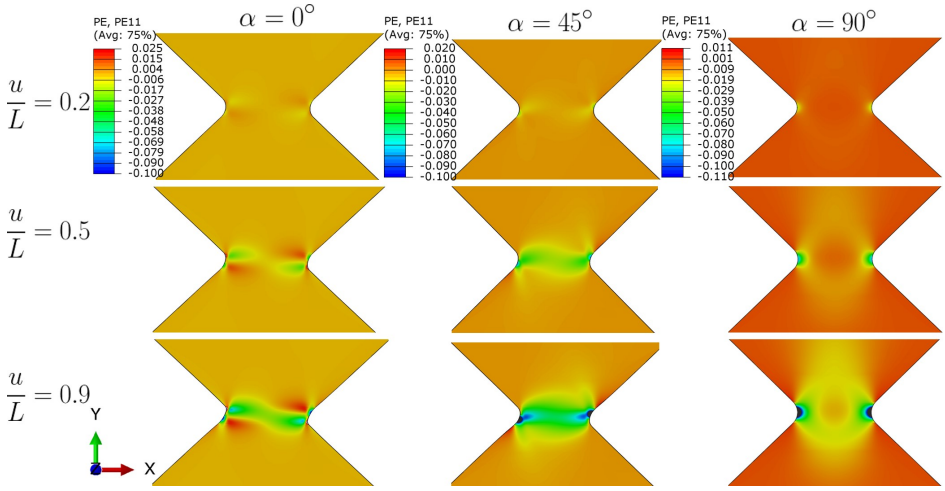

Figure 56: ϵ_{xx} strain maps in the specimens loaded under 0°, 45° and 90° at $\delta L/L_0 = 0.2, 0.5$ and 0.9.

Fig. 57 shows the contours of the component of shear strain in the XY-direction (ϵ_{xy}) at various levels of deformation ($\delta L/L_0 = 0.2, 0.5$ and 0.9.) and for different loading orientations *viz.* 0° 45° and 90°. As the shear component of the deformation increases, the formation of a localized band occurs in very early stages of deformation. With increased level of deformation in the 0° specimen, the band widens and grows in magnitude. In the later stages of the deformation a narrow localized band forms along the minimum section of the specimen, with the maximum values occurring slightly away from either notches. These maximum regions do not lie on a straight

line due to loss of the notch integrity. In case of the 45° specimen, the band forms at an angle to the line connecting the notch roots. Further deformation leads to formation of maximum values developing above and below the notch root which are connected by a narrow band of slightly lower magnitude. Shear strains are not seen to evolve till very later stages of deformation in the 90° specimen. In the later stages of deformation anti-symmetric strains develop in a small region above and below the notch.

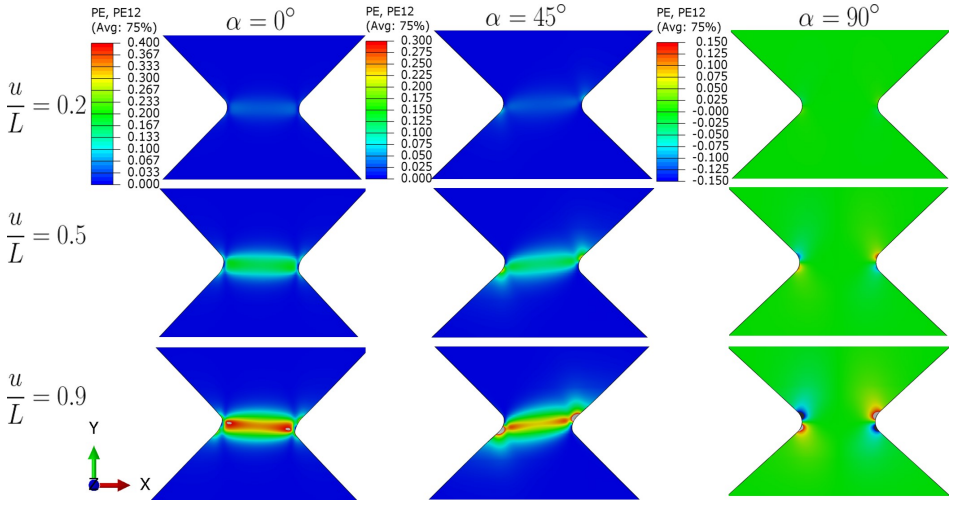

Figure 57: ϵ_{xy} strain maps in the specimens loaded under 0°, 45° and 90° at $\delta L/L_0 = 0.2, 0.5$ and 0.9.

Fig. 58 shows the z contraction and the magnitude of the strains along the z-direction for for different loading orientations *viz.* 0° 45° and 90°. We observed that the z-contraction was minimum for the 0° specimen and maximum for the 45° specimen. There is a positive and a negative band seen in the 0° specimen which is not symmetric. This is because there is very little z-strain observed during the initial stages of the deformation. Later due to structural effects loss of notch equity, the

formation of necked regions are observed in the specimens which are not symmetric about the center. The tensile specimen exhibits the strain distributed around the notch area while the 45° specimen shows a narrower localized band of z-stain forming at the notch root.

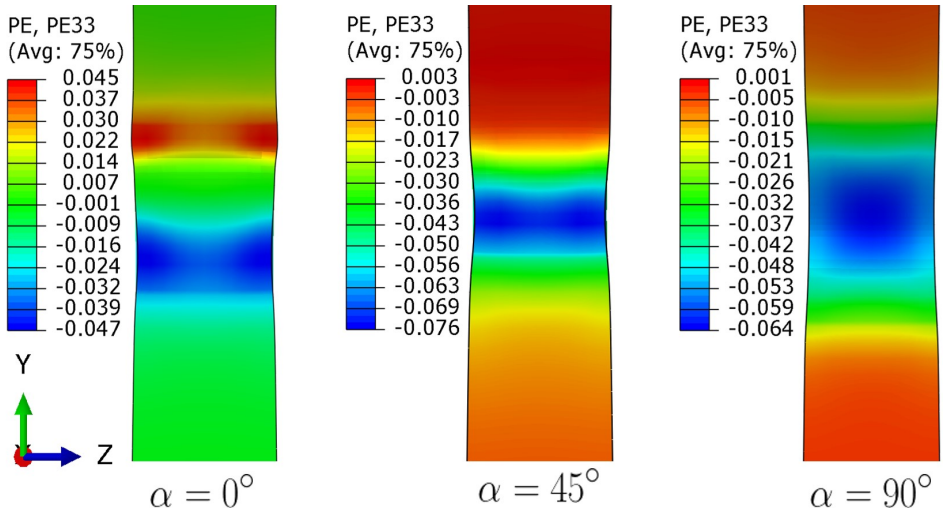

Figure 58: ϵ_{zz} strain maps in the specimens loaded under 0°, 45° and 90°.

In addition to the evolution of the components of strain across the specimen, evolution of stresses in the specimen is available from the FEM calculations that were not possible to extract from the experimental campaign. This sheds light on how stresses developed and how the loading orientation affected each component of the stress tensor. This also elucidates how the localization occurred in the specimen and how this could have impacted the failure mode and the initiation location of the crack. The absolute values of stresses are questionable for specimens other than 0 and 90 due to misfit exhibited in the load displacement response as seen in Fig.53.

Similar observations are made in case of evolution of the longitudinal stresses (σ_{yy}) in the specimen as shown in Fig. 59 close to fracture strains. As seen in case of σ_{xx}

the stresses are more or less anti-symmetric above and below the notch root for the case of 0° specimen and with increase in orientation angle α, the tensile dominance of the stresses increase. As opposed to the case of σ_{xx} evolution, the stresses σ_{yy} are seen to localize at an angle to the minimum section and the magnitude and width of this localization increases with increase in α.

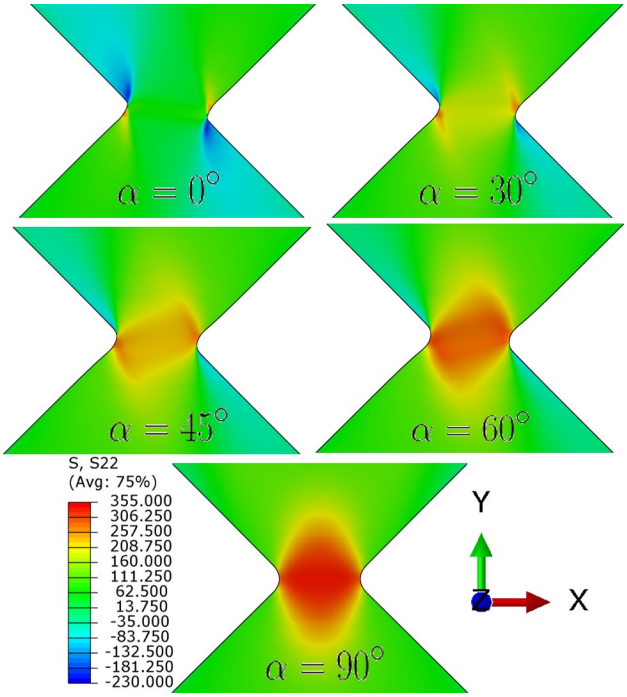

Figure 59: σ_{yy} strain maps in the specimens loaded under 0°, 30°, 45°, 60° and 90° orientations.

Fig. 60 shows the evolution of σ_{xx} in all specimen orientations close to fracture. It is observed that as the stress state changes from shear dominated to tensile dominated, the anti-symmetric distribution of the stresses as seen in 0° specimen is lost and the tensile stresses dominate in a band above and below the notch region parallel to the minimum section. These lines connect the edges in case of 90°, which shows

the greatest magnitude of lateral stress.

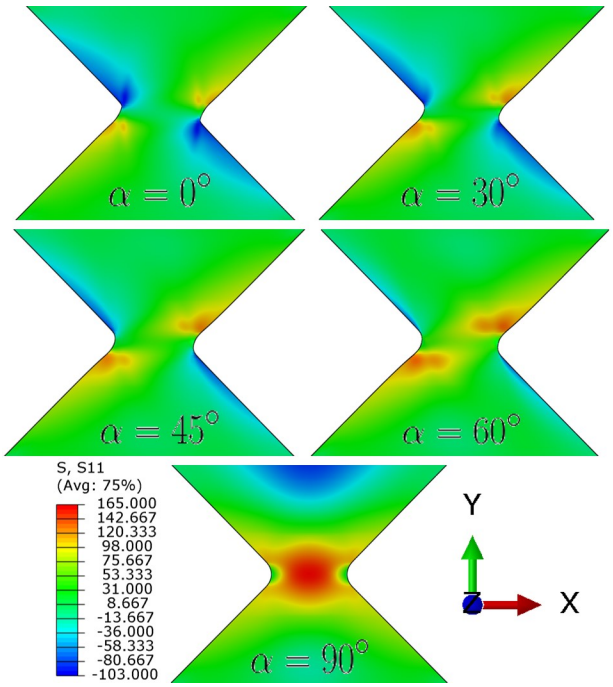

Figure 60: σ_{xx} strain maps in the specimens loaded under 0°, 30°, 45°, 60° and 90° orientations.

Fig. 61 ahows the evolution of σ_{xy} in all specimen orientations close to fracture strains. This shows an anti-symmetric evolution of stress state in case of 90° and change in value of α form 90 to 0 leads to formation of a localized band around the minimum section. The band is formed at an angle if the boindary condition is not shear dominated or tensile i.e. for 30°, 45° and 60°. Maximum magnitude if the shear strains are seen to be at the above and below the notches for all conditions except 0°, where the maximum is seen to exhibit in the minimum section of the specimen connecting the notch roots.

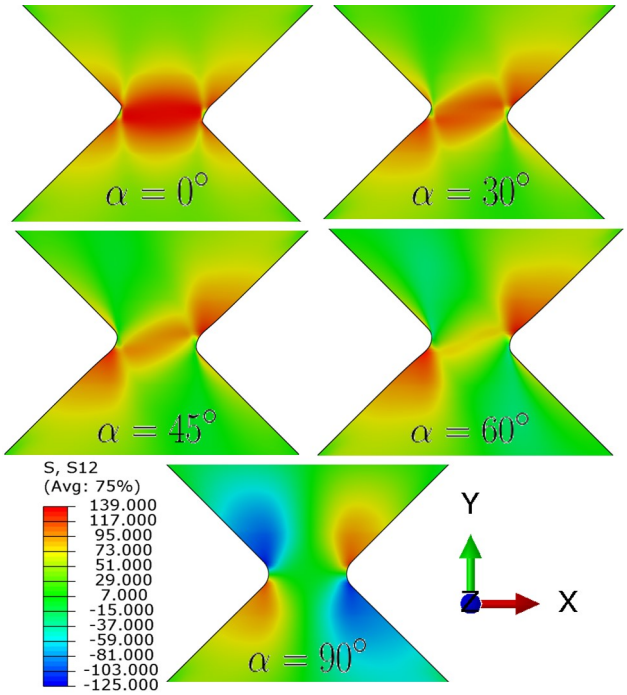

Figure 61: σ_{xy} strain maps in the specimens loaded under 0°, 30°, 45°, 60° and 90° orientations.

4.3.5 Triaxiality and Lode Parameter Evolution

While the absolute values of stresses are expected to carry errors resulting from the imperfect fit to global load deflections responses, the ratios of stress invariants to each other are expected to be only slight affected by such imperfections. Fig. 62 shows the distribution of stress triaixility across the specimen close to failure. This is intended to show the evolution of the stress state with orientation. The evolution of the stress triaixiality is seen to show similar trends as discussed in case of evolution of σ_{yy}. This is because the magnitude of σ_{yy} is maximum and would affect the evolution of T. In the minimum section of the specimen, 0° sample shows minimum value of stress triaxiality and the tensile dominant condition shows the maximum magnitude.

Fig. 63 shows the distribution of Lode parameter across the specimen close to

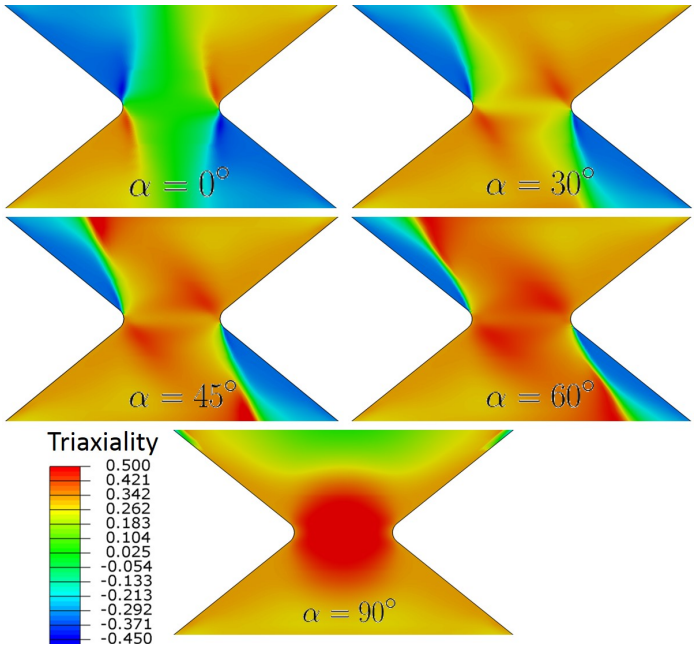

Figure 62: Spatial distribution of Stress triaxiality in 0°, 30°, 45°, 60° and 90° specimen.

failure. This is intended to show the evolution of the stress state with the orientation. In all orientations the value of L is 1 near the notch root. It is observed that the value of lode parameter stays close to 1 for all intermediate orientations i.e. 30°, 45° and 60°. The extreme conditions i.e. 0° and 90° show values of lode parameter varying within the minimum section. Presence of shear causes a change of sign of the lode parameter above and below the notch anti-symmetrically. This occurs through a transition region where the values change from -1 to 1. With introduction of tensile loadings, the value of this band narrows along with the region containing the values of lode parameter of -1.

The values of the stress triaxiality and lode parameter were extracted at locations of interest from the above shown contours to obtain the evolution of these stress state indicators with plastic strain. Fig. 64 shows the evolution of stress triaixiality

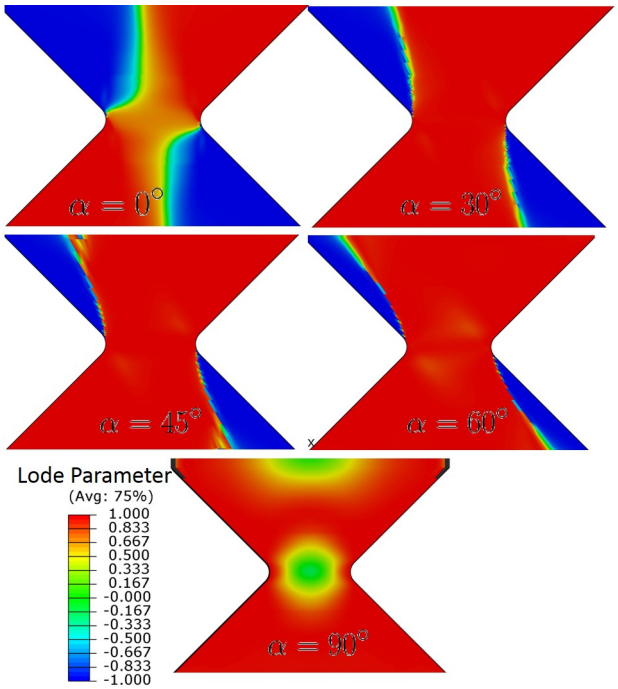

Figure 63: Spatial distribution of Lode parameter in 0°, 30°, 45°, 60° and 90° specimen.

and lode parameter with evolution of strain at the edge of the specimen in the minimum section, center of the specimen, average along the minimum section and at the location where failure is observed to occur from DIC images obtained from the experiments. In all set of curves the 'x' indicates the strain at which the calculations were stopped. These correspond to the experimentally observed values of strains.

In Fig. 64 (a) shows the evolution of the stress traixiality with strain at different locations on the sample. It is observed that the initial stress state is close to 0 and later emerges to small values greater than zero. This is due to structural effects as observed in the contours above. It is observed that the nodes very close to the edges, show a different slope for the evolution of stress state. The stress state at this location is seen to initially be zero and then quickly grows to higher values. Its is also observed that the strain at the edge evolves the least till fracture is met.

With the introduction of some tensile load the values of the stress triaxiality is seen to increase with increase in orientation angle α at all locations in the specimen, however, the edge stays close to traixiality of 1/3. Another interesting observation is that as the orientation of the specimen changes from shear dominated to tensile dominated, the strain at the edge increases from being the least measure of strain to being the highest measure of strain. As the value of triaxiality at the edge remains close to 0.33, the value of the triaxiality increases and becomes greater than 0.33 form orientation $\alpha >= 60$. Strain at failure location is found to be the largest value observed as failure in those conditions did not occur in the minimum section and was found to be above and below the notch.

The lode parameter evolution for each loading orientation is also plotted in Fig. 64. The lode parameter starts from a zero value initially for shear dominant loading and then increases rapidly. For other orientations, the lode parameter stays close to 1 at almost all locations. The only exception is the 90° orientation where the lode parameter away from the edge are seen to start at 0 and evolve to values lesser than 1.

4.3.6 Failure Loci

Fig. 65 shows the triaxiality evolution with strain at each location of interest for different orientations. It is seen clearly from all plots that the value of stress triaxiality increases with increase in orientation angle α. The strain at fracture at the center and edge clearly decreases with increase in shear dominant loadings. However, the value of T at the edge is close to 1/3 for all loading conditions except 0°. This is because the failure is at a location close to the edge for all loading orientations except 0° loading. Although a clear trend is seen in the center and average value of strain, no clear trend is seen in the strain to failure versus average triaxiality plot.

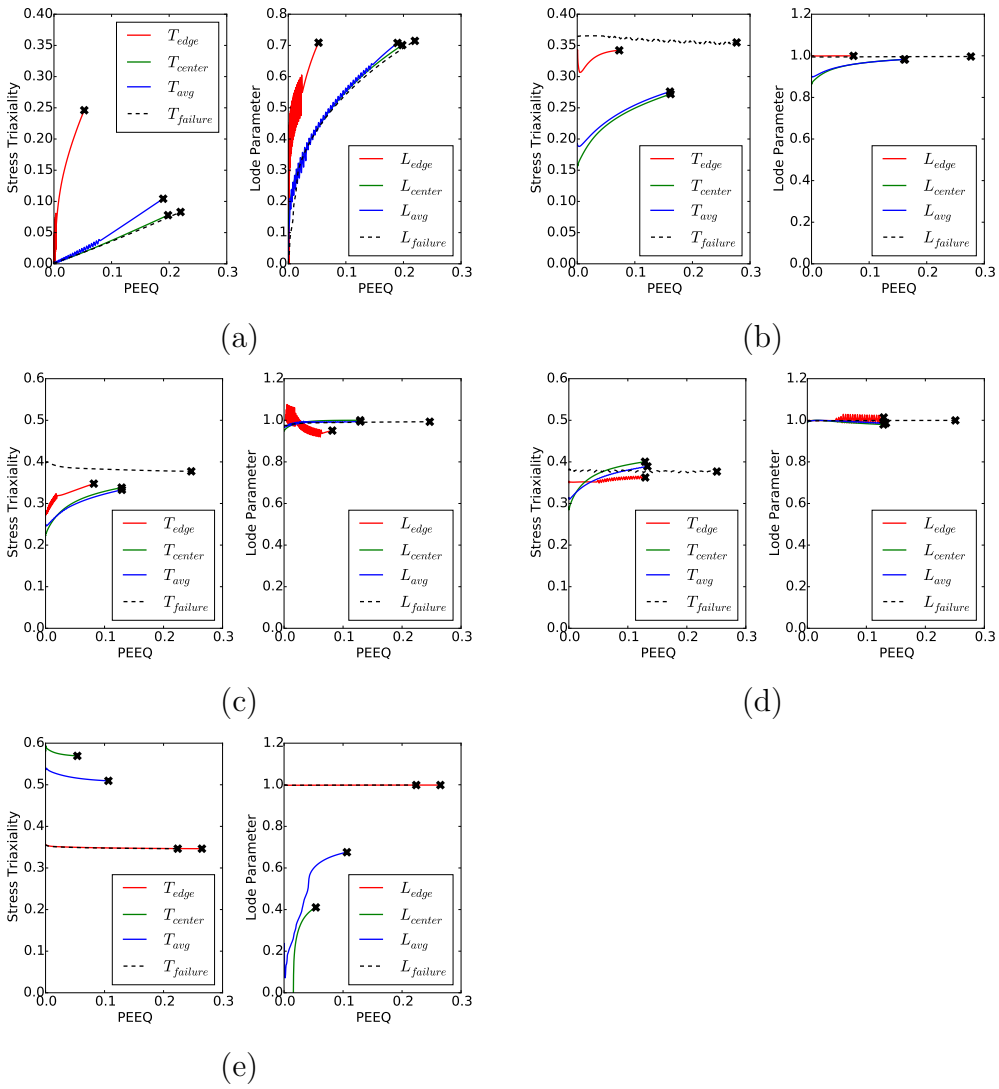

Figure 64: Evolution of Stress Triaxiality and Lode parameter with plastic strain in specimens along orientations (a) 0 (b) 30 (c) 45 (d) 60 (e) 90. The data is presented at different locations in the specimen; edge, center, averaged along the minimum section and at failure location.

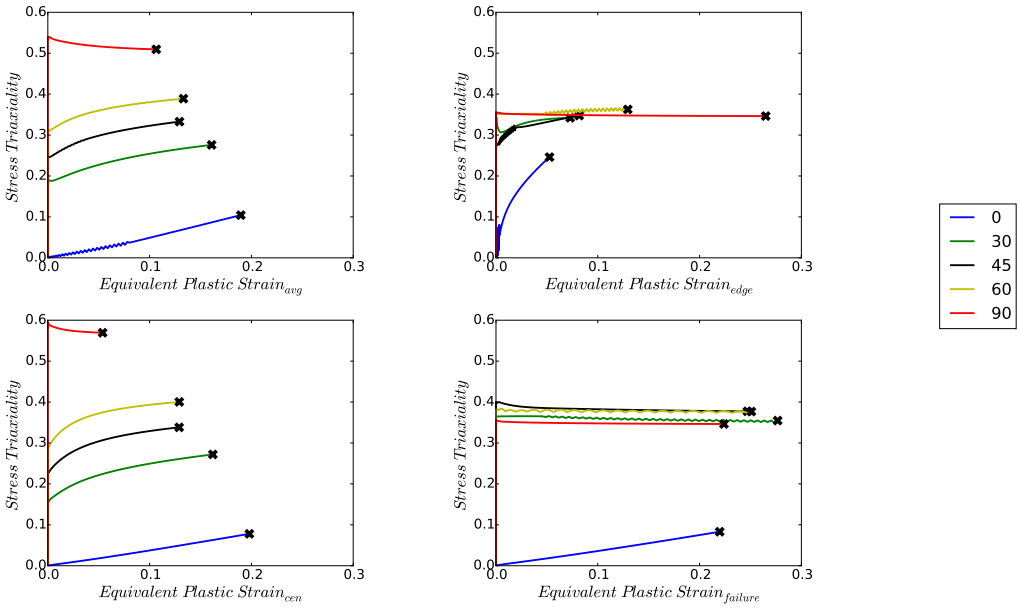

Figure 65: Stress triaxiality, T, versus the local strain $\bar{\epsilon}$ at that location in Arcan specimens. Each plot shows the evolution of T at notch root, center of the specimen, at failure location and averaged over the cross-section. The (x) refers to the value of $\bar{\epsilon}$ at which load drop occurred in the experiments, i.e., $\bar{\epsilon}_c$.

Fig. 66 show the locus of lode parameter with strain to failure at various locations. The lode parameter is seen to vary from zero to values less than 1 in 0° and 90° specimens and for all intermediate test the lode parameter is found to be 1. There is no clear trend seen in the effect of changing lode parameter on the failure strain.

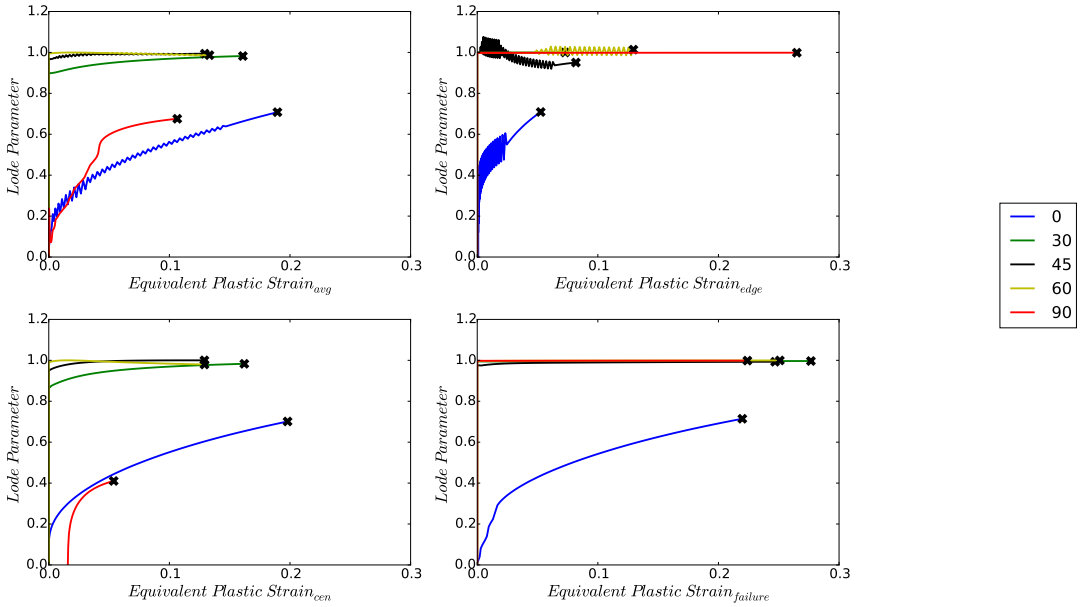

Figure 66: Lode parameter, L, versus the local strain $\bar{\epsilon}$ at that location in Arcan specimens. Each plot shows the evolution of L at notch root, center of the specimen, at failure location and averaged over the cross-section. The (x) refers to the value of $\bar{\epsilon}$ at which load drop occurred in the experiments, i.e., $\bar{\epsilon}_c$.

4.4 Discussion

The previous work by Basu and Benzerga[63] has shown that there is no locus that is intrinsic to the material that can be extracted from real life experiments. This is because a fracture strain extracted from any experiment is generally specimen-geometry dependent. This dependence manifests through the more or less severe

nonproportional nature of the loading. This deviation from proportionality is even more prominent in low triaixility experiments and hence there is a need to understand that any of the loci plotted in these experiments are not claimed to be intrinsic to the material. In practice, however, it is often convenient to represent the failure loci of a material by plotting the strain to failure as a function of the average or terminal stress triaxiality. This is typically done to compare various materials or to report experimental results. In the experiments by [63] the lode parameter was constant due to axisymmetric geometry and the triaxiality was as close as possible to proportionality. In these current experiments, due to geometry of the specimen both T and L vary with strain and hence a failure loci of $\bar{\epsilon}_c$ as a function of both T and L must be plotted.

Five different loading orientations were used to probe the region of low triaxilaity and comment on how the failure strains compare to that observed by a few prominent experiments in the literature [100, 102, 101] in the low triaxiality regime as shown in Fig 31. With the help of Digital Image Correlation technique it was possible to extract the value of local strain components at various locations across the sample. This led us to obtains strain from not only sites of interest but also obtain the location at which failure initiates. In shear dominant loadings, this is difficult to obtain from experiments, as the failure is sudden in most of these loadings. These findings shed light on the failure in structural metal sheets especially of light weight alloys like Mg alloys and help guide experiments and models in predicting sheet metal failure.

In an ideal situation[2] the fracture loci must have an asymptote at $T = 1/3$ irrespective of the material[120]. However, in real life experiments, this is not the situation. There would exist a finite value of $\bar{\epsilon}_c$ at that value of T. The question now

[2]Strictly holds for materials with pre-existing voids and failing by microvoid growth to coalescence

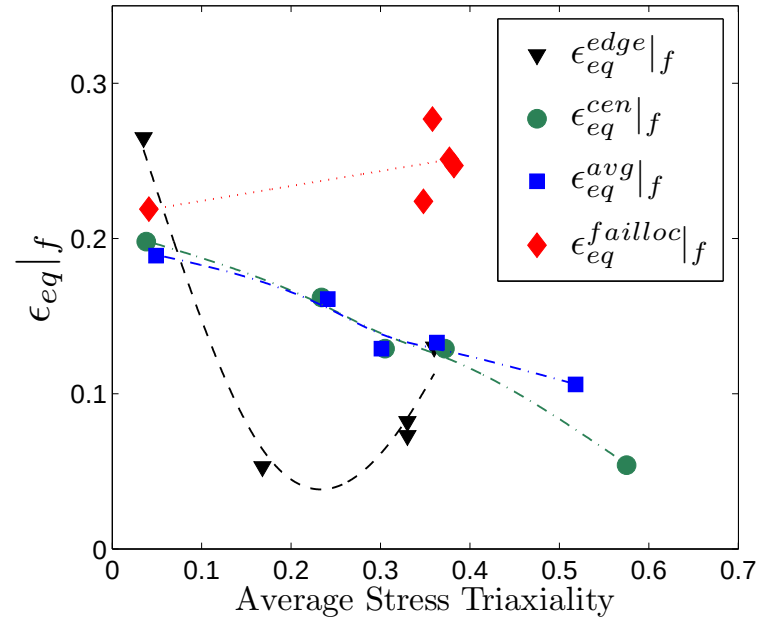

(a)

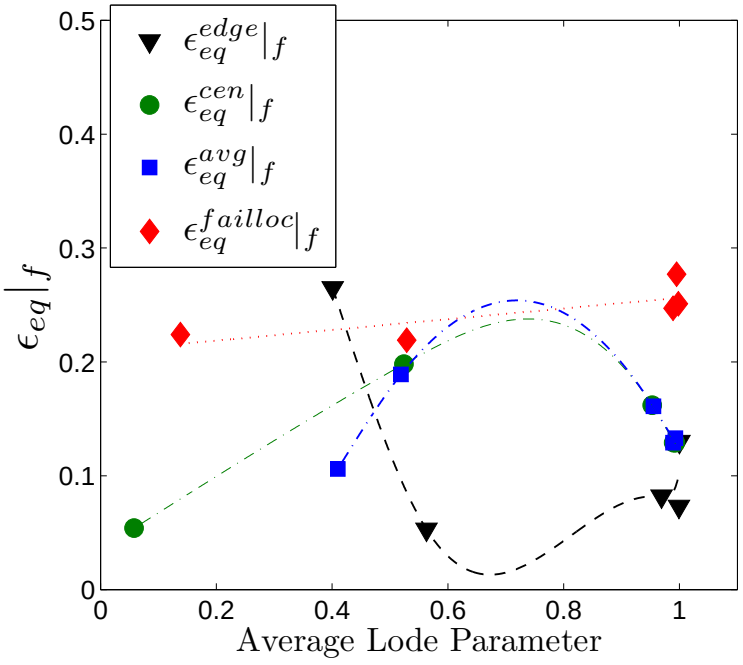

(b)

Figure 67: Failure strain with respect to orientation of the sample at maximum, center and averaged over the cross-section.

arises as to what would happen to the fracture loci for values of $T < 1/3$. Does the locus keep rising as would be expected from extrapolating the Hancock-Meckenzie [93], or would it be a decreasing function as reported by some authors[100, 102]. Fig. 67 (a) and (b) shows the failure loci of failure strains at different locations with respect to the strain weighted value of stress triaxiality and lode parameter respectively. It is observed that the failure loci based on stress triaxiality shows a different trend based on the location at which the value of the stress indicator is obtained. We see that if the stress traixiality is obtained at the center of the specimen or averaged over the minimum section, we obtain trends similar to that shown by Haltom et al.[101] i.e. the value of strain to failure increases with decreasing triaxility as shown in Fig 31. This is similar to the extrapolation of the Hancock & Mackenzie[93] curve to triaxialities lesser than 1/3. However, on assigning the failure location to the edge of the specimen, we see that the strain to failure decreases and then increases to when the loading becomes shear dominant. The initial part of the curve is similar to the trend shown by [100, 102]. However, none of these authors reported values of $\bar{\epsilon}_c$ to increase with the loading changing to shear dominant loading. When compared with the strains at failure location as observed in the experiments, the fracture strain seems to be insensitive to the triaxiality in this regime probed. All the curves except the one obtained at the observed failure initiation location exhibit highest value of $\bar{\epsilon}_c$ in shear dominant loading.

The loci of $\bar{\epsilon}_c$ as a function of the Lode parameter shows that with varying Lode parameter over a wide range i.e. from 0 to 1, we observe that there is minimal variation of the failure strain with the average lode parameter except for the case of the values assigned at the edge. The shear dominant loading 0° shows variation of failure strain with change in Lode parameter. This is however, not a good measure of failure strain as the failure does not initiate near the edge of the specimen under that

loading orientation. Overall, this was the first study to plot the value of measure of strain to failure as a function of Lode parameter. Since,minimal variation is seen in the value of the strain to failure with change in Lode parameter, we can claim that there is minimal effect of the Lode parameter on the failure strain.

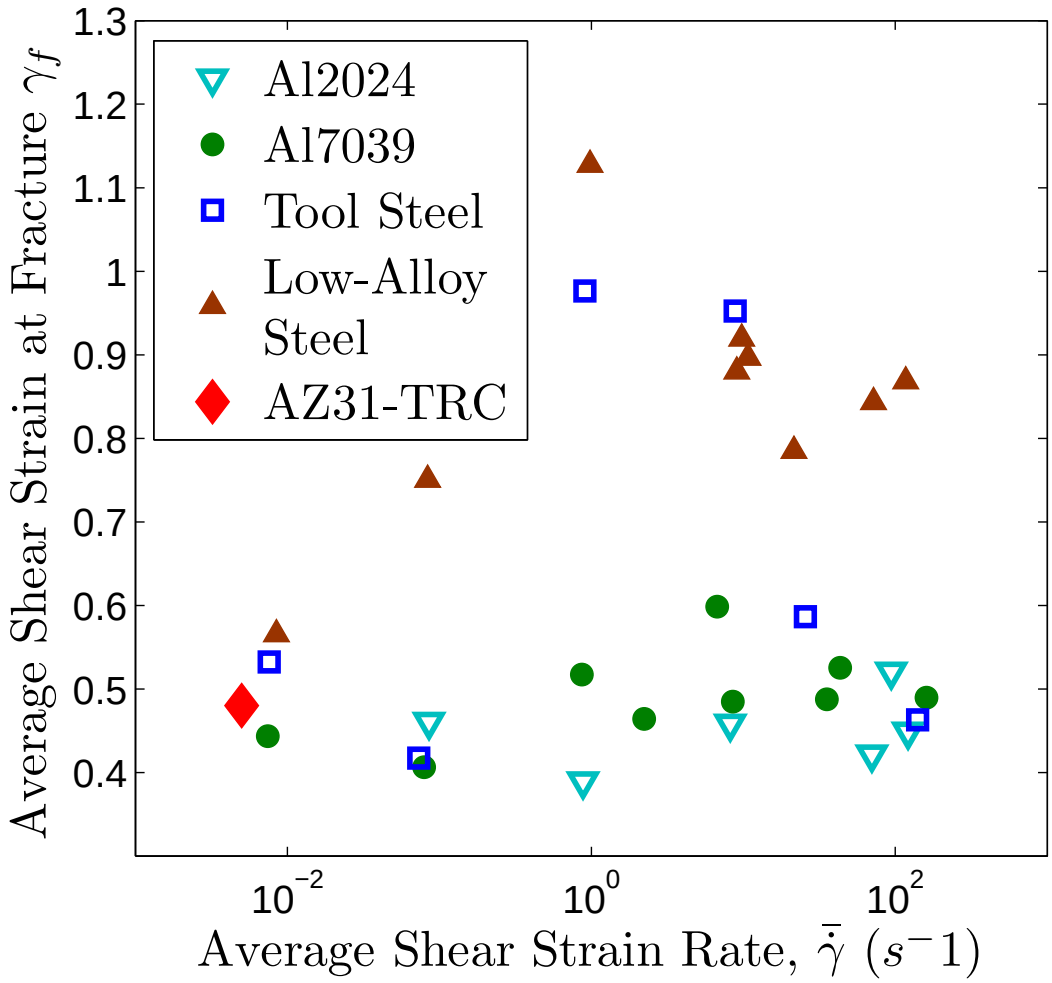

Figure 68: Reconstruction of average shear strain at fracture versus strain rate plot [99], to compare performance of Mg alloy AZ31 to other structural alloys.

This study also enabled us to understand how Mg sheets performed under shear dominant loadings which is not studied at all in the literature. This sheds light on how the materials performs under shear dominant loadings and how shear localization occurs in the material. Plotting the performance of this materials with the pioneering work of [98, 99], comparing the failure under shear for different structural alloys as shown in Fig. 68 indicate that Mg sheets can posses comparable ductility to various structural Al alloys.

5. HISTORY EFFECTS ON DUCTILITY*

5.1 Introduction

This work is motivated by the recent theoretical analyses of Benzerga et al.[24] who examined the effect of loading path on the fracture locus of ductile materials by means of micromechanical finite-element calculations of a periodic unit cell containing a central void. In the cell model, fracture is identified with an abrupt drop of stress carrying capacity of the cell due to plastic flow localization in the intervoid ligament and elastic unloading elsewhere. The unit cells were subjected to several proportional loading paths, characterized by constant values of stress triaxiality. The strain-to-failure was recorded for each path and the locus relating it to triaxiality was thus uniquely determined. The process was repeated for a set of nonproportional loading paths. For these cases, the strain-weighted average of stress triaxiality was used to plot the fracture locus. With these definitions, it was found that the failure locus for nonproportional loadings differs substantially from that for radial paths. Of particular importance are the cases where the strain to fracture decreased by a large amount as a result of nonproportional loading. One aim of this work is therefore to examine experimentally the validity of the findings of . Structural materials usually do not contain initial voids, and if they do the voids are not distributed periodically. In addition, load/strain path changes may affect the hardening behavior of the material in ways that were not represented accurately in the cell model where a simple J_2 flow model was adopted with power law hardening.

More broadly, this study aims at understanding the effects of load path changes

*Parts of this chapter are reprinted with permission from "On the path-dependence of the fracture locus in ductile materials: Experiments" by Basu S. and Benzerga A.A., 2015, *International Journal of Solid and Structures* 71 (2015), pp. 7990, Copyright (2016) by Basu, S.

and pre-straining on the ductility of materials. Industrial metal forming processes involve complex deformation histories which consist of numerous strain path alterations. Pipe reeling processes as well as cold bending, ground movement or simply accidental loading result in pre-straining the constituent materials. The effect of prestrain on the fracture toughness of steels was investigated by Clayton and Knott[121], Amouzouvi and Bassim[122] and Sivaprasad et al.[123] among others. A common trend is that prestrains in excess of some critical value are usually found to affect adversely the toughness. The critical prestrain is comparable with the uniform strain, and this establishes some connection between the decrease in toughness and the decrease in hardening capacity with prestraining. However, the effect of prestrain on the intrinsic damage and fracture mechanisms is not well understood. In another set of studies, the effect of non proportional loading was investigated in initially crack-free specimens of various steels [124, 125, 126]. Various kinds of deviations from a characteristic fracture locus obtained with no path change were evidenced but incompletely rationalized.

In the present work, the material is chosen so that cavitation induced failure prevails under tensile loadings. Cavitation here refers to the usual processes of void nucleation, growth and coalescence [23]. In addition, the loading conditions are chosen so that shear failure is avoided. Axisymmetric stress states are known to be more stiff with respect to shear banding [127]. Therefore, axisymmetric smooth and notched bars are exclusively used. Other types of specimens have gained interest in recent years in order to induce combined tensile and shear stress states [128, 129, 101]. The basic fact, however, that not all laboratory specimens can be mapped onto a characteristic fracture locus remains largely understated in the literature. Consider for instance some fracture strain nominally associated with a given specimen geometry. For this fracture strain to be characteristic of the material two conditions must

be met. First, a stress state indicator such as the triaxiality should undergo minimal variations in time at the location of crack initiation. Incidentally, spatial variations of triaxiality should also be minimized. Second, specimen level plastic instabilities, such as necking or shear banding, must be avoided. These conditions are rarely met *stricto sensu* in any specimen of any material. Nevertheless, deviations from the ideal characteristic locus may vary significantly from one specimen geometry to another. While triaxiality evolution post-necking is most often accounted for in reporting fracture loci, the strong nonproportionality inherent to shear band formation is commonly disregarded. As a result, the nominal fracture strain obtained from, or mapped onto the load-deflection curve is often erroneously associated with the triaxiality (or the stress state indicator) that was prevalent for most of the deformation history. Such nominal fracture strain may be representative of the specimen as a structure, not of the constituent material at the stress state prevalent prior to the onset of the plastic instability. As it turns out, the above two conditions are most closely met in round notched bars. By way of consequence, these specimens are also ideal for imparting controlled step-variations in triaxiality.

Ludwik and Scheu[130] tested specimens with circumferential notches of varying depth and sharpness. Mechanical analysis of these specimens naturally led to introducing the stress triaxiality parameter as the ratio of the mean normal stress to some deviatoric stress measure. Lode[131] subjected tubes of iron, copper, and nickel, to combined tension and internal pressure and examined the effect of intermediate principal stresses on yielding. Orowan[132] carried out some pioneering work to explain the physics of ductile fracture. He rationalized why the stress state arising from the geometry would concentrate plasticity-induced damage to the center of the specimen. Bridgman[133] developed a correction method to obtain the uniaxial true stress-strain relations beyond necking. Mackenzie et al.[93] and the Beremin group

(1981) documented the strong dependence of the strain to failure upon stress triaxiality and rationalized it on the basis of void growth theory [95]; also see Needleman and Tvergard[97]. In the past decade, several groups have revivified the interest in the Lode effect; see [129, 101] and references therein. One cannot emphasize enough that what is measured in these experiments is some apparent, not *intrinsic* fracture locus. The apparent locus may be affected by extrinsic factors such as the occurrence of plastic instabilities or emergence of strong gradients, as indicated above and discussed later.

Reduction of the vehicular weight by using lighter materials led to interest in magnesium alloys, with a superior strength to weight ratio compared to steel and aluminum. Wrought alloys in particular have been reported to have better mechanical properties than their casting counterparts [70]. Forming processes are among the most important metal-working operations to produce part tailored for specific applications. Failures such as wrinkling, springback, necking and splitting can lead to invalidating the part. One of the main limitations in industrial forming processes seems to be the appearance of localized necking. In addition presence of strong anisotropy in wrought Mg alloys lead to limited formability at room temperature along with catastrophic failure after limited necking, limiting their application in industries with sheet metal forming applications [71].

The limiting strains at the onset of localized necking can be predicted using a FLD [25, 26]. Numerous experimental [134, 135] results show that the formability of the material strongly depends on the loading history and on the plastic anisotropy of the rolled sheet. Complex industrial forming processes involving non-linear strain paths, and abrupt changes in the strain ratio invalidate the hypothesis of proportional loading. This strain path sensitivity in sheet materials is mainly classified in the literature into load reversal [136, 137] and orthogonal load path changes[138, 139].

While load reversal showed Bauschinger effect for most materials leading to lowering of stresses on loading after the prestrain stage, a sudden increase in the stresses were seen to emerge after reloading with orthogonal strain-path changes.

Very little study has been carried out on the effect of load path changes involving combined tension and shear loadings and how presence of a prestrain can affect the failure in metal sheets since failure by shear localization is a big issue in sheet material. This problem becomes even more technologically important for Mg sheets where the deformation is affected by the presence of strong anisotropy induced due to crystallographic orientation and due to thermo-mechanical processing. Presence of strong anisotropy is seen to aid early localization of stresses and thus failure.

The chapter is organized as follows. The experimental procedure is presented in Section 5.2. This includes tests with and without path change, a nominal definition of strain to failure that solely relies on experimental measurements, post-necking measurements in simple tension, and fractography. In addition experiments involving load-path changes in Mg sheets involve two different loading paths. The experiments without path change are discussed in chapter 4. Section 5.5 lays out the computational procedure used to infer the large-strain hardening behavior of the material as well as triaxiality variations in all specimens. All results are gathered in Section 5.6 and discussed in Section 5.8.

5.2 Experimental Procedure: Model Material

5.2.1 Material

The material used in this study is a medium-carbon A572 Grade-50 steel (0.23 C, 1.35 Mn, 0.05 S, 0.4 Si, all in %wt) supplied as a 2-inch cold-rolled thick plate. This steel is commonly used in applications that require high strength to weight ratio. The microstructure is ferrito-pearlitic with an average grain size of 25 μm, Fig. 69.

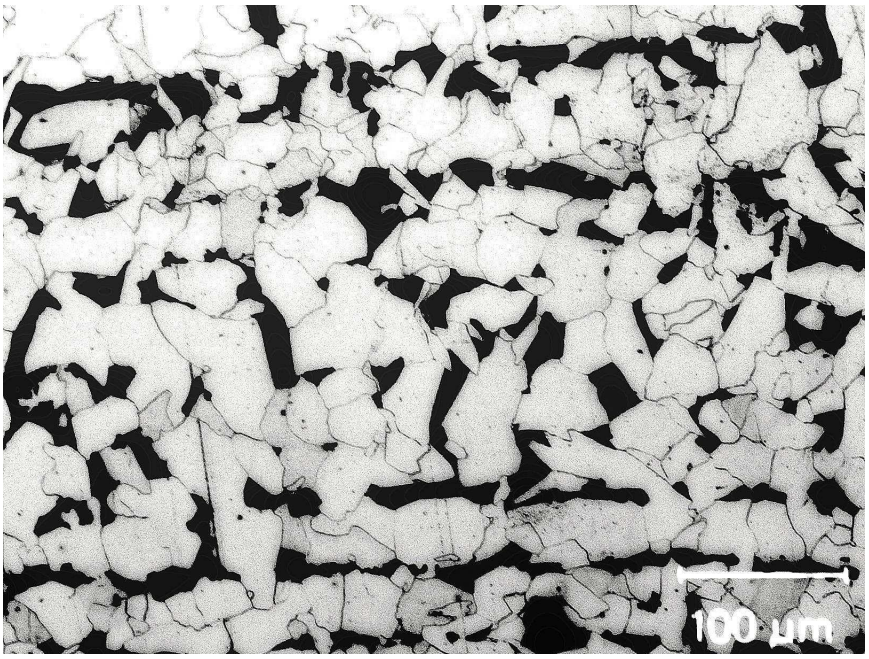

Figure 69: Microstructure of A572 steel with ferrite (bright phase) and pearlite (dark phase) revealed using a 5% nital solution. The rolling and through-thickness directions are horizontal and vertical, respectively.

This material is chosen because the microscopic damage mechanisms are well known. Under tensile loadings void nucleation occurs at rather small strains, either at sulfides or oxides. Significant progressive cavitation occurs until a macroscopic crack initiates induced by the coalescence of the largest voids; see e.g. [58]. Post-mortem fractography was used to ascertain the fracture mode in all tested specimens. The choice of a thick cold-rolled plate for this investigation is also expected to minimize complications associated with plastic anisotropy, which is typical of these microstructures when hot-rolled, much thinner plates are considered [58].

For the latter part of the study the materials used was a rolled sheet of Twin-roll cast AZ31b. Modified Arcan specimens were machined out from these sheets using CNC lathe. The geometry of the sample and the test setup are mentioned in detail

in above chapter.

5.2.2 Experiments Without Path Change

Slender rectangular bars were cut from the plate in the rolling direction, machined into 16 mm diameter cylinders then lathe machined into round notched (RN) bars and fine-polished in the notched region, Fig. 70(b). The diameter at the notch root was $\phi_0 = 5.12$mm. The notch acuity is described by the dimensionless parameter $\zeta = 10 * R/\phi_0$ with R the notch radius, Fig. 70(c).

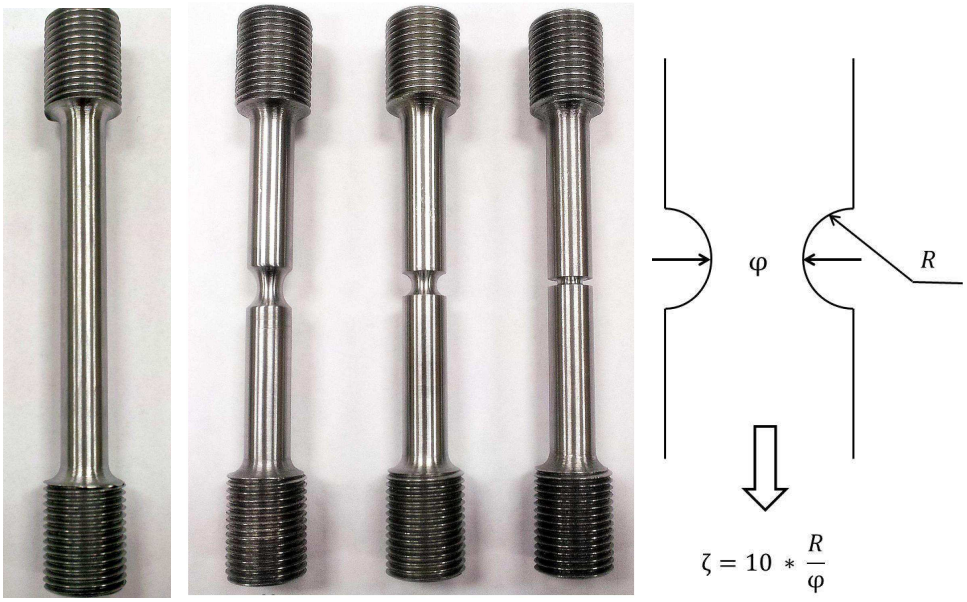

Figure 70: Representative round specimen geometries: (a) smooth bar; (b) notched bars; (c) Definition of notch acuity parameter ζ.

The three specimen geometries depicted in Fig. 70(b) have ζ values of 9.3, 4.6 and 1.5. The lower the value of ζ the sharper the notch and the higher the stress triaxiality. In addition, wider diameter ($\phi_0 = 9.2$mm) smooth tensile bars were

machined with a gage length of 66 mm, Fig. 70(a). The wider diameter was chosen in anticipation of the second set of experiments to be described next.

All specimens shown in Fig. 70 were deformed until rupture using a servo-hydraulic MTS machine with load cell capacity of 110 kN. Special threaded holders with 16 mm diameter were machined using the lathe to mount the samples on the machine. The cross-head speed was adjusted from one specimen to another so as to minimize variations in the nominal strain rate. The latter is defined as the cross-head displacement divided by the height of the notch. If the cross-head speed is kept the same then the strain rate in the sharpest RN bar would be up to two orders of magnitude higher than in the shallowest notch. This would eventually lead to uncertainties in interpreting the results. With this adjustment, the strain rate was in the range of 10^{-4} to 10^{-3}s^{-1} for all specimens with no incidence on the active damage mechanisms. In addition to the load and cross-head displacement, an axial strain based on a gage length $L_0 = 25.4\text{mm}$ was recorded using an Epsilon extensometer. Also, some measurements of diameter reduction were made, the details of which will be described in Section 5.2.4.

5.2.3 Experiments With Path Change

In the second set of experiments the following steps were involved:

- Loading 1: four wide-diameter ($\phi_0 = 9.2\text{mm}$) smooth tensile bars were pre-strained up to incipient necking, i.e., to a strain $\epsilon^* = 0.24$. At this stage, their diameter was $\phi^* = 8.15\text{mm}$.

- Each predeformed smooth bar was unloaded and a notch of desired acuity ζ was machined in the central region. The values of $\zeta = 10 * R/\phi^*$ investigated were 10.4, 3.5, 1.7 and 0.87, with R denoting the notch radius as above. There is some uncertainty on the uniformity of the sharpest notch ($\zeta = 0.87$) around

the circumference.

- Loading 2: the notched bars were loaded to rupture using the same machine at a nominal strain rate within the same range.

This process is illustrated in Fig. 71 for one specific ζ.

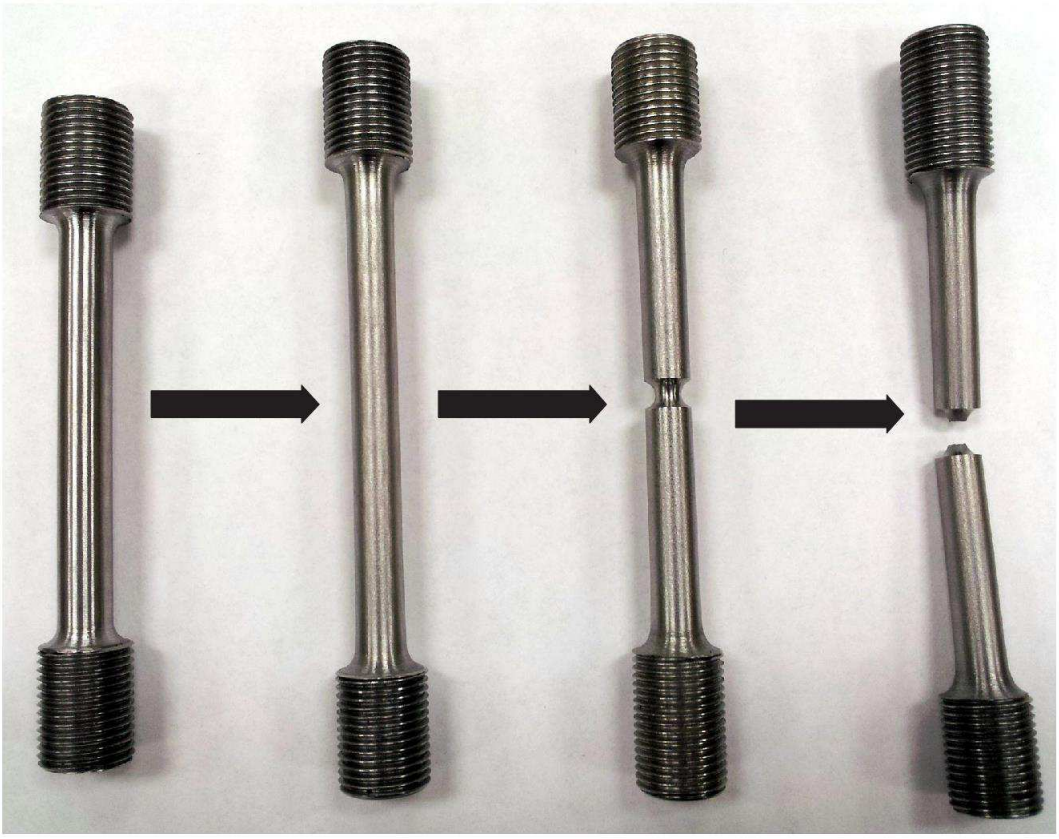

Figure 71: Rendering of the steps of a typical non-proportional loading experiment: the initial smooth bar is prestrained to $\epsilon^* = 0.24$; a notch is machined; the notched bar is deformed to fracture.

From what precedes, it appears that the designed loading program mimics a step-jump in triaxiality, as investigated by [24].

5.2.4 Strain to Failure

Following the literature, e.g., [140, 141] an average strain in the minimal section at the notch root is defined as

$$\bar{\epsilon} = 2 \ln \frac{\phi_0}{\phi} \tag{14}$$

where ϕ is the current diameter. Hence, an appropriate measure of strain to failure, $\bar{\epsilon}_{\mathrm{c}}$, in notched bars is commonly defined as the value of $\bar{\epsilon}$ when $\phi = \phi_c$ at crack initiation. This stage is identified with the knee in the load F versus diameter reduction $\Delta\phi = \phi_0 - \phi$ curve in sufficiently small specimens, Fig. 72(c).

Another measure of ductility is $\bar{\epsilon}_{\mathrm{f}}$ or the strain to complete fracture (i.e., separation of the specimen in two pieces), which is based on ϕ_f. As illustrated in Fig. 72(c), a crack propagates inside the specimen between stages (c) and (f) and this means that deviations from constant stress triaxiality are strong after crack initiation. For this reason, $\bar{\epsilon}_{\mathrm{c}}$ is considered a better measure of ductility even if $\bar{\epsilon}_{\mathrm{f}}$ is more convenient to obtain.

In some notched bars, a custom-made radial extensometer was used, as in recent work [50], to measure $\Delta\phi$. It consists of a pair of knives with adjustable flexibility mounted on a clip-on MTS extensometer, Fig. 72(a). The knifes, which are made of Inconel 718, were machined with ultra-high precision[2] and have graded thickness with tip-thickness of 0.4mm. Given the good ductility of this steel, the ability of the notched bars to contract was beyond the range of the extensometer. Since the diameter reduction was not continuously recorded all the way to fracture, at least one realization per test condition was interrupted at specific intervals to measure ϕ_c using a caliper. The initial and final diameters, ϕ_0 and ϕ_f respectively, were measured using a digital caliper and a laser device. Also broken samples were placed

[2]by Piper Precision, Inc., Friendswood, TX.

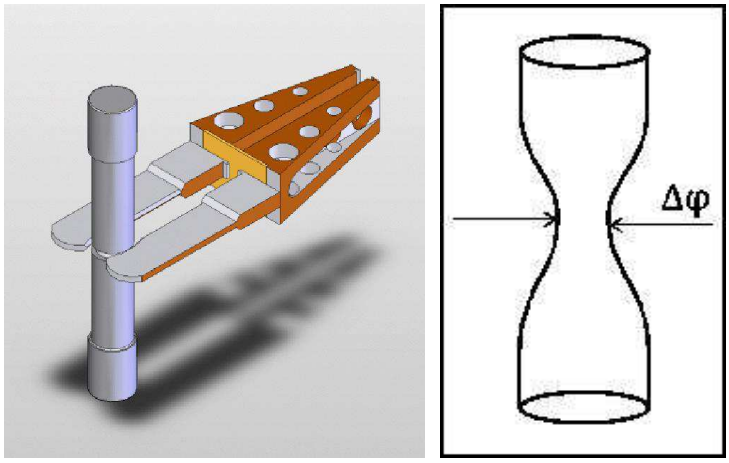

(a) (b)

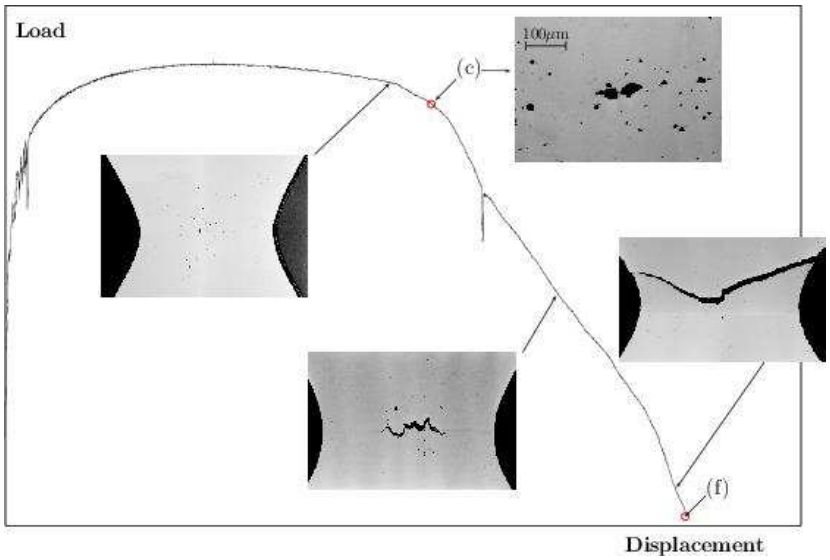

(c)

Figure 72: Radial strain measurements. (a) Custom-made radial extensometer mounted on sharp notched bar. (b) Sketch of post-necking diameter measurement in a tensile bar. (c) Typical load versus diameter reduction in a notched bar of a similar steel [58] showing the initial yielding, limit load, drop in the force associated with macrocrack initiation, stage (c), stable crack growth and final rupture, stage (f). Adapted from [45].

under a microscope to measure ϕ_f after separation of surfaces.

5.2.5 Post-necking Measurements

The simple tension tests include a necking-induced loading path change. This will be taken into account when presenting the results. Some smooth bar tests were also interrupted multiple times (over 30 instances) beyond necking to measure ϕ at the neck as sketched in Fig. 72(a). It is not possible to ensure where the neck would form and hence the radial extensometer could not be used. Although the post-necking diameter measurements alone are not sufficient to obtain the large strain hardening response of the material, they enable further comparisons with finite-element calculations of post-necking deformation.

5.3 Data in Literature

Four sets of published experiments have been analyzed using the simple fracture theory[**Thomas16**]. The first three are taken from Refs. [124, 142, 126] while the fourth set is from our recent experiments [63]. The loading paths considered in the first three studies are schematically shown in Fig. 73. All authors investigated loadings of Type 1, as per the above classification. In addition, Schiffmann et al. [142] considered mixed loadings reminiscent of a combination of Type 1 and Type 2.

5.3.0.0.1 Type 1 loading: Marini et al. [124] investigated step jumps in nominal triaxiality (Fig. 73a) whereas Schiffmann et al. [142] and Chae et al. [126] studied step drops of triaxiality (Fig. 73b and d). In experiments, as the triaxiality is not directly controlled, such paths were imparted using notched bars as follows. Marini et al. [124] prestrained a shallow notched bar ($T_0 > 1/3$) to various levels of (effective) prestrain ϵ^*.

This was followed by two different step jumps using sharper notches ($T^* > T_0 > 1/3$), and the specimens were then loaded to failure, as depicted in Fig. 73a. The

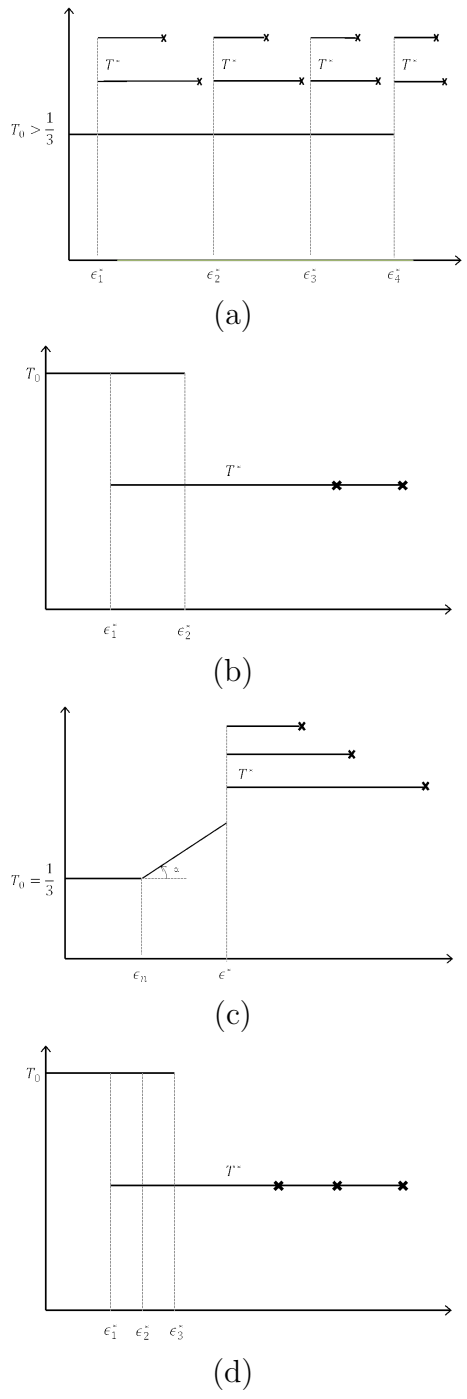

Figure 73: Schematics of experimental loading paths considered by (a) Marini et al. [124]; (b),(c) Schiffmann et al. [142]; and (d) Chae et al. [126]. Details are provided in Table 2

strains to failure were reported in [124]. In practice, each notched bar is defined by a notch acuity parameter ζ equal to ten times the notch radius to notch root diameter. The parameters defining their experiments are reported in Table 2.

Material	ζ_0	**prestrain** ϵ^*	ζ^*	**Source**
A508	10	0.07	4	Marini et al. [124]
	10	0.31	4	
	10	0.46	4	
	10	0.55	4	
	10	0.07	2	
	10	0.31	2	
	10	0.46	2	
	10	0.55	2	
FeE690	2	0.13	5.3	Schiffmann et al. [142]
	2	0.17	5.3	
	2	0.22	5.3	
	∞	0.55	2	
	∞	0.55	4	
	∞	0.55	8.6	
HY-100	2.5	0.03	10	Chae et al. [126]
	2.5	0.07	10	
A572	∞	0.23	10.4	Basu and Benzerga [63]
	∞	0.23	3.9	
	∞	0.23	1.7	
	∞	0.23	0.9	

Table 2: Summary of experiments from the literature.

Schiffmann et al. [142] started with a sharp notch ($\zeta = 2$ so that $T_0 > 1/3$) pre-strained to three different strain levels then machined smaller bars with a shallower notch (Table 2) so that $1/3 < T^* < T_0$ (Fig. 73d). The experiments of Chae et al. [126] were essentially similar, albeit for a different material (Table 2). For the sake of brevity, the analyses of their experiments are omitted here. Finally, the recent experiments of Basu and Benzerga [63] complements the above three sets by explor-

ing the case of lowest preloading triaxiality $T_0 = 1/3$ and four different reloading triaxiality T^* but for a single value of the prestrain (Table 2). In all studies, a set of standard notch bar experiments were also carried out with no path change. The resulting fracture loci serve as reference.

5.3.0.0.2 Type 2 loading: Every standard tensile testing of an initially smooth bar may fit in this category for materials whose plastic hardening can be approximated by a power-law. In the above cited works, such data was reported in [142] and [63]. In both, $T_0 = 1/3$ and $\varepsilon^* = \epsilon_{\mathrm{n}}$. Such paths are not included in Table 2.

5.3.0.0.3 Mixed Loading: Schiffmann et al. [142] also considered the loading path depicted in Fig. 73c. It is realized in two steps. In the first, a smooth bar is loaded beyond necking so that $T_0 = 1/3$ and $\varepsilon^* > \epsilon_{\mathrm{n}}$. In the second step, notched bars with three different notch geometries were machined inside the neck of the predeformed bar and loaded to failure, thus leading to step jumps in triaxiality. This loading path is also included in Table 2 where $\zeta \to \infty$ refers to the smooth bar and ζ^* is for the machined notches. Note that the first step of loading itself is amenable to a Type 2 loading with induced ε^* equal to the necking strain.

5.4 Experimental Procedure : Mg Sheets

All the above experiments above were aimed at performing load path changes by introduction of a step jump in stress-triaixiality by introduction of a notch after prestraining in uniaxial tension. These were aimed at probing the region of medium to high triaxiality regime. The current experimental campaign is designed to check the effect of strain path change in the low-triaxiality regime. The experimental setup used in this study is the same as shown in 4. The sample and the holder used in this case is shown in Fig. 34. Two different load paths were probed in this study. Path 1 as shown in Fig. 74 involves prestraining the specimen in tension ($\alpha = 90^\circ$)

followed by reloading it in in different orientation of loading. Orientation here refers to the angle α shown in Fig. 35(a). Path 2 as shown in Fig. 74 involves preloading in shear ($\alpha = 0°$) upto a certain ϵ^* followed by reloading at a different angle of α.

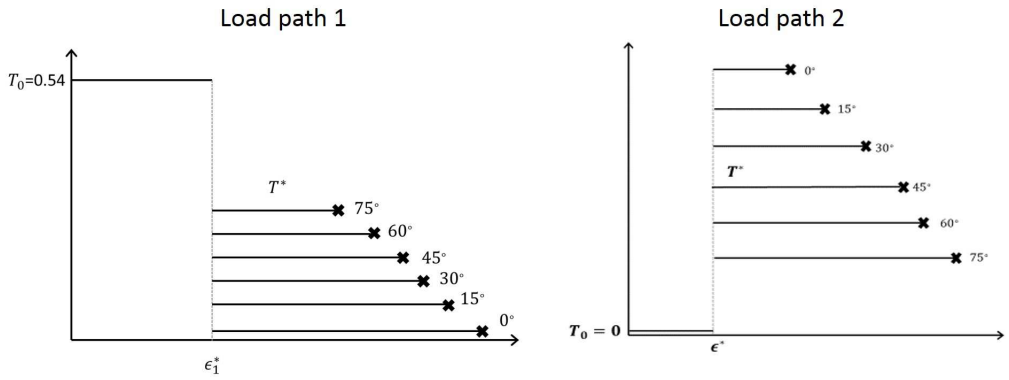

Figure 74: Schematic of the loading paths probed using these experiments. Path 1 involves prestraining under uniaxial loading followed by step decrease in the stress triaxiality by changing orientation of the sample. Path 2 involves prestraining under shear dominant loading followed by step jump in triaxiality.

The value of the prestraining was kept constant for each path of the experiment. The tests were interrupted when the load level reached 10.8 kN and 6.8 kN for path 1 and 2 respectively. These turned out to be close to the levels close to 50% of the equivalent strain in each material. The sample was then unloaded and the system involving the holder and the sample as shown in Fig. 74(c) was rotated to the reloading orientation α. For both loadings the reloading value of α is separated by 15° from one loading to the other. The second step involved reloading all the way to failure under that loading orientation. The strain to failure after path change can be reported as the total accumulated strain from both steps of the deformation or in form of the strain in the second step of the deformation which will be termed as residual strain from now.

Digital Image correlation was used to obtain the evolution of local strains in the specimen. Since data was extracted for the tension and the shear condition earlier in no-path change experiments, the data for the initial step will not be shown here and only step 2 of the loading will be compared. The definitions of the quantities used in force displacement response and for obtaining the equivalent strain measurement are kept similar to the ones in the experiments without path mentioned in section 4.2.

5.5 Numerical Procedure:Model Material

5.5.1 Principle

Elasto-plastic finite element calculations have been carried out using the commercial software ABAQUS[3] in order to (i) identify the material's hardening response up to large plastic strains; and (ii) evaluate triaxiality evolution in the various specimens. The plastic behavior was modeled using rate-independent J_2 flow theory with isotropic hardening. The hardening curve was supplied as tabulated data following an iterative procedure to be described below. In the simulation of the experiments with path change, the effect of prestrain on hardening is readily accounted for by disregarding the tabulated stress–strain data for effective strain values lower than ϵ^*. This is straightforward since all material points in the predeformed smooth bar undergo similar deformation. Any potential effect of kinematic hardening upon load path change is neglected. Also, the effect of strain-rate sensitivity at room temperature in the steel was minimized in the experiments by limiting strain-rate variations among the various specimens. Due to symmetry a quadrant of each smooth or notched specimen was meshed respectively using 1323 and 1443 4-noded axisymmetric elements with reduced integration (CAX4R), Fig. 75.

[3]Version 6.12, Simulia, Inc. and Dassault Systèmes

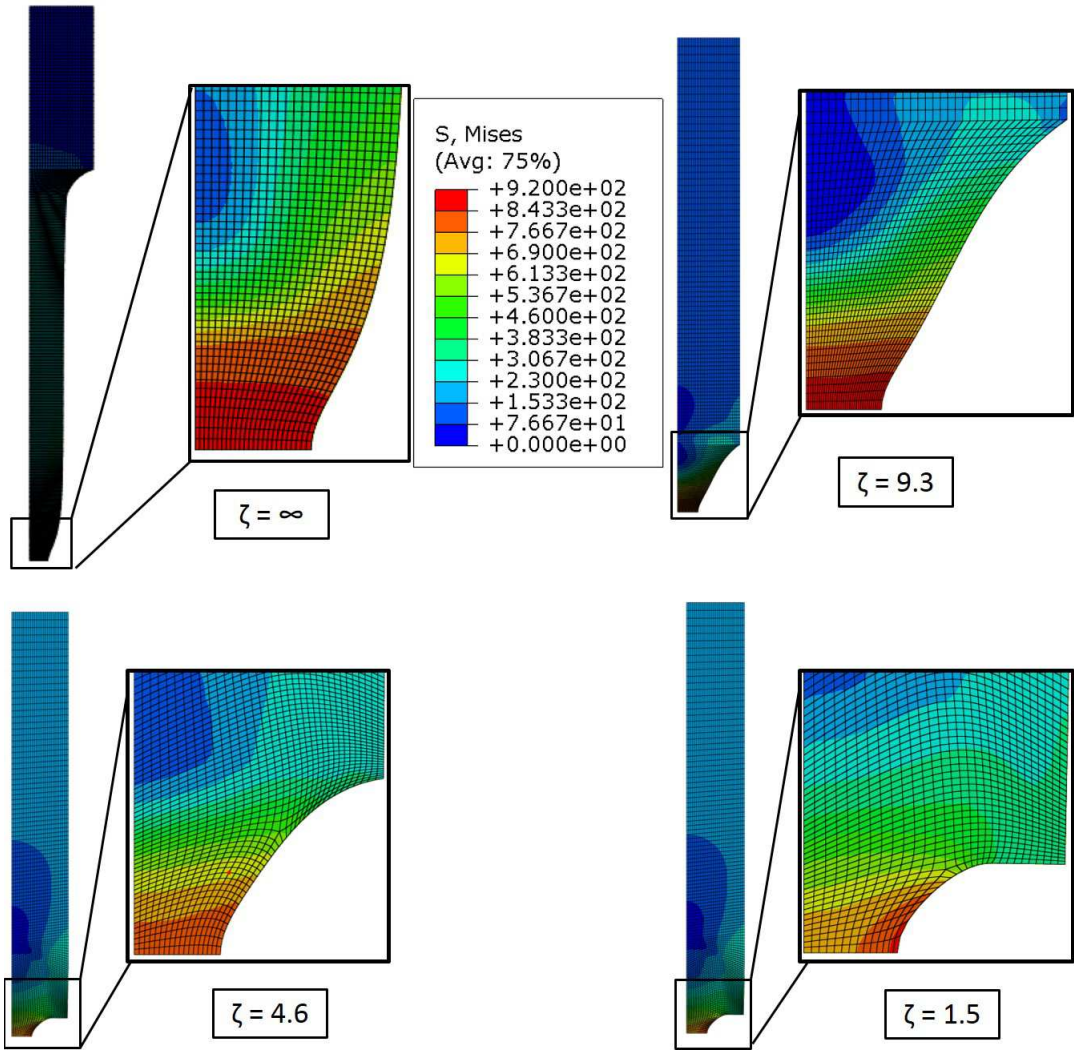

Figure 75: Finite element meshes and contours of effective stress in the smooth bar ($\zeta = \infty$) and some notched bars.

Displacement boundary conditions were applied at the top surface of each specimen. The calculations were stopped when the diameter reduction at the notch root was equal to $\Delta\phi_c$ at crack initiation, as determined experimentally.

5.5.2 Large Strain Behavior

The mesh of the smooth tensile bar included part of the loading ends (grips) so as to induce necking, as shown in Fig. 75(a). The true stress–strain hardening response was determined iteratively as follows. First, power-law hardening was assumed and identified on the basis of the true uniaxial stress–strain response prior to necking. Tabulated stress-strain data that match the power-law were used. The simulated load versus elongation response was compared with the experimental one using the same gauge length L_0. The difference between the two introduced an error function. The latter was used as a basis to correct the post-necking stress-strain tabulated data iteratively (see Appendix A).

An alternative way to obtain an estimate of the large-strain true stress–strain response is Bridgman's correction method. Implementing this method, however, requires continuous measurement of the neck cross section as well as the radius of curvature of the neck, and this requires video-monitored testing. Efforts of this kind are typical for polymers, e.g. [143], but were not pursued here.

5.5.3 Prestrain Effects

In the theoretical loading paths triaxiality variations are imposed by design. However, in the experimental loading paths they need to be determined with some level of accuracy. To achieve this, finite element calculations were carried out to simulate the actual load path changes in the various experiments in Table 2 using ABAQUS. The plastic behavior was modeled using rate-independent J_2 flow theory with isotropic hardening. Any potential effect of kinematic hardening due to load path change is

neglected. The calculations were terminated when the remotely imposed displacement, as reported by the various authors, reached a value corresponding to the onset of failure. In all experiments, failure is assumed to have initiated at the center of the specimen, as was explicitly mentioned in some of the sources.

For the experiments by Basu and Benzerga [63] the hardening curve was supplied as tabulated data following an iterative procedure to account for large strain corrections beyond necking. More details are provided in [63]. In the simulation of the experiments with path change, the effect of prestrain on hardening is readily accounted for by disregarding the tabulated stress–strain data for effective strain values lower than ϵ^* for the data in [63]. This is straightforward since all material points in the predeformed smooth bar undergo the same loading path prior to necking.

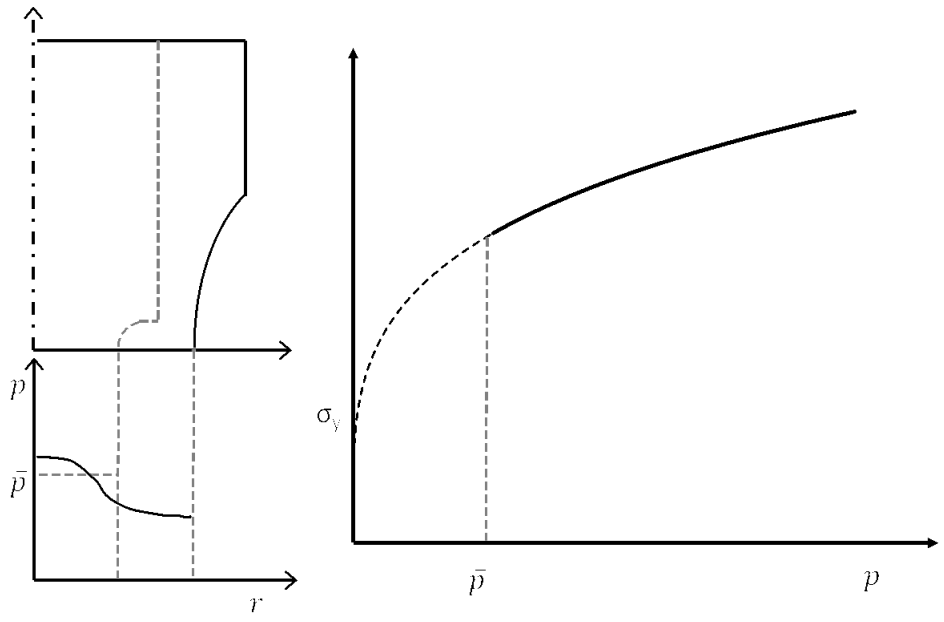

Figure 76: Procedure to account for prestrain effects on hardening in the finite element simulations.

For other experiments in the literature, the best power-law fit to the hardening curve was used, as the data provided in [124, 142, 126] was not sufficient to extract more accurate hardening laws at large strains. Nevertheless, the implication of such imperfections on the evolution of triaxiality is expected to be small. A more important issue is that in these experiments the first step involves deforming a notched bar so that the distribution of plastic strain in the specimen at the instant of load path change is nonuniform. The effect of predeformation on the hardening law to be used in the reloading step simulation must therefore be obtained in some approximate way. The following procedure was followed, which is represented schematically in Fig. 76. At the instant of load path change (i.e., when $\varepsilon = \varepsilon^*$) the distribution of effective plastic strain p is known. An accurate method would consist of projecting the fields at that instant onto the smaller notched specimen (shown in dashed). This would enable among other things to keep any residual stress field that would have resulted from the first loading step. For simplicity however, the effective plastic strain averaged over the minimal section of the smaller bar was retained as an indication of an average, supposedly uniform, plastic strain, $\bar{p}$, with no associated residual stress. Thus, in the second step, the portion of the hardening curve past $\bar{p}$ is retained for subsequent analysis. This procedure allows to account for the natural loss in hardening capacity that follows prestraining.

5.5.4 Triaxiality Variations

The stress triaxiality ratio (or simply the triaxiality T) is defined as the mean normal stress $\sigma_{\mathrm{m}} = \sigma_{kk}/3$ divided by the von Mises effective stress σ_{eq}. In uniaxial loading (smooth bars prior to necking) $T = 1/3$ is constant and uniform. This is not the case in the notched bars. In general, the triaxiality is a field which varies with the accumulated plastic strain p so that one can write $T(\mathbf{x}; p(\mathbf{x}))$ where $\mathbf{x}$ is the

position vector.

In associating a nominal triaxiality to a given specimen with notch acuity ζ one may simply use the triaxiality, T^{loc}, at the center of the specimen, since that is where the macroscopic crack initiates (Fig. 72(c)). Alternatively, one could average the triaxiality within the minimal cross-section to account for spatial gradients:

$$\langle T \rangle \equiv \frac{2}{\phi} \int_0^{\phi/2} T(r)\, r \, \mathrm{d}r \tag{15}$$

The evolution of both local and global triaxialities, according to the above definitions, were extracted from the finite-element simulations.

5.5.5 Fracture Loci

Unless the triaxiality is kept strictly constant throughout deformation, the only fracture locus that can be defined on the basis of experiments alone is the locus relating the strain to failure $\bar{\epsilon}_c$ defined in Section 5.2.4 versus the notch acuity parameter ζ. However, ζ is a geometric parameter that is implicitly related to a stress state indicator such as triaxiality. Here, three definitions of the fracture locus are adopted in order to show later the robustness of the conclusions drawn.

One convenient way to define the fracture locus is to obtain the curves giving the local triaxiality, T^{loc}, versus the strain measure $\bar{\epsilon}$ in equation (14) up to $\bar{\epsilon} = \bar{\epsilon}_{\mathrm{c}}$, i.e., at crack initiation. Fracture would then be identified with the locus $T_{\mathrm{c}}^{\mathrm{loc}}$ versus $\bar{\epsilon}_{\mathrm{c}}$, where $T_{\mathrm{c}}^{\mathrm{loc}}$ is the triaxiality at fracture. A dual plot consists of plotting $\bar{\epsilon}_{\mathrm{c}}$ against the strain-weighted average of T^{loc}:

$$\bar{T}^{\mathrm{loc}} = \frac{1}{\bar{\epsilon}_{\mathrm{c}}} \int_0^{\bar{\epsilon}_{\mathrm{c}}} T^{\mathrm{loc}}(\bar{\epsilon})\, \mathrm{d}\bar{\epsilon} \tag{16}$$

For proportional loading, the two dual definitions deliver the same locus.

A second definition consists of obtaining the curves of the local triaxiality at fracture, $T_{\mathrm{c}}^{\mathrm{loc}}$, versus the local plastic strain p, similar to the loci provided, for example, by [97]. The effective strain at failure, p_c, is mapped onto the global condition. $\bar{\epsilon} = \bar{\epsilon}_c$. A dual plot is the local strain to failure, p_c, versus the corresponding strain-weighted average of T^{loc}:

$$\bar{\bar{T}}^{\mathrm{loc}} = \frac{1}{p_c} \int_0^{p_c} T^{\mathrm{loc}}(p)\, \mathrm{d}p \tag{17}$$

A third definition is based on terminal values in curves giving the global triaxiality $\langle T \rangle$ defined in (15) versus the global strain $\bar{\epsilon}$. A dual plot is $\bar{\epsilon}_c$ against the following strain-weighted average of $\langle T \rangle$:

$$\overline{\langle T \rangle} = \frac{1}{\bar{\epsilon}_c} \int_0^{\bar{\epsilon}_c} \langle T \rangle(\bar{\epsilon})\, \mathrm{d}\bar{\epsilon} \tag{18}$$

Definition (3) is the most convenient. However, it relates a local measure of stress state to a global measure of strain. Definition (4) relates local quantities whereas definition (5) relates global ones.

5.6 Results:Model Materials

Fractography examinations confirmed that all tested specimens, including the pre-strained ones, have failed by a process of void nucleation, growth and coalescence. Fig. 77 shows fracture surfaces of selected specimens.

The macro-fractographs show that the initially circular sections remain essentially circular. Along with the discontinuous diameter reduction measurements in some cases, this shows that plastic anisotropy is insignificant in the A572 steel plate, as expected. The fractographs clearly reveal the dimpled character of the fracture surface. Images taken at much higher magnification revealed second-phase particles that sometimes remained attached to the material inside dimples. Energy dispersion

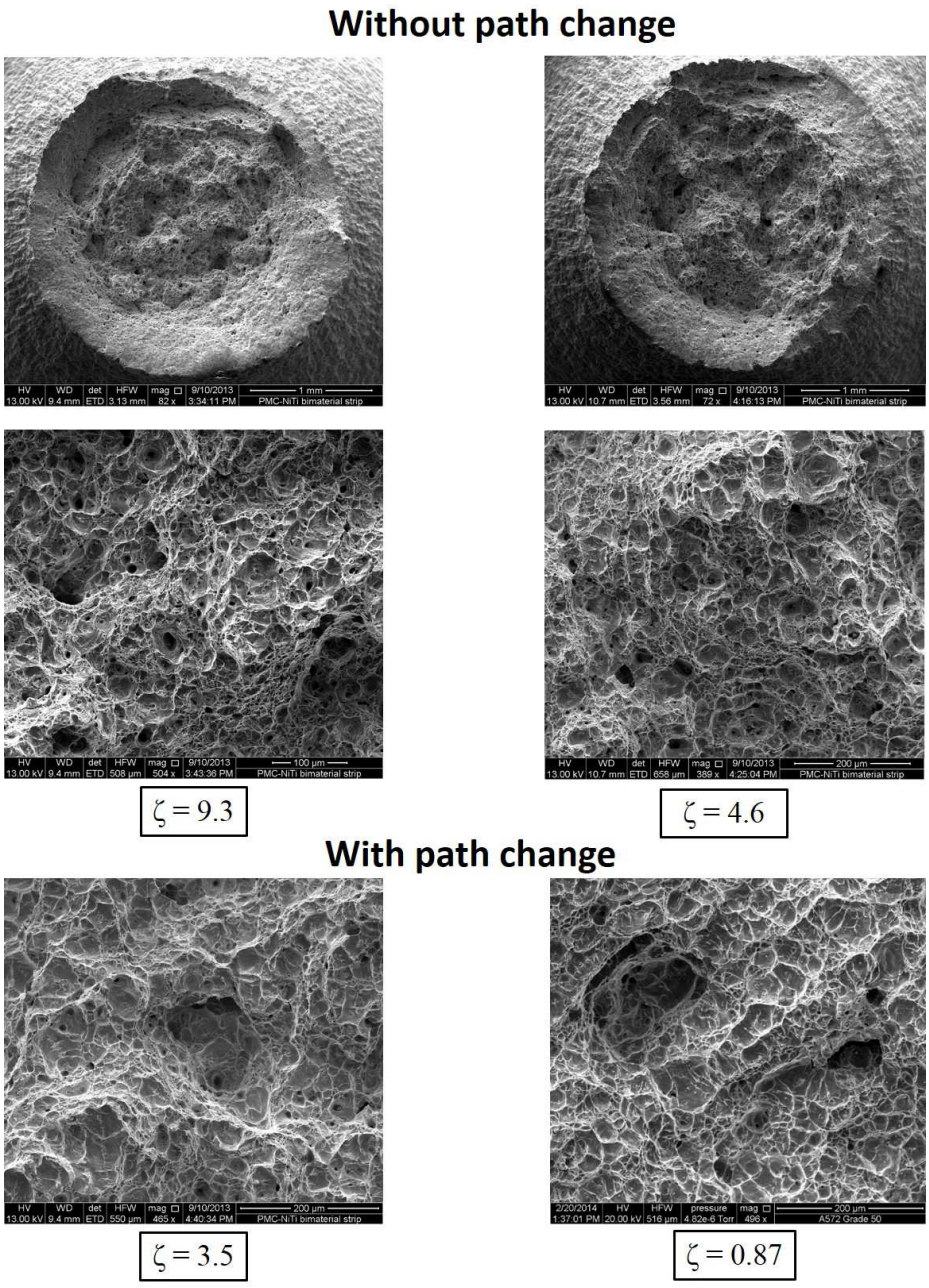

Figure 77: Scanning electron microscopy images of representative fracture surfaces of various notched bars. The fractographs confirm void nucleation, growth and coalescence as the main damage mechanisms in the steel.

spectroscopy (EDS) analysis enabled to identify the particles as either manganese sulfides (MnS) or carbides. It is also likely that alumina particles act as damage initiation sites.

Curves of the load, F, normalized by the initial cross-sectional area, A_0, versus elongation, $\delta L/L_0$, are shown for the notched bars without path change in Fig. 78(a) and with path change in Fig. 78(b).

The dual effect of notch severity on increasing the net axial stress required for plastic flow and on decreasing the strain to failure is evident in both figures. In Fig. 78(b) the initial part corresponds to pre-loading uniaxially to the same (total) prestrain of ϵ^* =0.24, as described in Section 5.2. The values of both measures of strain to failure: at crack initiation, $\bar{\epsilon}_{\mathrm{c}}$, and at fracture, $\bar{\epsilon}_{\mathrm{f}}$, are reported in Table 3 (see Section 5.2.4). The format ∞–ζ is used for the experiments with path change to indicate a significant change in the radius of curvature of the notch. In this format, the notation "∞" refers to prestraining a smooth tensile bar (no notch). The particular case of the smooth tensile bars where the change in ζ is induced by large post-necking deformation is included under the experiments with path change.

The load–elongation response of the initially smooth tensile bar is shown in Fig. 79.

The response exhibits a yield plateau typical of mild steel. Superposed onto this plot are two calculated load–elongation responses: one using the power-law hardening rule (dashed), the other using the tabulated hardening law that provides the best fit to the experimental response as per the procedure of Section 5.5.2 (see Appendix for details). Both hardening curves account for the initial yield plateau in tabulated form. It is worth noting that the value of the initiation strain $\bar{\epsilon}_{\mathrm{c}}$ reported for the smooth bar in Table 3 (first row of second column) is not extracted from the load–elongation response in Fig. 79. Instead, it is based on the discontinuous diameter

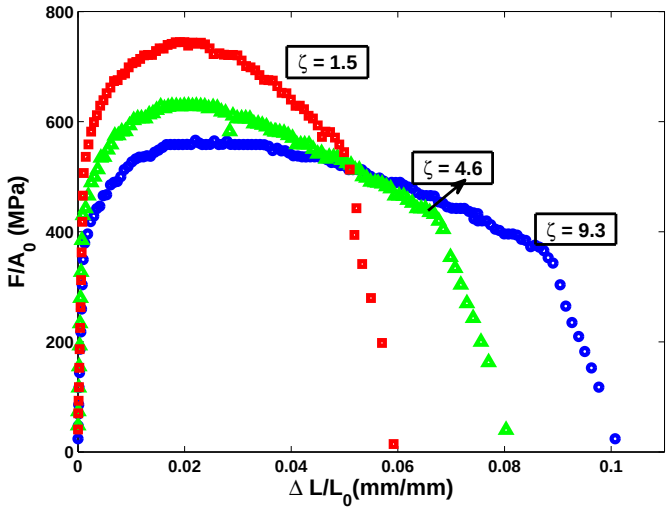

(a)

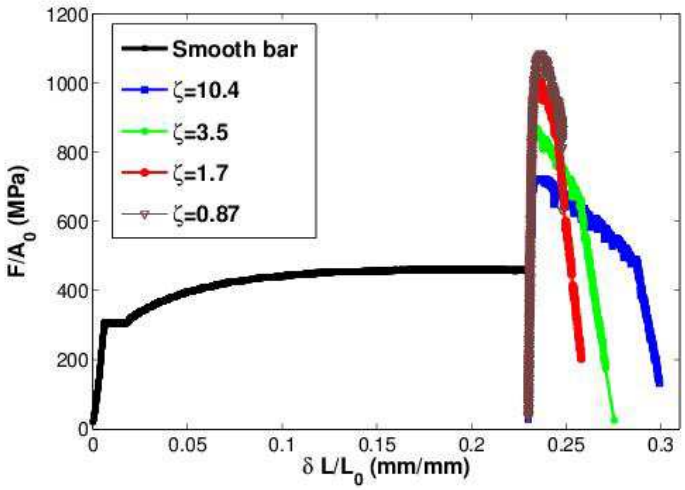

(b)

Figure 78: Load normalized by the initial cross-sectional area versus gauge length elongation for representative tests (a) without path change; (b) with path change.

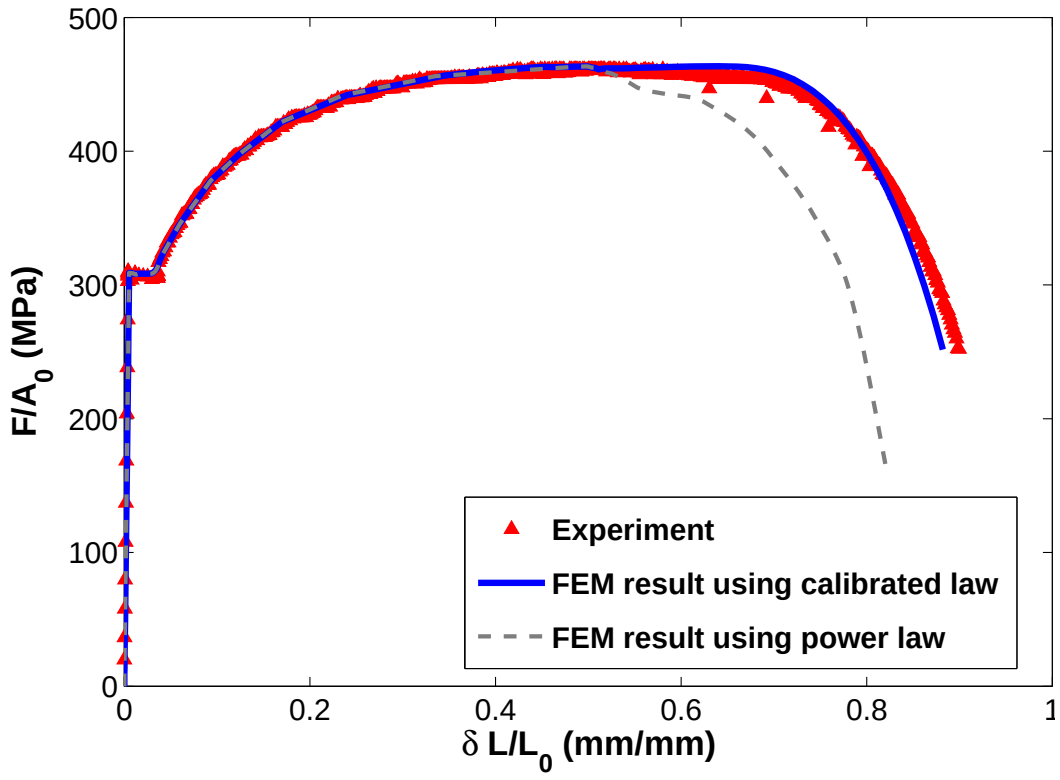

Figure 79: Measured versus computed load–elongation curves.

No path change			With path change		
ζ	$\bar{\epsilon}_c$	$\bar{\epsilon}_f$	ζ	$\bar{\epsilon}_c$	$\bar{\epsilon}_f$
			∞–ζ_{neck}	1.49	2.12
9.3	1.08	1.27	∞–10.4	1.08	1.21
9.3	—	1.33	∞–10.4	—	1.23
4.6	0.97	1.10	∞–3.5	0.82	1.03
4.6	—	1.08	∞–3.5	—	0.98
1.5	0.72	0.93	∞–1.7	0.75	0.81
1.5	—	0.97	∞–1.7	—	0.83
			∞–1.7	—	0.84
			∞–0.87	0.50	0.59
			∞–0.87	0.55	0.58
			∞–0.87	—	0.56
			∞–0.87	—	0.57

Table 3: Measured strains to crack initiation, $\bar{\epsilon}_c$, and final rupture, $\bar{\epsilon}_f$, as defined in Section 5.2.4. The values of $\bar{\epsilon}_f$ are averaged over up to three realizations (see Supplementary material online).

reduction measurements (Section 5.2.5).

Fig. 80(a) shows that the hardening curve of the material obtained as a result of the heuristic procedure lies below the power-law curve. For illustration, the power law overestimates the flow stress by about 75 MPa at a strain of 2.0. The corresponding evolution of the strain hardening rate is depicted in Fig. 80(b). The hardening rates of the power law and the corrected law are similar prior to necking then gradually deviate from each other at large strains.

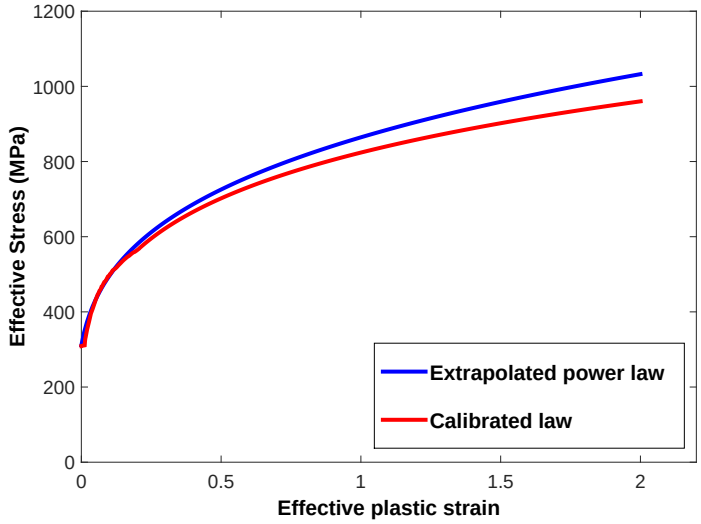

(a)

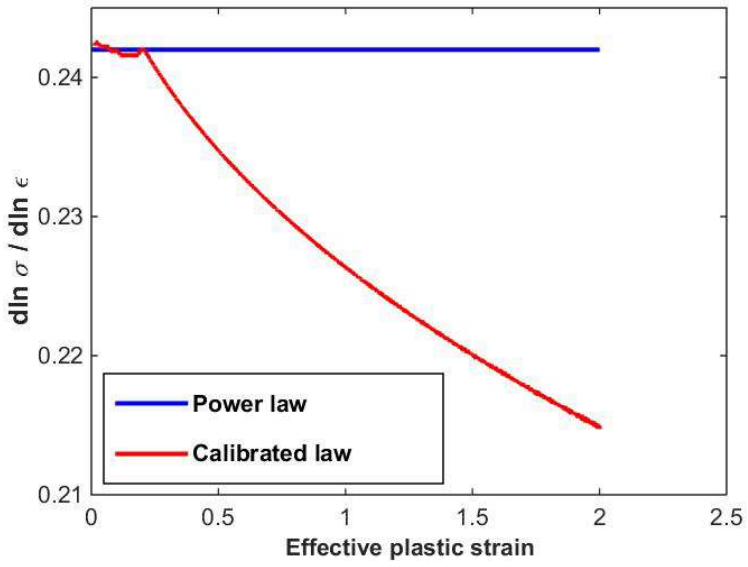

(b)

Figure 80: (a) Two hardening curves used in the finite-element simulations (beyond the yield plateau). (b) Corresponding hardening rates.

The heuristic procedure of Section 5.5.2 is based on the force–elongation response. The latter is not intrinsic to the material and depends on the geometry of the specimen. For this reason, one may question whether the hardening curve obtained using this procedure is representative. An additional check was made using the post-necking diameter measurements of Section 5.2.5.

Fig. 81(a) shows the experimental data of force, F, versus diameter reduction, $\Delta\phi$. The last recorded point was slightly before crack initiation and serves as basis for estimating $\bar{\epsilon}_c$ for the smooth bar, Table 3. It was not possible to record the descending part of the curve as for the notched bar experiments. The data is compared with the computed F–$\Delta\phi$ curve where $\Delta\phi$ is twice the displacement of the surface node at the neck. From this data one can plot the true axial stress, $\sigma_{22} \equiv F/A$ with $A = 4\pi\phi^2$ the current cross-sectional area, as a function of true axial strain estimated based on the $\bar{\epsilon}$ measure at the neck assuming plastic incompressibility throughout. This can be done for both experiments and computations. The comparison is depicted in Fig. 81(b). Both results in Fig. 81 increase confidence in the representativity of the hardening law reported in Fig. 80(a). All subsequent finite-element calculations of notched bars are carried out using this hardening law in tabulated form.

The computed force versus elongation responses are compared with their experimental counterparts for the three notched bars without path change and the four pre-strained bars (with path change) in Fig. 82(a) and Fig. 82(b), respectively.

The calculations in the latter figure account for the effect of pre-strain on hardening as described in Section 5.5.1. The computed curves match rather well the experimental ones up to the load drop. This indicates that the plasticity in the notched bars is well captured. The discrepancy noted for the $\zeta = 0.87$ specimen, Fig. 82(a), is likely due to the difficulty to realize a notch of such acuity, as pointed out in Section 5.2.3. The essential fact remains that the incidence on normalized

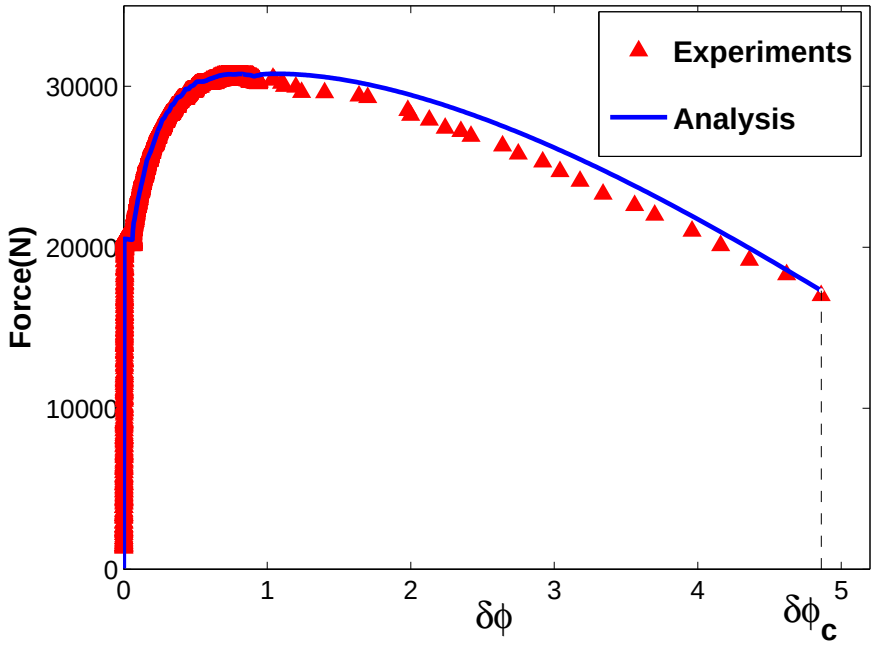

(a)

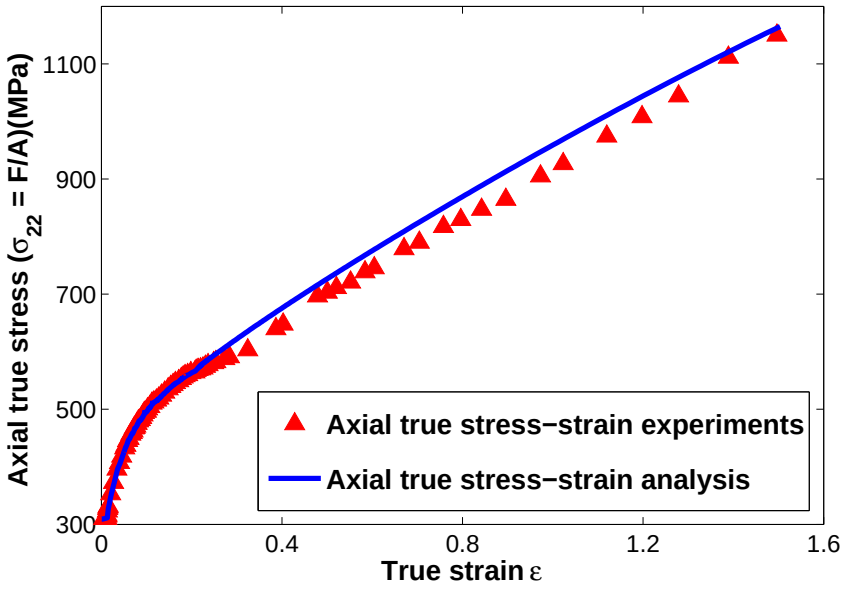

(b)

Figure 81: Refined analysis of post-necking response via the interrupted test technique. (a) Force versus diameter reduction, $\Delta\phi$, up to abrupt load drop at macrocrack initiation. (b) Axial true stress versus (total) true strain (assuming incompressibility) up to large strains.

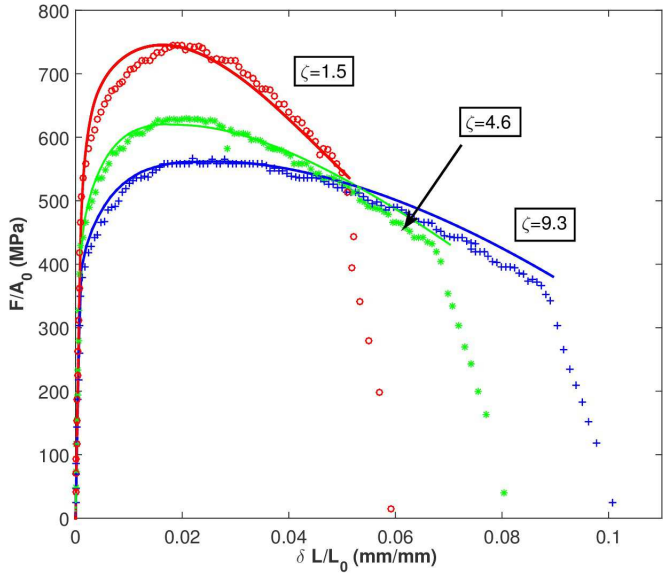

(a)

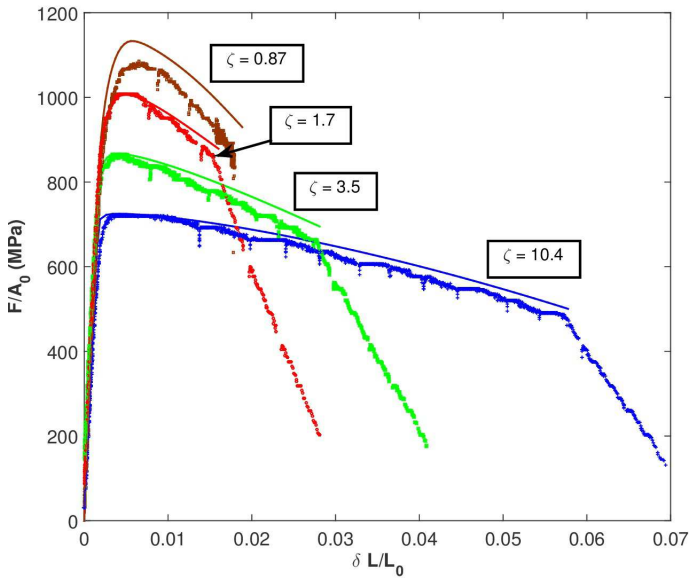

(b)

Figure 82: Calculated versus measured force-displacement responses of the notched bars: (a) without path change; (b) with path change (second step of loading only).

quantities, such as the triaxiality ratio, is small and without incidence on the central result.

As indicated above, the main objective of the finite-element calculations is to quantify the evolution of stress triaxiality in the specimens. This can now be addressed with good confidence placed in how the plasticity is captured in the notched bars. In what follows, details are only given for the local triaxiality, T^{loc}, which is evaluated at the Gauss point of the central element in each notched bar that is the closest to the center of the specimen. Furthermore, T^{loc} is given as a function of the global strain $\bar{\epsilon}$. The other two local (T^{loc} versus p) and global ($\langle T \rangle$ versus $\bar{\epsilon}$) relations are given as Supplementary Material online. Fig. 83(a) shows the evolution of triaxiality in the notched bars without path change whereas Fig. 83(b) gives the same in the pre-strained bars.

As expected, T^{loc} undergoes little variation in the plastic regime up to a strain $\bar{\epsilon} \sim 0.6$. Beyond this strain, the notch integrity changes in that the parameter ζ itself begins to evolve thus leading to an increase (or sometimes a slight decrease) in triaxiality. The variations are particularly significant in the bars with shallow notches where a neck develops at the notch root. It is worth noting that for sharp notches ($\zeta \leq 1.7$) the triaxiality is maximum near the notch root in the early stages of deformation. However, upon sufficient straining ($\bar{\epsilon} > 0.05$) the location of the maximum shifts to the center. There was no indication in the experiments that cracking initiated near the surface.

Both series of loading paths to fracture are superposed in one plot in Fig. 84. For the pre-strained bars, the uniaxial pre-loading is included. Consistent with the definitions in Section 5.5.5 the terminal triaxiality $T_{\text{c}}^{\text{loc}}$ versus $\bar{\epsilon}_{\text{c}}$ defines a fracture locus. Recall that $\bar{\epsilon}_{\text{c}}$ is associated with the knee in the load-deflection curve as per Section 5.2.4. The terminal values are shown as filled squares for the experiments

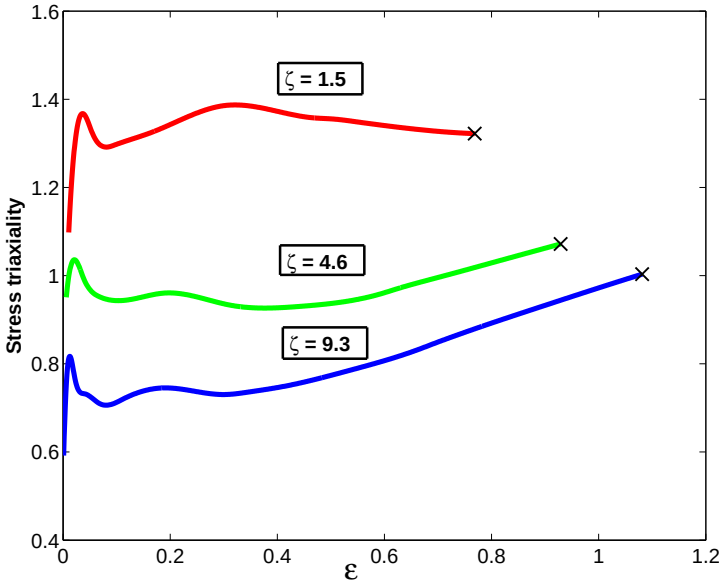

(a)

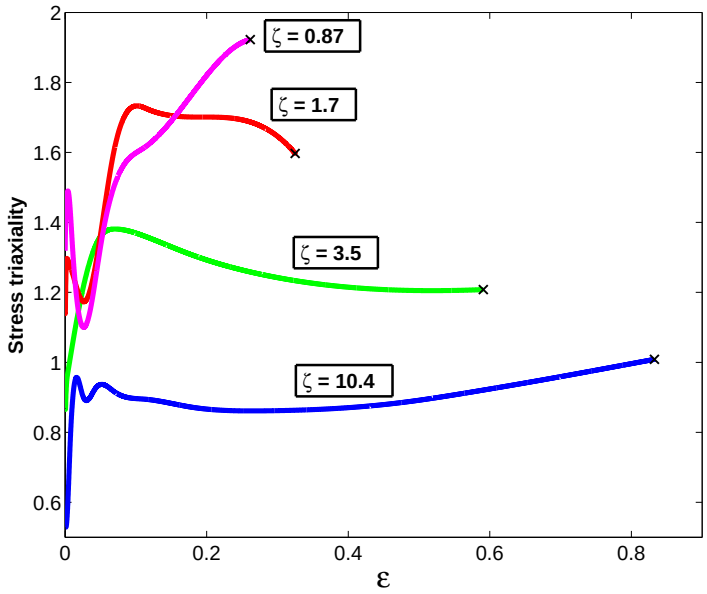

(b)

Figure 83: Stress triaxiality, T^{loc}, versus the global strain $\bar{\epsilon}$ in the notched bar specimens: (a) without prestraining; (b) with a 0.24 prestrain. The (x) refers to the value of $\bar{\epsilon}$ at which macrocrack initiation occurred in the experiments, i.e., $\bar{\epsilon}_{\text{c}}$.

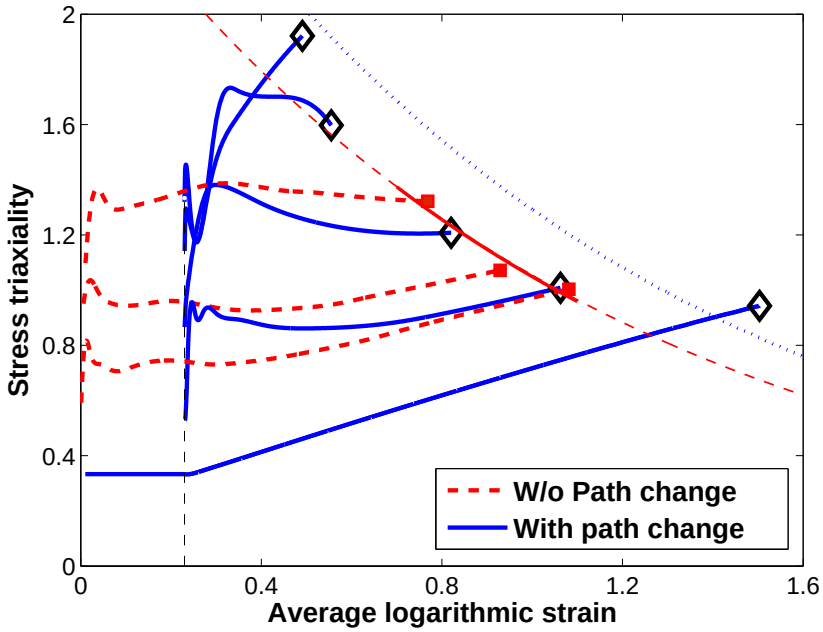

Figure 84: Evolution of stress triaxiality with global strain in representative experiments up to crack initiation. The plots are obtained by superposition of those in Fig. 83, adding the prestrain where appropriate and including the smooth bar specimen. The solid line is an exponential fit to the data without prestrain. The dotted line is obtained by translation of the solid one by ϵ^*. Scatter may be inferred from Table 3 or supplementary material online.

with no path change and as diamonds for the experiments with path change. The solid line joining the squares is a trend line used as a guide for the eye indicating the fracture locus with no path change. Interestingly, three data points corresponding to the experiments with path change fall close to that trend line. On the other hand, the two specimens that undergo the largest triaxiality variations beyond pre-straining, i.e., the $\zeta = 0.87$ specimen and the tensile bar, break at a strain beyond the trend line. These results, along with the dashed trend line in Fig. 84, will be further discussed in Section 5.8.

Fig. 85 shows the fracture loci corresponding to both series of experiments in terms of the strain to failure $\bar{\epsilon}_{\rm c}$ versus the strain-weighted average of triaxiality $\bar{T}^{\rm loc}$ defined by (16). For each series of experiments, the locus is dual to the corresponding locus in Fig. 84. Equation (16) is specified further as

$$\bar{T}^{\rm loc} = \frac{\epsilon^*}{\bar{\epsilon}_{\rm c}} T_0 + \frac{1}{\bar{\epsilon}_{\rm c}} \int_{\epsilon^*}^{\bar{\epsilon}_{\rm c}} \frac{\sigma_{\rm m}}{\sigma_{\rm eq}} \, {\rm d}\bar{\epsilon} \tag{19}$$

where $\epsilon^* = 0.24$ and $T_0 = 1/3$. In this kind of plots, load path changes impart a peculiar shape to the fracture locus. Obviously, this results from the averaging procedure. However, it illustrates the fact that multiple values of the fracture strain may be associated with the same average triaxiality, in keeping with the theoretical results of [24]. The datum corresponding to simple tension (where strong triaxiality variations are necking-induced) is included in the variant plot of Fig. 85(b). Note that the association of $\bar{\epsilon}_{\rm c}$ with the knee in the load-deflection curve introduces an uncertainty. In the present material, the maximum error is ± 0.02 strain, which is well within the experimental scatter.

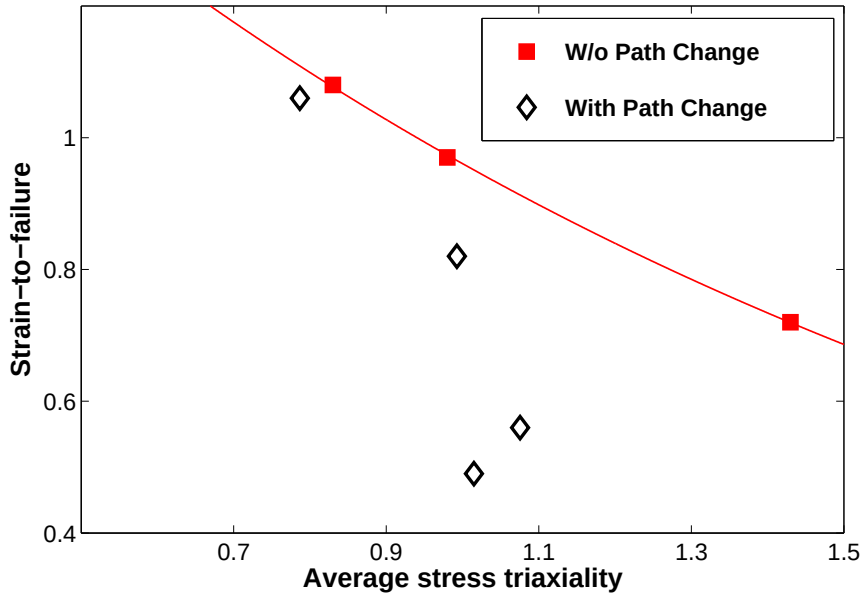

(a)

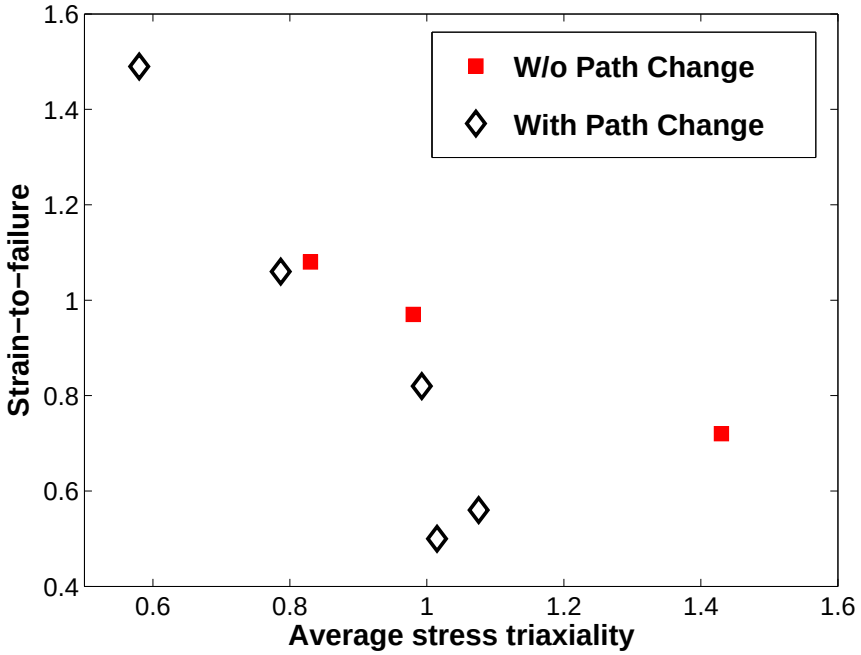

(b)

Figure 85: Dual fracture loci of those shown in Fig. 84. (a) Global strain to fracture $\bar{\epsilon}_c$ based on (14) versus the local $\bar{\epsilon}$-weighted triaxiality $\bar{T}^{\text{loc}}$ in (16) for the two sets of experiments. (b) Same plot including the smooth bar datum point. Strain measurement error in notched bars is ± 0.01; see Supplementary material online for scatter.

5.6.1 Data in Literature

Experimental nonradial loading paths described in Section 5.3 were analyzed using the simple fracture theory. For each set of experiments, actual loading paths were determined using the finite element calculations described in Section 5.5 and the fracture parameter $(R/R_0)_c$ was calibrated using models which will be discussed below.

5.6.1.1 Experiments of Marini et al.

Marini et al. [124] considered Type 1 loading, as sketched in Fig. 73a. Calculated triaxiality versus effective strain paths experienced by a material point at the location of failure initiation are shown in Fig. 86a for their experiments. The 'X' symbol here denotes the onset of failure as inferred from the experiments. The results in Fig. 86a are consistent with those of similar calculations in [124]. In particular, some anomalies in the data are to be noted. While reloading at a high triaxiality leads to lowering the fracture strain for most prestrain values, the data corresponding to $\varepsilon^* = 0.47$ seems inconsistent. No information was provided on neither the repeatability of this trend nor the applied strain rates. Also included in the figure are the three data points (squares) corresponding to experiments with no path change. These nominally define the radial fracture locus from Marini et al.

On plotting their findings on a strain to failure versus average stress triaxiality locus (Fig. 86b) it is observed that there are deviations from the radial locus. However, no overall trend can be deduced.

5.6.1.2 Experiments of Schiffmann et al.

Schiffmann et al. [142] considered Type 1 loading of the triaxiality step drop kind, as sketched in Fig. 73b. Calculated T–ε paths at the location of failure initiation

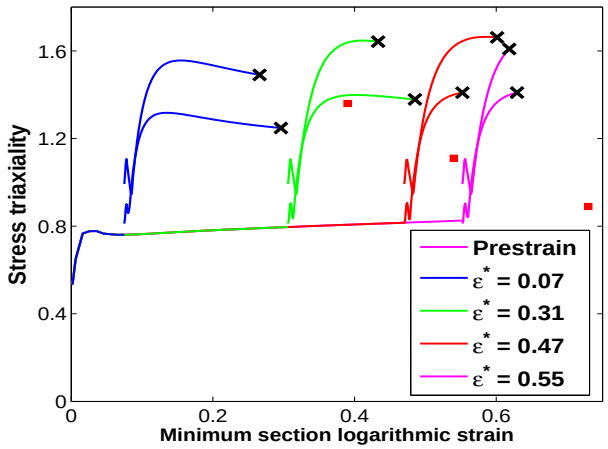

(a)

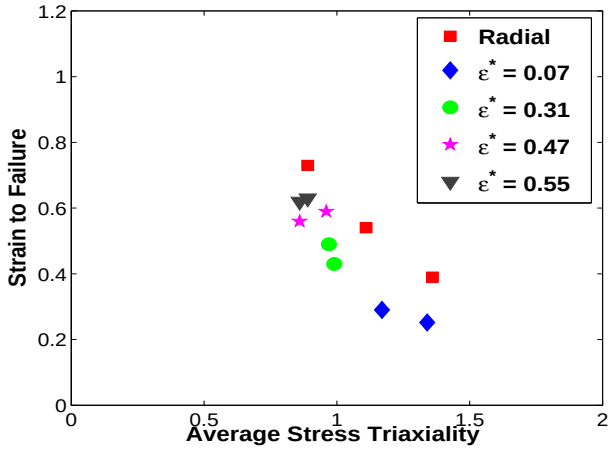

(b)

Figure 86: (a) Stress triaxiality, T, vs strain for a few load paths realized by [124]. Different prestrain levels are denoted by different colors and there are two different values of step jump in stress triaxiality at each prestrain. (b) strain to fracture versus the strain weighted triaxiality $\bar{T}$ for the two sets of experiments described in Fig 86(a).

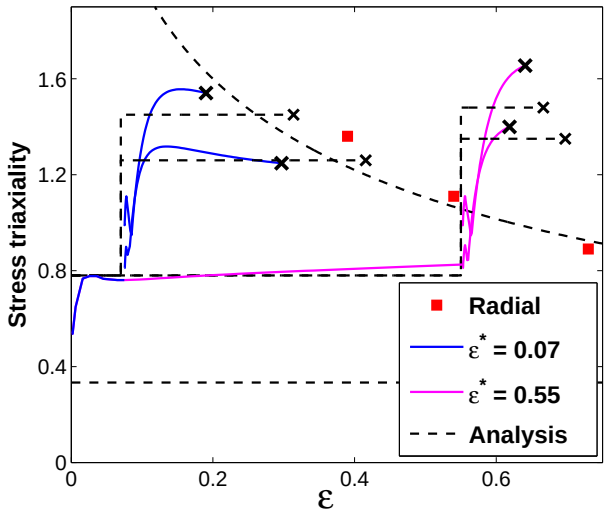

(a)

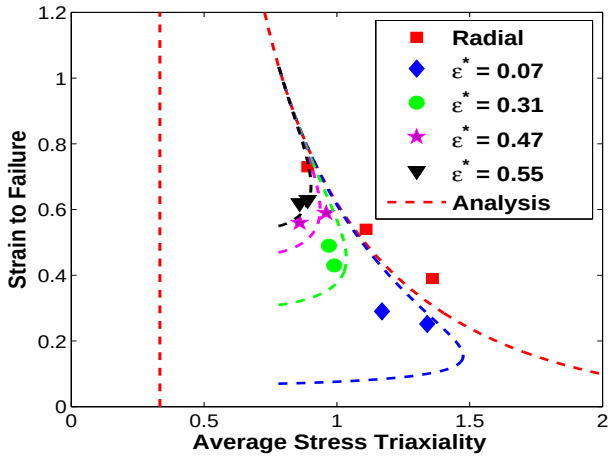

(b)

Figure 87: (a) Evolution of stress triaxiality with strain for a few loading paths for [124] with the analysis data superimposed on the experimental plots as dashed lines. Each path comprises of a step jump to 2 different values of stress triaxiality ratio after a prestrain to different values of ϵ^*. Each color represents the different prestrain levels under step 1 of loading. (b) Failure loci for proportional and non-proportional loading paths shown in fig. 86(a).

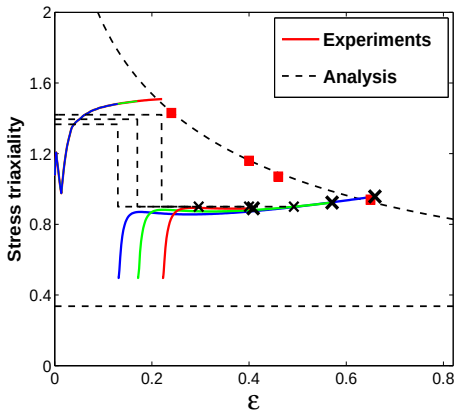

(a)

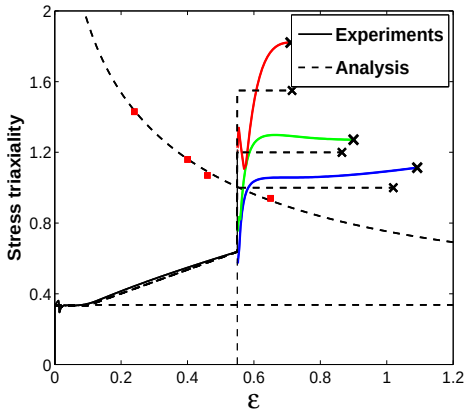

(b)

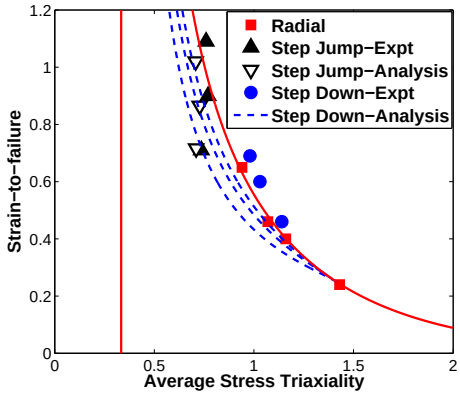

(c)

Figure 88: Load paths for loadings adopted by Schiffmann et al.[142] (a) step jump & (b) step decrease. (c) Failure loci in the strain to fracture versus the strain-weighted triaxiality $\bar{T}$ for the data shown in Fig 88(a)&(b).

are shown in Fig. 88a where the large 'X' symbol again stands for failure from their experiments; also see Table 2 for path parameters. Also included in the figure are four data points (squares) corresponding to experiments with no path change as reported in [142]. The loading paths shown dashed in the figure are idealized paths (strict T step drops). The small 'x' symbol in these corresponds to onset of failure as predicted by the model. The analytical model used to fit the radial experimental data had C=0.6775 and a $(\frac{R}{R_0})_c = 1.25$. Discrepancies aside, the results indicate that the fracture strains lie below the radial fracture locus.

Schiffmann et al. [142] also considered the mixed type loading sketched in Fig. 73c. Calculated T–ε paths at the location of failure initiation are shown in Fig. 88b along with idealized paths shown in dashed. As above, the large 'X' and small 'x' symbols stand for measured [142] and predicted fracture strains (extended model); also see Table 2 for path parameters. As in Fig. 88a, the four experimental data points (squares) defining the nominal radial locus are included. The discrepancies here between measured and fracture strains are much smaller. Here, the key observation is that the fracture strains lie above the radial fracture locus

When the results of Schiffmann et al. [142] for both types of loading are plotted on a ε_{f}–$\bar{T}$ locus (Fig. 88c) deviations from the radial locus are noted, just like for the data of Marini et al. in Fig. 86b. However, once again no overall trend stands out. On the other hand, when predictions based on the simple theory are superposed onto the experimental data, it is possible to rationalize the trends, although the unavoidable quantitative discrepancies come in the way of a clearer picture. We emphasize that solely based on the data, it is difficult to uncover the fundamental trend because the data is limited for a given choice of prestrain.

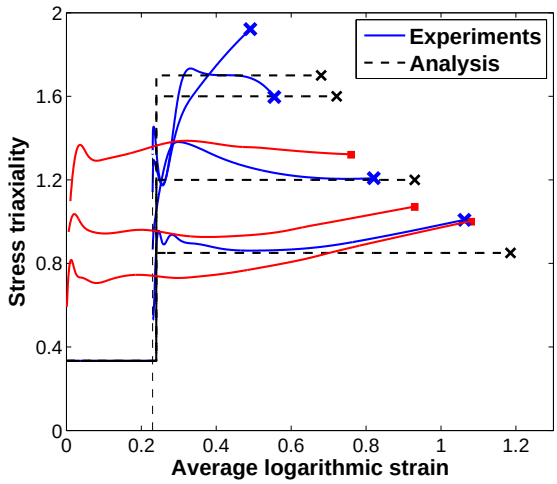

(a)

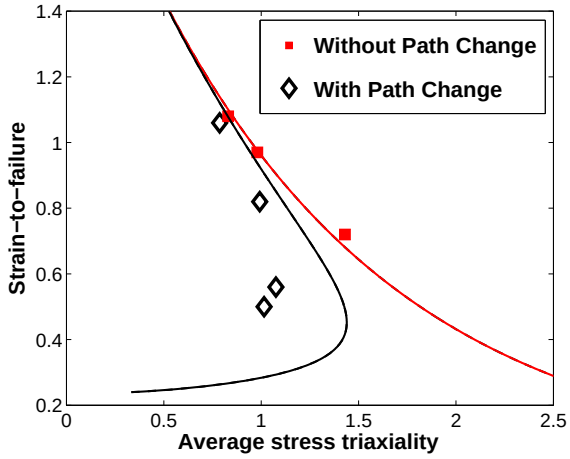

(b)

Figure 89: (a) Evolution of stress triaxiality with global strain in representative experiments up to crack initiation by [63]. The solid line refers to the data from the experiments while dashed lines are obtained superimposing the model predictions on the experimental data. (b) Fracture loci of the loadings shown in Fig.89(a) with the results of the model plotted in solid lines

5.6.1.3 Experiments of Basu & Benzerga

Basu and Benzerga [63] considered Type 1 loading that complements the experiments in [124, 142]. The paths they studied are sketched in Fig. 73d. Calculated T–ε paths at the location of failure initiation for some of their experiments are shown in Fig. 89a (solid lines). Path and model parameters were provided in Tables 2. Idealized paths used in fracture prediction are shown dashed as above and the square data points correspond to experiments with no path change from [63]. Also, the 'X' and 'x' symbols bear the same meanining as in preceding figures. On the basis of the theoretical analyses[144], specifically the results for $T_0 = 1/3$, the predicted fracture points 'x' are expected to lie on a curve translated from the radial locus by the amount of prestrain, here 0.23. This holds, albeit approximately due to model imperfections to be further discussed below. Analytical function given in equation 20 is used to calibrate the radial curve.

$$\frac{\dot{R}}{R} = 0.427 \exp\left(\frac{3}{2}\frac{\Sigma_m}{\bar{\sigma}}\right)\dot{\epsilon} \tag{20}$$

Here too, if the data are represented in the ε_{f}–$\bar{T}$ plot (Fig. 89b) then the following is observed. First, the deviations from the radial locus are much clearer than in previously published experiments; for reference see Fig. 86b and Fig. 88c for the data in [124] and [142], respectively. This is due to the consideration of very sharp notches ($\zeta < 2$) upon load path change in [63]. In addition, the simple fracture theory rationalizes the trend (solid line in Fig. 89b) inspite of the quantitative discrepancy.

5.7 Results: Mg Sheets

5.7.1 Global Response

The force in step 2 of the loading was resolved into components along the two principal directions as shown in section4.2; T denotes transverse force along the x-direction and N corresponds to normal force along the y-direction. Both vertical and horizontal displacements were extracted from the DIC with corrections for rigid body motion. The normal component of the force shown as N in Fig. 90 were plotted against the vertical component of the displacement v. The transverse component of the force T is plotted against the horizontal displacement u. It is observed that the transverse component of the load displacement curve shows a higher hardening rate as seen from the slope of the curves indicating that the material hardens more rapidly in shear. One possible reason for this is that some compressive stresses develop in the plane of the sheet. Although not dominant, such compressive stresses must be accommodated, which leads to positive through-thickness strains in some regions. The latter can be accommodated through some pyramidal slip but also some extension twinning, which is known to be a soft deformation system. Also, when extension twinning is active, the stress-strain curve typical exhibits the S-shape. Detailed analysis of such phenomena would require crystal plasticity or lower scale simulations.

It was observed that the force displacement plots show similar trends to that seen in no path change experiments; with increase in angle α the value of T decreases and the value of N increases. Similarly, the resolved force versus displacement response for step 2 of path 2 is shown in Fig. 91 for all loading orientations. The difference that was observed from the no path change experiments is that the hardening response for the step 2 of the loading reduced compared to both load path changes and no

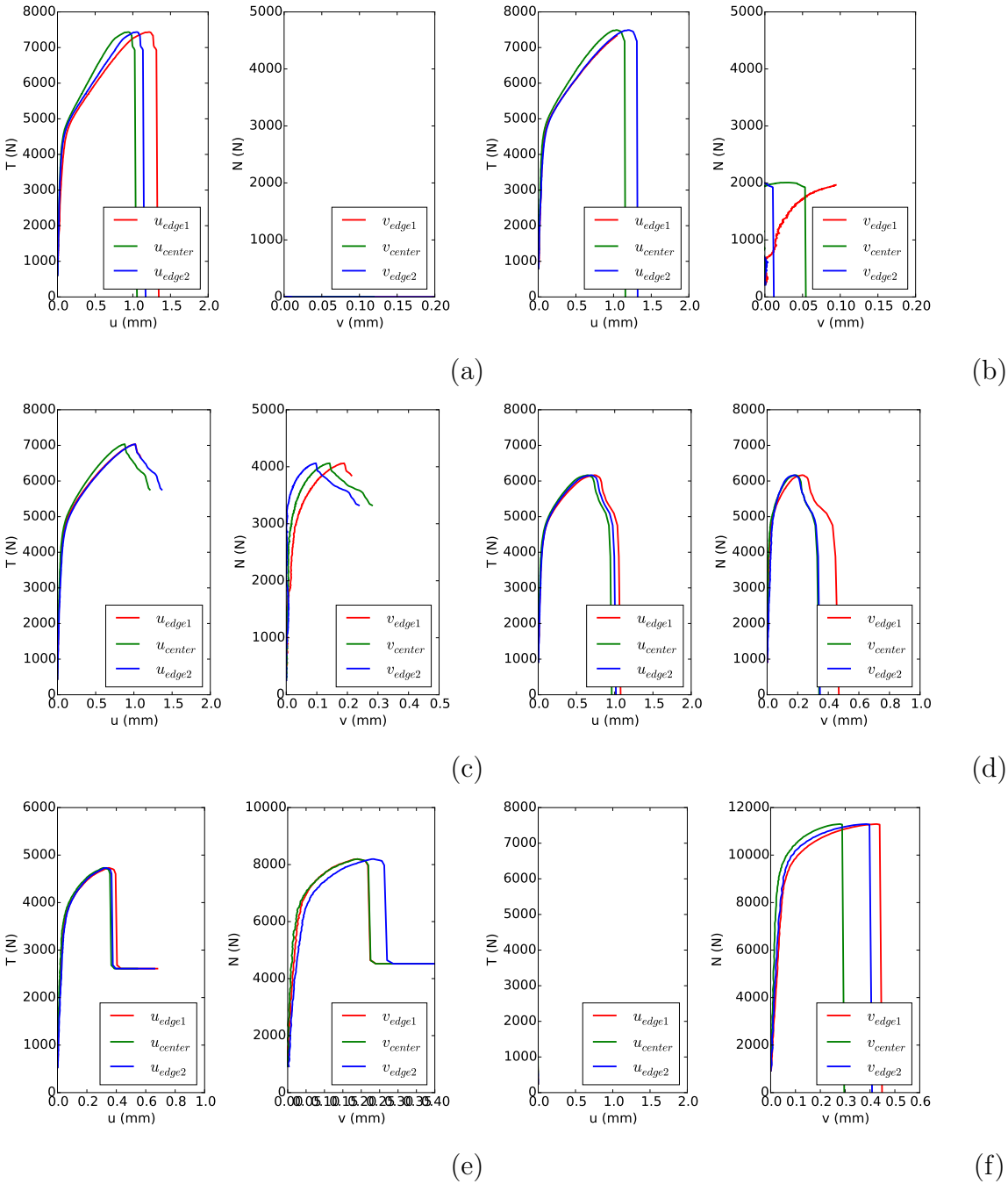

Figure 90: Force versus displacement plot resolved for experiments for different orientations (a) 0° (b) 15° (c) 30° (d) 45° (e) 60° (f) 75° after prestraining in tension($\alpha = 90°$).

path change experiments. The hardening for the normal part of the loading is seen to improve with increase in reloading α.

5.7.2 Strains at Different Locations

Digital image correlation strains indicate similar trends in the evolution of components of the strain tensor in experiments with path change compared to the samples without path change. The evolution of decomposed force with the respective decomposed measure of strains was plotted at the maximum, center and the average values for step 2 of loading paths as shown in Fig.104 and Fig.105. As seen in step 2 of strain path change involving prestraining in tension, on reloading in step 2, we observe that the hardening of the stress strain response reduces slightly.

Figure 106 and Fig.107shows the decomposed force with the respective decomposed measure of strains evolution after strain path change involving prestraining in shear. It is seen that reloading after prestraining in shear leads to similar load levels after reloading, however, the hardening rate is reduced. The values of the strains are smaller compared to the experiments without path change. The value of strain at the the max location is seen to drastically increase in most of the loading in the tensile part of the loading, indicating the presence of a moment as a result of the top and the bottom loading screws not being aligned in a straight line due to the prestrain. The figures are reported in the Appendix as the figures were bulky.

5.7.3 Load Paths

Fig.92 shows the normalized load versus equivalent strain plot at center, maximum location and averaged over the minimum section. This is plotted for the complete loading path 1. The common prestrain for all samples remain the same followed by reloading under different loading orientations.

No stark differences are seen from the no path change experiments, except that

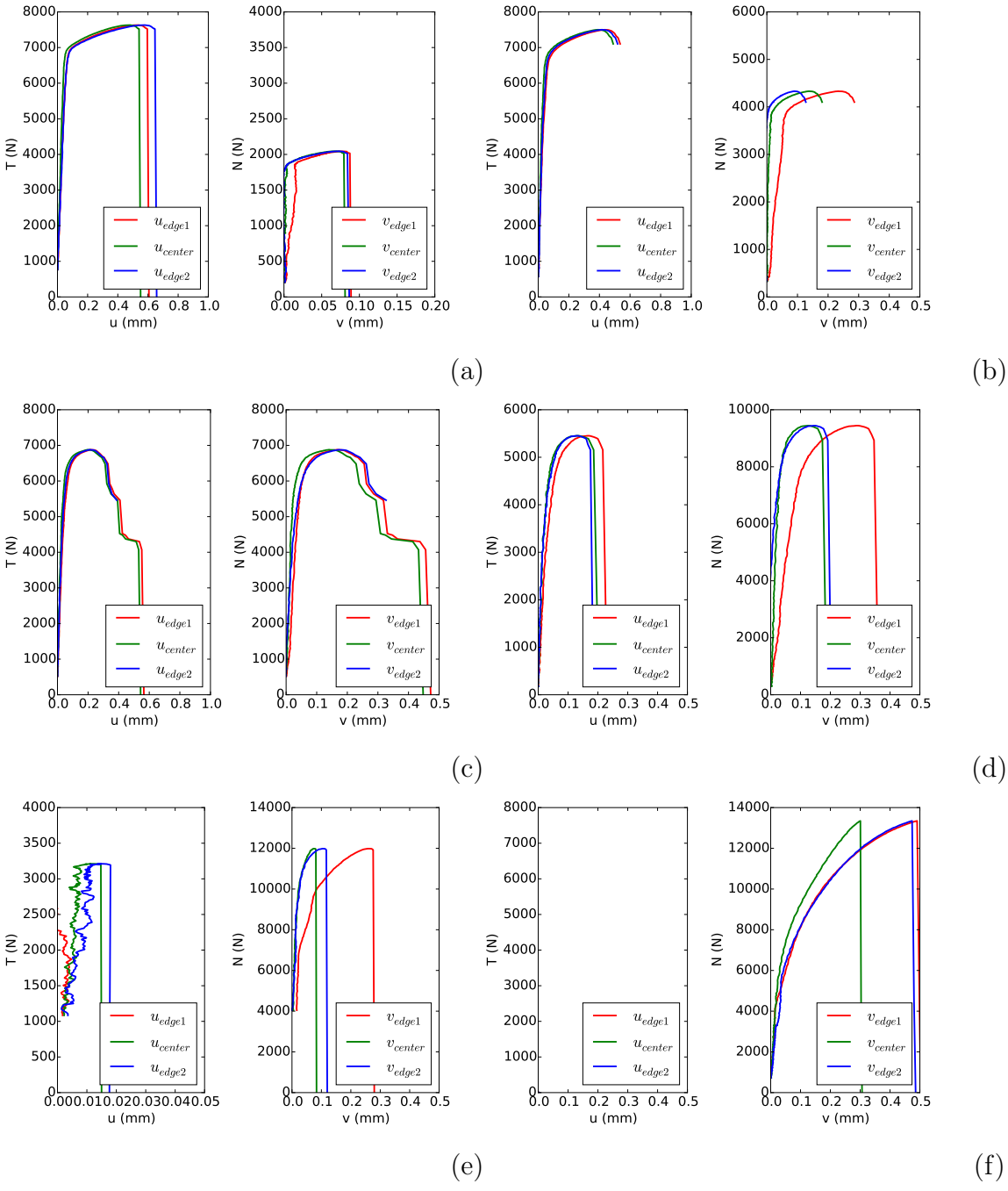

Figure 91: Force versus displacement plot resolved for experiments for different orientations (a) 15° (b) 30° (c) 45° (d) 60° (e) 75° (f) 90° after prestraining in shear($\alpha = 0°$).

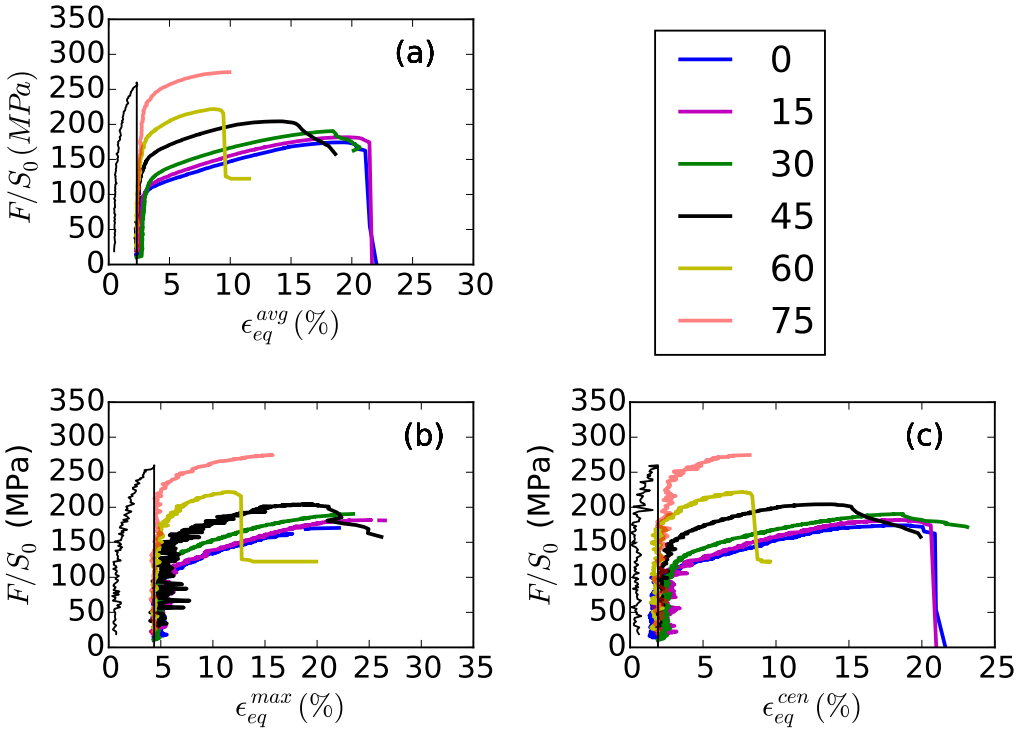

Figure 92: Force versus displacement response for experiments with path change for step decrease involving prestraining under orientation 90° followed by reloading at different orientations to failure.

the response in the low angle α loadings are lumped closer together in terms of load levels and comparable ductility. There is an increase in ductility under 75° loading compared to the 60°. The 60° plot shows a flat part in the curve after load drop indicating that the sample does not undergo complete failure.

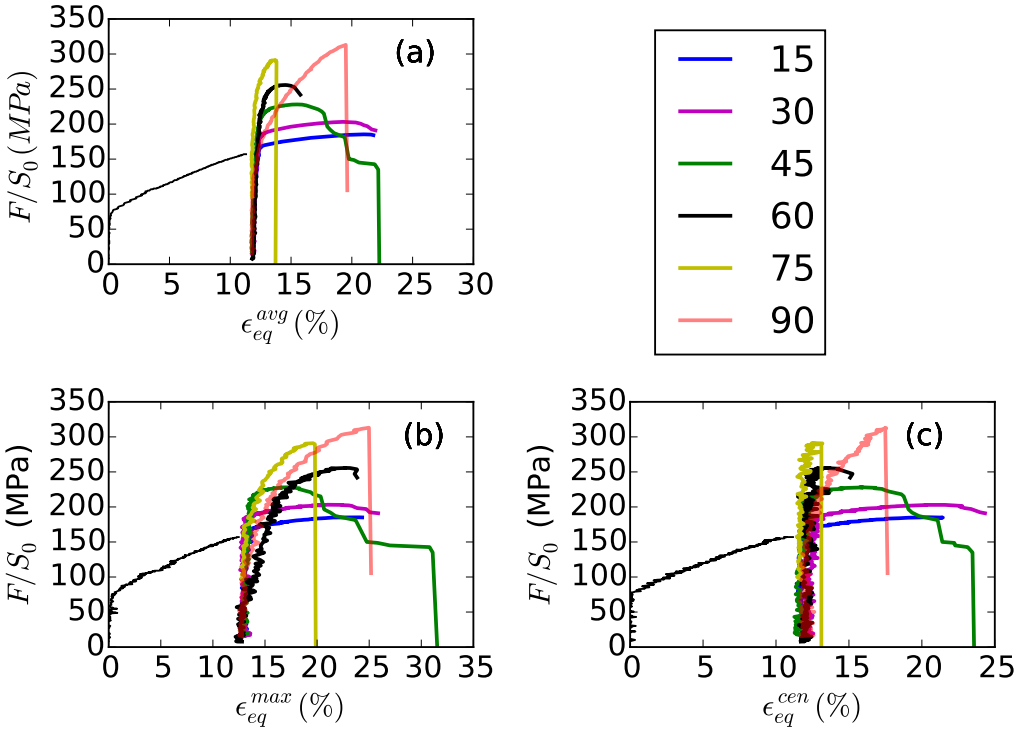

Figure 93: Force versus displacement response for experiments with path change for step jump involving prestraining under orientation 0° followed by reloading at different orientations to failure.

Fig.92 shows the normalized load versus equivalent strain plot at center, maximum location and averaged over the minimum section. This is plotted for the complete loading path 1. The common prestrain for all samples remain the same followed by reloading under different loading orientations. As observed, the total

load path shows comparable ductility levels compared to the experiments without path change. The only exception in this case is the 90° orientation that shows improvement in ductility with the path change.

5.7.4 Failure Loci

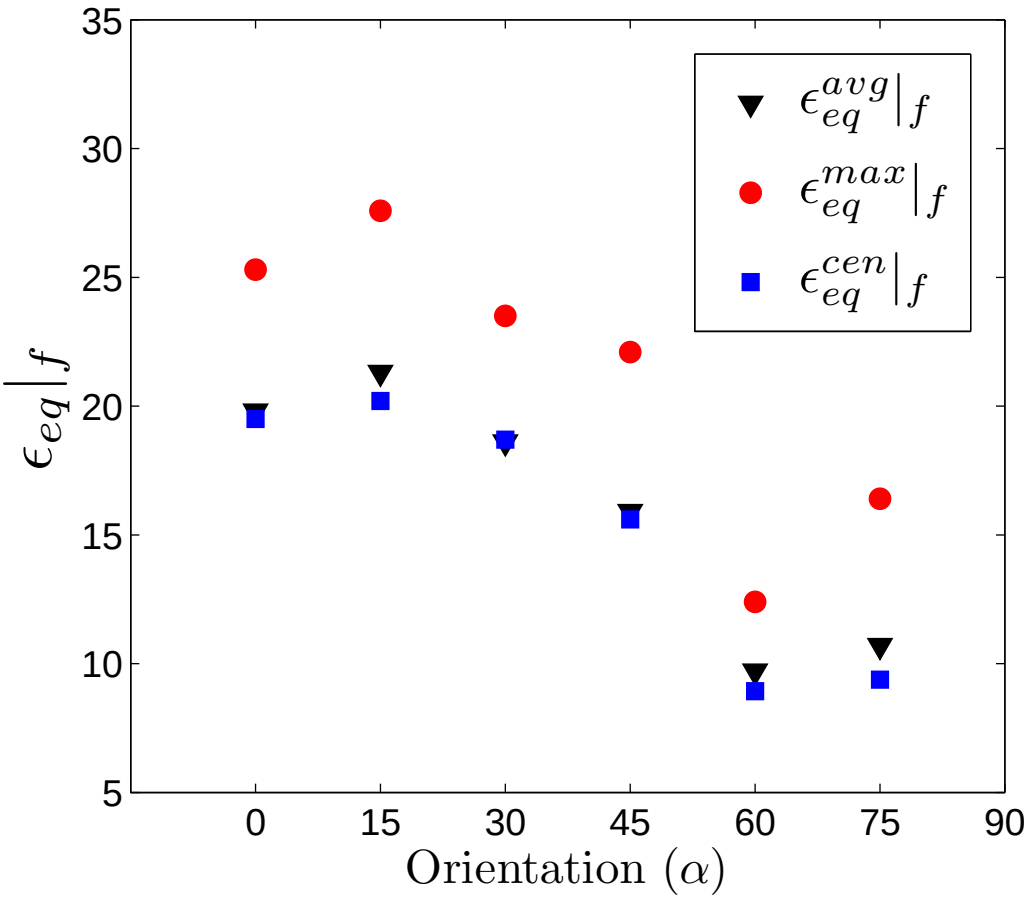

Figure 94: Total failure strain with respect to orientation of the sample at maximum, center and averaged over the cross-section for path 1 involving prestraining in tension.

Finally the value of the total failure strains at maximum, average and at the center of the specimen were plotted with respect to the orientation of each specimen

during loading as shown in Fig. 94 to show the loci of failure for path 1 of the loading, which involves prestraining in tension followed by reloading at a different orientation till complete failure. The trend observed is the value of the strain to failure totaled over the whole path shows a decreasing trend overall with the first and the last data points 0° and 75° being slight outliers in all measures of failure strains.

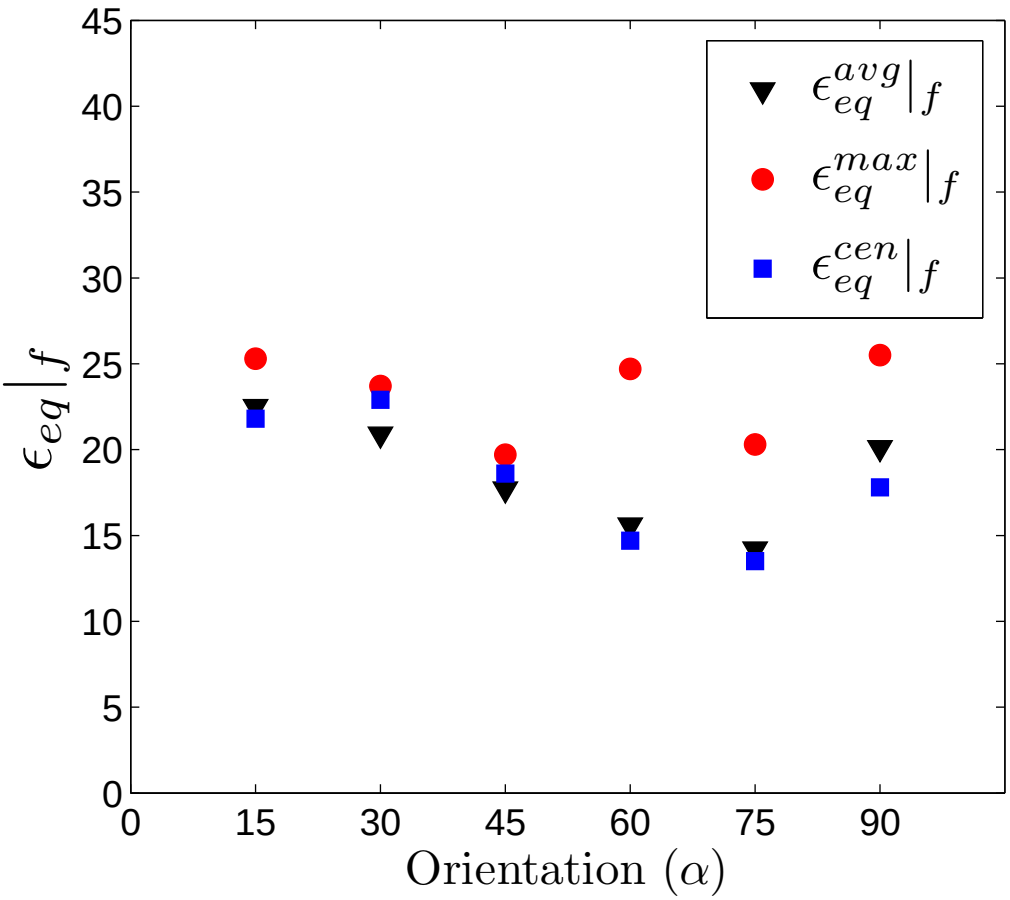

Figure 95: Total failure strain with respect to orientation of the sample at maximum, center and averaged over the cross-section for path 2 involving prestraining in shear.

Fig.95 shows the loci of failure strain at various locations of the sample after

prestraining in shear. The strains reported are the total strains over the whole path of the loading. It is observed that the failure strains in all measures decreases with increase in angle of orientation α till the loading is predominantly shear. As the loading orientation changes to predominantly tensile the value of the failure strain at the maximum locations increases, while the center and the average strain keep reducing. The only exception is the orthogonal loading 90° where all measures of strain to failure increases and to values that are greater than most other loadings.

Fig.96 shows comparison of the failure loci under each measure of $\bar{\epsilon}_c$ with the same measure of strain for no path change. It can be seen in Fig.96(a), (b) and (c) that the values of the failure strains with or without path change coincide for a few loading orientations, however, a few orientations show lower or greater values of strains compared to no path change experiments.

Fig.97 shows the value of the failure strain as a loci of the orientation angle α at maximum, center and average locations. Strains at failure at different locations indicate that the value with path change show higher values of $\bar{\epsilon}_c$ than the experiments without path change. This difference is found to be the highest in the case of reloading $\alpha = 90°$.

5.8 Discussion

5.8.1 On the Notion of Fracture Locus

When all components of the stress tensor are increased proportionally and the ductile material deforms to fracture[4], the ratio of any two stress invariants, properly nondimensionalized, remains constant. Hence, not only the stress triaxiality T but also the Lode parameter, L, remain constant in the course of deformation. An intrinsic fracture locus may be defined in terms of the strain-to-failure $\bar{\epsilon}_c$ viewed as

[4]In the present context, fracture means incipient macroscopic cracking.

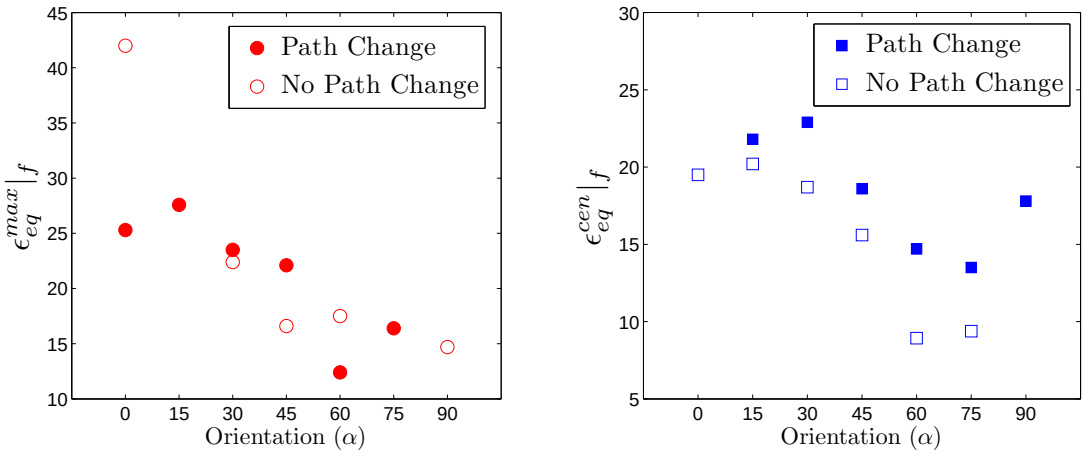

Figure 96: Total failure strain for path 1 at (a) maximum (b) center and (c) average location for experiments with and without path change shown in filled and unfilled symbols respectively.

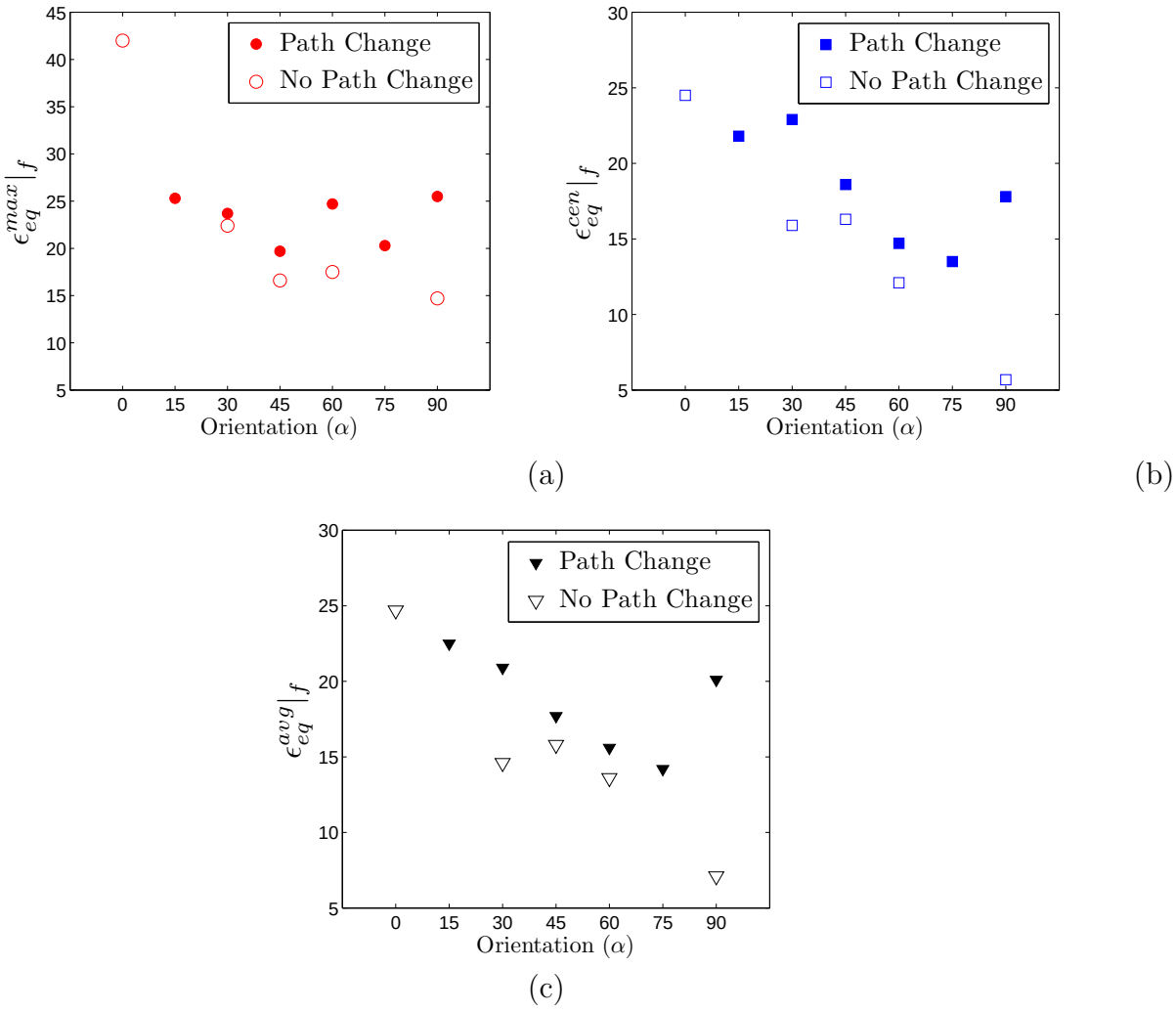

Figure 97: Total failure strain for path 2 at (a) maximum (b) center and (c) average location for experiments with and without path change shown in filled and unfilled symbols respectively.

a function of T and L.

An important fact that is understated in the recent literature is that, with the above definition, the intrinsic fracture locus of a ductile material is *not* accessible to experimental measurement for it is impossible, in general, to impose constant-T and L loadings. Deviations from proportionality in real experiments are more prominent at very low (e.g., simple tension or shear) or very high (crack tip) triaxiality. The aim of this and previous companion work has been to explore the type and magnitude of deviations from the so-defined intrinsic locus that would follow from non-proportional loadings. In the computations of [24] the intrinsic locus was readily accessible because T and L were held strictly constant. Here, the round notched bar experiments realize a locus that is the closest to the intrinsic one. The latter is represented by the solid lines in Figs. 84 and 85. It is emphasized that the trend line is strictly valid within the investigated range of triaxiality. Any extrapolation outside this range requires a theory of ductile damage.

5.8.2 On the Interpretation of Deviations

The magnitude of deviation from the nominally intrinsic locus clearly depends on what definition is adopted for the fracture locus under nonproportional loadings, as may be inferred by comparing Figs. 84 and 85. There is duality between the two loci ($\bar{\epsilon}_c$ versus either the terminal or average triaxiality). This duality obviously disappears under proportional loading but can be exacerbated for certain types of nonproportional loadings. Here, with the choice made for uniaxial preloading ($T_0 = 1/3$) and a step-jump in triaxiality, the largest deviations are obtained when the strain-weighted average triaxiality is used (Fig. 85).

The reason for this is two-fold. Obviously, the use of a strain-weighted average of triaxiality over the loading path is one. This, however, is not sufficient as the

damage accumulation rule must be nonlinear. Indeed, analysis shows that a damage accumulation rule that is linear in T would deliver indistinguishable loci under proportional and step-jump in T type loadings [24]. In view of the active damage processes (Fig. 77) it is expected that the rate of increase of damage (mainly in the form of porosity in this material) is rather exponential in T within the range explored. In fact, the use of triaxiality averaging is neither sufficient nor necessary for the emergence of large deviations from the intrinsic (or proportional) fracture locus. For instance, [144] have shown that for a step-decrease in triaxiality, the largest deviations from the intrinsic locus are often obtained when using the $\bar{\epsilon}_c$ versus terminal, not average, triaxiality.

[24] rationalized the difference between the computed fracture loci under proportional and nonproportional loading on the basis of (i) the exponential dependence of void growth on stress triaxiality; and (ii) the averaging of stress triaxiality over the loading path. To some extent, the same rationale applies here. The reader is, therefore, referred to the companion paper for more details. In what follows, focus is laid on interpreting the results in Figs. 84 and 85 with due respect given to differences between numerical and actual experiments. Indeed, the steel used in the experiments does not contain initial voids and when the latter nucleate they are not distributed periodically, as assumed in the cell model studies. In addition, load path changes affect the hardening behavior of the material in ways that were not included in the cell model calculations. There are other differences, of course, but they play a secondary role. For example, there is a potential effect of the material's rate-sensitivity. Given the care taken to minimize nominal strain-rate variations in the experiments, this effect is small.

Consider first the fracture loci in Fig. 84. When the analysis framework initiated in [24] and further developed recently by [144], is applied to a step-jump in triaxiality

(as realized here with $T_0 = 1/3$) the fracture locus is found to be a simple translation of the intrinsic locus by the amount of prestrain ϵ^*. The translated locus is shown dashed in the figure. In other words, the fracture strains should lie on the translated curve. Clearly, there is no trend for this happening in Fig. 84: the datum for the smooth bar overshoots while three other points lie on the intrinsic locus; this seems fortuitous. There are two reasons for this behavior. The first is rooted in the decrease in the hardening capacity of the material after prestraining, which was not accounted for in the above-mentioned analyses. The lower the hardening rate the faster the rate of void growth, e.g., [145]. One way to verify this is to anneal the specimens after unloading from step 1 and prior to machining the notched bars for step 2 loading. This work is underway and will be reported elsewhere, given that the outcome would not affect the essential message of the present work. The second reason is that the analytical model used by [144] does not predict any net void growth during prestraining at $T_0 = 1/3$, which is the exact micromechanical response; see [45] for an overview of void shape effects. In the real experiments, if nucleation occurs during prestraining, some void growth does take place in uniaxial loading due to a particle-induced void locking phenomenon [146]; see Fig. 3.4 in the monograph by [45].

In summary, the experimental fracture loci in Fig. 84 are in qualitative agreement with the theoretical results: cell model simulations [24] and analytical [144]. The quantitative differences result from the fact that (i) some porosity growth occurs during prestraining in the experiments but not in the simulations or analytical model; and (ii) void growth in the pre-strained notched bars accumulates faster than in the bars loaded straight to failure due to a lower hardening rate in the former. Both effects contribute to the ductility under load-path-change being lower than expected. This in turn makes the effect of this type of nonpropotional loading worse than

expected on the basis of theory.

5.8.3 Sensitivity of Trends to Fracture Locus Definition

When the fracture strain is plotted against the average triaxiality the deviations from the nominally intrinsic locus are large for the type of loadings considered here (Fig. 85). This deviation has to do with the averaging procedure. Having introduced other definitions of fracture loci in Section 5.5.5, the question arises as to how sensitive the reported trends are to the specific choice of fracture locus definition.

Fig. 98(a) depicts the locus of local effective plastic strain at failure, p_c, versus $\bar{\bar{T}}^{\mathrm{loc}}$, the average local triaxiality defined in (17). Also, Fig. 98(b) shows the locus of global strain to failure $\bar{\epsilon}_{\mathrm{c}}$ versus $\overline{\langle T \rangle}$, the strain-weighted and spatially averaged triaxiality, defined in (18).

It is emphasized that all six definitions (the above three and their dual plots with terminal triaxialities) collapse into a unique locus (the intrinsic one) under spatially uniform proportional loading. For the sake of brevity, the metadata needed to make Fig. 98 is omitted and provided as Supplementary Material online. Examination of Figs. 85 and 98 shows that the quantitative details vary from one plot to the other but that the qualitative trends are preserved.

Interestingly, the locus labeled "without path change" is less sensitive to the adopted definition. This is consistent with this locus being close to the intrinsic one. However, obtaining the latter over a broader range of triaxialities is difficult, if at all possible. As mentioned above, the intrinsic fracture locus, in its full extent, is not accessible to experimentation alone. In practice, what can be measured are (an infinity) of fracture loci under nonproportional loadings out of which laboratory experiments single out a small subset. As such, these loci inform indirectly about the damage constitutive response of the material. In particular, it would be deficient

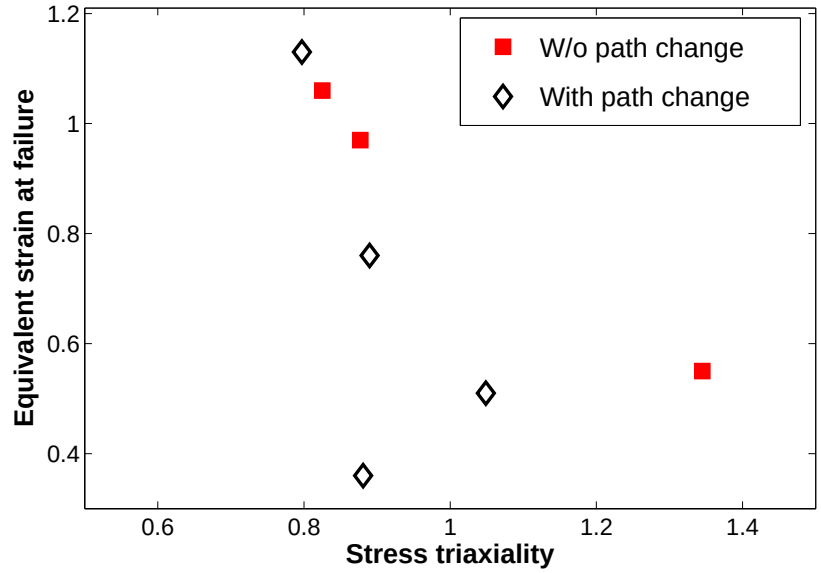

(a)

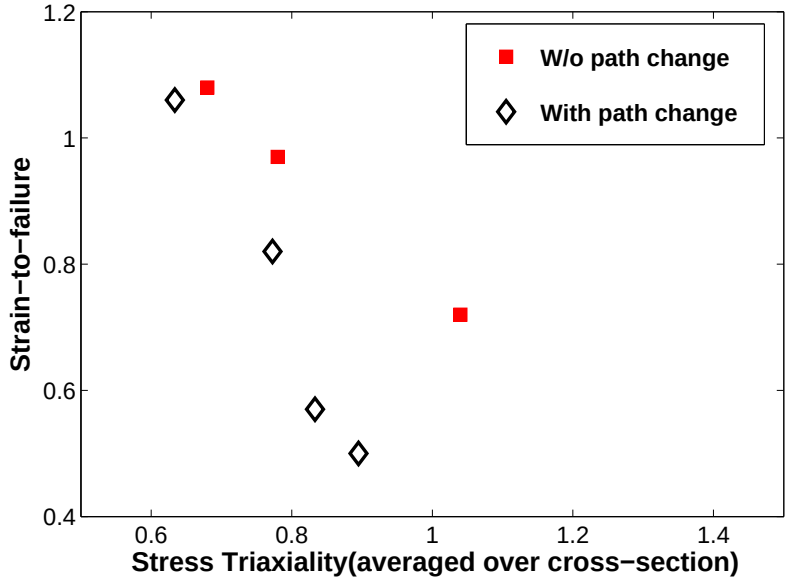

(b)

Figure 98: (a) Loci of local strain to fracture p_c versus the local p-weighted triaxiality $\bar{\bar{T}}^{\text{loc}}$ in (17) for the two sets of experiments. (b) Loci of global strain to fracture $\bar{\epsilon}_c$ based on (14) versus the global $\bar{\epsilon}$-weighted triaxiality $\overline{\langle T \rangle}$ in (18).

to use an experimentally measured fracture locus to construct a fracture model.

5.8.4 Reanalysis of Data in Literature

Nearly three decades after the publication of the first experiments on this topic by Marini et al. [124] it is fair to say that the picture on nonproportional loading effects in ductile fracture was at best cloudy. On the one hand, the various investigators indicate that the nonproportional loading paths do not end on the radial fracture locus [124, 142, 126, 63]. On the other hand, interpretations of the various experiments have remained elusive and sometimes conflicting. In addition, when the fracture strain ε_{f} is plotted versus the strain-weighted average triaxiality the data appears so clustered that the trends are inconclusive; see for instance Fig. 86b and Fig. 88c. Here again, the simple theory proved useful in providing a rationale for the experimental trends, some of which were reported in this paper (Figs. 87b, 88c and 89b.)

Reanalysing data from the literature and understanding trends with the help of an analytical model have helped us confirm the loading histories predicted by the model in this paper. In general, effects of nonproportional loading can manifest in various ways. The general scenario is quite complex because of unavoidably intertwined history effects on both damage-free *plasticity* and plasticity-induced *damage*. Even when kinematic hardening is small, as is probably the case in the steels used in the experiments [124, 125, 142, 126, 63], the loss of isotropic strain hardening capacity due to prestraining must be accounted for in any quantitative prediction. The simple fracture theory above is insensitive to strong hardening effects since the term $\Sigma_e/\bar{\sigma}$, which involves the matrix flow stress, is lumped into the triaxiality. In part, this explains the discrepancy noted between the measured and predicted fracture strains in the various results reported above. Another factor is that the idealized loading

paths impart some additional errors compared with the actual paths calculated by finite elements.

Another aspect that is worth discussing in the context of nonradial loading experiments on steels is potential complications associated with the onset of cleavage, as reported for example by Enami [147]. In the experimental results from the cited literature [124, 125, 142, 126] it was not clear whether the authors had maintained the same nominal strain rate in the notched region upon reloading in step 2. For example, Basu and Benzerga carefully rescaled the remote displacement rates in their experimemnts so as to ensure the same nominal strain rate prior to and after path change. This is important because if the remote displacement rate is kept the same, then the strain rate inside the notch would be much higher, thus possibly leading to fracture by cleavage. This is illustrated in Fig. 99

showing fractographs from additional experiments not reported in [63]. In turn, such spurious strain rate effects may also explain some inconsistencies in the data found in the literature. In all experiments reported in [63] cleavage was avoided when extremely sharp notches were used in the reloading step.

5.8.5 History Effects on Failure under Combined Tension and Shear

It is important to realize how history of deformation can effect failure in sheet metal. This is important as most metal forming processes involve complex deformation histories. Many of these steps may involve prestraining the metal in tension or shear of complex mixed mode loadings. The experiments performed here are aimed at studying the effect of load path changes on ductile fracture in sheet material. Two different load paths were applied here to study how these would affect the failure strains. We have seen in Fig.96 and Fig.97, how the total strains are affected by these load path changes. It is however important to compare how each prestraining would

(a)

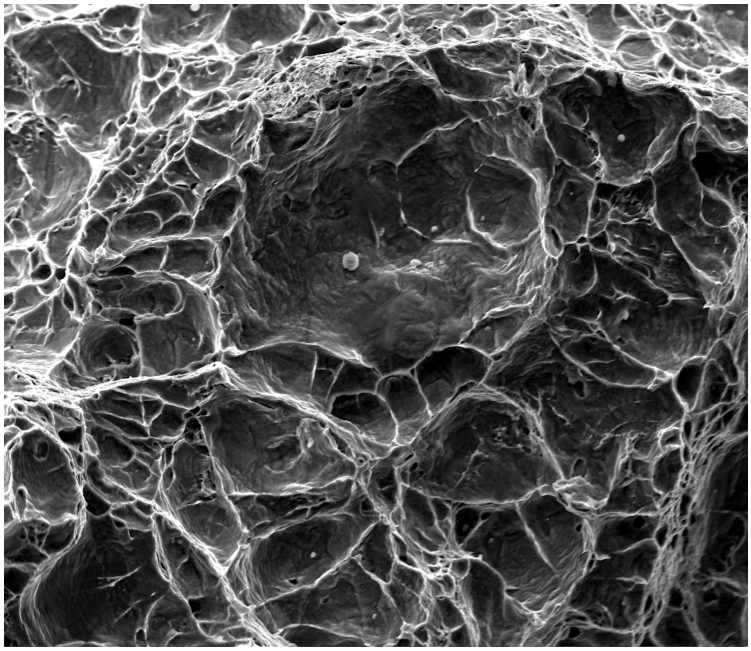

(b)

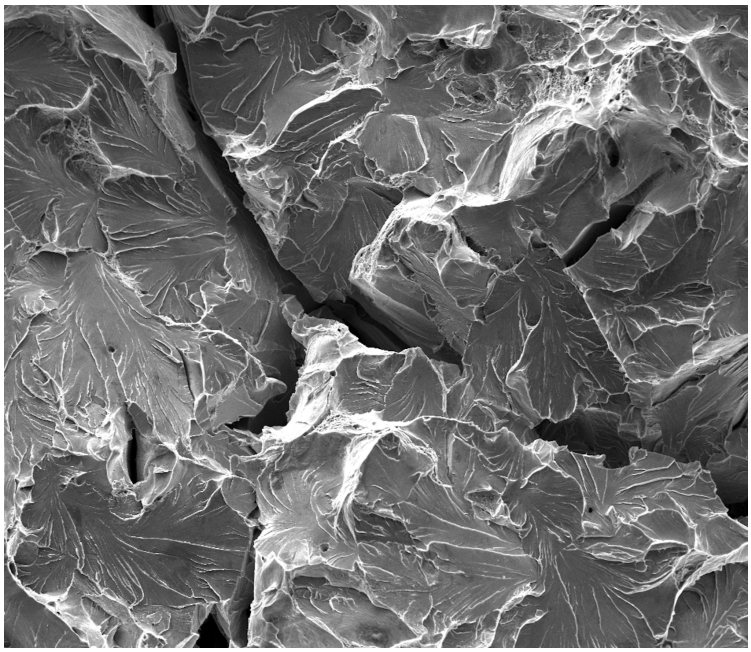

Figure 99: Fracture surfaces of A572 steel specimens with notch acuity $\zeta = 0.9$ prestrained in tension (see Table 2) and reloaded at a strain rate of (a) $\dot{\varepsilon} \sim 5\,10^{-4}\mathrm{s}^{-1}$; and (b) $\dot{\varepsilon} \sim 2\,10^{-2}\mathrm{s}^{-1}$.

affect the residual ductility in the material, defined as the ductility of the specimen exclusive of the prestrain, whether in shear or tension, is the failure strain is step 2 of loading..

Fig.100 shows how prestraining in tension affects the residual ductility. In this case the value of the residual ductility is only plotted at the average location and the other measures are not plotted as the average strain is representative of the trends observed. We see that there is a clear reduction in the residual ductility due to prestraining in tension. However, the reduction is comparable to the amount of prestrain applied. The only outlier in this is the path involving reloading in 30° after prestraining. This could be amenable to effect of anisotropy on activation of deformation systems or due to scatter in the data. The latter seems to be more probable as the data point for no path change experiments also lies away from the failure loci formed by experiments without path change.

Fig.101 shows how the residual ductility is affected by prestraining in shear dominant loading. The material was prestraining in shear upto $0.5\bar{\epsilon}_f$ and then loaded in various orientation involving combined tension and shear. Fig.97 did not show any clear indication of how load path changes the ductility in the material. Here the prestraining ductility is plotted with the reloading orientation. We observe that for all reloading orientations except 90° orientation, there is a drastic decrease in the ductility with shear prestrain.

It must be noted that in both paths the materials were prestrained to $0.5\bar{\epsilon}_f$ of their corresponding orientations. These values however, vary drastically as the material exhibits higher ductility under shear dominant loading. The only exception observed in the trends is how orthogonal path changes affect the failure strain. It can be commented that tensile prestrain reduces ductility under shear dominant loading while shear prestrain followed by tensile loading leads to slight increase in ductility.

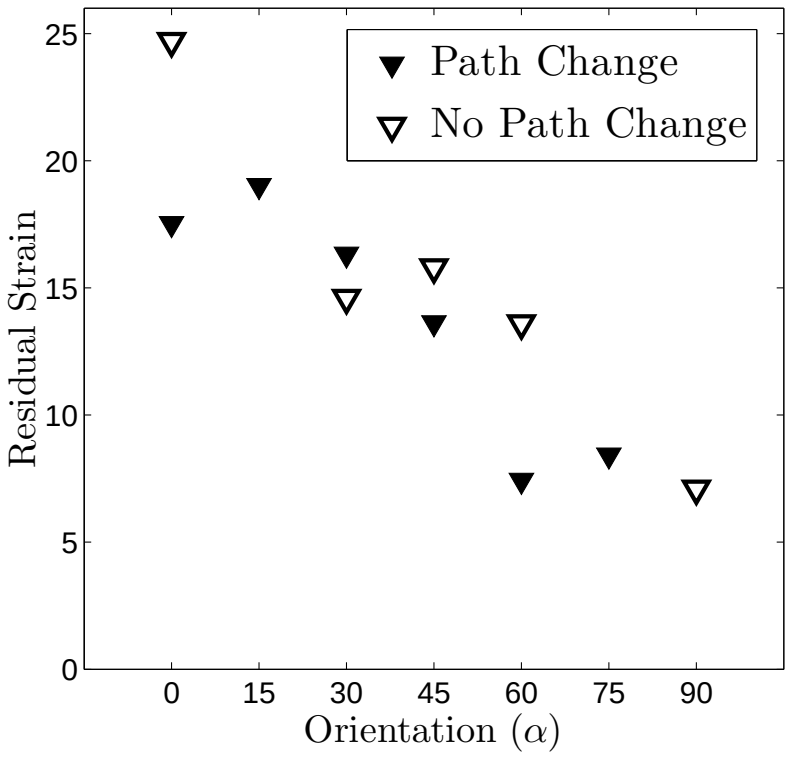

Figure 100: Residual strain after prestraining for path 1 averaged over the minimum section for experiments with and without path change shown in filled and unfilled symbols respectively.

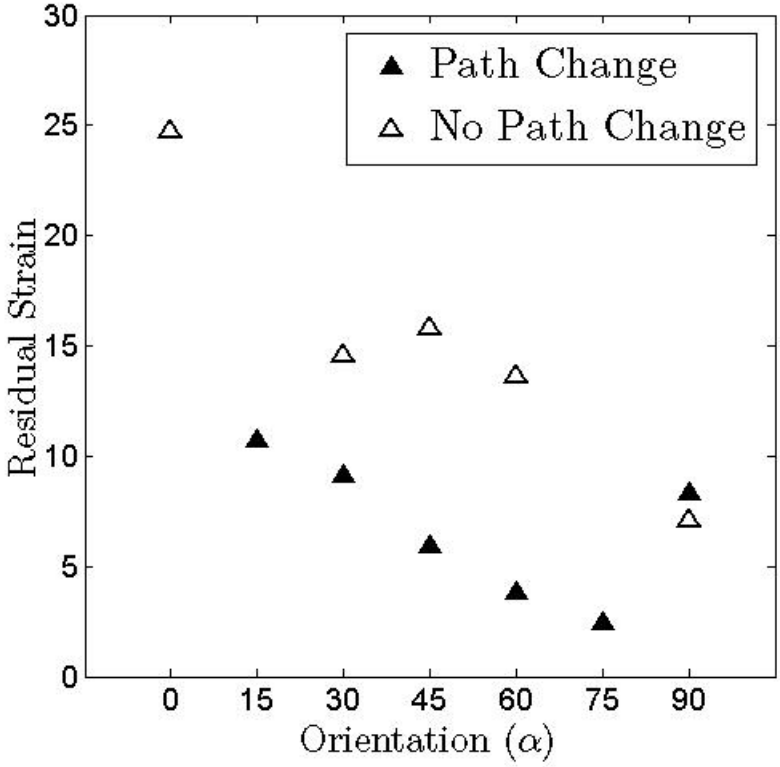

Figure 101: Residual strain after prestraining for path 2 averaged over the minimum section for experiments with and without path change shown in filled and unfilled symbols respectively.

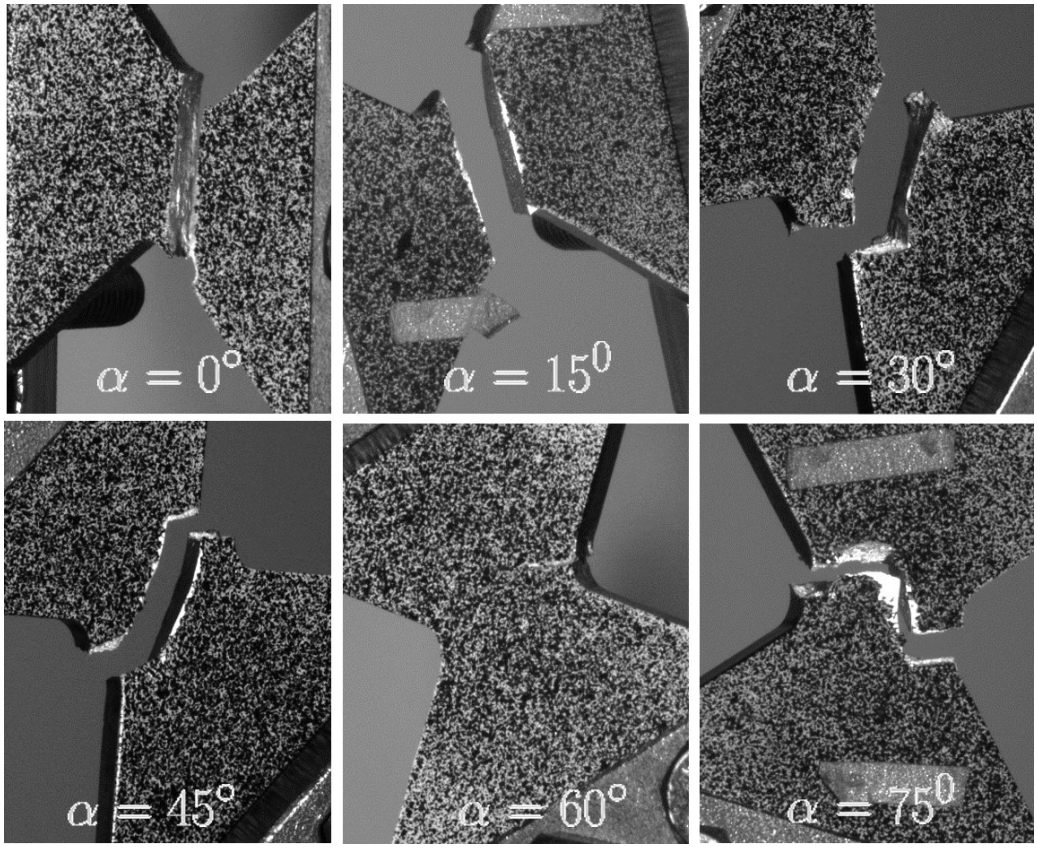

Figure 102: Failure mode in samples tested under various orientation of loading after prestraining in tension($\alpha = 90°$). In all cases the loading direction is vertical.

Fig. 102 shows the mode of failure under different reloading orientations after prestraining in tension. The fracture surfaces show flat failure surface as seen in the case of shear dominant loadings for no path change experiments. In most of the cases the failure initiates in the notch regions. For orientations 0° and 15° the faiure initiates near the notch root and leads to complete failure. However the angle of the fracture surface changes due to orientation of the loading. In the case of loadings α>15° the failure initiates at the opposite edges and is connected by in plane shear failure. The 60° specimen did not undergo complete failure. No crack was seen to deviate into the bulk of the material as seen in a few loading orientations for no path change experiments.

Fig.103 shows the failure mode in experiments involving prestraining in shear followed by reloading along other orientations. These fractured specimens show the trend similar to that seen in path 1 sample for values of α<60°. The fracture is initiated above and below the notch root and connected through in plane shear localization. For samples 60° and 75° the fracture mode involves two cracks starting at opposite locations above and below the notch root and do not connect by in-plane shear localization. Instead these cracks keep propagating independently till one of the ligament fails. The 90° specimen failed indicating an inclined fracture surface indicating out of plane shear. This was also observed in the 90° specimen for no path change experiments.

5.9 Summary

Nonproportional loading paths to fracture have been investigated in steel, as a simpler model material, then in Mg sheet metal. The conditions in the steel were such that (i) failure was cavitation dominated; and (ii) no shear failure occurred. The loading paths were triaxiality step-jumps which mimic those considered in the

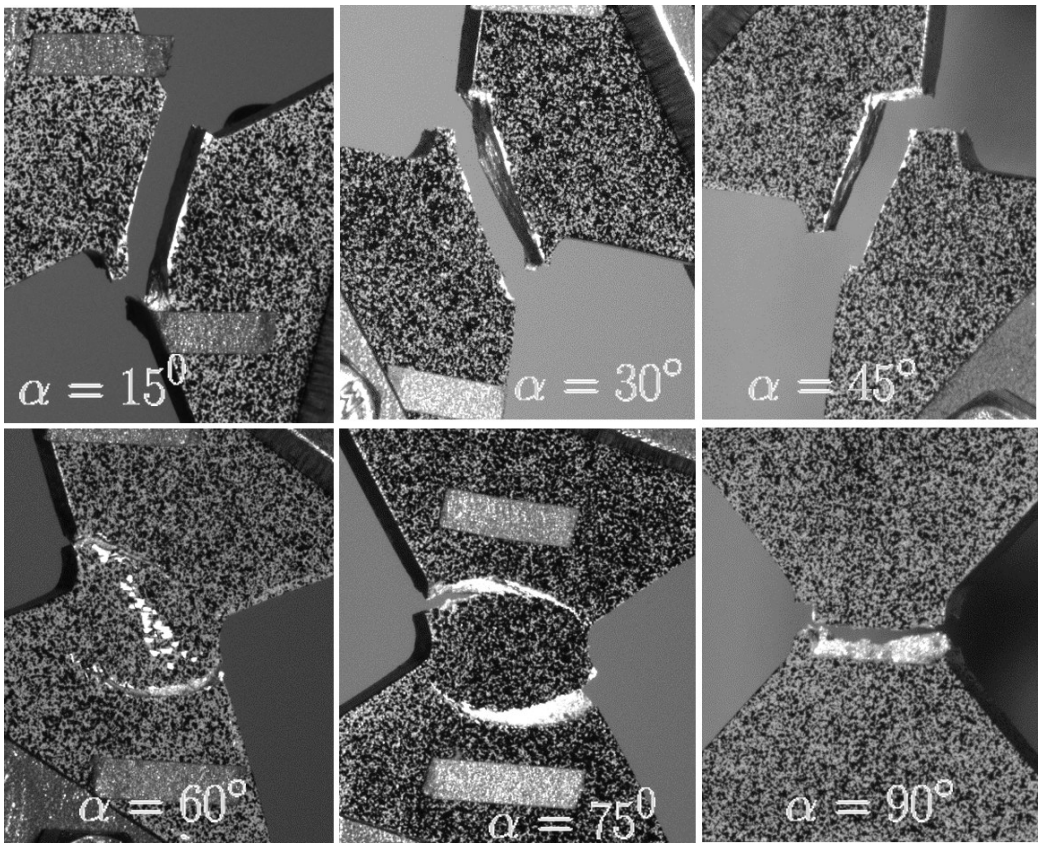

Figure 103: Failure mode in samples tested under various orientation of loading after prestraining in shear($\alpha = 0°$). In all cases the loading direction is vertical.

cell model studies by [24]. When the strain to failure initiation is plotted against some strain-weighted average of the stress triaxiality ratio the fracture locus not only is non-monotonous, it is not one-to-one. For the same value of average triaxiality several values of the strain to failure can be realized. The effect can be quite severe since the latter can decrease by a large factor. These findings are consistent with the theoretical predictions of [24]. Any qualitative differences between the two investigations are due to the decrease in hardening capacity induced by prestraining as well as to the absence of initial voids in the experiments.

Examination of alternative definitions of the fracture loci has shown that the above findings are robust. A major premise of this work has been that the intrinsic fracture locus of a material is accessible experimentally only over a narrow range of stress states. A major implication of the above findings is that positing a critical-strain failure criterion for ductile materials on the basis of experimental measurements alone can lead to significant errors. In particular, specimen geometries that are notorious for promoting shear-banding induced failure are not suitable to construct the intrinsic fracture locus. The fracture strains associated with such geometries only represent those specimens and not the constituent material at the stress state prevalent prior to the onset of instability.

Re-analysing the data from the literature[63, 124, 142] demonstrates that the results for a step loading used in this study can carry over to other non-radial loading paths. While deviations from non-proportionality are large, there are significant regimes over which deviations are milder.

Both the theoretical–computational predictions [24] and the experiments were for a specific kind of nonproportional loading paths. The question arises generally as to whether such large deviations from the intrinsic fracture locus would persist for other types of nonproportional loadings. This is being investigated and findings will

be reported elsewhere.

Load path change on ductile fracture of Mg sheets indicate that prestraining in tension and shear lead to damaging the material, however, the effect is mild during tensile prestrain and significantly high during shear prestrain. Orthogonal path change involving shear prestrain followed by tensile loading lead to increase in residual ductility with path change.

6. CONCLUSIONS AND FUTURE WORK

Failure mechanism in ductile metals would involve one or a combination of ductile fracture (based on initiation, growth and coalescence of voids), shear fracture (based on shear band localisation), instability with localised necking (followed by ductile or shear fracture inside the neck area). The failure strains under these mechanisms would depend majorly on strain rate, temperature, anisotropy, stress state and history of loading. In this thesis, their has been an attempt to study the effects of each of these factors on the failure mechanism of a technologically important alloy.

Low density, high specific strength, good castability, good machinability, improved corrosion resistance, availability in abundance, excellent electrical and thermal conductivity and recyclablility are among the few advantages that make it ideal candidate for structural applications. However, in order to have high strength and ductility of applications such as the transportation industry, these alloys must be used in the wrought form. Poor cold workability and failure with limited post-necking ductility have restricted the application of these alloys. Strong plastic anisotropy induced by thermo-mechanical processing has often been blamed as the major reason for poor mechanical performance.

In this study, the main hypothesis was to engineer this anisotropy to improve ductility. This was guided through micromechanical calculations that suggested that certain forms of anisotropy can be beneficial for ductility. This measure of anisotropy is lumped in a scalar invariant(AED factor) whose value must be above a threshold value in order to expect improved ductility irrespective of the direction. Equal Channel Angular Extrusion was used to engineer texture in Mg alloys and thus anisotropy. Three different materials with different values of AED factor were used.

The AED factor was capable of capturing the trends observed in ductility. Definition of ductility was probed over a variety of stress states which indicated some interesting findings. There is also a need to investigate the competing effects of plastic anisotropy on enhancing ductility & causing shear failure. The success of the AED factor will help guide new processing routes to obtain textures aiding ductility.

The final motive of these studies are to improve the formability of these alloys at low homologous temperatures and hence the above hypothesis was used to study if engineering the texture could lead to improvement of formability. Punch experiments using a Olsen type punch was used to check the formability of ECAE processed plates. Effect of variation of warm temperature on the formability of these textures plates was checked. The findings corroborate with the hypothesis stated earlier. One of the alloys showed marked temperature effect while the others did not.

Important applications such as sheet metal forming, may involve complex loadings and deformation paths. Failures may be classified into failure in shear vs failure by shear rupture. Experiments involving the combined tension and shear were aimed at understanding how Mg sheets performed under shear dominant loadings which is not studied at all in the literature. With the help of Digital Image Correlation local strains could be measured at different locations and initiation of fracture could be tracked. Numerical simulations using ABAQUS helped understand the evolution of stress state. Plotting the failure loci as a plot of failure strain as function of the average triaxiality and Lode parameter for experiments in the shear dominant region. Results indicate that failure strain is geometry dependent and depending on the location assigned to it, the trend in the failure loci can vary, none of which are intrinsic to the material. In all measures of strain to failure, there is limited effect of varying lode parameter, even though a wide range of lode parameter is probed.

Metal forming processes involving non-linear strain paths, and abrupt changes in

the strain ratio invalidate the hypothesis of proportional loading. In general, effects of nonproportional loading can manifest in various ways. The effect was initially tested on a model material (steel) where the damage mechanism was known to be via. ductile fracture mechanisms. The path dependence of the fracture locus was observed and the extent of the deviations were quantified. Reanalysing the data in the literature demonstrates that the above obtained results can carry over to other non-radial loading paths. The effect of load path changes were probed in Magnesium alloy sheets by prestraining in tension and shear. It was observed that the prestraining both in tension and shear reduced the residual ductility, however, the effect was more prominent in shear prestrains. The rate of loss of hardening capacity of the material was found to be strongly affected by the anisotropy of the material. Further, simulations with load path changes need to be carried out to probe the effect of stress state on the failure loci under load path changes.

BIBLIOGRAPHY

[1] A Stalmann et al. "Properties and processing of magnesium wrought products for automotive applications". In: *Advanced Engineering Materials* 3 (2001), pp. 969–974.

[2] Edward F. E. "Principles of magnesium technology". In: *Pergamon Press, New York* (1966).

[3] S. R. Agnew et al. "Study of slip mechanisms in a magnesium alloy by neutron diffraction and modeling". In: *Scripta Materialia* 48 (2003), pp. 1003–1008.

[4] J Koike et al. "The activity of non-basal slip systems and dynamic recovery at room temperature in fine-grained AZ31B magnesium alloys". In: *Acta Materialia* 51 (2003), pp. 2055–2065.

[5] J Koike. "Enhanced deformation mechanisms by anisotropic plasticity in polycrystalline Mg alloys at room temperature". In: *Metallurgical and Materials Transactions A*. 36A (2005), pp. 1689–1696.

[6] S. B. Yi et al. "Deformation and texture evolution in AZ31 magnesium alloy during uniaxial loading". In: *Acta Materialia* 54 (2006), pp. 549–562.

[7] X. Gao and J. F. Nie. "Characterization of strengthening precipitate phases in a Mg-Zn alloy". In: *Scripta Materialia* 56 (2007), pp. 645–648.

[8] L. Capolungo, I. J. Beyerlein, and C. N. Tome. "Slip-assisted twin growth in hexagonal close-packed metals". In: *Scripta Materialia* 60 (2009), pp. 32–35.

[9] M. Al-Maharbi et al. "Microstructure, crystallographic texture, and plastic anisotropy evolution in an Mg alloy during equal channel angular extrusion

processing". In: *Materials Science and Engineering:A* 528 (2011), pp. 7616–7627.

[10] M. R. Barnett. "Twinning and the ductility of magnesium alloys Part II. "Contraction" twins". In: *Materials Science and Engineering:A* 464 (2007), pp. 8–16.

[11] H Somekawa and T Mukai. "Effect of texture on fracture toughness in extruded AZ31 magnesium alloy". In: *Scripta Materialia* 53 (2005), pp. 541–545.

[12] D. Ando, J. Koike, and Y. Sutou. "Relationship between deformation twinning and surface step formation in AZ31 magnesium alloys". In: *Acta Materialia* 58 (2010), pp. 4316–4324.

[13] Jan Bohlen et al. "The texture and anisotropy of magnesium–zinc–rare earth alloy sheets". In: *Acta Materialia* 55.6 (2007), pp. 2101–2112.

[14] B. Kondori and A. A. Benzerga. "On the notch ductility of a rare-earth magnesium alloy". In: *ActaMat* In Preparation (2014).

[15] T Mukai et al. "Ductility enhancement in AZ31 magnesium alloy by controlling its grain structure". In: *Scripta Materialia* 45 (2001), pp. 89–94.

[16] SR Agnew et al. "Enhanced ductility in strongly textured magnesium produced by equal channel angular processing". In: *Scripta Materialia* 50.3 (2004), pp. 377–381.

[17] A.A. Benzerga and J. Besson. "Plastic potentials for anisotropic porous solids". In: *European Journal of Mechanics* 20.3 (2001), pp. 397–434.

[18] S. M. Keralavarma and A. A. Benzerga. "A constitutive model for plastically anisotropic solids with non-spherical voids". In: *Journal of the Mechanics and Physics of Solids* 58 (2010), pp. 874–901.

[19] A Yamashita, Z Horita, and T. G. Langdon. "Improving the mechanical properties of magnesium and a magnesium alloy through severe plastic deformation". In: *Materials Science and Engineering:A* 300 (2001), pp. 142–147.

[20] S. S. Park et al. "Microstructure and tensile properties of twin-roll cast Mg-Zn-Mn-Al alloys". In: *Scripta Materialia* 57 (2007), pp. 793–796.

[21] D. C. Foley et al. "Grain refinement vs. crystallographic texture: Mechanical anisotropy in a magnesium alloy". In: *Scripta Materialia* 64 (2011), pp. 193–196.

[22] S. Suwas, G. Gottstein, and R. Kumar. "Evolution of crystallographic texture during equal channel angular extrusion (ECAE) and its effects on secondary processing of magnesium". In: *Materials Science and Engineering: A* 471.1 (2007), pp. 1–14.

[23] W. M. Garrison and N. R. Moody. "Ductile Fracture". In: *J. Phys. Chem. Solids* 48.11 (1987), pp. 1035–1074.

[24] A. A. Benzerga, D. Surovik, and S. M. Keralavarma. "On the path-dependence of the fracture locus in ductile materials – Analysis". In: *International Journal of Plasticity* 37 (2012), pp. 157–170.

[25] S. P. Keeler. *Circular grid systema valuable aid for evaluating sheet metal formability.* Tech. rep. SAE Technical Paper, 1968.

[26] G. M.a Goodwin. *Application of strain analysis to sheet metal forming problems in the press shop.* Tech. rep. SAE Technical Paper, 1968.

[27] A. K. Ghosh and W. A. Backofen. "Strain hardening and instability in biaxially streched sheets". In: *Metallurgical Transactions* 4.4 (1973), pp. 1113–1123.

[28] HM Shang, GS Tan, and WCM Tan. "Effects of prestrain with strain gradient present on sheet metal formability". In: *Journal of Engineering Materials and Technology* 107.4 (1985), pp. 298–306.

[29] S. R. Agnew and J. F. Nie. "Preface to the viewpoint set on: The current state of magnesium alloy science and technology". In: *Scripta Materialia* 63 (2010), pp. 671–673.

[30] J. Hirsch and T. Al-Samman. "Superior light metals by texture engineering: optimized aluminum and magnesium alloys for automotive applications". In: *Acta Materialia* 61.3 (2013), pp. 818–843.

[31] S. R. Agnew and O Duygulu. "Plastic anisotropy and the role of non-basal slip in magnesium alloy AZ31B". In: *International Journal of Plasticity* 21 (2005), pp. 1161–1193.

[32] M. R. Barnett et al. "Influence of grain size on the compressive deformation of wrought Mg-3Al-1Zn". In: *Acta Materialia* 52 (2004), pp. 5093–5103.

[33] W. B. Hutchinson and M. R. Barnett. "Effective values of critical resolved shear stress for slip in polycrystalline magnesium and other hcp metals". In: *Scripta materialia* 63.7 (2010), pp. 737–740.

[34] G. I. Taylor. "Plastic Strain in Metals". In: *J. Inst. Metals* 62 (1938), p. 307.

[35] L. Remy and A. Pineau. "Twinning and strain-induced F.C.C.–H.C.P. transformation in the FeMnCrC system". In: *Materials Science and Engineering* 28 (1977), pp. 99–107.

[36] J. W. Christian and S. Mahajan. "Deformation twinning". In: *Progress in Materials Science* 39 (1995), pp. 1–157.

[37] M. H. Yoo. "Slip, twinning, and fracture in hexagonal close-packed metals". In: *Metallurgical Transactions* 12 (1981), pp. 409–418.

[38] E. A. Ball and P. B. Prangnell. "Tensile-compressive yield asymmetries in high-strength wrought magnesium alloys". In: *Scripta Materialia* 31 (1994), pp. 111–116.

[39] N Stanford and MR Barnett. "The origin of rare earth texture development in extruded Mg-based alloys and its effect on tensile ductility". In: *Materials Science and Engineering: A* 496.1 (2008), pp. 399–408.

[40] J. Bohlen et al. "The texture and anisotropy of magnesium-zinc-rare earth alloy sheets". In: *Acta Materialia* 55 (2007), pp. 2101–2112.

[41] K. Hantzsche et al. "Effect of rare earth additions on microstructure and texture development of magnesium alloy sheets". In: *Scripta Materialia* 63 (2010), pp. 725–730.

[42] S. Sandloebes et al. "On the role of non-basal deformation mechanisms for the ductility of Mg and Mg-Y alloys". In: *Acta Materialia* 59 (2011), pp. 429–439.

[43] S. Sandloebes et al. "Ductility improvement of Mg alloys by solid solution: Ab initio modeling, synthesis and mechanical properties". In: *Acta Materialia* 70 (2014), pp. 92–104.

[44] B. Kondori and A. A. Benzerga. "On the notch ductility of a magnesium-rare earth alloy". In: *Materials Science and Engineering:A* 647 (2015), pp. 74–83.

[45] A. A. Benzerga and J.-B. Leblond. "Ductile Fracture by Void Growth to Coalescence". In: *Advances in Applied Mechanics* 44 (2010), pp. 169–305.

[46] A. Pineau, A. A. Benzerga, and T. Pardoen. "Failure of metals I. Brittle and Ductile Fracture". In: *Acta Materialia* 107 (2016), pp. 424–483.

[47] VM Segal. "Severe plastic deformation: simple shear versus pure shear". In: *Materials Science and Engineering: A* 338.1 (2002), pp. 331–344.

[48] R. Z. Valiev and T. G. Langdon. "Principles of equal-channel angular pressing as a processing tool for grain refinement". In: *Progress in Materials Science* 51.7 (2006), pp. 881–981.

[49] E Dogan et al. "Role of starting texture and deformation modes on low-temperature shear formability and shear localization of Mg–3Al–1Zn alloy". In: *Acta Materialia* 89 (2015), pp. 408–422.

[50] B. Kondori and A. A. Benzerga. "Effect of Stress Triaxiality on the Flow and Fracture of Mg Alloy AZ31". In: *Metallurgical and Materials Transactions A.* 45 (2014), pp. 3292–3307.

[51] A. A. Benzerga, J. Besson, and A. Pineau. "Modèle couplé comportement–endommagement ductile de tôles anisotropes". In: *Actes du* 3$^{\text{ème}}$ *Colloque National en Calcul des Structures*. Ed. by B. Peseux et al. Presses Académiques de l'Ouest, 1997, pp. 673–678.

[52] S. M. Keralavarma and A. A. Benzerga. "An Approximate Yield Criterion for Anisotropic Porous Media". In: *Comptes Rendus Mecanique* 336 (2008), pp. 685–692.

[53] R. Hill. "A theory of yielding and plastic flow of anisotropic solids". In: *Proceedings of the Royal Society of London A* 193 (1948), pp. 281–297.

[54] A. A. Benzerga. "Rupture ductile des tôles anisotropes". PhD thesis. Ecole Nationale Supérieure des Mines de Paris, 2000.

[55] B. Kondori. "Ductile fracture of Magnesium alloys: characterization and modeling". PhD dissertation. Texas A&M University, USA, 2015.

[56] D. Steglich, X. Tian, and J. Besson. "Mechanism-based modelling of plastic deformation in magnesium alloys". In: *European Journal of Mechanics* 55 (2016), pp. 289–303.

[57] B. Selvarajou et al. "On Plastic Flow in Notched Hexagonal Close Packed Single Crystals". In: *Journal of the Mechanics and Physics of Solids* (2016). In Press.

[58] A. A. Benzerga, J. Besson, and A. Pineau. "Anisotropic ductile fracture. Part I: experiments". In: *Acta Materialia* 52 (2004), pp. 4623–4638.

[59] A. A. Benzerga, J. Besson, and A. Pineau. "Anisotropic ductile fracture. Part II: theory". In: *Acta Materialia* 52 (2004), pp. 4639–4650.

[60] S. Basu and A. A. Benzerga. "On the path-dependence of the fracture locus in ductile materials – Experiments". In: *IJSS* Under Review (2014).

[61] AK Rodriguez et al. "Effect of strain rate and temperature on fracture of AZ31B magnesium alloy". In: *Acta Mater To appear* (2016).

[62] E Dogan et al. "Reduction in tension–compression asymmetry via grain refinement and texture design in Mg–3Al–1Zn sheets". In: *Materials Science and Engineering: A* 610 (2014), pp. 220–227.

[63] S. Basu and A. A. Benzerga. "On the path-dependence of the fracture locus in ductile materials: Experiments". In: *International Journal of Solids and Structures* 71 (2015), pp. 79–90.

[64] FH Froes, D Eliezer, and E Aghion. "The science, technology, and applications of magnesium". In: *Jom* 50.9 (1998), pp. 30–34.

[65] E Aghion, B Bronfin, and D Eliezer. "The role of the magnesium industry in protecting the environment". In: *Journal of Materials Processing Technology* 117.3 (2001), pp. 381–385.

[66] K. U. Kainer and B. L. Mordike. *Magnesium alloys and their applications*. Wiley Online Library, 2000.

[67] Mordike B. L. and Ebert T. "Magnesium: Properties applications potential". In: *Materials Science and Engineering:A* ().

[68] H Friedrich and S Schumann. "Research for a new age of magnesium in the automotive industry". In: *Journal of Materials Processing Technology* 117.3 (2001), pp. 276–281.

[69] IJ Polmear. "Magnesium alloys and applications". In: *Materials science and technology* 10.1 (1994), pp. 1–16.

[70] C. J. Bettles and M. A. Gibson. "Current wrought magnesium alloys: Strengths and weaknesses". In: *JOM* 57 (2005), pp. 46–49.

[71] M. M. Avedesian, H. Baker, et al. "ASM specialty handbook: magnesium and magnesium alloys". In: *ASM International, Materials Park, OH* (1999), p. 15.

[72] PG Partridge. "The crystallography and deformation modes of hexagonal close-packed metals". In: *Metallurgical reviews* 12.1 (1967), pp. 169–194.

[73] Alan Luo et al. "Magnesium castings for automotive applications". In: *Jom* 47.7 (1995), pp. 28–31.

[74] J. K. Solberg et al. "Superplasticity in magnesium alloy AZ91". In: *Materials Science and Engineering: A* 134 (1991), pp. 1201–1203.

[75] HS Yang et al. “High temperature deformation of a magnesium alloy with controlled grain structures”. In: *Materials Science and Engineering: A* 158.2 (1992), pp. 167–175.

[76] Zhang G. Y. et al. “Mechanism of effects of rare earths on microstructure and properties at elevated temperatures of AZ91 magnesium alloy”. In: *Journal OF Rare Earths* 25 (2007), pp. 348–351.

[77] MR Barnett. “Influence of deformation conditions and texture on the high temperature flow stress of magnesium AZ31”. In: *Journal of Light Metals* 1.3 (2001), pp. 167–177.

[78] A Jäger et al. “Tensile properties of hot rolled AZ31 Mg alloy sheets at elevated temperatures”. In: *Journal of Alloys and Compounds* 378.1 (2004), pp. 184–187.

[79] H. Watanabe et al. “Effect of texture on tensile properties at elevated temperatures in an AZ31 magnesium alloy”. In: *Scripta Materialia* 52.6 (2005), pp. 449–454.

[80] SB Yi, S Zaefferer, and H-G Brokmeier. “Mechanical behaviour and microstructural evolution of magnesium alloy AZ31 in tension at different temperatures”. In: *Materials Science and Engineering: A* 424.1 (2006), pp. 275–281.

[81] A. S. Khan et al. “Mechanical response and texture evolution of AZ31 alloy at large strains for different strain rates and temperatures”. In: *International Journal of Plasticity* 27.5 (2011), pp. 688–706.

[82] I Ulacia et al. “Tensile characterization and constitutive modeling of AZ31B magnesium alloy sheet over wide range of strain rates and temperatures”. In: *Journal of Materials Processing Technology* 211.5 (2011), pp. 830–839.

[83] M Nebebe Mekonen et al. “Mechanical characterization and constitutive modeling of Mg alloy sheets”. In: *Materials Science and Engineering: A* 540 (2012), pp. 174–186.

[84] M Cusick et al. “Towards superplastic forming of AZ31 magnesium alloy with controlled microstructure”. In: *6th EuroSPF Coference* 3 (2008), pp. 1–11.

[85] E Doege and K Dröder. “Sheet metal forming of magnesium wrought alloysformability and process technology”. In: *Journal of Materials Processing Technology* 115.1 (2001), pp. 14–19.

[86] N Hort, Y. D. Huang, and K. U. Kainer. “Intermetallics in magnesium alloys”. In: *Advanced Engineering Materials* 8 (2006), pp. 235–240.

[87] S. Lee, Y. Chen, and J. Wang. “Isothermal sheet formability of magnesium alloy AZ31 and AZ61”. In: *Journal of Materials Processing Technology* 124.1 (2002), pp. 19–24.

[88] D. Sorgente et al. “Blow forming of AZ31 magnesium alloy at elevated temperatures”. In: *International Journal of Material Forming* 3.1 (2010), pp. 13–19.

[89] Fuh-Kuo Chen, Tyng-Bin Huang, and Chih-Kun Chang. “Deep drawing of square cups with magnesium alloy AZ31 sheets”. In: *International Journal of Machine Tools and Manufacture* 43.15 (2003), pp. 1553–1559.

[90] Oleg D Sherby and Jeffrey Wadsworth. “Superplasticityrecent advances and future directions”. In: *Progress in Materials Science* 33.3 (1989), pp. 169–221.

[91] S. Basu et al. "Towards Designing Anisotropy for Ductility Enhancement: A Theory-Driven Investigation in Mg-alloys". In: *ActaMet* Under Review (2016).

[92] K. Anand and W. A. Spitzig. "Initiation of localized shear bands in plane strain". In: *Journal of the Mechanics and Physics of Solids* 28 (1980), pp. 113–128.

[93] A. C. Mackenzie, J. W. Hancock, and D. K. Brown. "On the influence of state of stress on ductile failure initiation in high strength steels". In: *Engineering Fracture Mechanics* 9 (1977), pp. 167–188.

[94] Beremin, F. M. and Pineau, A. and Mudry, F. and Devaux, J.C. and DEscatha, Y. and Ledermann, P. "Experimental and numerical study of the different stages in ductile rupture: application to crack initiation and stable crack growth". In: *Three-Dimensional Constitutive relations of Damage and Fracture*. Ed. by Nemat-Nasser, S. North Holland: Pergamon press, 1981, pp. 157–172.

[95] J. R. Rice and D. M. Tracey. "On the enlargement of voids in triaxial stress fields". In: *Journal of the Mechanics and Physics of Solids* 17 (1969), pp. 201–217.

[96] F. A. McClintock. "A criterion for ductile fracture by the growth of holes". In: *Journal of Applied Mechanics* 35 (1968), pp. 363–371.

[97] A. Needleman and V. Tvergaard. "An analysis of ductile rupture in notched bars". In: *Journal of the Mechanics and Physics of Solids* 32 (1984), pp. 461–490.

[98] G. R. Johnson et al. “Response of various metals to large torsional strains over a large range of strain ratesPart 1: Ductile metals”. In: *Journal of Engineering Materials and Technology* 105.1 (1983), pp. 42–47.

[99] G. R. Johnson et al. “Response of various metals to large torsional strains over a large range of strain ratespart 2: less ductile metals”. In: *Journal of Engineering Materials and Technology* 105.1 (1983), pp. 48–53.

[100] Y. Bao and T. Wierzbicki. “On fracture locus in the equivalent strain and stress triaxiality space”. In: *International Journal of Mechanical Sciences* 46 (2004), pp. 81–98.

[101] S.S. Haltom, S. Kyriakides, and K. Ravi-Chandar. “Ductile failure under combined shear and tension”. In: *International Journal of Solids and Structures* 50 (2013), pp. 1507–1522.

[102] I. Barsoum and J. Faleskog. “Rupture mechanisms in combined tension and shear-Experiments”. In: *International Journal of Solids and Structures* 44 (2007), pp. 1768–1786.

[103] D Liang and CB Cowley. “The twin-roll strip casting of magnesium”. In: *JOM* 56.5 (2004), pp. 26–28.

[104] NJ Pagano and JM Whitney. “Geometric design of composite cylindrical characterization specimens”. In: *Journal of Composite Materials* 4.3 (1970), pp. 360–378.

[105] NJ Pagano, JC Halpin, and JM Whitney. “Tension buckling of anisotropic cylinders”. In: *Journal of Composite Materials* 2.2 (1968), pp. 154–167.

[106] A Feldman, J Tasi, and DA Stang. "Experimental determination of stiffness properties of thin-shell composite cylinders". In: *Experimental Mechanics* 6.8 (1966), pp. 385–394.

[107] JM Whitney and JC Halpin. "Analysis of laminated anisotropic tubes under combined loading". In: *Journal of Composite Materials* 2.3 (1968), pp. 360–367.

[108] M Arcan et al. "A method to produce uniform plane-stress states with applications to fiber-reinforced materials". In: *Experimental Mechanics* 18.4 (1978), pp. 141–146.

[109] SC Hung and KM Liechti. "Finite element analysis of the Arcan specimen for fiber reinforced composites under pure shear and biaxial loading". In: *Journal of composite materials* 33.14 (1999), pp. 1288–1317.

[110] A Ghahremaninezhad and K Ravi-Chandar. "Ductile failure behavior of polycrystalline Al 6061-T6 under shear dominant loading". In: *International Journal of Fracture* 180.1 (2013), pp. 23–39.

[111] DE Walrath and DF Adams. "The losipescu shear test as applied to composite materials". In: *Experimental Mechanics* 23.1 (1983), pp. 105–110.

[112] SS Wang and A Dasgupta. "Development of losipescu-type Test for Determining Shear Properties of Fiber Composite Materials: Critical Anisotropic Elasticity Analysis and Experiment". In: *Mechanical Eng. Dept., Univ. of Houston* (1986).

[113] M Kumosa and D Hull. "Mixed-mode fracture of composites using Iosipescu shear test". In: *International Journal of Fracture* 35.2 (1987), pp. 83–102.

[114] M. Dunand and D. Mohr. "On the predictive capabilities of the shear modified Gurson and the modified Mohr-Coulomb fracture models over a wide range of stress triaxialities and Lode Angles". In: *Journal of the Mechanics and Physics of Solids* 59 (2011), pp. 1374–1394.

[115] AK Rodriguez et al. "Effects of the strain rate and temperature on the microstructural evolution of twin-rolled cast wrought AZ31B alloys sheets". In: *Journal of Materials Engineering and Performance* 22.10 (2013), pp. 3115–3125.

[116] B. Kondori and A. A. Benzerga. "Fracture strains, damage mechanisms and anisotropy in a Magnesium alloy across a range of stress triaxialities". In: *Experimental Mechanics* In Press (2013), doi:10.1007/s11340–013–9812–8.

[117] B. Kondori. "Ductile fracture of Magnesium alloys: Characterization and modeling". PhD dissertation. Texas A&M University, USA, 2015.

[118] Jing Zhang and Shailendra P Joshi. "Phenomenological crystal plasticity modeling and detailed micromechanical investigations of pure magnesium". In: *Journal of the Mechanics and Physics of Solids* 60.5 (2012), pp. 945–972.

[119] Y. Madi, A.A. Benzerga, and J Besson. "Modeling the 3D plastic anisotropy of magnesium AZ31B alloy". In: *International Congress of Theoretical and Applied Mechanics* 24 (2016).

[120] A Pineau, AA Benzerga, and Thomas Pardoen. "Failure of metals I: Brittle and ductile fracture". In: *Acta Materialia* 107 (2016), pp. 424–483.

[121] JQ Clayton and JF Knott. "Observations of fibrous fracture modes in a prestrained low-alloy steel". In: *Metal Science* 10.2 (1976), pp. 63–71.

[122] KF Amouzouvi and MN Bassim. “Effect of the type of prior straining on the fracture toughness of AISI 4340 steel”. In: *Materials Science and Engineering* 60.1 (1983), pp. 1–5.

[123] S Sivaprasad et al. “Effect of prestrain on fracture toughness of HSLA steels”. In: *Materials Science and Engineering: A* 284.1 (2000), pp. 195–201.

[124] B. Marini, F. Mudry, and A. Pineau. “Ductile rupture of A508 steel under nonradial loading”. In: *Engineering Fracture Mechanics* 22 (1985), pp. 375–386.

[125] J Arndt, H Majedi, W Dahl, et al. “Influence of strain history on ductile failure of steel”. In: *Journal de Physique IV* 6.C6 (1996).

[126] D Chae, JP Bandstra, and DA Koss. “The effect of pre-strain and strain-path changes on ductile fracture: experiment and computational modeling”. In: *Materials Science and Engineering: A* 285.1 (2000), pp. 165–171.

[127] J.R. Rice. “The localization of plastic deformation”. In: *14th int. cong. Theoretical and Applied Mechanics*. Ed. by W.T. Koiter. North–Holland, Amsterdam, 1976, pp. 207–220.

[128] M. Dunand and D. Mohr. “Optimized butterfly specimen for the fracture testing of sheet materials under combined normal and shear loading”. In: *Engineering Fracture Mechanics* 78 (2011), pp. 2919–2934.

[129] Jonas Faleskog and Imad Barsoum. “Tension–torsion fracture experiments–Part I: Experiments and a procedure to evaluate the equivalent plastic strain”. In: *International Journal of Solids and Structures* (2013). In press.

[130] P. Ludwik and R. Scheu. “Ueber Kerbwirkungen bei Flusseisen”. In: *Stahl u. Eisen* 43 (1923), pp. 999–1001.

[131] W. Lode. "The influence of the intermediate principal stress on yielding and failure of iron, copper and nickel". In: *Engineering Fracture Mechanics* 5 (1925), pp. 142–144.

[132] E. Orowan. *Notch, Brittleness and the Strength of Metals*. Institution of Engineers and Shipbuilders in Scotland, 1945.

[133] J. W. Bridgman. *Studies in Large Plastic Flow and Fracture*. McGraw–Hill, New York, 1952.

[134] K Nakazima, T Kikuma, and K Hasuka. "Study on the formability of steel sheets". In: *Yawata Tech. Rep., Sept. 1968,–264–, 8517-8530* (1968).

[135] A. Graf and W. Hosford. "The influence of strain-path changes on forming limit diagrams of A1 6111 T4". In: *International Journal of Mechanical Sciences* 36.10 (1994), pp. 897–910.

[136] T. Hasegawa, T. Yakou, and S. Karashima. "Deformation behavior and dislocation structures upon stress reversal in polycrystalline aluminum". In: *Materials Science and Engineering* 20 (1975), pp. 267–276.

[137] J. Chaboche. "On some modifications of kinematic hardening to improve the description of ratchetting effects". In: *International Journal of Plasticity* 7.7 (1991), pp. 661–678.

[138] S Thuillier and EF Rauch. "Development of microbands in mild steel during cross loading". In: *Acta Metallurgica et Materialia* 42.6 (1994), pp. 1973–1983.

[139] EV Nesterova, B Bacroix, and C Teodosiu. "Microstructure and texture evolution under strain-path changes in low-carbon interstitial-free steel". In: *Metallurgical and Materials Transactions A* 32.10 (2001), pp. 2527–2538.

[140] A. A. Benzerga, J. Besson, and A. Pineau. "Coalescence–Controlled Anisotropic Ductile Fracture". In: *Journal of Engineering Materials and Technology* 121 (1999), pp. 221–229.

[141] A. Pineau. "Development of the local approach to fracture over the past 25 years: theory and applications". In: *International Journal of Fracture* 138 (2006), pp. 139–166.

[142] R. Schiffmann, W. Bleck, and W. Dahl. "The influence of strain history on ductile failure of steel". In: *Computational materials science* 13.1 (1998), pp. 142–147.

[143] X. Poulain et al. "Determination of the intrinsic behavior of polymers using digital image correlation combined with video-monitored testing". In: *International Journal of Solids and Structures* 50 (2013), pp. 1869–1878.

[144] N. Thomas, Shamik Basu, and A. A. Benzerga. "On fracture loci of ductile materials under nonproportional loading". In: *International Journal of Mechanical Sciences* (2016). Submitted.

[145] J. Koplik and A. Needleman. "Void growth and coalescence in porous plastic solids". In: *International Journal of Solids and Structures* 24.8 (1988), pp. 835–853.

[146] K. Siruguet and J.-B. Leblond. "Effect of void locking by inclusions upon the plastic behavior of porous ductile solids—I: theoretical modeling and numerical study of void growth". In: *International Journal of Plasticity* 20 (2004), pp. 225–254.

[147] K. Enami. “The effects of compressive and tensile prestrain on ductile fracture initiation in steels”. In: *Engineering Fracture M echanics* 72.7 (2005), pp. 1089–1105.

APPENDIX A

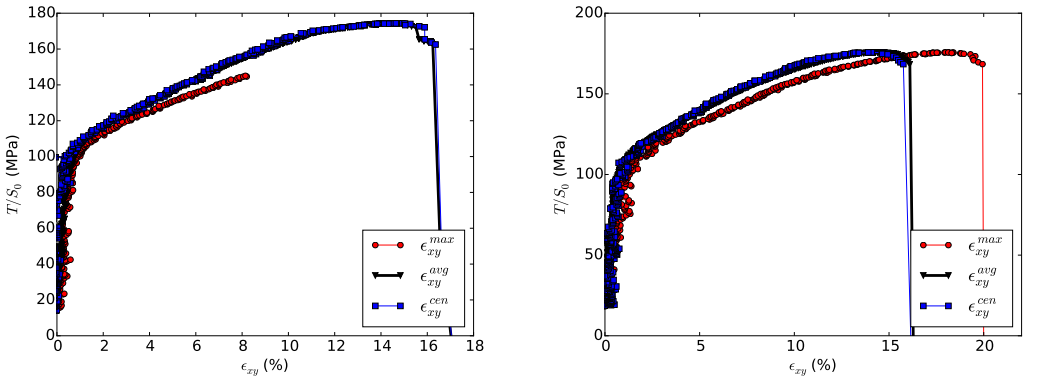

(a) (b)

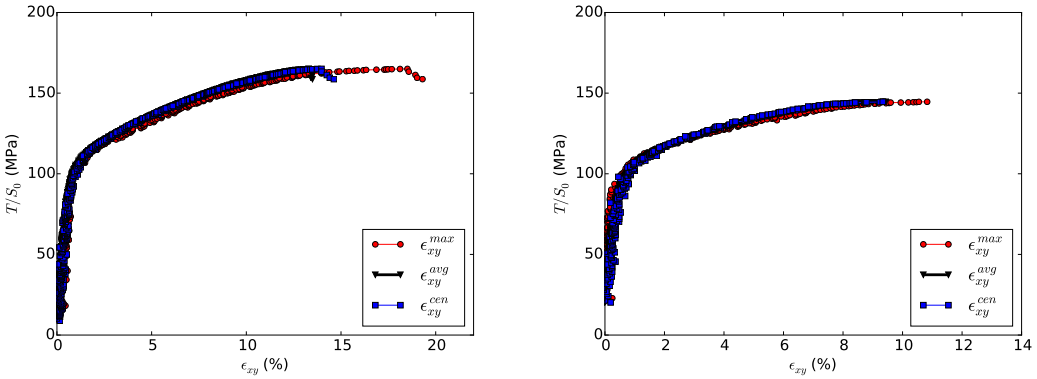

(c) (d)

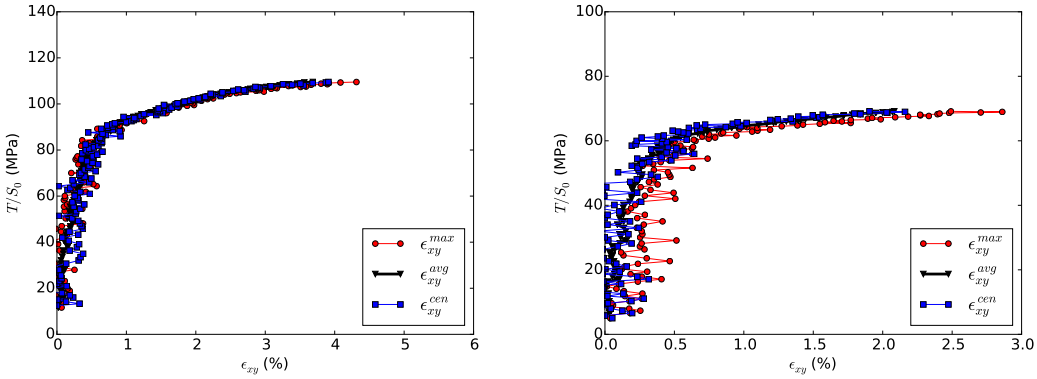

(e) (f)

Figure 104: Normalized force versus ϵxy plot resolved for experiments for different orientations (a) 0° (b) 15° (c) 30° (d) 45° (e) 60° (f) 75° at center, maximum locations and average over the minimum section after prestraining in tension($\alpha = 90°$).

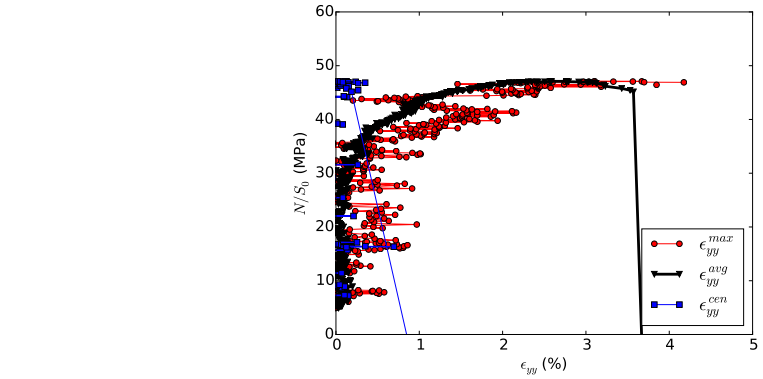

(a)

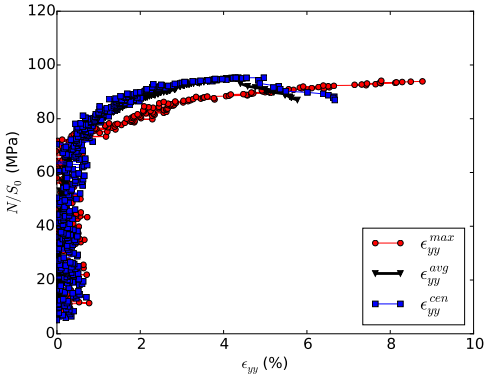

(b)

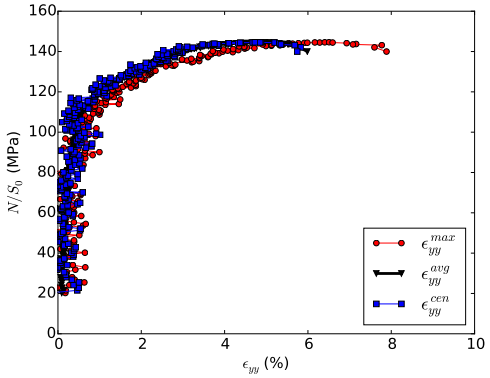

(c)

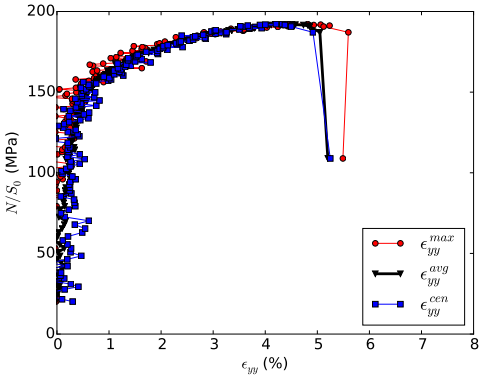

(d)

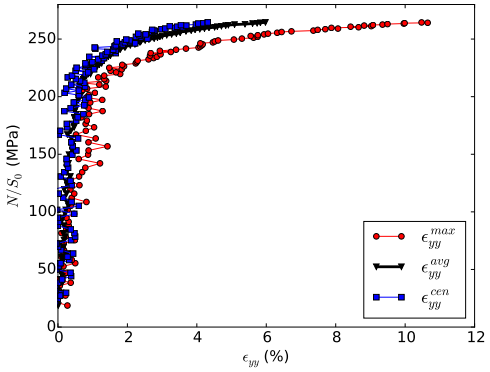

(e)

Figure 105: Normalized force versus ϵyy plot resolved for experiments for different orientations (a) 0° (b) 15° (c) 30° (d) 45° (e) 60° (f) 75° at center, maximum locations and average over the minimum section after prestraining in tension($\alpha = 90°$

.

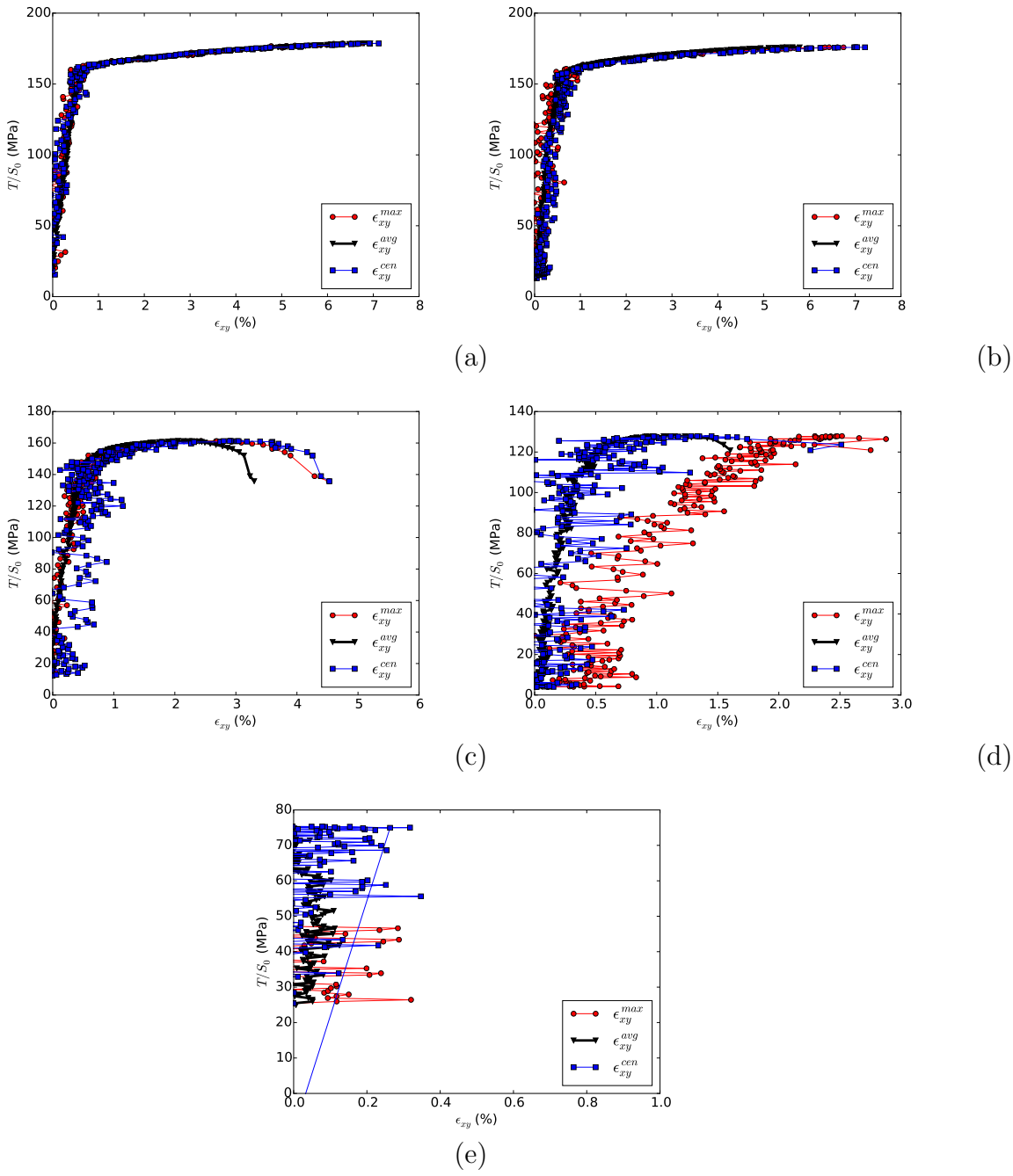

Figure 106: Normalized force versus ϵxy plot resolved for experiments for different orientations (a) 0° (b) 15° (c) 30° (d) 45° (e) 60° (f) 75° at center, maximum locations and average over the minimum section after prestraining in shear($\alpha = 0°$

.

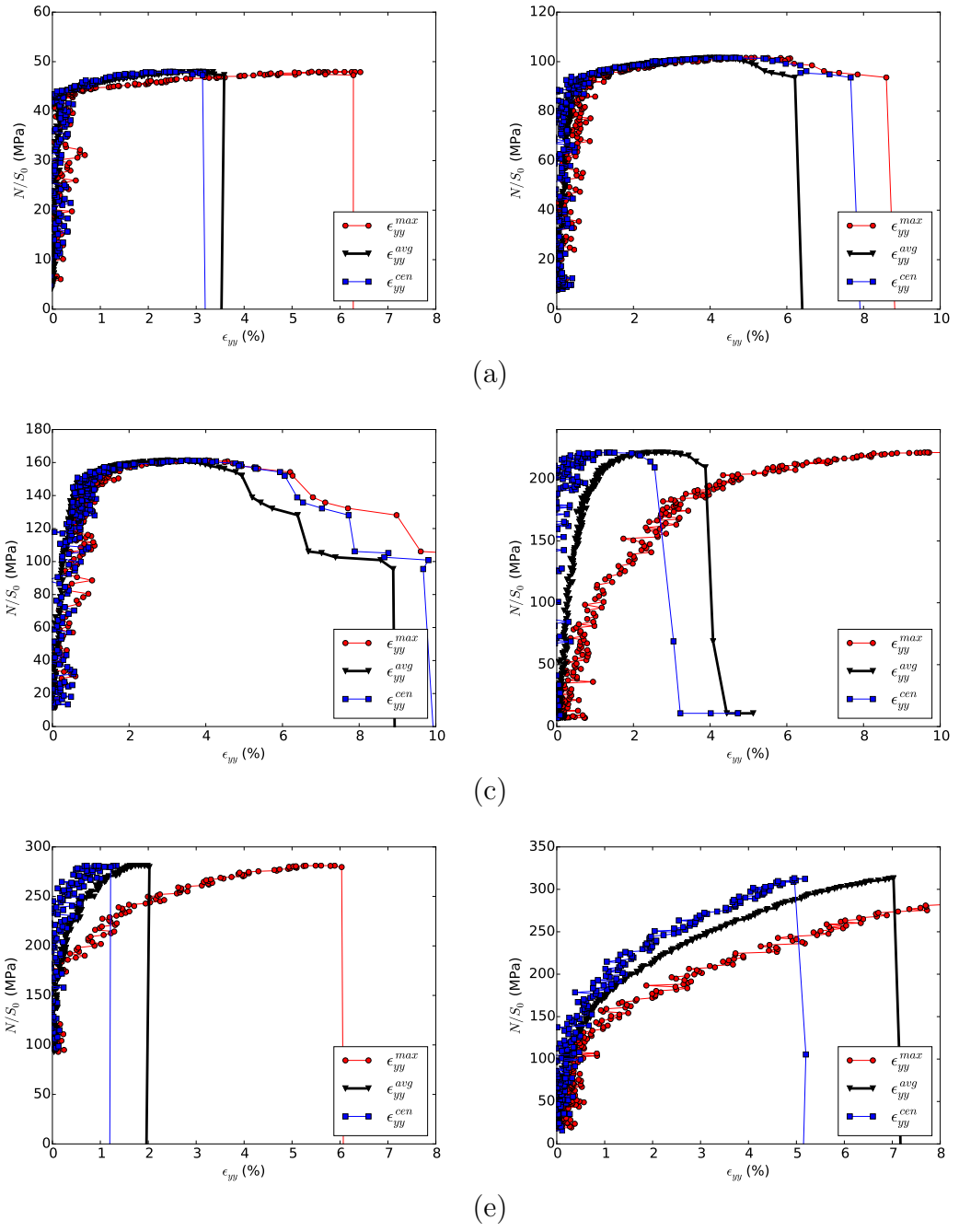

Figure 107: Normalized force versus ϵyy plot resolved for experiments for different orientations (a) 0° (b) 15° (c) 30° (d) 45° (e) 60° (f) 75° at center, maximum locations and average over the minimum section after prestraining in shear($\alpha = 0°$

APPENDIX B

The following relationships hold between the anisotropy coefficients entering the quadratic Hill criterion (1) and the strain ratios defined in Section 2.3.3.2:

$$\frac{h_F}{h_E} = 1 - \frac{3(R^E R^F - 1)}{R^E R^F - 2R^E - 2} \tag{21}$$

$$\frac{h_L}{h_E} = 1 - \frac{3R^E(R^F - 1)}{R^E R^F - 2R^E - 2} \tag{22}$$

$$\frac{h_{FL}}{h_E} = -\frac{1}{2}\frac{(2R^{LF} + 1)(R^E + 1)}{R^E R^F - 2R^E - 2} \tag{23}$$

$$\frac{h_{EL}}{h_E} = -\frac{1}{2}\frac{(2R^{LE} + 1)(R^E + 1)R^E}{R^E R^F - 2R^E - 2} \tag{24}$$

$$\frac{h_{EF}}{h_E} = -\frac{1}{2}\frac{(2R^{FE} + 1)(R^E R^F + 1)}{R^E R^F - 2R^E - 2} \tag{25}$$

These relations are adapted from [17]; see [54] for details. Since the yield criterion is expressed in terms of the stress deviator only, the yield locus is entirely determined by specifying the above five ratios to any one of the six anisotropy coefficients (here h_{E} was chosen). If the yield stress $\bar{\sigma}$ appearing on the right hand side of equation (1) is specified, say for uniaxial loading along the E direction, then the following constraint holds:

$$4h_{\mathrm{E}} + h_{\mathrm{F}} + h_{\mathrm{L}} = 6 \tag{26}$$

which in turn determines the absolute magnitudes of the h_i coefficients, hence the AED index in equation (4).